2017

An Investigation of the Native and Manipulated Effects of Shear Imbalanced Melt Flows during Molding Processes

Qi Li
Lehigh University

An Investigation of the Native and Manipulated Effects of Shear Imbalanced Melt Flows during Molding Processes

By

Qi Li

Presented to the Graduate and Research Committee

of Lehigh University

in Candidacy for the Degree of

Doctor of Philosophy

in

Mechanical Engineering

Lehigh University

January 2017

Certificate of Approval

Approved and recommended for acceptance as a dissertation in partial fulfillment of the requirements for the degree of Doctor of Philosophy.

_____
Date

_____
Accepted Date

Dissertation Advisor:

_____
John Coulter

Committee Member:

_____
Raymond Pearson

_____
Edmund Webb

_____
David Angstadt

Acknowledgements

I would like to thank my parents for their continuous support and encouragement throughout my studies. I would like to deeply thank my fiancée for her encouragement and constant offer of positive words whenever I ran into difficulty in research. I would also like to thank my close friends for being there for me over the years. I am thankful for our discussions leading to research ideas and surprising discoveries.

I am greatly appreciative of Professor John P. Coulter for his advisory and friendship during my graduate education at Lehigh. He has taught me a great deal about meaningful research and how to cultivate a positive perspective when research does not go according to plan.

Thank you to Professor Raymond Pearson, Professor Edmund Webb, Professor David Angstadt, Professor John Beaumont, and Professor Alicyn Rhoads for all of your advice and guidance. Your collective expertise has served to further my research to greater levels. I would to reserve special thanks to Professor John Beaumont and Professor Alicyn Rhoads for providing injection molding facilities, investigation materials, and experimental equipment at Erie. I would like to thank Eli Towne, Dick Towne, Laura Moyer, Binay Patel, and Muhammed Naazer Ashraf for their technical support and help in the injection molding and other related the experiments I conducted at the Mechanical Engineering and Mechanics, and the Materials Science Engineering Departments at Lehigh University. Thank you to Tyler Skiba for his previous research contribution to the current investigation. Thank you to Sung Rok

Choo for his contributions to the real-time monitoring study in this project. I would also like to thank Israd Jaafar for his advisory in writing and wording of this Dissertation.

Thank you to the members of the Manufacturing Science Laboratory past and present, including John Rodgers, Majed Alsarheed, Chandresh Thakur, Ali Rajhi, Alaauldeen Duhduh, Jiheng Zhang, and Peng Gao.

Table of Contents

List of Tables

List of Figures

List of Equations

Abstract

Runner-based shear imbalances is a common feature in injection molding of polymers. Its effect on the melt flow is a main concern, causing problems even in cases where the mold cavities are naturally balanced and the geometry is traditionally defined. Melt rotation technology has been applied to address this issue, as well as that of shrinkage and warpage.

In the present study, this technology is taken several steps further with the goal of exploring and solving product quality variations that is attributed to the imbalanced polymer melt flow problem. Molding trials were conducted with and without melt rotation using several types of polymers, and the resultant effects on the physical, thermal, and mechanical properties of the molded products were explored. The study found that important product quality parameters such as crystallinity and tensile modulus vary significantly throughout conventionally molded products, and that these can be dramatically altered by implementation of the melt rotation technology. For semi-crystalline materials, specimens taken from product regions associated with higher melt flow shear levels exhibited higher crystallinity levels as well as higher tensile moduli due to the localized shear rate variation.

This work also includes visual analysis of how shearing of the polymer through the runner system affects mold filling in real-time. Multi-cavity molding is widely used to increase manufacturing efficiency by primarily reducing time and cost. It is mainly generally accepted that the optimal runner design is one that is geometrically balanced. However, is now also understood that imbalances are also due to the

shearing of the polymer melt as it is pushed through the runner system. To gain a deeper understanding on how this occurs, a custom-built mold with transparent mold inserts and runner system was utilized. Cavity filling of polymers into different cavity designs was captured using a high-speed camera. Analysis of this visual data would provide aid in finding methods to mitigate the non-uniform behavior of molten polymers undergoing shear-thinning. Molding trials were implemented and experimental results have been found to support the effectiveness of the melt rotation technology.

The results in this work also show the potential of adopting the technology for a broader range of applications that require a homogeneous polymer melt flow for ensuring efficient manufacturing and desired quality products.

1 Introduction

1.1 Problem Description and Opportunities

Injection molding has, for decades, been one of the most successful methods for mass production. Most polymeric materials, thermoplastic or thermoset, can be formed into products via injection molding. [1] A main advantage of injection molding is that the products can be finished in short cycle times that ranging within minutes or even seconds. Due to the high volume of products manufactured, another advantage is its low operation cost per piece. The process essentially requires feeding raw polymer in the form of pellets into an injection molding machine, which melts and plunges the material into cavities within a mold. The solidified product is then ejected. This molding cycle is repeated sequentially. Once the optimum operating parameters are set, the only required manual input is ensuring raw material is sufficiently fed, and monitoring of the operation to avoid possible clogging.

Polymer injection molding is a huge industry. In 2010, the global industrial injection molding market was estimated to consume up to 79 million tons of polymers, with a market value of about 168 billion US Dollars. This amount is still growing, and is expected to pass 116 million tons by 2018. [2]

In addition to low cycle times, a main reason that facilitates injection molding wide use in mass production is the use of multi-cavity molds, allowing the production of multiple-products in each molding cycle. An essential requirement for this is a geometrically balanced runner system. However, even in such a case, the runner

system still has been shown to have localized rheological problems that cause the final products to have non-uniform shape and quality. The main problem is attributed to an inherent shear imbalance of the melt as it flows through the runner. In an industry, which seeks an increasing level of consistency and reliability, further understanding through research is vital to find a viable solution to this problem.

During an injection molding cycle, the polymer melt travels through a runner system to reach the mold cavity. The melt rheology within the runner has been studied and found to have an inherent problem. The major cause is the melt's shear rate gradient across the radial cross section of the runner as illustrated in Figure 1-1. The melt experiences high rates of shear close to the runner wall, and relatively low rates of shear towards the chamber's core section. [3] [4] [5]

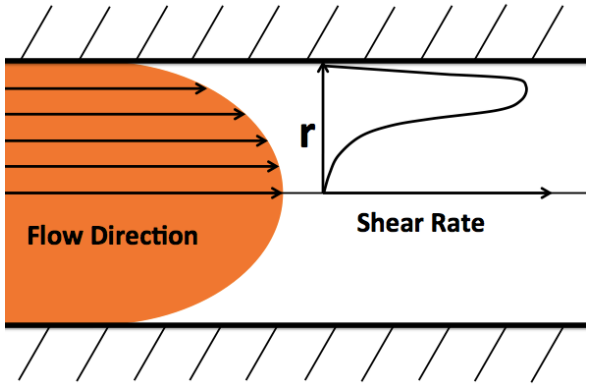

Figure 1-1. Shear rate variation during melt flow through a runner section

As polymers typically exhibit a shear-thinning behavior (viscosity that drops with increasing shear rate), the melt portion that lies within the higher shear rate region acquires a lower viscosity and higher velocity (and temperature). A melt flow imbalance is thus be generated resulting in products that have non-uniform properties,

both within a single molded product and between products from multiple cavities. [3] [4] [5]

As shown in Figure 1-2, high shear regions exist near runner walls while relatively low shear regions are found in the center of the flow channels. When the melt flow reaches an intersection, such as a T-junction leading to secondary runner channels, it will be split from the geometrical center, causing the asymmetric shear distribution in the melt flow in the secondary runners. [6] (Figure 1-2 (b) and Figure 1-3)

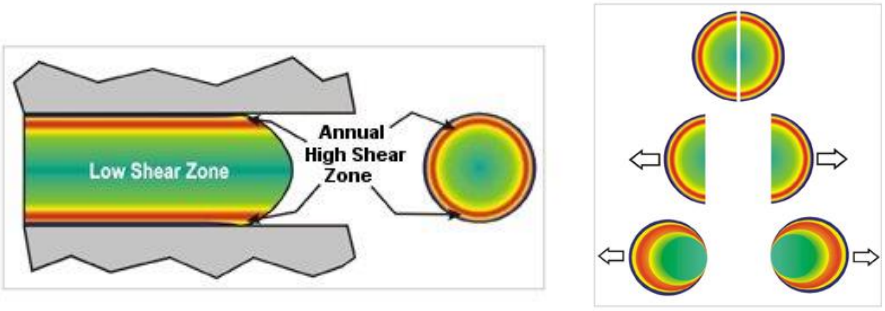

(a) (b)

Figure 1-2. (a) Profile view of the shear induced melt flow in a primary runner; (b) Shear flow splitting that occurs at T-section junctions leading to secondary runners [6]

When the melt flows through a second T-junction leading to tertiary runners, it further splits again. When this happens, the high shear region, which is hotter and has lower viscosity, fills the associated inner mold cavities faster than the low shear region, which is cooler and has higher viscosity, fills the associated outer mold cavity. This problem, as shown in Figures 1-3, with example results as shown in Figure 1-4a,

happens even if the multi-cavity geometry is “naturally balanced” as traditionally defined.

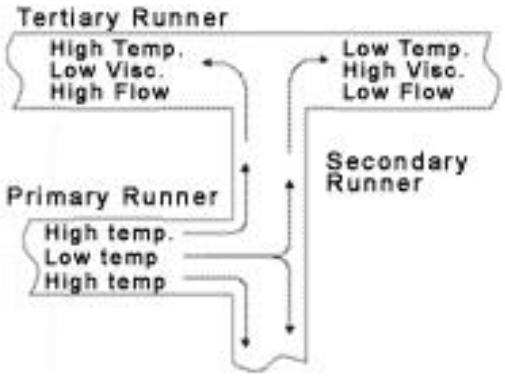

Figure 1-3. Shear flow distribution in the primary, secondary and tertiary runners [7]

If cavity filling was the only goal, alternative machine level processing condition adjustments could be considered to promote complete physical product formation even in the last (in this case outer cavity) tooling regions reached by the molten polymer. Even if this were successful, however, the polymer melt ending up in different product cavities (and even different regions in a single-cavity) would have been exposed to dramatically different temperature and shear histories during processing. This could potentially lead to significant differences in critical product quality attributes, such as size, weight, crystallinity and mechanical properties. [6]

To address the problem described above, Melt Rotation Technology (MRT) has been developed at Beaumont Technologies Inc. The basis for melt rotation is the intelligent modification of runner flow paths to reconfigure or “rotate” high and low shear laminates in the melt flow to reorganize the resultant spatial material shear history distribution. As shown in Figure 1-4 (b), the appropriate implementation of melt rotation technology can lead to more balanced cavity filling and melt rheology.

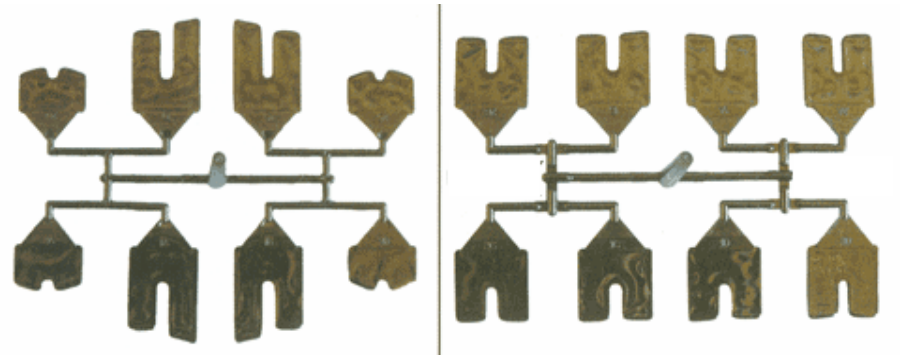

(a) (b)

Figure 1-4. Imbalanced filling (a) and balanced filling (b) of the same cavity system; (a): molded without melt rotation, (b): molded with melt rotation [5]

As supported by previous researches, MRT is an efficient method to solve the shear imbalance problem. MRT has existed in many forms for years, and it has been shown to have the ability of altering physical, mechanical and thermal property distributions of the injection molded samples. Unfortunately, none has been completely accepted as of yet by the industrial world. As a result, shear induced problems still exist and often detrimentally affect the quality of injection molded products. For MRT to be realized, further evidence is needed to validate the product quality enhancement benefits.

1.2 Dissertation Objectives

The overall objective of this research is to further probe shear induced imbalance effects and explore MRT as a means to address associated processing and product quality problems. In this research, injection molding with the application of MRT was employed in order to modify and optimize the injection molding conditions and results. The research included analysis of data acquired through tests that include tensile testing, Differential Scanning Calorimetry and Wide Angle X-ray Scattering.

Cavity filling during injection molding was also monitored in real time with a high speed camera through specially designed mold bases and inserts, in order to further prove the existence and effects of shear induced filling imbalances.

This research has focused on the following two major related objectives:

1. Realizing modified properties throughout products by optimizing runner conditions and applying Melt Rotation Technology

In order to further probe the shear induced imbalance phenomena and explore the benefits of MRT, specific polymers were selected and injection molded with and without the application of the technology. Selected molded product properties were then tested and compared. This was done with both single-cavity and multi-cavity molds.

2. Real time monitoring of cavity filling during injection molding

The main goal of this component of the research was to capture the video of traditional injection molding processes in real time and obtain some useful data to support the shear induced imbalance theory.

1.3 Overall Investigation Approach

The major phenomenon associated with shear imbalances to date has been non-uniform filling results in molding cavities, even in cases where the cavities are balanced in space and position. Researchers have extensively studied this problem. However, shear induced problems still exist and there is yet a single universally accepted solution.

In this study, several polymeric materials were selected and injection molded into both single-cavity molds and multi-cavity molds. The molded product properties were analyzed and compared between the samples, which were taken from high shear regions (with high-shear polymer flow) and those from low shear regions (with low-shear flow).

The target characteristics, which were expected to be distinguishable for comparison, include crystallinity, thermal and mechanical properties. Traditional Differential Scanning Calorimatry (DSC) and flash DSC were applied for cristallinity study and thermal behavior analysis. Also by utilizing Wide Angle X-Ray Scattering (WAXS), additional data was obtained related to crystallinity variation. For mechanical property investigation, tensile testing was applied to dog bone shaped specimens molded from different polymer materials.

For both single-cavity molding and multi-cavity molding, MRT was used in the molding process and again, similar comparisons were executed to observe whether or not the technology could alter or minimize the differences between samples with various shear histories.

Real time monitoring of injection molding was used to develop a deeper understanding of shear induced imbalances. For this, a custom-built mold along with a variety of cavity inserts was utilized in conventional injection molding. As initially developed during previous studies [8] [9], a steel mold set served as the mold base. On both sides of the mold base, transparent windows, made from polycarbonate (PC) were incorporated. This allowed light from one side of the mold base to penetrate

through the windows. A high speed camera on the other side of the mold base then captured the cavity filling processes.

Polarized light could be introduced for the simultaneous monitoring of both flow front progression and molecular orientation during the process.

The molding system design and the molding processes were also simulated analytically by using Autodesk® Moldflow, in order to provide theoretical basis to support the shear imbalance and melt rotation study.

1.4 Structure of The Dissertation

This dissertation is composed of three major sections. These are the scientific background and related prior studies, the progression of the current research, and conclusions and future recommendations.

The three general sections of the dissertation are distributed into 9 chapters. Chapter 1 and Chapter 2 provide the motivation and the research background of this study. In Chapter 1, problems in the current injection molding industry are indicated and an innovative solution to the problems is suggested simultaneously. Chapter 2 illustrates the development of the related scientific fields. Detailed introductions of this research background, such as the development of polymer injection molding, illustrations of crystallinity and related polymer properties, the problems caused by shear imbalances during injection molding, the methods for mitigating the imbalance problem, and the efforts previously accomplished at Lehigh University, are included.

From Chapter 3 to Chapter 6, the progress of this research is elaborated on and explained. Chapter 3 focuses on the selection of research materials and proposing the essential experiments for product property analysis. In Chapter 4, traditional injection molding processes for making testing samples are introduced. Chapter 5 provides details of the real-time monitoring of injection molding processes. The efforts of how to create new molds and set up the monitoring system are explained. For Chapter 6, there are four major experiments, which are Differential Scanning Calorimetry (DSC), tensile testing, Flash DSC and Wide Angle X-Ray Scattering (WAXS), emphasized for analyzing property variations among samples with different shear imbalanced results.

The remaining chapters in the dissertation are presented to explore and discuss the results from the experimental analysis. In Chapter 7, testing results from DSC, Flash DSC, tensile test, WAXS and real-time monitoring study are provided and discussed. Characterizations, such as crystallinity, mechanical property and real-time resin progressions during injection molding, are verified and compared. Additionally, simulations from a theoretical point of view are important to this study. To support the shear imbalance concept, simulated polymer injection molding processes are explored using appropriate software in Chapter 8. Chapter 9 summarizes the entire research study and provides some conclusions. The expected conclusions of exploring shear induced imbalance and the melt rotation technology are generated, and new ideas or recommendations are presented for future studies.

2 Related Scientific Development

2.1 Injection Molding

An injection molding machine consists of two main parts, which are the feeding/injection unit and the clamping unit. (Figure 2-1)

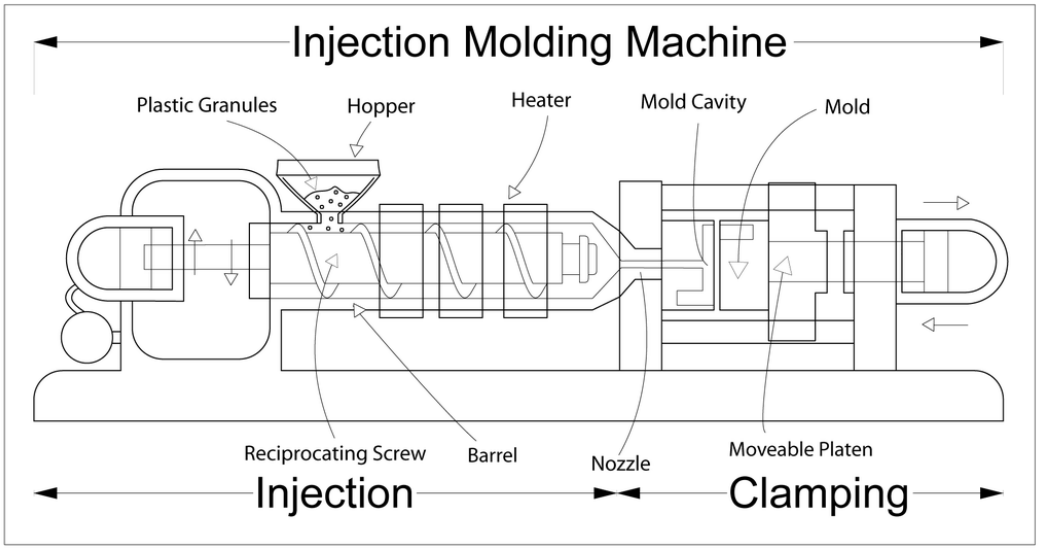

Figure 2-1. Common components of an injection molding equipment [10]

The injection unit includes the material hopper, where the raw pellets are fed into the equipment. The clamping unit usually includes ejection pins, used to push the cooled products out of the mold cavity.

The injection molding cycle is composed of several elements. These are, the feeding, heating, injecting, packing, cooling, and ejecting cycles. Figure 2-2 presents the entire cycle, which begins with the mold closing. The molten material is injected into a custom designed mold cavity or cavities, followed by packing and cooling procedures. During the packing and cooling stages, a pre-determined packing pressure is applied on the molded products in order to minimize defects. These defects include,

for example, shrinkage of the material as it cools down, and solidifies in this cavity. In the next step, the injection screw turns back to reload the molten raw material to the front of the screw, for the next injection cycle. Once the product is sufficiently cooled down as determined by the operator, the mold opens and ejects the products. [11] [12]

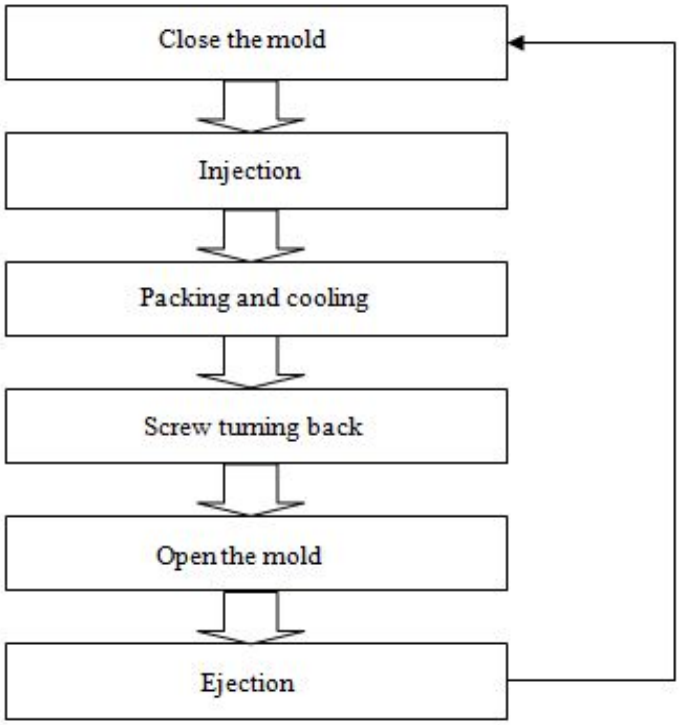

Figure 2-2. Injection Molding Cycle [11]

Injection molding requires certain parameters to be determined before hand. These parameters include injection speed, pressure, temperatures, packing pressure, cooling time, and mold temperature. These parameters are generally determined by both the properties of the polymer material and quality attributes of the final product.

The injection molding market has grown tremendously over the years, especially a world market that requires high volume production of end-user and industrial

products. The global production of injection molded products was over 79 million tons in 2010. The compound annual growth rate of the market wealth is expected to be at least 5.3% from 2013 to 2018, where by then the market value is expected to reach 252 billion US Dollars. [2]

The pacific rim region was the largest injection molding market in 2011. Asia specifically, holds 37.2% of the global market, followed by North America, and Europe. The huge boom of polymer use in housewares and personal care products as well as the rigid packing industry has significantly contributed to this growth. [2]

2.2 Crystallinity and Related Polymer Properties

2.2.1 Polymer Classifications

The most common way of classifying polymers is to separate them into three groups: thermoplastics, thermosets, and elastomers. [13]

A thermoset plastic solidifies irreversibly when heated and cannot be reshaped by heating. Thermosets usually are three-dimensional networked polymers, in which there is a high degree of cross-linking between polymer chains. The cross-linking structure restricts the motion of the chains and leads to a rigid material.

Elastomers are rubbery polymers that can be stretched easily to several times their un-stretched length, and rapidly return to their original dimensions when the applied stress is released. Elastomers are also cross-linked, but they have a low cross-link density. The polymer chains still have some freedom to move, but are prevented from permanently moving relative to each other by the cross-links.

In thermoplastics, the molecules are held together by relatively weak intermolecular forces, so that the material softens when exposed to heat and returns to its original condition when cooled. [14] Thermoplastic polymers can be repeatedly softened by heating and solidified by cooling. This research focuses on this polymer type.

2.2.2 Crystallinity and Influencing Factors

Thermoplastic polymers have variations of microstructures, such as amorphous, crystalline or semi-crystalline, which depend on their molecule arrangements.

In general, an amorphous structure is composed of large numbers of randomly aligned polymer molecules (Figure 2-3 (a)), and the molecules, which are in neat and orderly alignments, form the crystalline regions in polymer products (Figure 2-3 (b)).

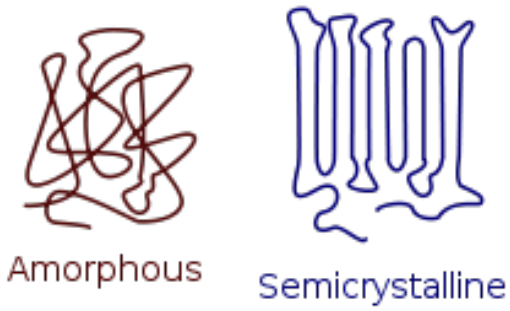

(a) (b)

Figure 2-3. Amorphous structure (a) and crystalline structure (b) formed by polymer molecule chains [15]

In crystalline structures, molecule chains are likely to stretch out. However, they cannot always stretch in straight lines. In fact, very few polymers can stretch out perfectly straight. [16] [17] [18] Instead, most polymer chains can only stretch out for a short distance before they fold back on themselves. (Figure 2-4) For instance, the

length molecular chains in polyethylene will stretch before they fold back about 100 angstroms. [16] [17] [18]

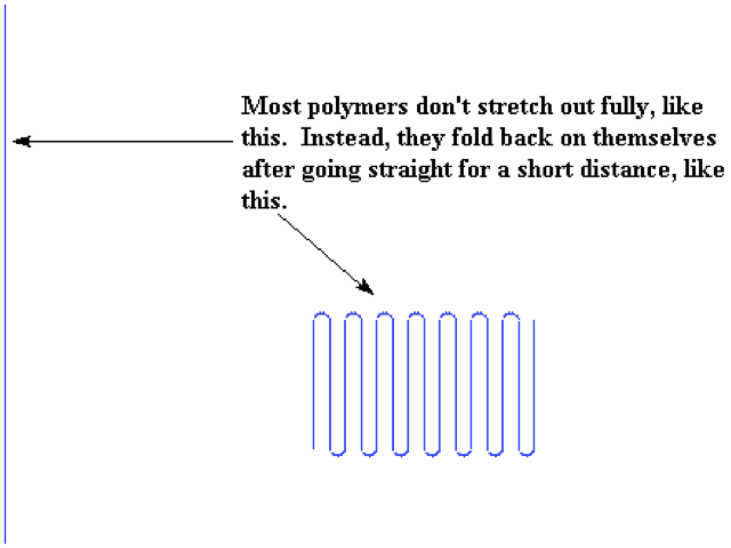

Figure 2-4. Molecule chains stretch out and fold back, other than forming a straight line [16] [17] [18]

Polymer molecules also typically form these folded chains in stacks. Stacked molecule groups, which are crystal lamellae existing in three dimensions, form the crystalline spherulite or crystalline unit in polymers. Sometimes, a part of a chain is not included in this crystal lamella, but in the amorphous regions. [16] [17] [18] Some of the escaped molecule chains are able to find a way back into the original lamella, but, more often, these chains will stretch out into an adjacent lamellae, or remain in the amorphous region. As a result, polymers are not entirely crystalline (Figure 2-5). In between the crystalline lamellae, there are regions, where there is no order to the arrangement of the polymer chains. These disordered regions are the amorphous regions.

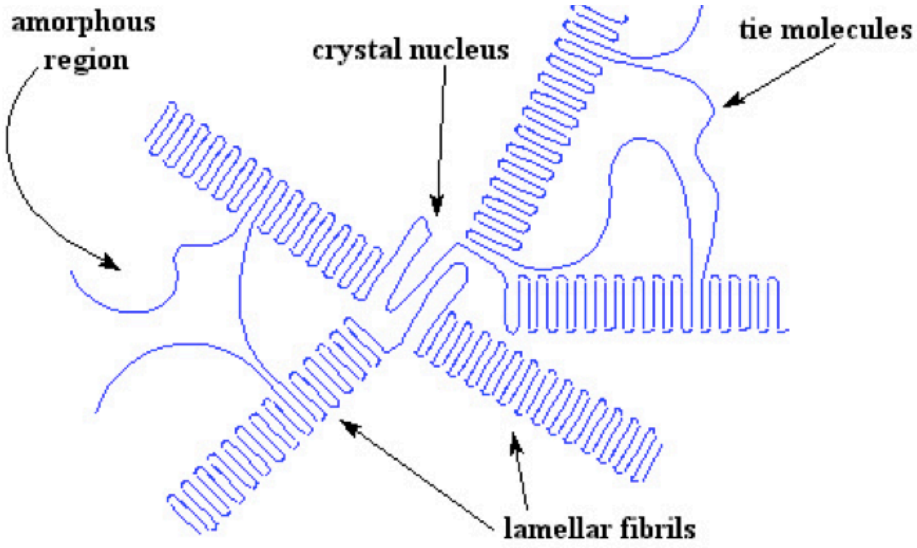

Figure 2-5. Example of polymer crystalline spherulite and adjacent amorphous regions [16] [17] [18]

Crystalline polymers are usually composed of both amorphous and crystalline regions, and crystallinity is utilized to describe the percentage of the crystalline parts in polymers. Hence polymers are usually a mix of amorphous and crystalline regions, but some are highly crystalline and some are more amorphous. [16] [17] [18] Some of the polymers that tend toward the extremes are listed in Table 2-1.

Table 2-1. Polymers in more crystalline form or amorphous form

Highly Crystalline Polymers	Highly Amorphous Polymers
Polypropylene	Poly (methyl methacrylate)
Syndiotactic polystyrene	Atactic polystyrene
Nylon	Polycarbonate
Polyketones	Polybutadiene

Two major factors, polymer structure and intermolecular force, influence polymer crystallinity. Tacticity is used to describe the structure arrangement of the substituents along the polymer molecule chains. Figure 2-6 provides the tacticities of polypropylene.

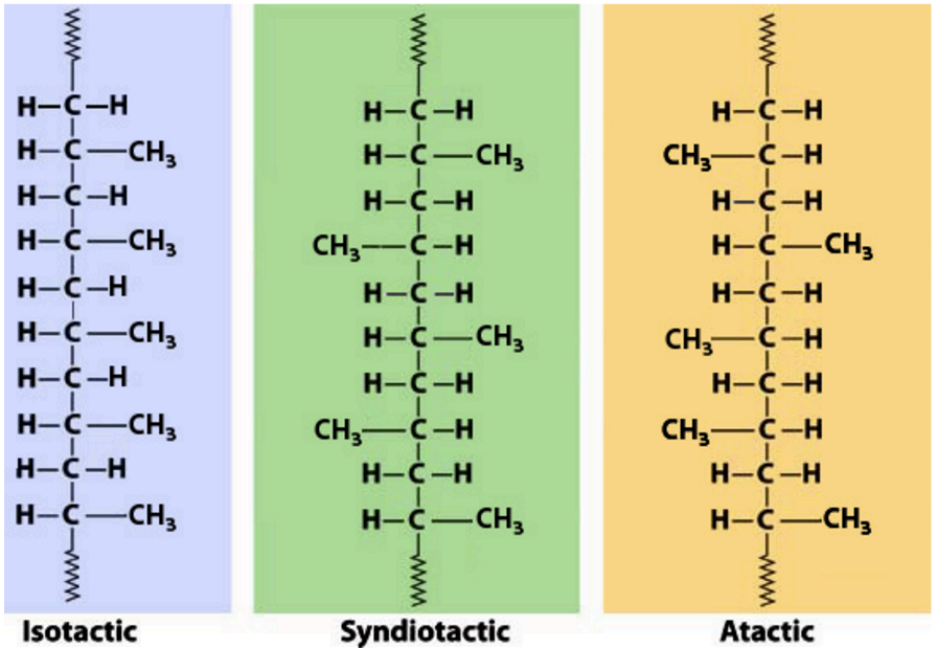

Figure 2-6. Taciticity of polypropylene molecule [19]

As shown in Figure 2-6, there are three types of tacticity: isotactic, syndiotactic, and atactic. For the isotactic polymer chain, all of the substituents are located on the same side of the macromolecular backbone, while the substituents have alternate positions along the chain for syndiotactic structures. In atactic molecules, the substituents are located on sides randomly positioned along the chain backbone. Not all polymers have all three forms of tacticity. For example, polystyrene cannot form the isotactic structure. (Figure 2-7)

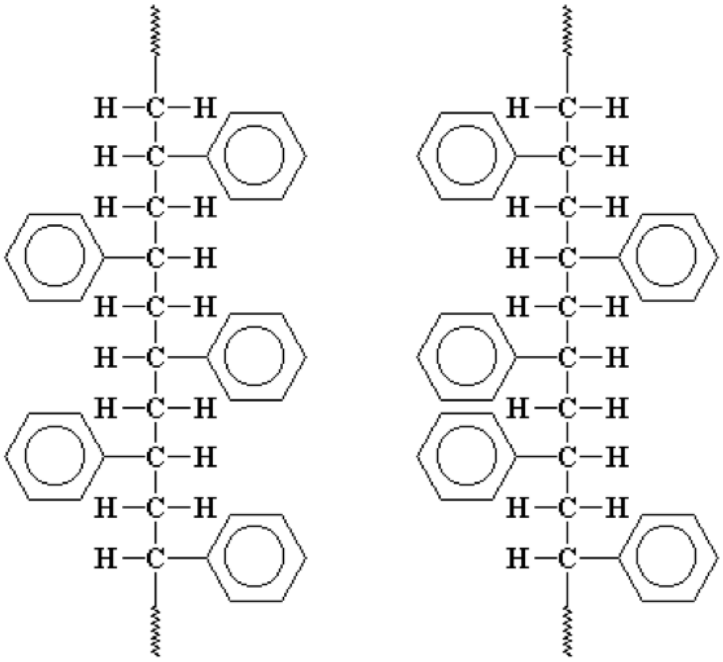

(a) (b)

Figure 2-7. Tacitcity of polystyrene molecule [16] [17] [18]

In general, more regular backbone structures support a polymer material that is more crystalline, since it is easier for the molecules to pack into a crystal form. Isotactic, syndiotactic polypropylene, and syndiotactic polystyrene have a more ordered molecular backbone structure. The methyl groups are all on the same side of the molecule backbone for isotactic polypropylene. The methyl groups and the phenyl groups in polypropylene and polystyrene fall on alternating sides of the chain. In this way, it is very easy for the polymer molecules to form into crystals. However, for atactic polypropylene and polystyrene, there is no such order for the methyl and phenyl groups. As a result, the chains do not pack very well. Hence this causes atactic polypropylene and polystyrene to be very amorphous. [16] [17] [18]

Intermolecular force is another key factor that can affect a polymer is its tendency to form crystals. Taking nylon for instance, the polar amide groups in the backbone chain of nylon 6'6 are strongly attracted to each other, resulting in the formation of strong hydrogen bonds between molecules (Figure 2-8). This strong bonding causes the molecule chains to line up in an orderly fashion, allowing the polymer to form stronger crystal structures.

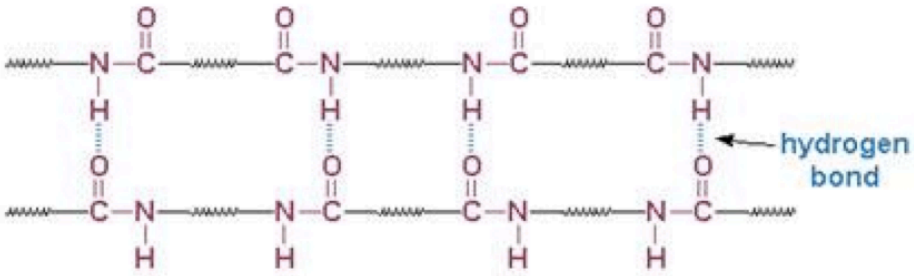

Figure 2-8. Parallel nylon chains are bound together through hydrogen bonding between amide groups [21]

A polyester, poly (ethylene terephthalate) (PET), is another example. The polar ester groups hold the polyesters into strong crystals. (Figure 2-9)

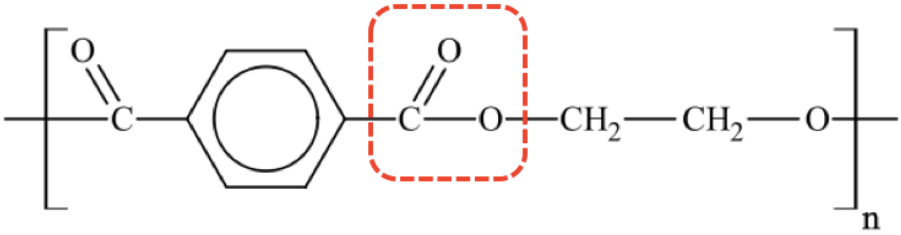

Figure 2-9. Ester function group in poly (ethylene terephthalate) [22]

Furthermore, the aromatic rings in the backbones are likely to stack together, making the crystal even stronger. [16] [17] [18] (Figure 2-10)

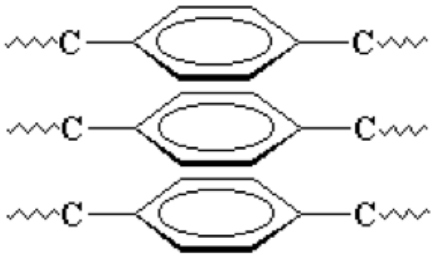

Figure 2-10. The aromatic rings or phenyl rings in PET stack close to each other [16] [17] [18]

The cooling rate also influences crystallinity. Slow cooling provides more time for greater amounts of crystallization to occur, however, fast rates, such as rapid quenches, may yield highly amorphous materials.

2.2.3 Crystallization and Properties Related to Crystallinity

The process of forming crystalline regions in polymers is called crystallization. From a thermodynamic point of view, the crystalline state exists at a lower free energy state than the movable liquid when the temperature drops below the equilibrium melting point, T_m^{∞}, which represents the melting point of an infinitely long crystal of finite molecular weight.

In Figure 2-11, the changes of the Gibbs free energy (G) with temperature, of a melt and crystal is schematically shown. For any spontaneous phase transformation, which is usually under a constant temperature and pressure, ΔG should be a negative value. Hence, the process of crystallization is spontaneous below the equilibrium melting point, T_m^{∞}, while the reverse process, which is from crystal to liquid, is spontaneous above T_m^{∞}. The equilibrium condition exists between crystal and liquid, as the value for both phases are $\Delta G = 0$. (Equation 2-1)

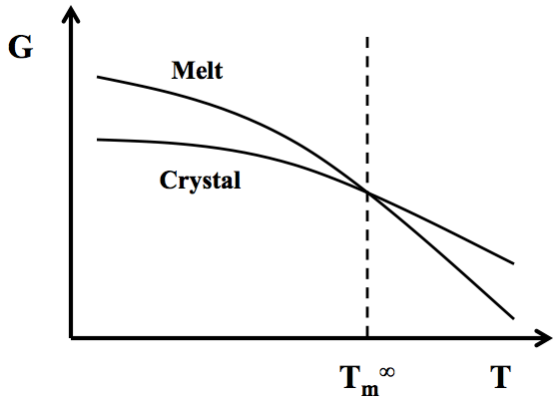

Figure 2-11. Change of Gibbs free energy vs. temperature, equilibrium at T_m^∞

$$\Delta G = \Delta H - T \cdot \Delta S = 0, \text{at } T = T_m^\infty \quad \text{[Equation 2-1]}$$

During the general crystallization that most semi-crystalline polymers experience, the fundamental structure is in the shape of a lamellar crystal. Storcks et al. firstly reported and gave evidence of the lamellar structures for the vast majority of semi-crystalline polymers crystallized from the bulk. [23] [24] Schlesinger and Leeper, Jaccodine, and several other researchers concluded that lamellar crystal habit is the dominant structure mode of crystallization for a large number of polymeric materials. [23] [25] [26] [27] [28] [29]

At the start of polymer crystallization, the first action to take place is primary nucleation, which can be defined as the formation of a small amount of crystalline regions due to fluctuations in material density or order. [23] [30] It is followed by the continuation of crystallization on the growth surface by inducing more and more polymer molecules or crystal lamellae. This is referred to as the secondary nucleation. In order to form the stable nuclei in primary nucleation, the free energy barrier to crystallization needs to be overcome. The size of the critical nucleus depends on this

free energy barrier, as larger critical nuclei require a longer time to create. [23] [31] (Figure 2-12)

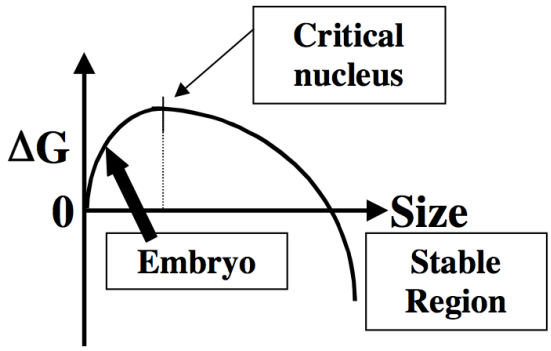

Figure 2-12. The variation of free energy with nucleus size [23] [31]

Figure 2-12 shows the reduction of the overall Gibbs free energy to form a solid phase and maintain equilibrium for nucleation.

In any nucleation process, the free energy is given by:

$$\Delta G = \Delta\mu_v + \Delta\mu_s \qquad \text{[Equation 2-2]}$$

where ΔG is the total change of Gibbs energy for the formation of the nucleus, $\Delta\mu_v$ is the change of Gibbs free energy for volume energy, and $\Delta\mu_s$ is the change of Gibbs free energy for surface energy. $\Delta\mu_v$ and $\Delta\mu_s$ can be described as:

$$\Delta\mu_v = \frac{4}{3}\pi r^3 \Delta G_v \qquad \text{[Equation 2-3]}$$

$$\Delta\mu_s = 4\pi r^2 \gamma \qquad \text{[Equation 2-4]}$$

where r is the radius of the spherical nucleus, ΔG_v is the change of Gibbs free energy per unit volume of the solid phase, and γ is the surface energy per unit area. From

Equations 2-2, 2-3 and 2-4, the total change of the chemical potential for the formation of the nucleus, ΔG, can be shown as follow: [32]

$$\Delta G = \Delta\mu_v + \Delta\mu_s = \frac{4}{3}\pi r^3 \Delta G_v + 4\pi r^2 \gamma \qquad \text{[Equation 2-5]}$$

After nucleation, it is common to possess three-dimensional symmetry for polymers. [23] [33] [34] These types of spherical structures consist of radial fibrils originating from the primary nucleus at the center, and the structure can be observed using polarized optical microscope. [23] [35]

The fibrils contain lamellae radiating outward with the chain folding direction generally being transverse to the growth direction. The tie chains between these lamellae play an important role in improving the mechanical properties with these bridging units, which are inter-lamellar or inter-spherulitic in origin. These links help in maintaining the inter-lamellar connections when the polymer product is drawn. [23] [36]

Crystallinity influences many of the polymer properties. In general, higher crystallinity makes a material stronger, but it also makes it brittle, as the amorphous regions provide certain elasticity and impact resistance. [37] [38] A completely crystalline polymer would be too brittle to be used as a plastic. The amorphous regions provide the polymer its toughness, which is the ability to bend without breaking. [23] [39] Because of a more compact packing of aligned polymer chains, increasing crystallinity leads to the increase of strength and a more thermal stable state for

polymers, as the secondary bonding is enhanced when the molecule chains are closely packed and parallel. [15] [37] [38] [40] [41]

In most polymers, the combination of crystalline and amorphous structures forms a material with advantageous properties of strength and stiffness. The isotactic structure of polypropylene is the most widely used of the three tacticity types. Isotactic PP has a semi-crystalline structure that offers good mechanical properties such as stiffness and tensile strength. [42]

Additionally, different kinds of crystalline forms could be generated during crystallization for different kinds of polymers. This will be further illustrated in the material selection chapters.

2.3 Shear Induced Imbalance

Most polymeric materials share a similar characteristic, which is known as shear-thinning. [3] [4] [5] [43] [44] [45] [46] [47] It is also the dominant reason underlying the shear induced imbalance issue.

Viscosity, η, is defined as the shear stress, τ, divided by the shear rate, γ (Equation 2-6). For a Newtonian fluid, viscosity is a function of only temperature, T, so the stress varies linearly with shear rate (Equation 2-7). In the case of a shear-thinning fluid, the viscosity is no longer a function of only T, but also of γ. (Equation 2-8). Shear-thinning implies that as γ increases, η will nonlinearly decrease. [43]

$$\eta = \frac{\tau}{\gamma} \qquad \text{[Equation 2-6]}$$

$$\eta(T) = \frac{\tau}{\gamma} \qquad \text{[Equation 2-7]}$$

$$\eta(T,\gamma) = \frac{\tau}{\gamma} \qquad \text{[Equation 2-8]}$$

Shear-thinning behavior is more common than shear-thickening behavior in polymer melt flows. [48] For a cold runner system, the temperature in the molten material close to the runner wall should always be lower than the temperature of the center material. However, the heat distribution is also dominated by local shear rate. According to previous theories and researches, the amount of local heat generated is proportional to the square of the shear rate. [49] Since the highest shear rate exists in the outer rim of the material close to the runner wall and the shear rate influence overcomes the traditional heat gradient, the maximum temperature of the melt flow occurs in the regions near the frozen layers of the melt material. (Figure 2-13)

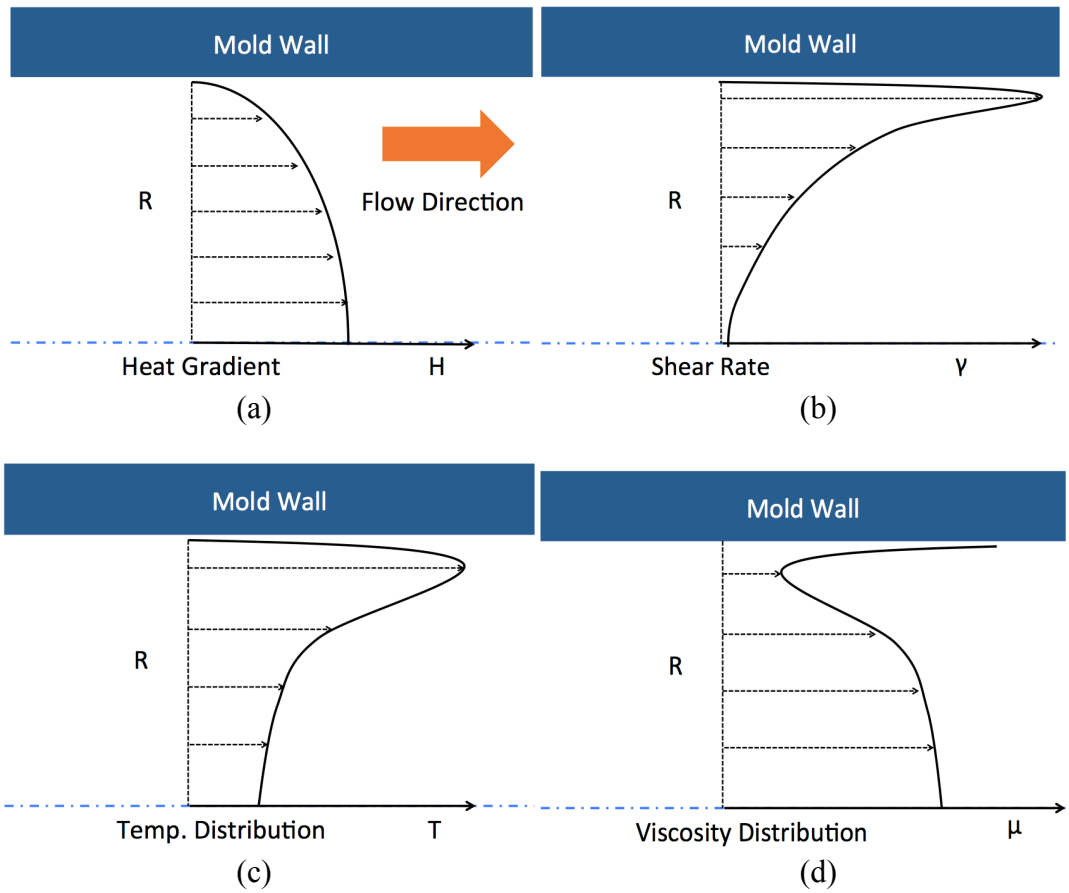

Figure 2-13. Heat gradient (a), and shear rate distribution (b); resulted temperature distribution (c), and viscosity distribution (d) of the melt flow in the runner system during injection molding [50]

Viscosity is in-turn influenced by the combination of direct shear-thinning behavior and the resulting heat distribution. These two factors cause the coiled polymer molecules to disentangle and flow around each other more easily. As a result, the melt material assumes that the minimum viscosity state is in the same regions where the maximum shear rate and the maximum temperatures occur. Since it is not sheared as much, the center molten material maintains a relatively higher viscosity condition. (Figure 2-13)

The consequence of all of this is the uniform injection pressure in the runner system will drive the melt flow with higher temperature and lower viscosity faster than the melt flow in the center with lower temperature and higher viscosity. When the melt flow splits from the primary runner into secondary runners, from secondary runners into subordinate runners, and then eventually driven into the product cavities, the melt flow entering each mold cavity has experienced a unique shear rate, temperature, viscosity, and flow rate history. This results in non-uniformed cavity filling. (Figures 2-14, 2-15 and 2-16)

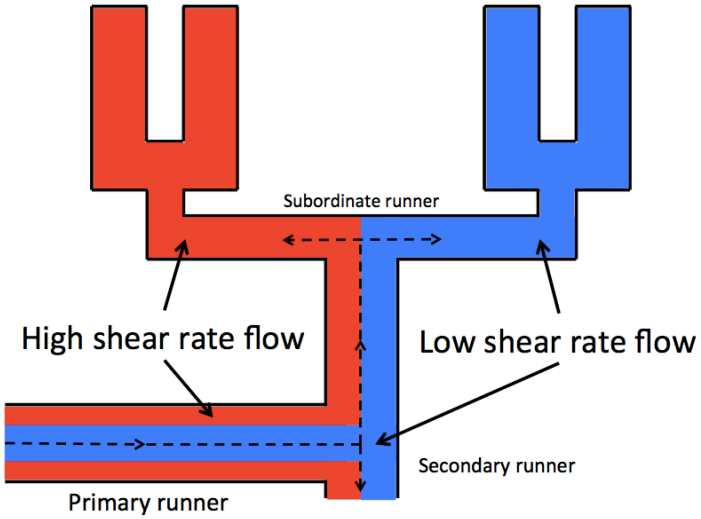

Figure 2-14. Shear rate flow distribution in runners and cavities during injection molding process for multi-cavity molding [50]

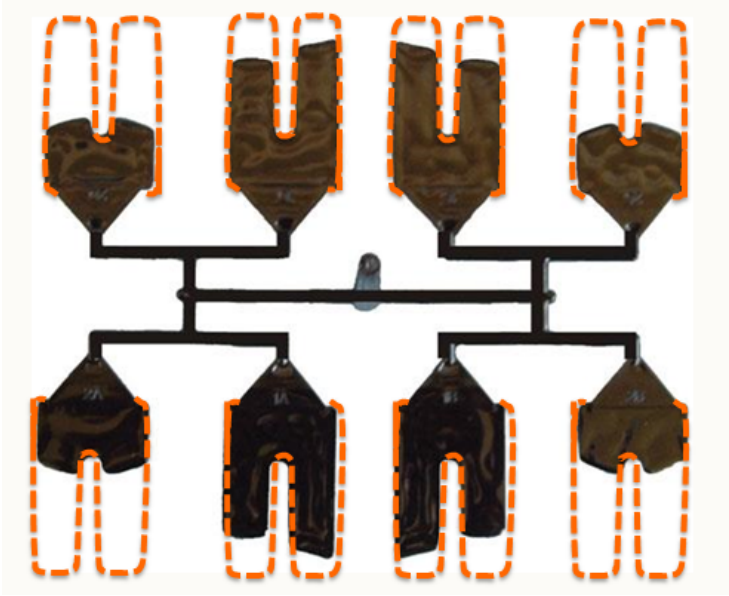

Figure 2-15. Imbalance fillings in “naturally balanced” mold cavities for multi-cavity molding [5]

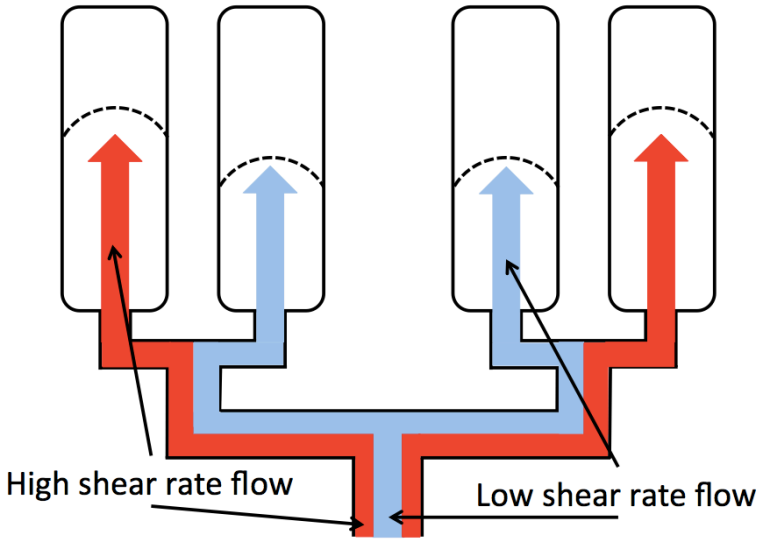

Figure 2-16. Shear rate flow distribution for multi-cavity molding [51]

Consequently, the cavity filling pattern will vary from what otherwise might be expected for both single-cavity and multi-cavity molds. For a single-cavity mold, such as a disc shaped product, the high shear rate flow fills the edge section of the disc cavity, faster than the low shear rate flow fills the center region. (Figure 2-17) Because

the high shear flow is hotter and has lower viscosity. As a result, a gas trap or a weld line may formed in the final product. (Figure 2-18)

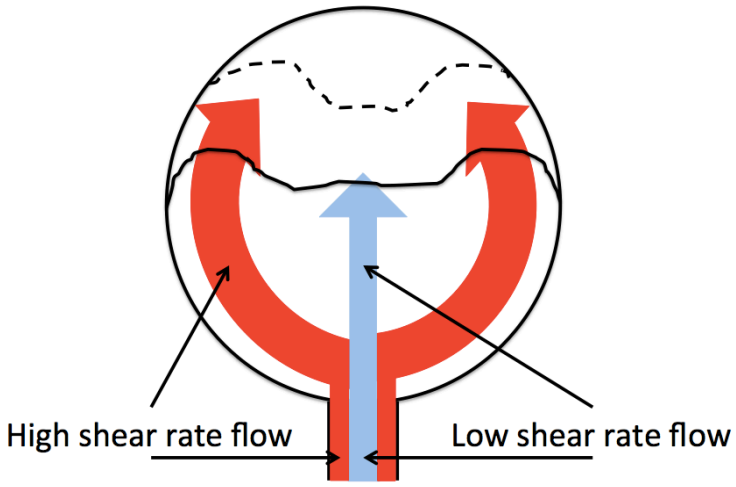

Figure 2-17. Shear rate flow distribution for single-cavity molding [51]

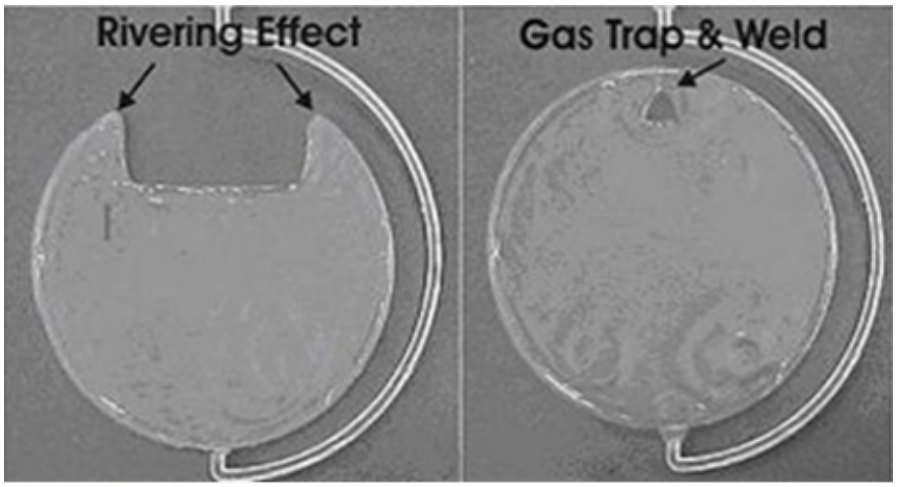

Figure 2-18. Shear imbalance filling patterns in single-cavity molding [52]

In essence, during processing, melt flow regions with higher temperature and lower viscosity travel through the runner system faster. This means that final molded parts in cavities filled by material with various shear rate, temperature and viscosity histories could have ranges of thermal properties, mechanical conditions and physical

characteristics, [53] even if the mold cavities are designed and positioned geometrically symmetric.

Shear rate imbalances that naturally occur with polymer flows influence the temperature, viscosity, and localized velocity gradients developed in runner systems, which in turn impacts the uniformity of the molded product properties, Melt Rotation Technology was originally invented and developed by Beaumont et al. [54] to solve the imbalanced filling patterns and optimize the molding results to be better balanced.

In order to further explore the ability to manage shear-induced imbalances with Melt Rotation Technology, several experimental studies have been conducted in this study.

2.4 Melt Rotation Technology

No practical solution has yet been developed to address and completely solve the shear imbalance problem elaborated in the previous section. [49] However, Melt Rotation Technology has been developed and applied to dramatically improve molding processes in this regard.

Melt Rotation Technology (MRT) was originally created and developed by Beaumont et al. to solve the shear imbalance issue observed between cavities in geometrically balanced multi-cavity molding solutions. [54] The basis for melt rotation is that the intelligent modification of runner flow paths will reconfigure or "rotate" high and low shear laminates in the melt flow in order to reorganize the resultant spatial material shear history distribution, resulting in more equalized or balanced properties in the final products. As shown in Figures 2-19 and Figure 2-20,

the appropriate implementation of MRT can lead to more balanced cavity filling, rheology, and molded part shrinkage. [53]

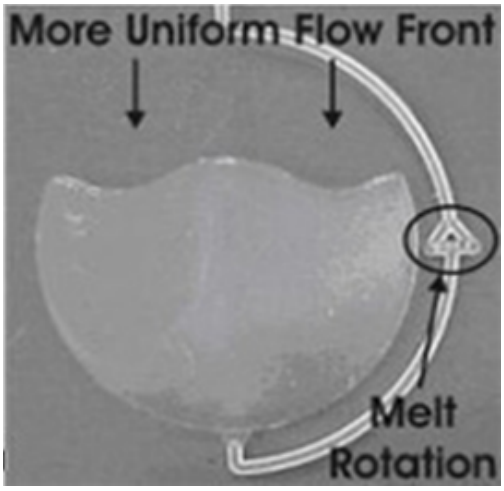

Figure 2-19. Modified filling observed in single-cavity molding process [5] [52]

(a) (b)

Figure 2-20. Cavity filling results: imbalanced (a), balanced (b)
(Same cavity system, but group (b) was molded with melt rotation technology) [5]

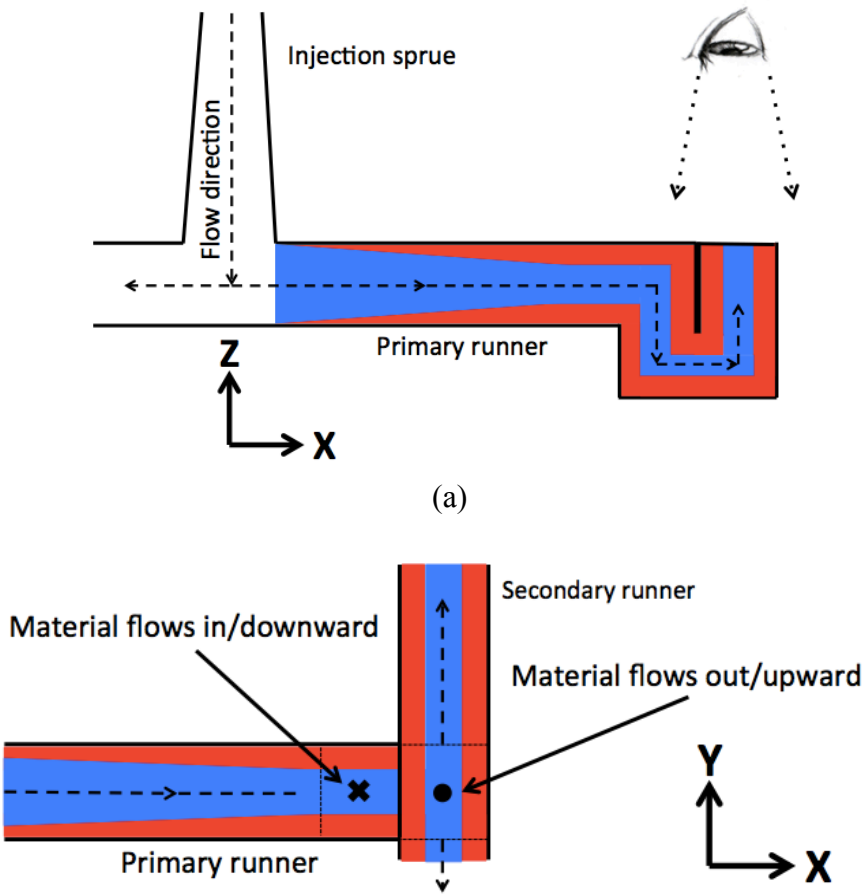

Figure 2-21. Melt Rotation Technology basic implementation at junctions (a); rotated flow results from the eye side view (b) [50]

Figure 2-21 provides one of the basic forms of melt rotation implementation. The melt rotation device is located at the runner junctions. As shown in Figure 2-21, the melt flow is directed downward and then upward to the level of the secondary runners. The consequence is that the melt flow is coming from the bottom and then flowing into the secondary runners, as if the primary runner integrates into the secondary runners from the z-direction rather than from the x-direction. As a result, the melt flow is rotated into the secondary runners. When the flow splits again into the subordinate runners, equal amounts of the material with the high shear flow and the

low shear flow travel into the subordinate runners, leading to a balanced filling and more uniform specimen properties. [49] (Figure 2-19 and Figure 2-20)

In the high volume manufacturing industry, it is vital to ensure quality and consistency in products. This includes shape, size, thermal history, and mechanical properties. Melt Rotation Technology has been proven in laboratory settings to meet almost all of the requirements.

2.5 Previous Lehigh University Research

2.5.1 Melt Rotation Studies

This investigation is the continuation, combination and further development of previous research conducted at Lehigh University. The overall goal is to further understand the shear imbalance theory and MRT, while simultaneously exploring the impacts of applying the technique.

Previous work has focused on filler migrations induced by shear imbalances. [55] [56] [57] [58] [59] [60] [61] [62] In Skiba's work for example, glass-filled polypropylene was injection molded using a multi-cavity mold system both with and without Melt Rotation Technology implementations. As the fillers are easily pushed to the melt flow regions where the particle collision is lower, the relatively low filler concentration was found near the mold walls where the shear rate is high. Meanwhile, the particle concentration was higher in the center regions of the melt flow. [49] With the application of MRT, this shear-induced variation in filler concentration level was effectively reduced. This yielded a more uniform filler distribution between parts from

different cavities, and also in sections of different distances from the cavity gate within one mold cavity. [49]

2.5.2 Injection molding with real time monitoring

The phenomenon of optical birefringence has been widely used in many studies, focused on stress analysis. However, it has not been widely been investigated in the injection molding process. In a previous research by Angstadt, a custom-designed mold with built-in windows for the observation of the polymer melt flow in the mold cavity was utilized. The melt flow was viewed through crossed polarizing films to reveal the birefringence pattern in the melt during the filling segment of the molding cycle. [8] (Figures 2-22 and 2-23)

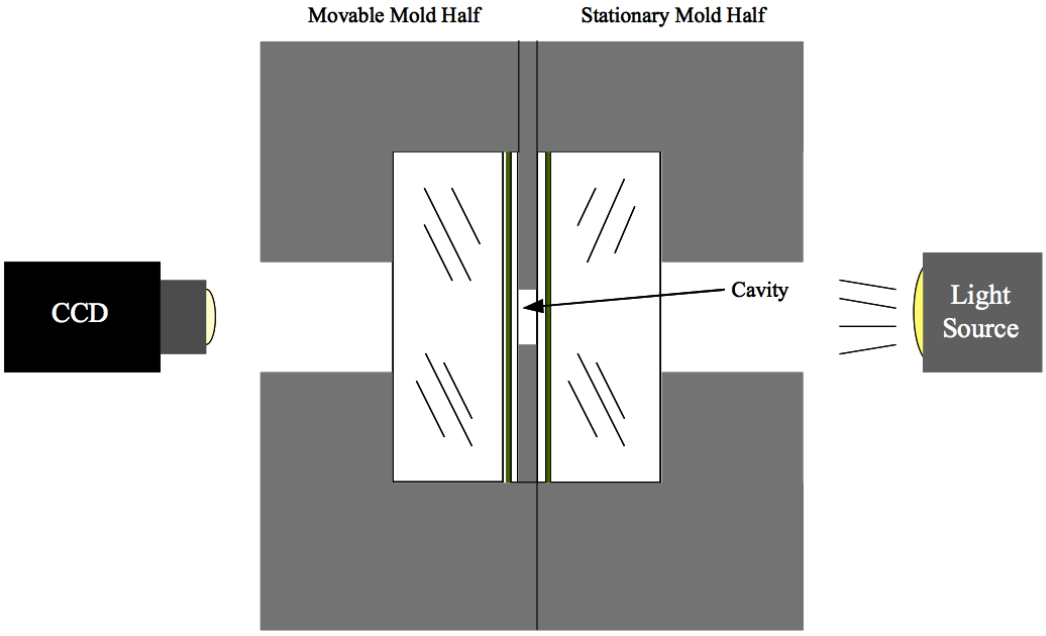

Figure 2-22. Schematic view of the mold with observation windows and the camera system

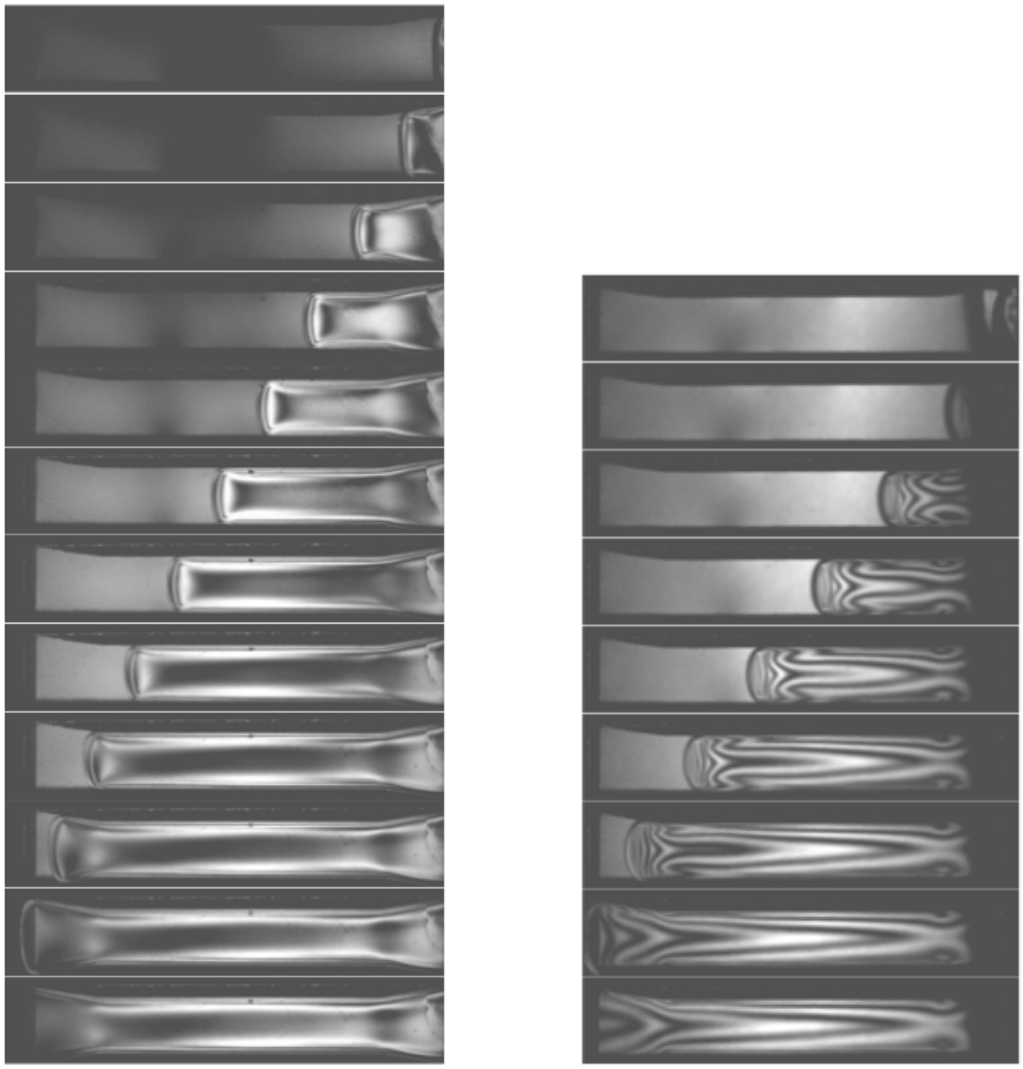

Figure 2-23. Birefringence pictures of mold cavity filling processes captured by the CCD camera for different polymers [9]

2.5.2.1 Birefringence and Tensile Studies in Vibration-Assisted Injection Molding

As shown in Figure 2-22, a high-speed CCD camera was utilized to video the birefringence pattern associated with cavity filling in real time. The captured images of birefringence provided the filling status and the information regarding the molecular orientation of the polymer under different processing conditions. [8]

There are several advantages of utilizing the transparent mold. Primarily, unlike conventional molds that are opaque, the transparent mold allows for visual investigations through the mold window. Since the mold window penetrates the entirety of the mold, light can pass through the window, which in this case is made of PMMA. Filling processes could be observed and recorded through the mold window, and when certain films are applied, additional studies such as birefringence patterns could be observed as well. Furthermore, there are opportunities to conduct thermal testing and even compare different polymers for a set of given processing parameters.

This transparent mold is also used in the current study. In observing birefringence patterns during Vibration-Assisted Injection Molding (VAIM), the mold set shown in Figure 2-24 was utilized.

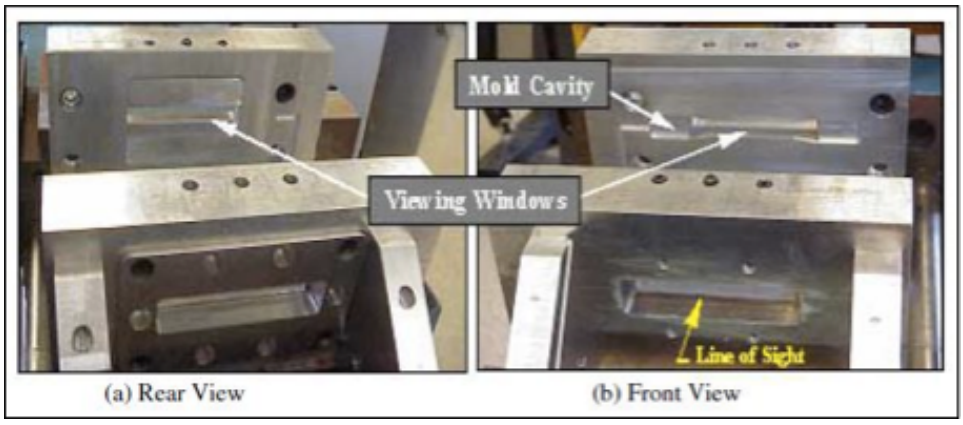

Figure 2-24. Custom mold set for birefringence study of polymers [8]

During VAIM, these birefringence patterns may yield information on the molecular orientation of the polymer. The evident birefringence patterns are due to the velocity difference of two orthogonal beams of polarized light passing through the polymer. A beam is retarded by a certain distance due to the anisotropic nature of the

specific polymer. [8] Additionally, since the polymer is anisotropic, the molecular orientation also affects the tensile strength of the final product.

Polystyrene (PS) and polycarbonate (PC), which are said to be birefringent polymers since they exhibit this light phase shifting behavior [8], were used in this study. Although only two polymers were tested, there were a total of six variations, which included 100% virgin PS (IM), 50% virgin/50% recycled PS (VAIM), 75% virgin/25% recycled PS (VAIM), 100% virgin PS (VAIM), PC (IM), and PC (VAIM). Each of these was tested with conventional injection molding (IM) or Vibration-Assisted Injection Molding (VAIM) as indicated in the parentheses for each polymer make-up. It is noted that not only did the testing yield a visual difference in birefringence between IM and VAIM (Figure 2-25), it also yielded variations for ultimate tensile strength results (Figure 2-26).

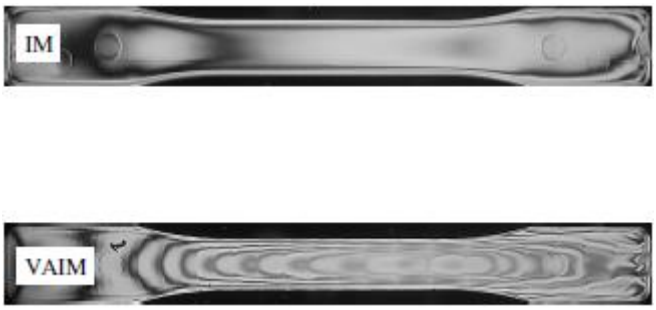

Figure 2-25. Birefringence pattern differences between IM and VAIM of PS [8]

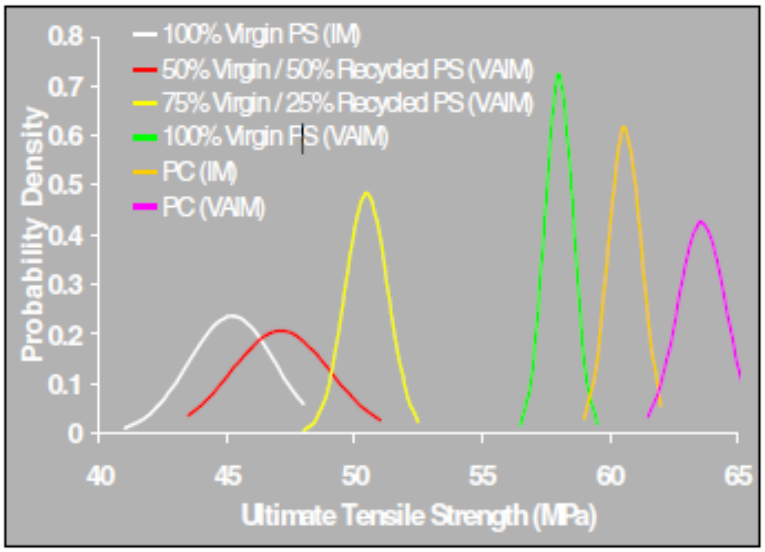

Figure 2-26. Comparison of ultimate tensile strength results of tested polymers [8]

In addition to these results, the mold itself was under examination, since a transparent mold has never been utilized before. It was necessary to prove that the mold was able to endure the injection molding conditions and provide consistent and reliable results both for the final molded parts and for the video recordings of the process.

2.5.2.2 Birefringence and Tensile Studies in Delayed Packing Injection Molding

This study involved observation of the molecular orientation during injection molding with a delayed packing stage. A new custom modified transparent mold was used to observe the birefringence patterns during the injection molding process. (Figures 2-27 Figure 2-28)

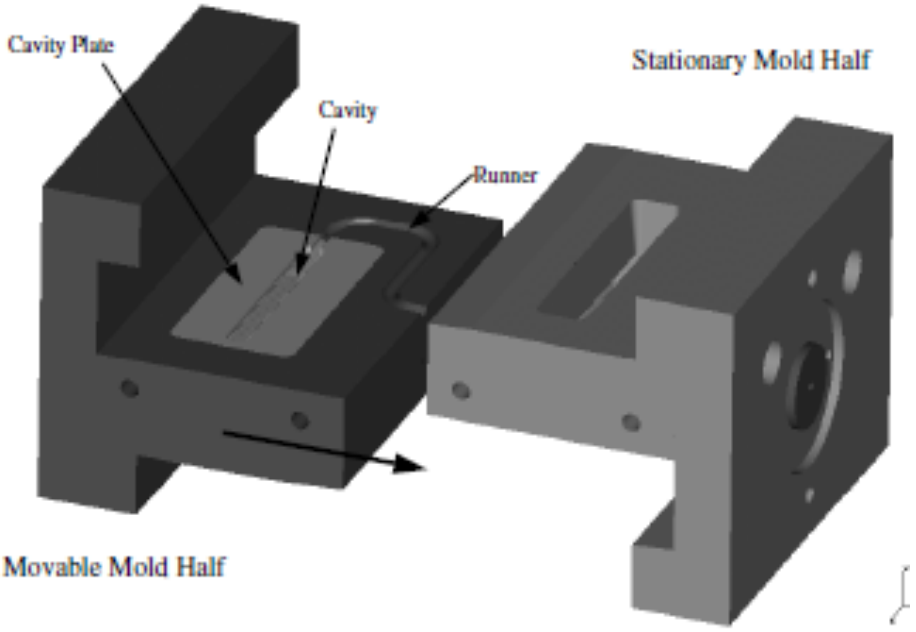

Figure 2-27. Modified "Over-Under" mold design [63]

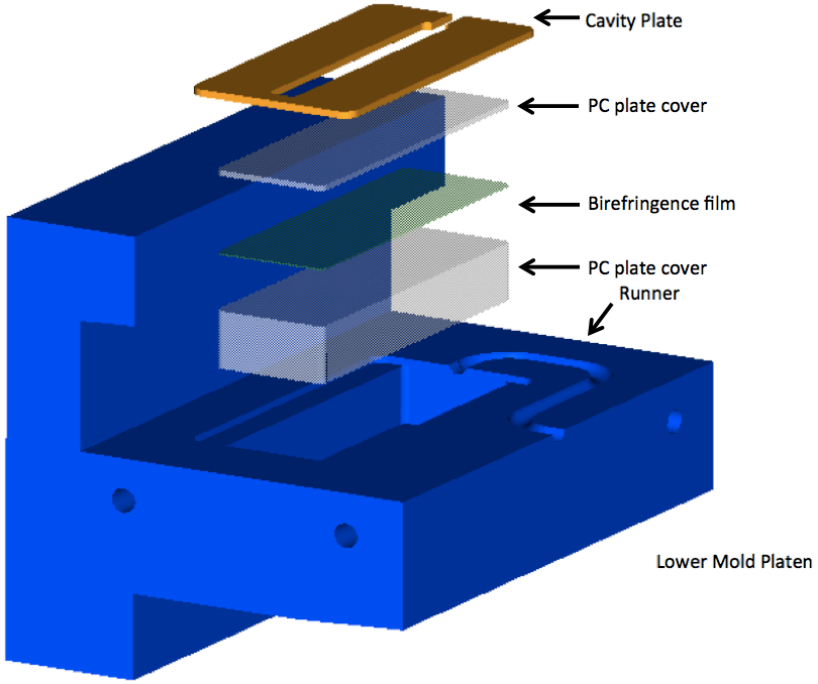

Figure 2-28. Window assembly of lower/movable mold half

This new “over-under” mold design, unlike conventional molds that simply press two mold halves together, allows the movable and stationary molds to slide into each other in order to close the mold completely with high force.

Compared to the previous study, in Delayed Packing Injection Molding (DPIM), the time between cavity filling and pressure application to the mold is increased (delayed). Once the mold cavity is completely filled, the screw retracts to relieve the pressure. The delay in packing pressure application takes place when the polymer filling the cavity starts to cool. Following this delay, the screw moves forward again to apply the packing pressure. This pressure relief and retraction of the screw before the delay similarly mimic the vibration amplitude in VAIM. Hence results show similar birefringence patterns as in VAIM. [63] In testing the effects of DPIM, the packing pressure, melting temperature of the polymer, and the packing pressure delay time were all variables, where as the injection pressure was kept constant (at 65 MPa). [63] The DPIM tests results were compared to that of VAIM, holding all the parameters equal, except for the eight seconds of vibration application compared to the four seconds delay before applying the packing pressure. (Figure 2-29)

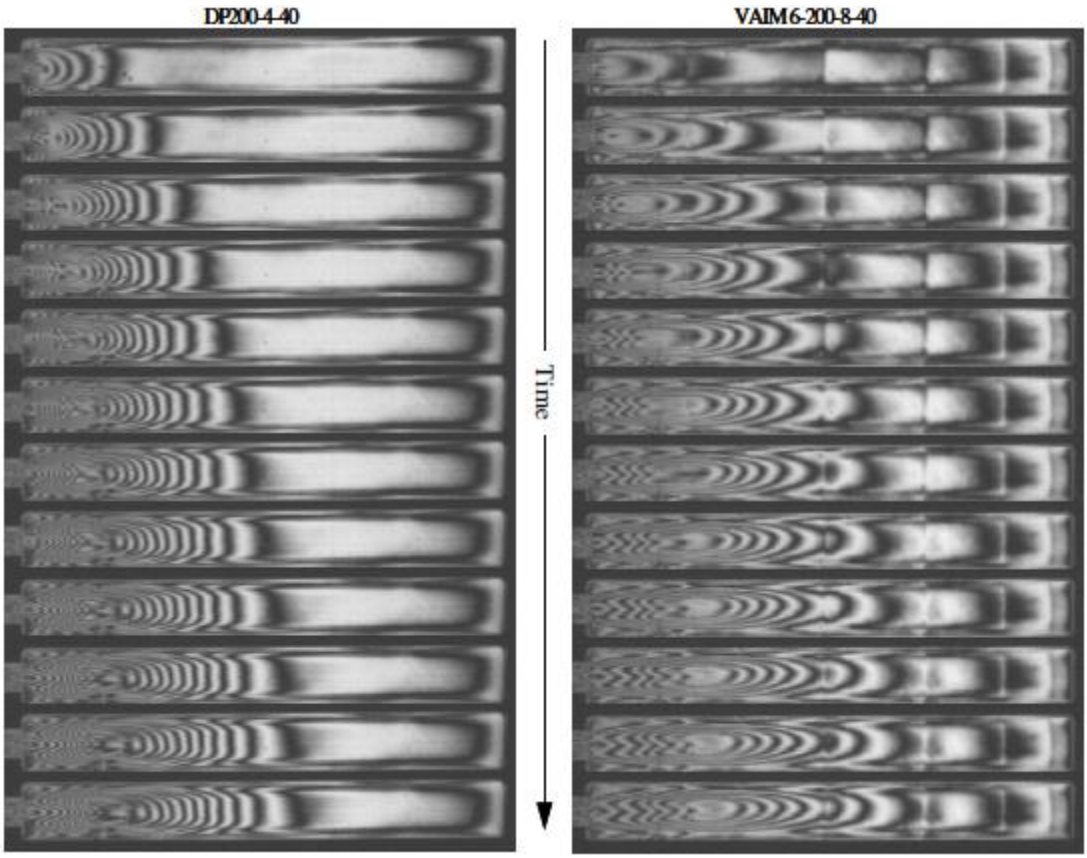

(a) (b)

Figure 2-29. Birefringence images of the processes for (a) Delayed Packing Injection Molding (4 sec delay) vs. (b) Vibration-Assisted Injection Molding (8 sec vibration) of polystyrene [63]

Results show that generally, a higher temperature, higher pressure, and lower delay time resulted in a more uniform distribution throughout the length of the cavity. A lower temperature, lower pressure, and longer delay time also showed more birefringence bands near the cavity injection gate with less uniformity as the polymer flowed further along the cavity. In terms of ultimate tensile strength, comparison of DPIM to both VAIM as well as conventional injection molding, DPIM averaged an ultimate tensile strength of 72.2 MPa, followed by 64.6 MPa for conventional injection molding, and 71.9 MPa for VAIM. [63] DPIM apparently results in increases

in ultimate tensile strength comparable to VAIM. However both DPIM and VAIM resulted in about a 10% increase in ultimate tensile strength compared to conventional injection molding.

In addition to identifying the effects of the parameters of pressure, temperature, and delay time in DPIM, as well as comparing the DPIM tests to the VAIM tests, an interesting observation of the birefringence patterns was made during the testing regarding flow-induced shear. Although these particular tests were not directly designed to test the shear-thinning or shear-heating of the polymer, the effects of the flow-induced shear was apparent.

In Figure 2-30, it is observed that the molecular orientation, made observable via birefringence patterns, dissipates rapidly after the mold was filled since there was more allowable molecular mobility in conventional injection molding. [63]

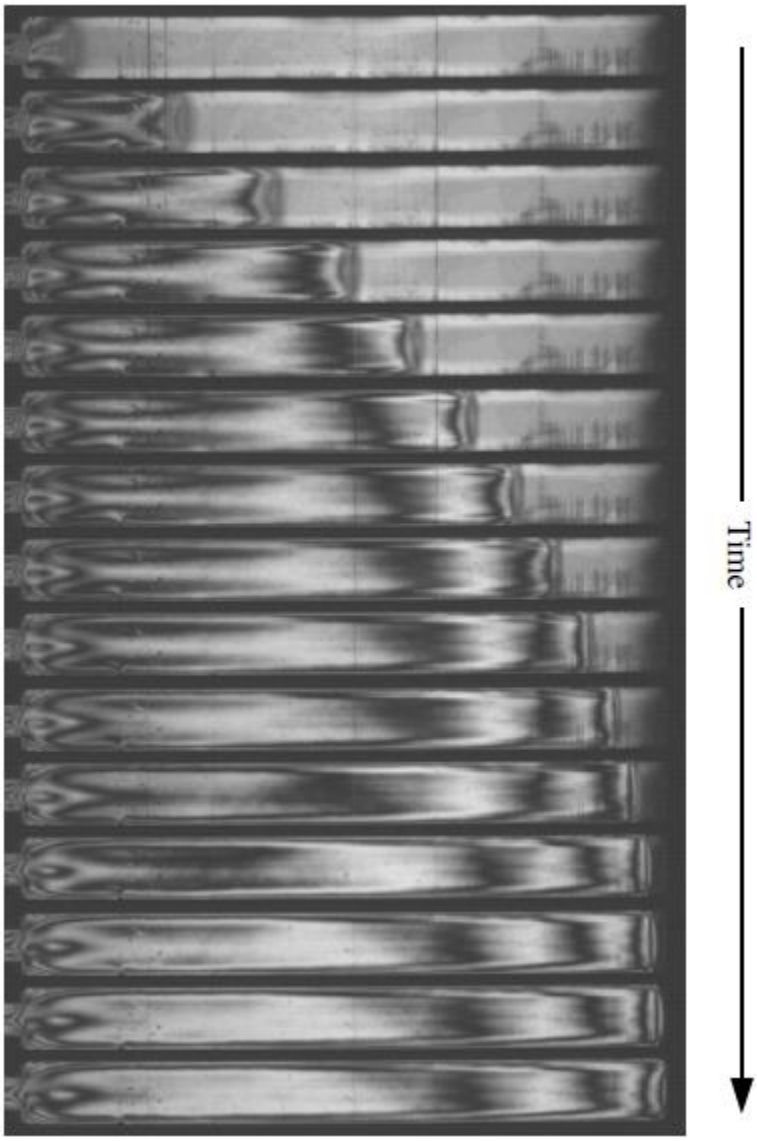

Figure 2-30. Frame sequence of cavity filling in traditional injection molding of virgin polystyrene [63]

The birefringence bands were more apparent near the injection gate and immediately after the gate, where the shear is the greatest along the runner. After the flow passed the gate area, the birefringence bands were more obvious near the cavity wall. Additionally, it can be seen that the flow close to the cavity wall was driven slightly faster by the injection pressure than the melt flow in the center area of the

cavity. These evidences support that flow-induced shear will affect the filling of the cavity and could potentially effect the process of molding and properties of the final product.

2.6 Remaining Questions to Be Answered

Previous research in this area has yielded valuable results and valuable scientific knowledge. However, there are still a lot of questions that remain to be answered and avenues for investigate to be further explored. Although the shear induced imbalance of the melt flow has been discovered and found to be problematic, further concerns, such as what characteristics of the polymer product the shear imbalance could affect, how the shear imbalance influences the properties, or how much the shear effect could alter the properties of the molded products for different polymeric materials, still need to be addressed.

Traditional molds do not allow researchers to examine how the material is travelling through the runners and cavities in real time. The shear induced imbalance patterns could only be viewed after the molds are open, and when the polymer has already cooled down to room temperature. (Figure 2-31) Although even with this delay, the shear imbalance result is apparently observed in the molded product, direct observation during cavity filling cannot be made.

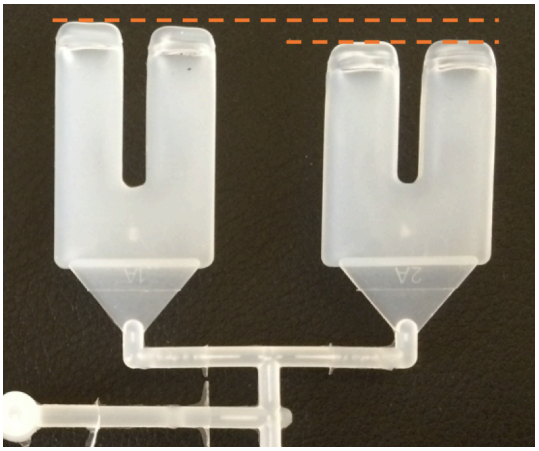

Figure 2-31. Ending tip variations caused by shear imbalance during multi-cavity injection moldings (short shot) [50]

Furthermore, in past work, the real-time monitoring of injection molding was limited to single-cavity filling. The cavity was also a single slim rectangular geometry. (Figures 2-23, 2-27, 2-28, 2-29 and 2-30) Real-time observations of cavity filling for single-cavities of various geometries or for multi-cavity molding have not been investigated. In this work, several experiments are introduced, involving additional types polymeric materials to further expand research in this area, to help address the concerns mentioned above, related to the shear imbalance phenomenon.

3 Material Selection and Experiment Design

3.1 Materials for Investigation

Distinct polymeric materials are selected for this investigation. Materials, such as polypropylene (homo-polymer and copolymer), polyoxymethylene copolymer (POM), Nylon 6'6 (neat and 50% glass filled), polybutylene terephthalate (PBT) and polystyrene (PS), are provided by companies that include Braskem America Inc., LyondellBasell Industries, Ticona, DuPont Performance Polymer, Ascend Performance Materials Operations LLC, Mitsubishi Engineering-Plastics Corp., and Americas Styrenics LLC. These materials are commonly used due to the abundance in raw material source, their firm and stable market price, their amenability to injection molding, and physical and thermal properties. The market for these materials have grown significantly in resent years due to increasing demands for lightweight products. [2] [64] [65] [66] [67]

In this investigation, materials will be injection molded by applying the single-cavity mold and the multi-cavity mold, with and without Melt Rotation Technology. The specific materials used were FPT350WV3 (polypropylene homo-polymer), SR549M (polypropylene copolymer, containing 20% ethylene), HOSTAFORM® C 9021 unfilled resin (polyoxymethylene (POM) copolymer), Zytel® 101L NC010 (Nylon 6'6, for single-cavity molding only), Zytel® HTN 53G50HSLR NC010 (50% glass filled Nylon 6'6, for single-cavity molding only), Vydyne® 21SPC (Nylon 6'6, for multi-cavity molding only), NOVADURAN® 5010R5 (polybutylene terephthalate)

and Styron® 666D (polystyrene). Table 1 gives basic information related to these materials.

Table 3-1. Properties of the polymer materials investigated in this study

Material	Flow Rate	Melt Temp.
PP ho / iPP	35 g/(10 min) at 230°C	160°C ~ 170°C
PP co	11 g/(10 min) at 230°C	200°C ~ 228°C
POM	9.6 g/(10 min) at 190°C	166°C
N66	24 g/(10 min) at 325°C	262°C
N66_50	7.81 g/(10 min) at 325°C	260°C
PBT	32.75 g/(10 min) at 250°C	224°C
PS	8 g/(10 min) at 200°C	240°C

In the table, "PP ho" or "iPP" represents polypropylene homo-polymer; "PP co" represents polypropylene copolymer; "PP co MF" represents polypropylene copolymer (molded with MeltFlipper®); "POM" represents polyoxymethylene copolymer; "N66" represents Nylon 6'6; "Nylon 66_50 or N66_50" represents 50% glass filled Nylon 6'6; "PBT" represents polybutylene terephthalate; "PS" represents polystyrene.

The polymers that were used in the real-time monitoring study were polypropylene and polystyrene, which are common thermoplastic polymers.

In general, the melt flow rate (MFR, also known as melt flow index MFI) of polypropylene, which is a measure of how easily a melted plastic flows, has a range between 5 and 60 g/10 min. The MFR for polystyrene was 8 g/10 min. Generally the higher the MFR the greater the fluidity of the polymer. For comparison, Table 3-2 below tabulates multiple plastics and their MFR.

Table 3-2. Melt Flow Rate (MFR) of Plastics [68]

Plastic Material	Melt flow rate range (g / 10 min)
Polypropylene	5 ~ 60
Polystyrene	5 ~ 25
AS resin	10 ~ 40
ABS resin	5 ~ 60
Acrylic resin	1 ~ 35
Polyamide 6	10 ~ 80
Polyamide 66	10 ~ 80
Polyacetal	3 ~ 70
Polycarbonate	2 ~ 30
PBT	20 ~ 100
PPO	7 ~ 30
PSU	7 ~ 18
PES	17 ~ 30
Cyclo olefin polymer	7 ~ 60
TPX	21 ~ 80
PEEK	1 ~ 20

The MFR however is a general characterization, since it is viscosity at a single flow rate. Therefore, the large range in MFR is due to the shear rate dependence of this parameter. The apparent viscosity decreases as the shear rate increases when the polymer is pushed through the injection molding machine. The MFR is a simple way to roughly characterize the polymer's fluidity and sensitivity to shear should also be considered. The broad MFR ranges of polypropylene and polystyrene show that they are in fact sensitive to shear. Literature even reports MFR of polypropylene ranging between 0.5 g/10min to 1000 g/10 min. [69]

Among the polymers used for this research, the viscosity of polypropylene is relatively less sensitive to changes in melt temperature and shear heating. It is thus expected to have the smallest reaction to shear induced melt variations developed in the runner. As shown in Figure 3-1, the short shot results from an eight-cavity mold

for three polymeric materials. Each material was injected into the cavity at the same injection rate, thereby each undergoes an equivalent shear rate. The figure shows that filling imbalance, resulting from melt rheology variation, is significantly less with polypropylene.

In this study, polypropylene is the major materials investigated in all experiments. The assumption was made that if iPP can show the shear imbalanced results, the other materials would be possible to behave more seriously in the same injection molding conditions.

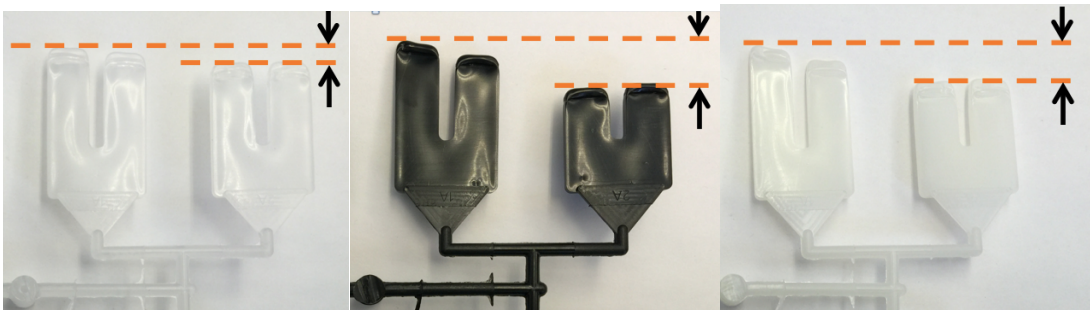

(a) (b) (c)

Figure 3-1. Ending tip differences of the frozen flow for (a): polypropylene (iPP), (b): polybutylene terephthalate and (c): nylon 6'6, in multi-cavity injection molding [51]

The viscosity of polypropylene decreases in a non-linear fashion as the shear rate increases, as shown in Figure 3-2. [69] Figure 3-2 also shows the correlation between a higher MFR and lower viscosity. Therefore, polypropylene was deemed a suitable polymer for this study.

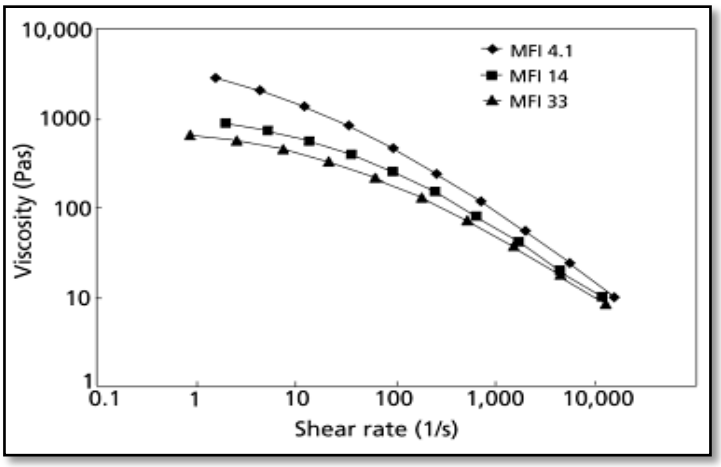

Figure 3-2. Viscosity vs. shear rate of polypropylene (iPP) at different melt flow rates [69]

The main drawback of using polypropylene is that it is an opaque plastic. It thus lacks optical birefringence patterns, which is only visible in glassy polymers.

From Figure 3-3 to Figure 3-8, the relationships between shear rate and viscosity for PP co, POM, N66, N66_50, PBT and PS are presented.

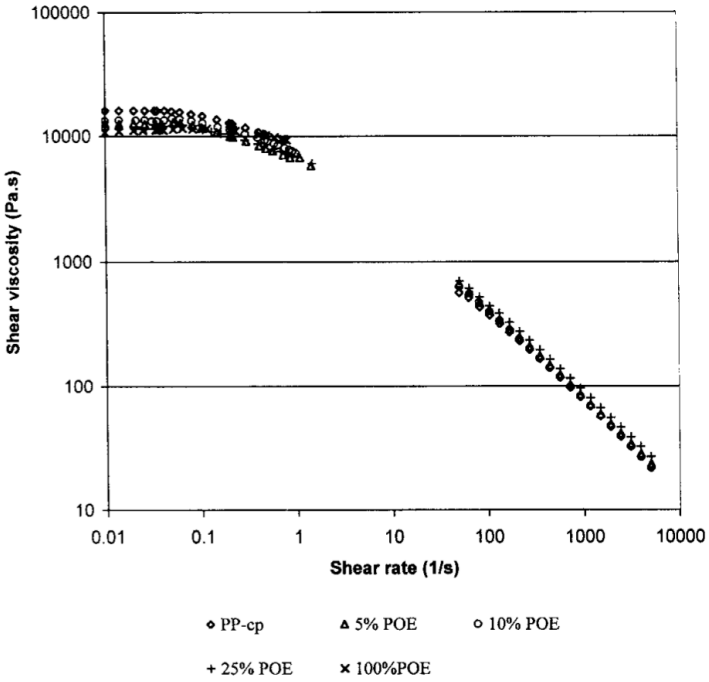

Figure 3-3. Viscosity vs. shear rate of PP co (PP-cp, ethylene copolymerized) and other blended materials [70]

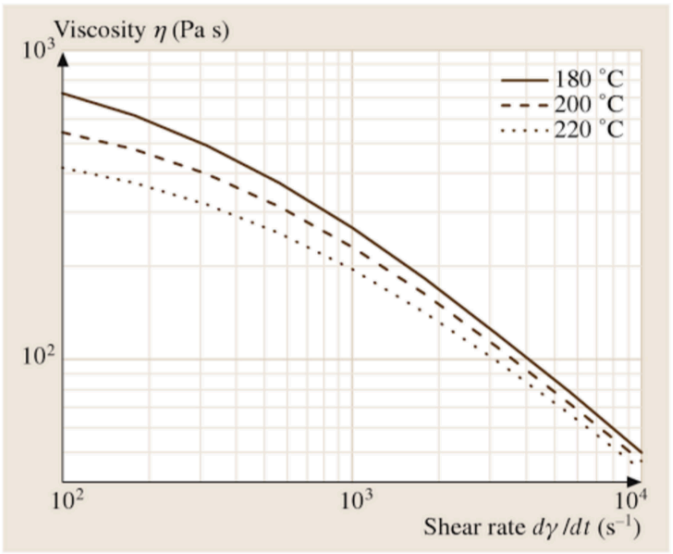

Figure 3-4. Viscosity vs. shear rate of POM at different temperatures [71]

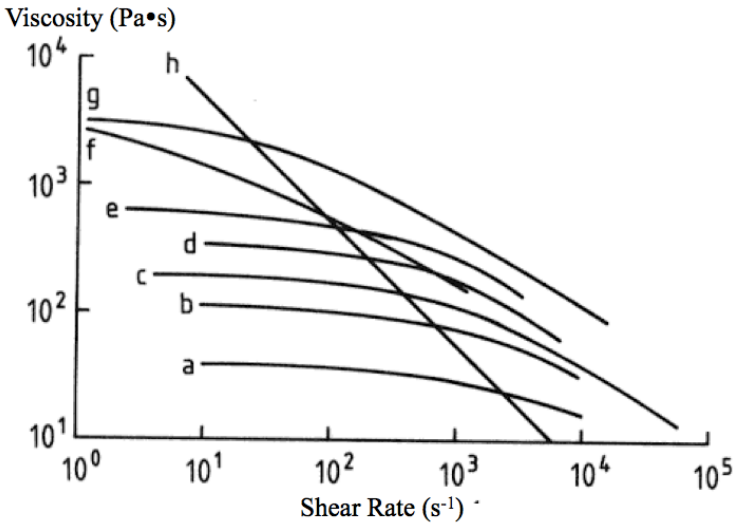

Figure 3-5. Viscosity vs. shear rate of N66 (c) and other materials [72]

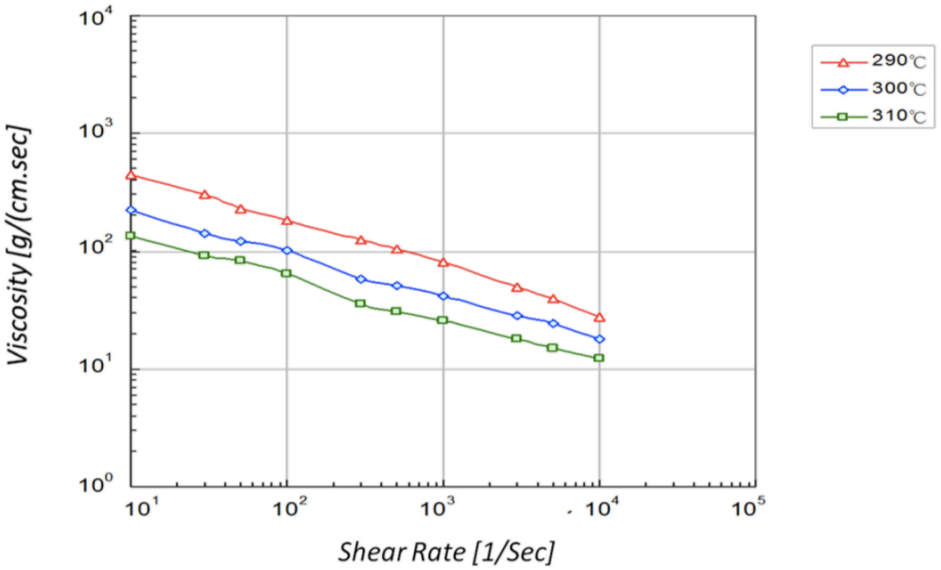

Figure 3-6. Viscosity vs. shear rate of N66_50, 1 g/(cm.sec) = 0.1 Pa.s [73]

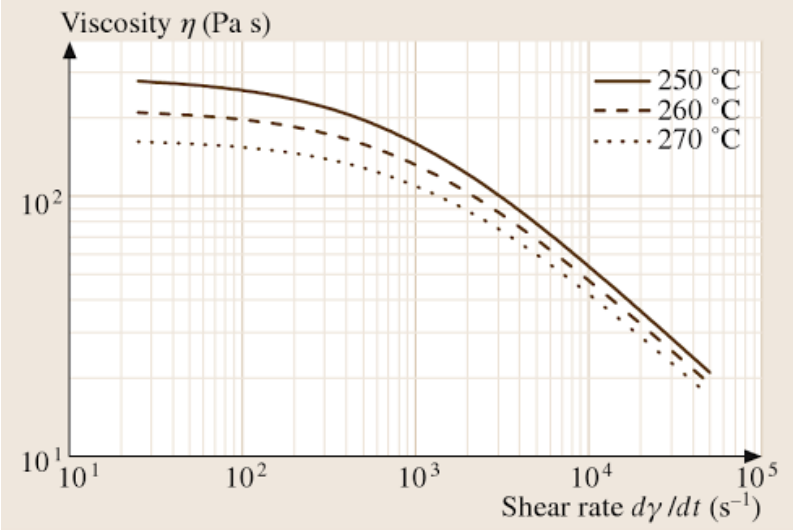

Figure 3-7. Viscosity vs. shear rate of PBT at different temperatures [71]

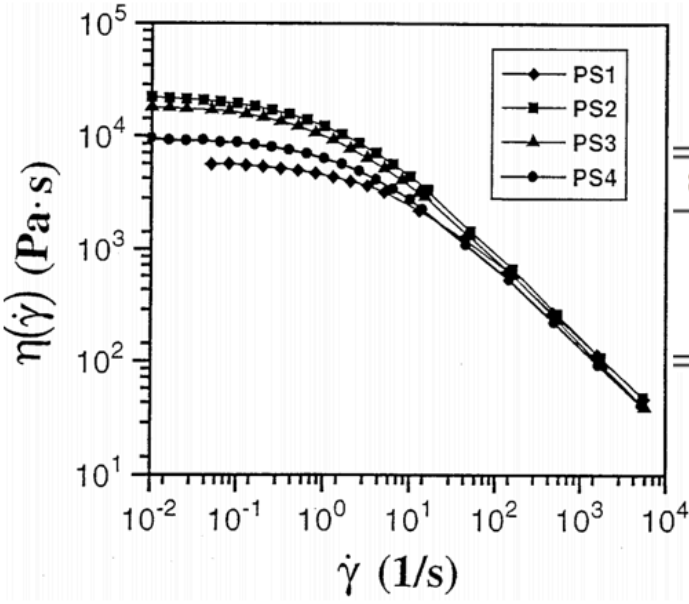

Samples	M_w
PS1	196 986
PS2	274 686
PS3	297 760
PS4	242 741

Figure 3-8. Viscosity vs. shear rate of PS with different molecular weight at 200°C [74]

The viscosity of these materials all decrease in a non-linear fashion as the shear rate increases. The plot in Figure 3-9 shows that PS and PP may be more sensitive to shear rate than the other materials. The iPP curve was created based on the MFI 33 plot in Figure 3-2, the POM curve was from the plot for 180°C in Figure 3-4, the N66_50 curve was from the plot for 290°C in Figure 3-6, and the PBT curve was from

the plot for 250°C in Figure 3-7. These were all related to real material properties or molding conditions in this investigation.

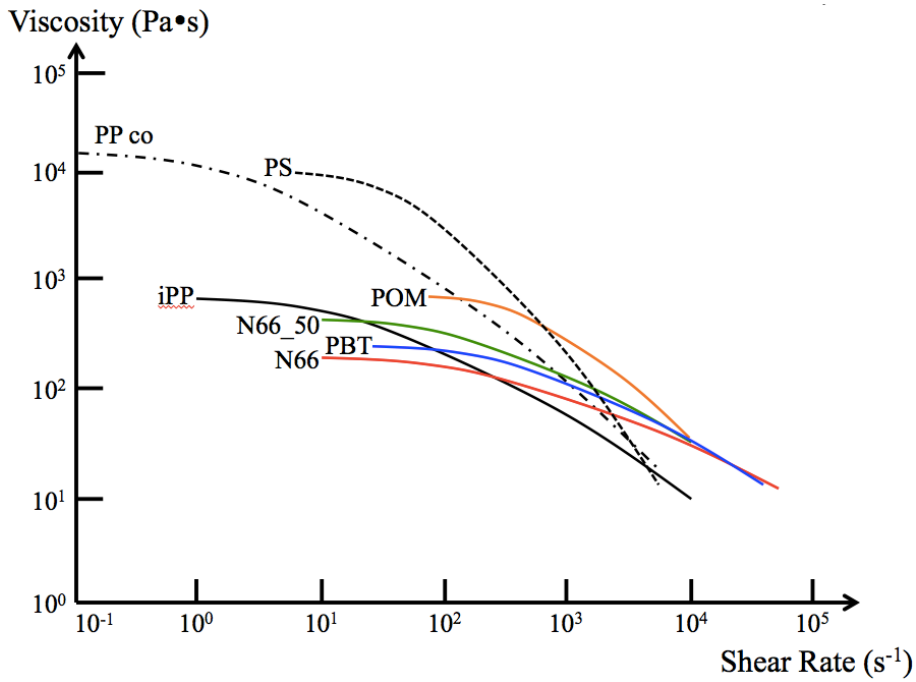

Figure 3-9. Viscosities vs. shear rates of all materials related in investigation

Although, the viscosity of melting polymer may be influenced by shear variation, it may also depend on molecular weight and chain length, density, and polymer backbone characteristic.

According to previous studies and literatures, high molecular weight may result in high polymer density. [75] Long molecular chains have a low melt index, whereby the material will exhibit a higher melt viscosity and greater melt strength. [76] This means that large polymers molecules would have a viscous melt flow relative to those with smaller molecules. [77] [78] The alignment of the highly anisotropic chains may also result have an influence in viscosity. [44] The more anisotropic the molecule backbone, the easier it is to disentangle the molecules and reduce the viscosity through

shear-thinning. However, it is possible that the relationship between molecular weight, polymer chain structure, material density, shear rate and viscosity may not be as straightforward. [79] [80]

3.2 Experiments in Investigation

Crystallinity is the main data sought in this research as it has a significant effect on a polymer's thermal and mechanical properties. In this study, Differential Scanning Calorimetry (DSC) was used to investigate the crystallinity variations and melting point shift caused by the shear induced imbalances. Flash DSC testing was also used to monitor the melting behavior differences. Tensile testing was included in order to explore the differences in yield stress and Young's modulus of the injection molded specimens. Additionally, Wide Angle X-Ray Scattering (WAXS) was the method to further explore crystallinity and the crystal components affected by shear imbalances in the polymer samples. A more detailed description of each of these experiments is presented in Chapter 6.

4 Traditional Injection Molding

All injection molding experiments were carried out at the Manufacturing Science Laboratory in Lehigh University and Beaumont Technology, Inc..

4.1 Traditional Injection Molding

For the traditional injection molding part of the investigation, selected materials were utilized in both single-cavity molding and multi-cavity molding, with and without the application of Melt Rotation Technology.

4.1.1 Single-cavity injection molding

For single-cavity injection molding, the mold cavity is designed in the shape of a disc plate with a radius of 40 mm and a thickness of 2 mm. The material will be injection molded into products by conventional means, without application of packing pressure. This is in order to minimize the packing influence on the final products and to ensure the shear induced problems can be clearly observed. Additionally, short shots were intentionally molded, filling only about half of the cavity. This is done to isolate and observe the imbalanced cavity filling. (Figure 4-1)

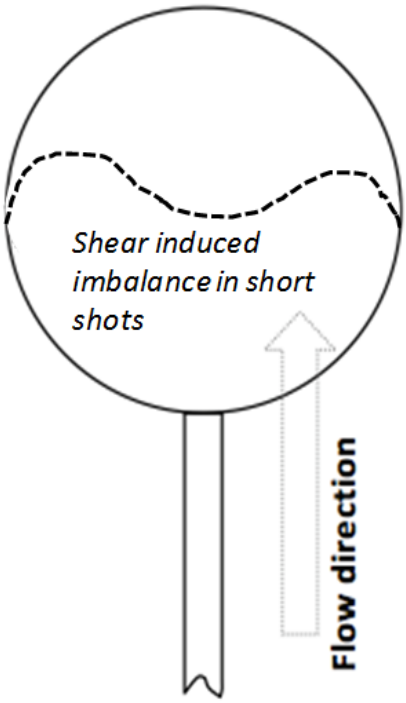

Figure 4-1. Short shots in single-cavity molding and the filling imbalance

For experiments involving injection molding with Melt Rotation Technology experiments, a similar strategy is adopted. (Figure 4-2) For all of the disc parts molded with and without the melt rotation device, test samples were taken from the side edge (Area 1 in Figure 4-2) and centralized regions (Area 2 in Figure 4-2) respectively. For the parts molded without MRT, samples from Area 1 would contain polymer material that had experienced higher shear and higher temperature than those samples, which ended up in the center or Area 2 of the product. [3] [4] On the other hand, for the specimens molded with MRT, samples from Area 1 and Area 2 are expected to present more uniform properties.

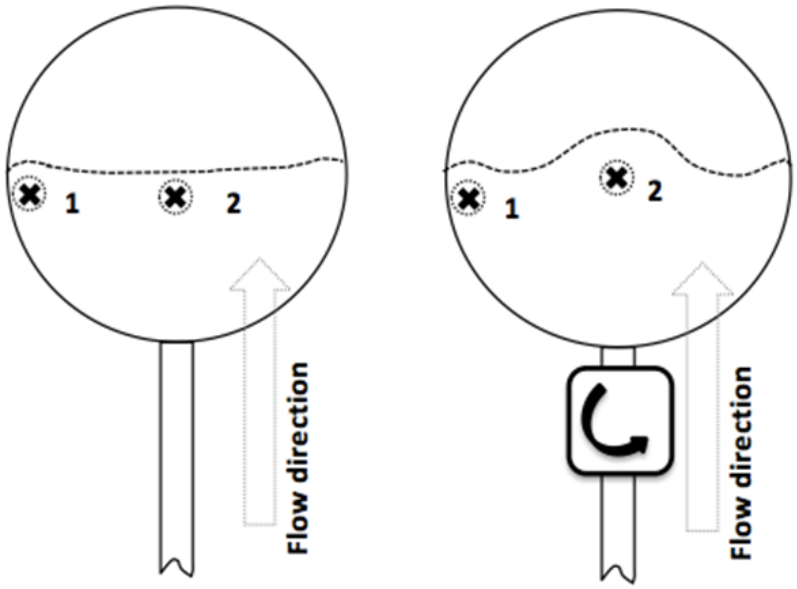

(a) (b)

Figure 4-2. Single-cavity injection molding without (a) & with (b) MRT, and the sampling spots from Area 1 and Area 2

All the selected materials were molded in a similar half disc shape (Figure 4-3) using a Boy 22-ton injection molding machine.

Figure 4-3. 50% cavity filled disc molding parts [53]

The fill time for single-cavity molding was controlled to be less than 1 second, without application of packing pressure, during the 7 seconds of packing time. This is

in order to minimize packing effects such as additional material that might be fed into the cavity. The molding parameters used for different materials are presented in Table 4-1. These were determined based on the material supplier recommendations for conventional molding conditions.

Table 4-1. Dominant molding parameters utilized during single disc-cavity molding (MF = MeltFlipper®)

	Fill Time	Fill Pressure	Injection Speed	Cooling time	MF Usage
Units	*sec.*	*MPa*	*cm^3/sec*	*sec.*	
PP ho	0.35	15.17	32.31	10	No
PP co	0.37	15.17	32.31	10	No
PP co	0.5	15.17	32.31	10	Yes
POM	0.83	15.17	32.31	15	No
N66	0.32	12.1	57.02	10	No
N66	2.03	7.8	9.5	10	No
N66_50	0.32	13.6	57.02	10	No
N66_50	0.49	13.6	57.02	10	Yes

The four temperatures for the materials at the nozzle, front, middle and rear section of the injection screw were also set according to material provider recommendations. (Table 4-2)

Table 4-2. Screw temperature settings for different polymer materials of the single disc-cavity molding

Section	Nozzle	Front	Middle	Rear	Mold
Unit	°C				
PP ho / iPP	221	221	221	221	32
PP co	221	221	221	221	32
PP co MF	221	221	221	221	32
POM	200	200	200	200	90
N66	293	271	271	271	70
N66_50	293	290	290	290	90

The melt rotation device used during the study was custom designed to effectively reposition/redistribute the melt regions of high and low shear history. With melt rotation applied, the relatively hot and lower viscosity material regions are therefore expected to be more uniformly distributed as the polymer enters the cavity.

4.1.2 Multi-cavity injection molding

In addition to the single-cavity molding, a series of 8-cavity molding trials will also be conducted using a conventional runner system with and without application of MRT.

For tensile tests, polymers were molded in the size and shape of a Type V tensile bar using a geometrically balanced 8-cavity mold. The dimensions for the tensile bars were determined according to ASTM standard D638-10.

During initial mold filling, most of the high sheared material will initially flow into cavity 1 relative to cavity 2. However, after cavity 1 is filled, some of the highly sheared material will then divert to complete the filling of the unfilled cavity 2. (Figure 4-4) The result is that portions of cavity 2 will be formed with different mixes of high and low sheared materials. As this study is intends to capture molded product material properties as formed by high and low sheared materials, short shots were intentionally aimed at. (Figure 4-4) This prevents the highly sheared melt, filling cavity 1 from being diverted to cavity 2.

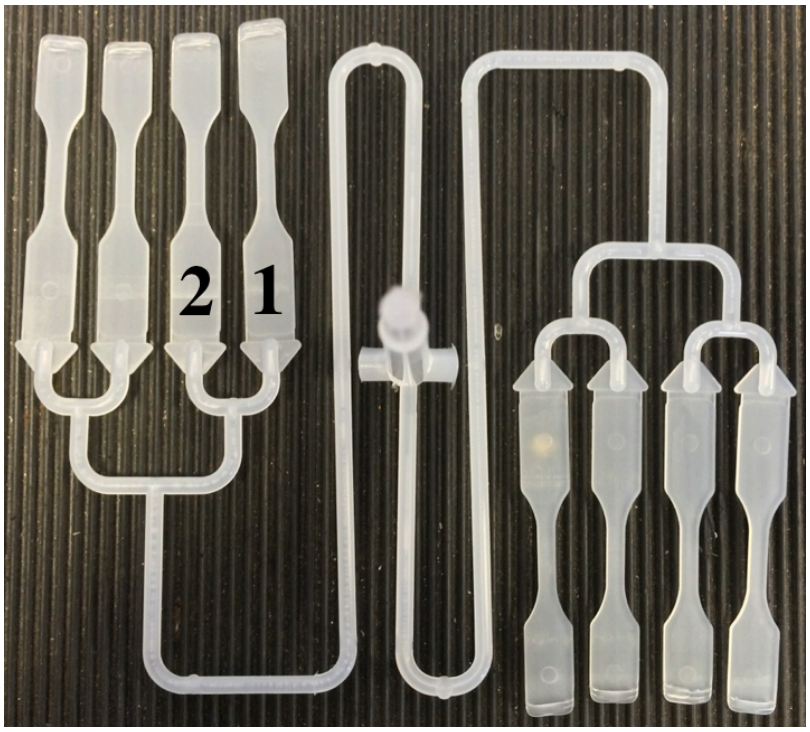

Figure 4-4. Short shot tensile bars; The bars with mark 1 contained the high shear melt flow and the bars with mark 2 contained the low shear melt flow [53]

As short shots are also utilized again in 8-cavity molding trials, tensile bars labeled as Group 1 were taken from cavities associated with the higher shear and temperature history material. Those labeled as Group 2 were associated with the lower shear and temperature history material. It was anticipated that Group 1 samples would likely exhibit higher tensile moduli relative to those from Group 2. (Figure 4-4)

Injection molding of the tensile bars was performed using a 40-ton Nissei PS40 injection molding machine. The injection time was kept at 0.35 sec and 0.37 sec for molding PP ho and PP co samples. The cooling time was set at 20 seconds for all molding runs. The injection speed and resultant injection pressure are shown in Table 4-5. The packing pressure again was set very low to once again minimize packing effects in the results.

Table 4-3. Dominant molding parameters for polypropylene 8-cavity molding trials

Material	PP ho / iPP	PP co
Injection Speed (cm^3/sec)	28.4	28.4
Injection Pressure (MPa)	55.02	91.7

In all cases, four replicates of testing samples were obtained, with the obtained testing results averaged for comparative analysis and presentation purposes.

For crystallinity and other material property investigations, the injection molding process was executed using a KrausMaffei KM40-1225C injection molding machine. In this situation, a unique designed U-shape, eight-cavity mold, with the T-type runner system, was employed to manufacture the iPP, PBT and Nylon specimens. (Figure 4-5)

The specimens were injection molded with and without MRT. Similar to previous cases, the samples molded with and without the melt rotation device was also intentionally molded resulting in a short shot. This is in order to isolate the shear induced imbalance result. (Figure 4-5) Similarly, packing pressure was also not applied to minimize the packing influence.

The melt rotation devices, which is named as MeltFlipper® and patented by Beaumont Technologies, Inc. were located at the T- junctions between the primary and secondary runners, and also between the secondary and subsequent subordinate runners. As a result, the melt flow was “rotated” twice before it enters each cavity. This ensures each cavity has an injected material with the same shear history. (Figure 4-6)

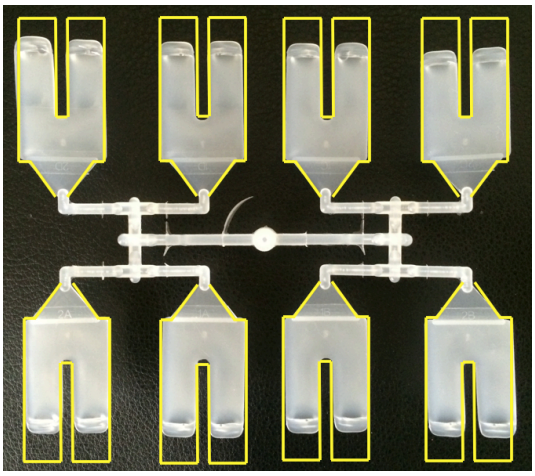

Figure 4-5. Mold cavities, runner system and insufficient shot samples for U-shape cavity molding [50]

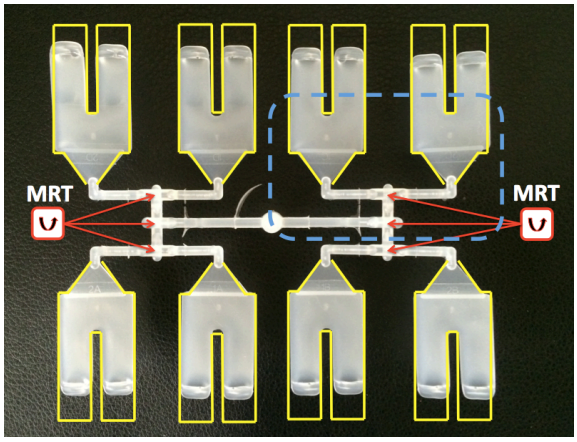

(a)

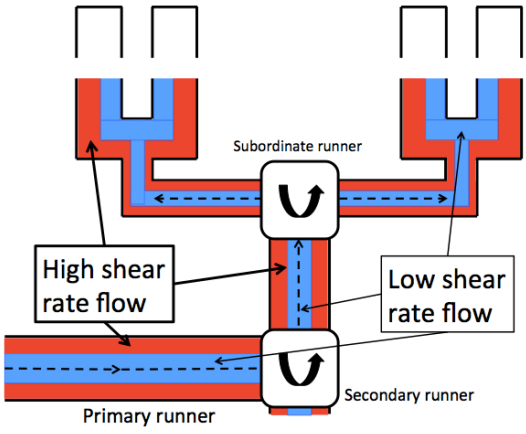

(b)

Figure 4-6. (a): Melt Rotation Technology (MRT) implementations in runners; (b): Zoomed from dashed area in (a) and the "rotated" results of the sheared flow [50]

For each of the selected materials (iPP, PBT and Nylon 6'6), three trials of injection molding conditions were applied based on the theories previously discussed in Chapters 2 and 3. These three conditions are: 1) fast molding without MRT, 2) slow molding without MRT, and 3) fast molding with MRT. These processing conditions were chosen because they have helped in facilitating the examination of shear imbalanced molding, and the ability of MRT in shear redistribution within the melt.

The molding parameters are listed in Tables 4-4, 4-5, and 4-6 for iPP, PBT and N66 respectively. Tables 4-7, 4-8 and 4-9 list the temperatures set at each section of the injection screw and the mold barrel for all these materials. These parameters were set according to material supplier recommendations.

Table 4-4. General molding parameters for each molding conditions for iPP molding (MRT = Melt Rotation Technology)

Molding Condition	Fill Time	Fill Pressure	Injection Speed	Cooling time	MRT Usage
(Units)	(sec.)	(MPa)	(cm^3/sec.)	(sec.)	-
1) Fast no MRT	0.27	38.4	81.9	10	No
2) Slow no MRT	2.03	21.1	11.1	10	No
3) Fast MRT	0.27	38.6	81.9	10	Yes

Table 4-5. General molding parameters for each molding conditions for PBT molding

Molding Condition	Fill Time	Fill Pressure	Injection Speed	Cooling time	MRT Usage
(Units)	(sec.)	(MPa)	(cm^3/sec.)	(sec.)	-
1) Fast no MRT	0.33	186.2	81.9	10	No
2) Slow no MRT	2.12	108.2	11.1	10	No
3) Fast MRT	0.34	196.5	81.9	10	Yes

Table 4-6. General molding parameters for each molding conditions for N66 molding

Molding Condition	Fill Time	Fill Pressure	Injection Speed	Cooling time	MRT Usage
(Units)	(sec.)	(MPa)	(cm^3/sec.)	(sec.)	-
1) Fast no MRT	0.32	73.9	65.5	10	No
2) Slow no MRT	2.05	39.7	10.6	10	No
3) Fast MRT	0.29	74.2	65.5	10	Yes

Table 4-7. Molding temperature settings at injection screw sections and the mold barrel for iPP molding

Section	Nozzle	Front	Middle	Rear
Unit	(K)			
1) Fast no MRT	477.6	477.6	477.6	477.6
2) Slow no MRT	477.6	477.6	477.6	477.6
3) Fast MRT	477.6	477.6	477.6	477.6

Table 4-8. Molding temperature settings at injection screw sections and the mold barrel for PBT molding

Section	Nozzle	Front	Middle	Rear
Unit	(K)			
1) Fast no MRT	505.4	505.4	505.4	505.4
2) Slow no MRT	505.4	505.4	505.4	505.4
3) Fast MRT	505.4	505.4	505.4	505.4

Table 4-9. Molding temperature settings at injection screw sections and the mold barrel for N66 molding

Section	Nozzle	Front	Middle	Rear
Unit	(K)			
1) Fast no MRT	555.4	544.3	544.3	544.3
2) Slow no MRT	555.4	544.3	544.3	544.3
3) Fast MRT	555.4	544.3	544.3	544.3

According to the shear imbalance theory, the samples taken from Area 1 are expected to contain material that has undergone high shear, while those from Area 2 would contain those which has undergone a relatively low shear. This is for both of

the fast and slow injection molding processes, without MRT utilization. (Figure 4-7) Similarly, for the specimens molded under the molding condition (with MRT), the labeling terminology of Areas 1 and 2 was applied.

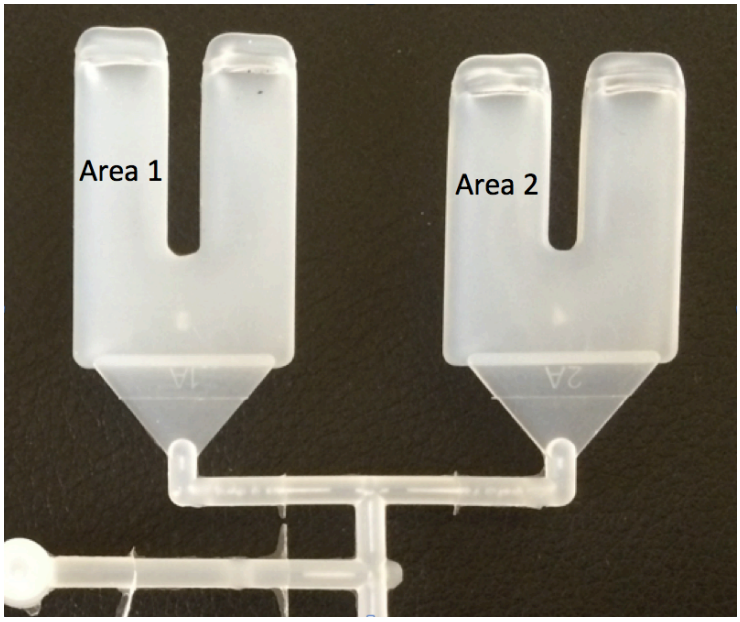

Figure 4-7. Labeling samples from the high shear zone (Area 1) and the low shear zone (Area 2) [50]

5 Injection Molding with Real-Time Monitoring

To further expand on David Angstadt's work related to flow-induced shear problems in runner and cavity filling, this research aimed to study the shear imbalance effect in real time. Since the transparent mold was already fabricated, and proved to be reliable and consistent [8] [63], only a couple of modifications were made to accommodate the aims of the current work.

5.1 Original Cavity Insert Design

In Angstadt's results, it was apparent that shear was greatest at the injection gate of the cavity, thus implying that shear imbalance effects are accumulated as the polymer is pushed through the runner. In order to amplify this shearing effect for the current study, the runner length was greatly extended on the insert plate. On the other hand, the cavities were shortened, only utilizing about one third of the mold window.

A total of three insert designs were made from steel, each with a unique geometry. Figure 5-1 below outlines these three insert designs. Common features shared between the designs however are that each plate was an eighth of an inch (3.18 mm) thick, 3 inches (76.2 mm) wide, and 6 inches (152.4 mm) long.

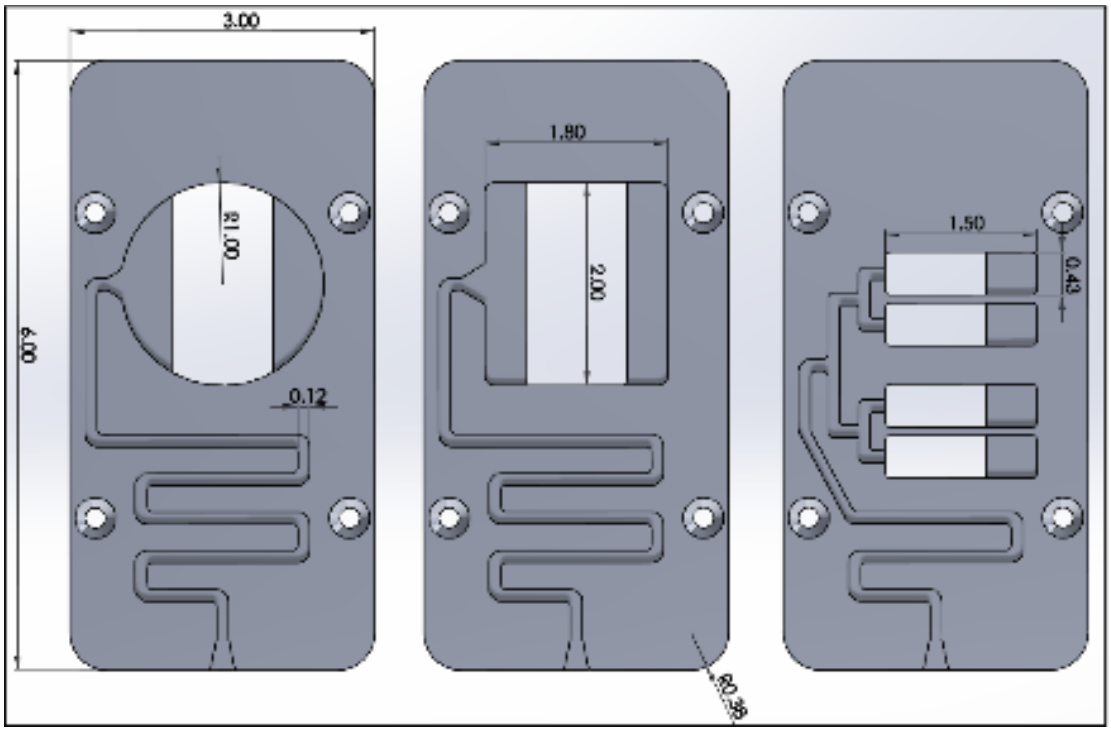

Figure 5-1. Mold insert designs with circular cavity (left), rectangular cavity (middle), and split-cavity (right) [51]

Since the runner system was designed to be only on the insert plate, the runner depth was thus limited by the insert plate thickness. Hence, the runner was designed with a width was 0.12 inches (3.05 mm), with a larger entrance width of 0.25 inches (6.35 mm), and a depth was 0.07 inches (1.78 mm).

In single-cavity molding, the high shear rate flow is expected to fill the edge section of the disc cavity faster than the low shear rate flow filling the center cavity. (Figures 5-2 and Figure 5-3) This is because according to shear-thinning theory, the high shear flow is hotter and has lower viscosity.

For multi-cavity molding, the high shear flow and the low shear flow will be split into different cavities. The high shear flow, which is hotter in temperature with lower viscosity, fills the associated outer mold cavities (A1 and A2) quicker than the

low shear region flow, which is cooler in temperature with higher viscosity, filling the associated inner mold cavities (B1 and B2). (Figure 5-4)

The cavity filling predictions for all three inserts are shown in Figures 5-2, 5-3 and 5-4 for the circular, rectangular, and split-cavities respectively.

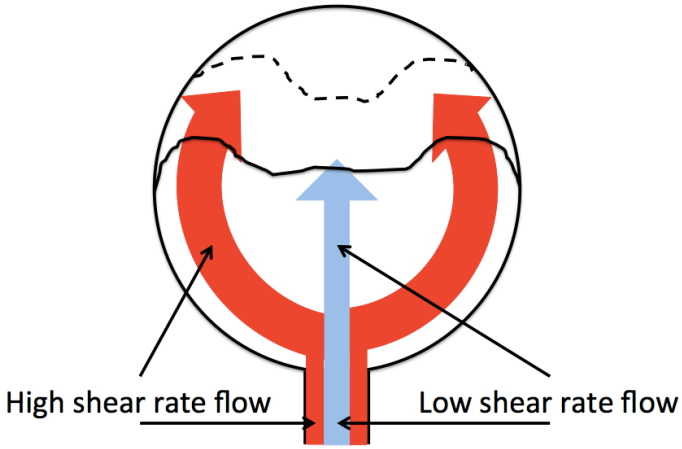

Figure 5-2. Cavity filling prediction of single-cavity (circular cavity) injection molding (same to Figure 2-7) [51]

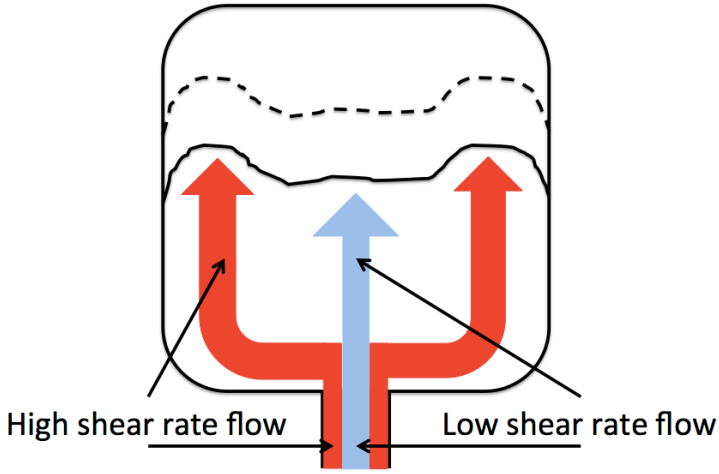

Figure 5-3. Cavity filling prediction of single-cavity (rectangular cavity) injection molding [51]

A1 B1 B2 A2

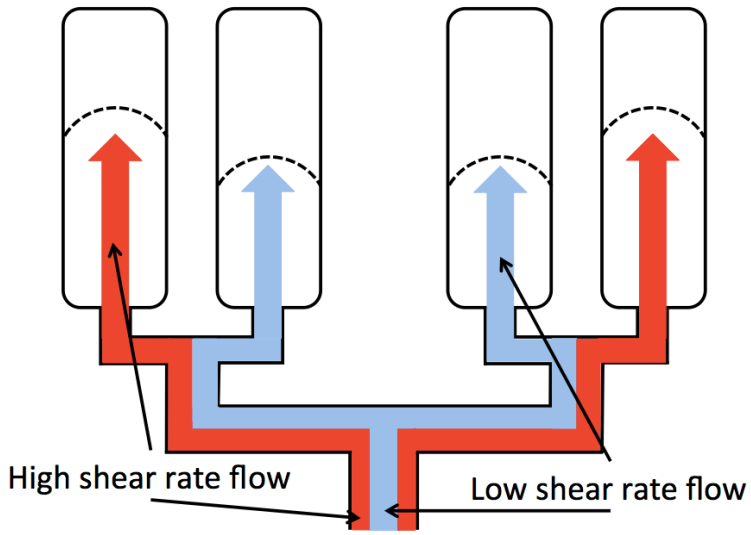

Figure 5-4. Cavity filling prediction of multi-cavity injection molding
(Outer cavities: A1 and A2, Inner cavities: B1 and B2; same to Figure 2-6) [51]

As only one section of the cavity was machined through the entire insert plate (Figure 5-1), each insert cavity was fit with a rectangular polycarbonate window with a thickness of one sixteenth of an inch (1.59 mm) on the opposite of the insert plate. This is shown in Figure 5-5. The thickness of the polycarbonate window was a little greater than the depth of the polycarbonate window groove (0.055 in or 1.40 mm) in order to account for the compression, which the polycarbonate would undergo due to the mold clamping. The depth of each cavity was also 0.07 inches (1.78 mm). A model of the complete mold and insert setup is shown in Figure 5-6.

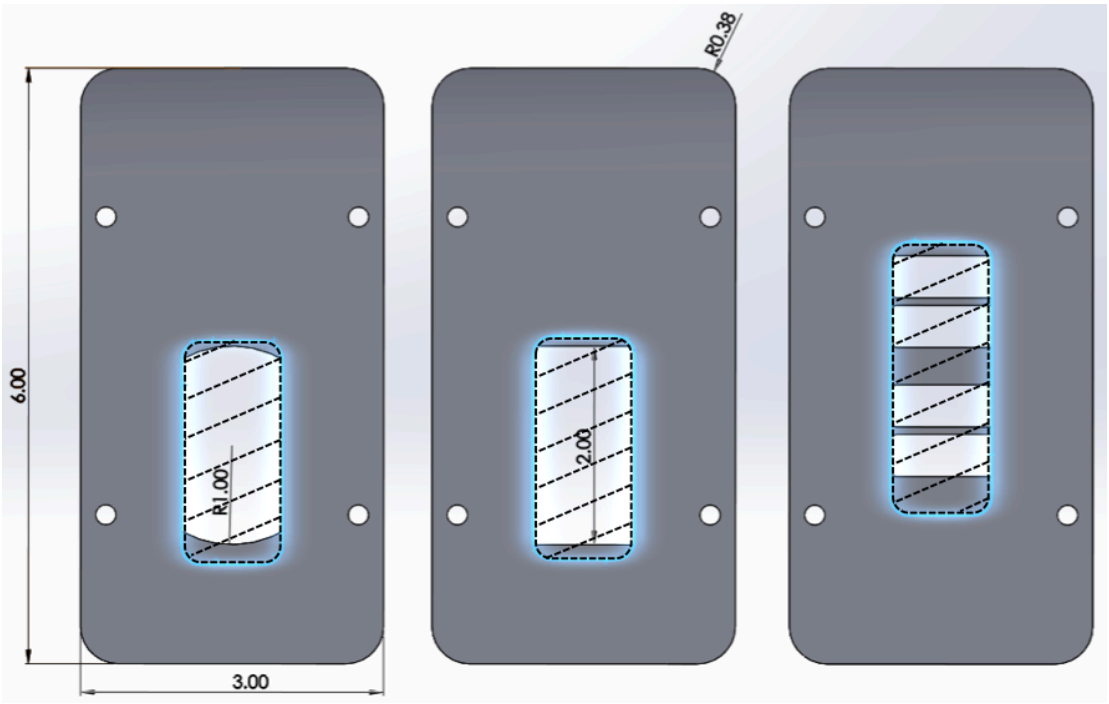

Figure 5-5. Polycarbonate window designs for mold insert plates
(all 1 in or 25.4 mm of width, dotted areas) [51]

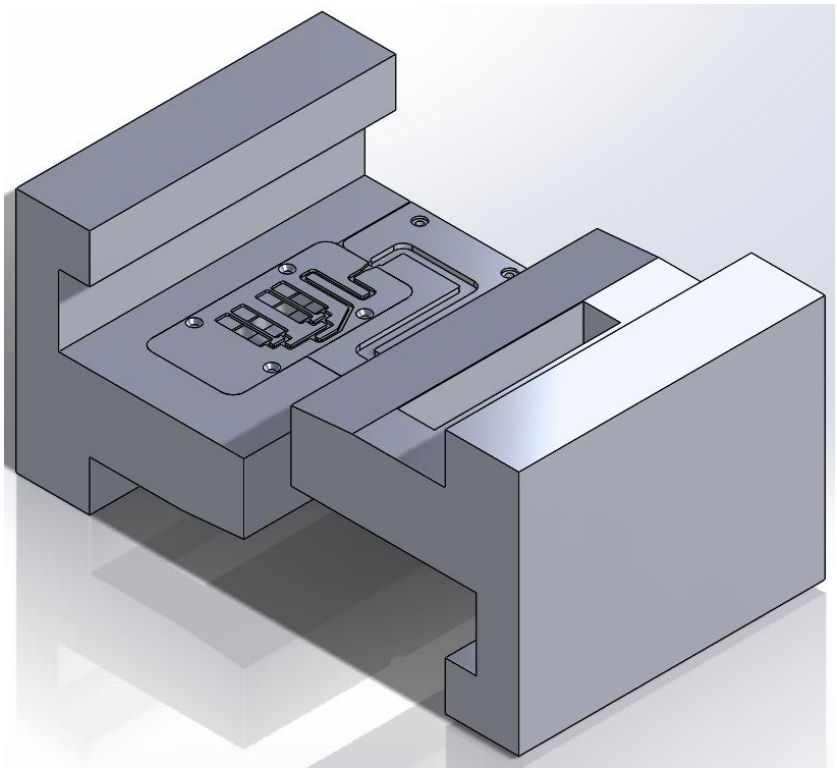
Figure 5-6. Complete mold and insert setup [51]

5.2 Camera and Accessories

To capture a live video of the mold filling process, a Pulnix TM-6740GE GigE Progressive Scan Camera was used. Table 5-1 below tabulates the camera's features. The camera set-up required 2 out of the12-pin Hirose connectors. This was connected directly to the computer control, via a Gigabit Ethernet (GigE) cable. It should be noted that certain computer models may need a Peripheral Component Interconnect (PCI) network interface card.

Table 5-1. Features of the high-speed camera

Resolution	640 (h) x 480 (v)
Frame Rate (fps)	265
Pixel Size (μm)	7.4 (h) x 7.4 (h)
Interface	GigE (Ethernet)
Sensor Type	CCD
Voltage (VDC)	12 V
Shutter Speed (μs)	15.60 (min), 16667 (max)
Power (watts)	5
Weight (g)	194
Dimensions (mm)	84 L x 51 W x 51 H

The software used to control the high-speed camera was the JAI Software Development Kit (SDK) and Control Tool, which requires a 64-bit platform. The maximum real-time acquisition frame rate was 265 fps, while the capture rate in this investigation was limited to 200 fps. This was deemed high enough to capture and provide slow motion sequences of the entire cavity filling process.

After frame capture, an external software, Final Cut, was used to compile the frames and develop them into .mov files. The motion videos of cavity filling trials

were compiled successfully for all the experiments. Two video versions were recorded made for each capture - one at 60 fps (slow motion) and another in real time at 200 fps.

The injection molding machine used (Nissei PS40E5A 40 ton injection molding machine), did not have a camera mount. Hence this was built, as shown in Figure 5-7. The mount was used to position the camera and provide a fixture to accommodate the light. The light source was placed under the mold as shown in Figures 5-8 and 5-9.

This system set up allowed natural light to penetrate through the mold window. In this way, the high-speed camera mounted above the mold windows was able to detect the motion in the mold cavities and capture the live images.

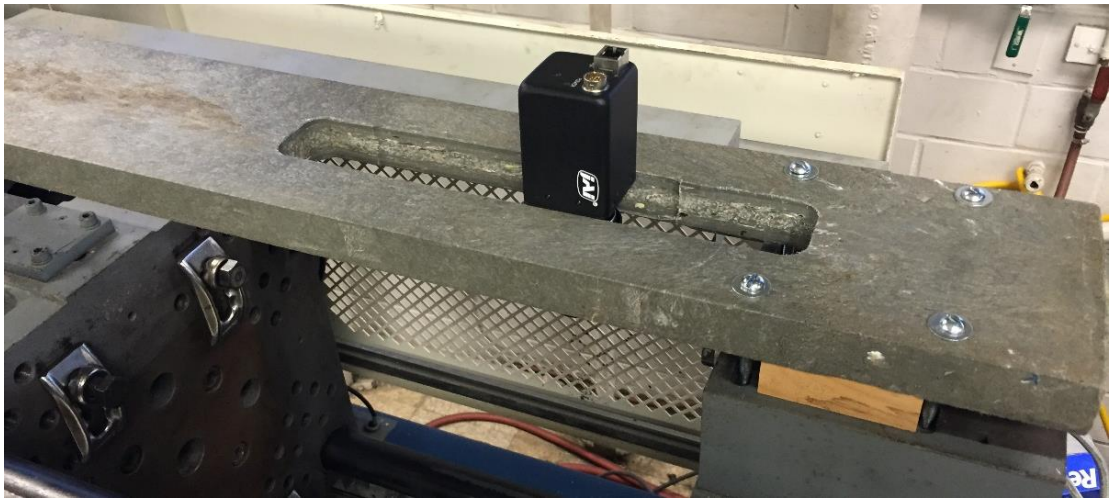

Figure 5-7. Camera mount and camera position above the molds (no wiring)

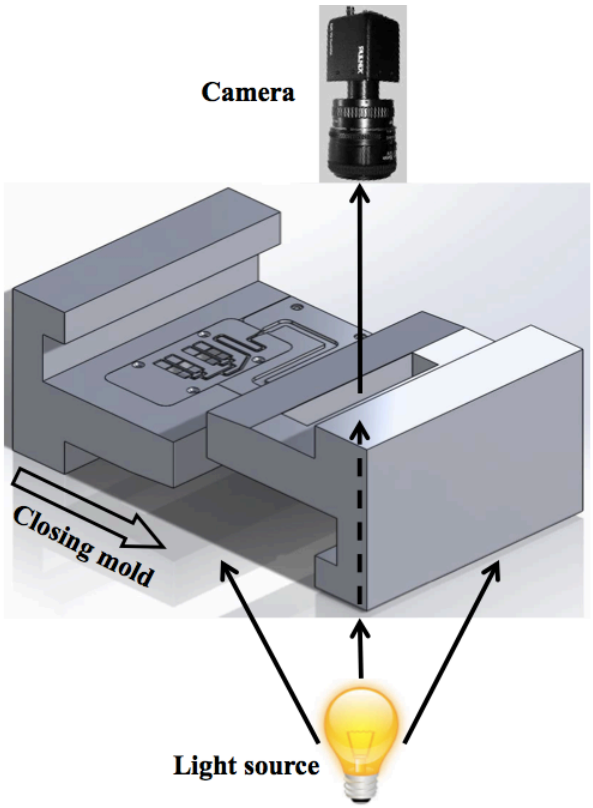

Figure 5-8. Positions of CCD camera, injection molds and light source

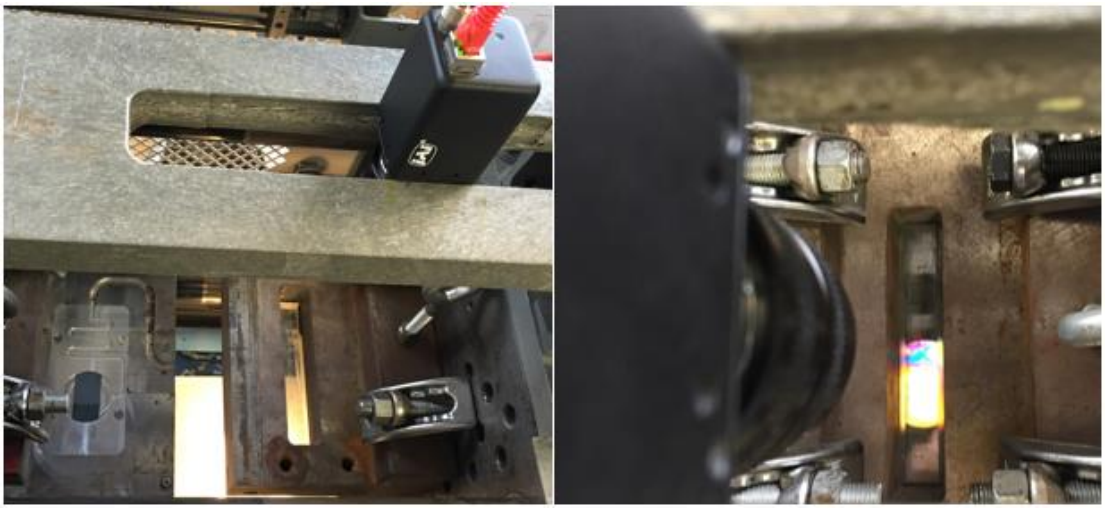

(a) (b)

Figure 5-9. Camera mount (a) and light source setup (b) (seen from the camera side) [51]

5.3 System Adjustments and Injection Molding

5.3.1 Pressure Related Adjustment

At the earliest stages of the cavity insert design, it was agreed upon that the cheapest and quickest route in machining the inserts was to use aluminum instead of steel, the latter of which was used in previous studies. However the first round of injection molding experiments produced an excess of flash, which was caused by the insert bending due to the pressure of the polymer injection.

Several possible reasons may be attributed to this issue. First, the shot size and injection pressure may have been too high to begin with, since they were at 60 mm (screw displacement) and 35 % of the full pressure (about 64 MPa), respectively. Additionally, upon further inspection of the mold, the portion of the moveable mold half (Figures 2-27 and 2-28 and Figure 5-6) which held the insert, was supported solely by the polycarbonate plastic, which may have also deformed under high pressure. In fact, under the insert runner gate half of the insert plate, the polycarbonate plate had already been compressed by about 0.5 to 1 mm relative to the steel mold. This may have allowed the aluminum insert to deform freely when the polymer would transition from the wider (0.37 in) runner to the smaller (0.12 in) insert runner at the given injection pressure. This was unexpected since previous studies by David Angstadt, did not encounter such bending issues.

It was hypothesized that this issue did not occur in the previous study since the runner in that case did not extend out onto the insert plate. Previously, the insert plate was the entire cavity, which had a larger space for the polymer to fill. This exerted

much less pressure on it. This insert bending incident prompted further investigation of the polycarbonate window on the stationary half of the mold. Unfortunately, it was found that the polycarbonate window, which was 0.0625 in thick, had fractured into multiple pieces with the primary fracture along the center of its length.

In order to fix the issue, it was determined that steel inserts were required. Each insert was then made again using steel. To combat the spacing issue, which was caused by the deformation of the polycarbonate that normally provide support under the insert plate, necessary spacers, which were simply made of paper and tape, were placed under the insert to make up for the empty space. It was also necessary to taper the spacers, since the deformation of the underlying polycarbonate was not uniform. The gap was greater toward the insert runner gate edge and lessened toward the middle of the window. The polycarbonate window on the stationary half of the mold was completely replaced as seen in Figure 5-10 below. In order to create a tighter seal between molds, the new window was reinforced with clear tape to increase the thickness of the window. This additional thickness would help reduce flash as the polymer reached the runner on the insert plate.

Figure 5-10. Polycarbonate window after replacement

With these additional modifications and the recreated steel insert plates, molding tests were conducted incrementally starting from shot sizes of 20 mm screw displacement, as well as a lower injection pressure starting at 5% (9 MPa) of maximum machine capacity. As the pressure, shot size, and velocity were raised incrementally, a point, where the flow front would no longer progress along the insert plate runner was reached. Once the injection pressure was raised too high, however, the polymer would flash again and run along the entirety of the insert plate, ignoring the runner. At this point further testing of higher pressures was not conducted in order to avoid bending of the insert plate.

5.3.2 Runner Length Related Adjustment

The runner length had to be adjusted since it was found that the flow front would solidify before the polymer had a chance to reach the cavity. It was hypothesized that the insert plate runner length was too long, especially since the plate was only an eighth of an inch (3.16 mm) thick with a runner depth at only 0.07 inches (1.78 mm) and 0.12 inches (3.05 mm) in width. However, before shortening the runner

length, which would require machining a short cut through the existing runner geometry, widening the runner width was adopted as the first option. The insert plate runners were further machined from a 0.12 inches width to a 0.22in width (5.588 mm). After each insert plate runner was widened, a series of tests were run and it was found that the flow front was still freezing before adequate cavity filling. As a result, it was confirmed that the runner lengths were the main issue. To shorten the runners, shortcuts were machined on the originally designed insert plates to create a new runner route, as shown in Figure 5-11 below.

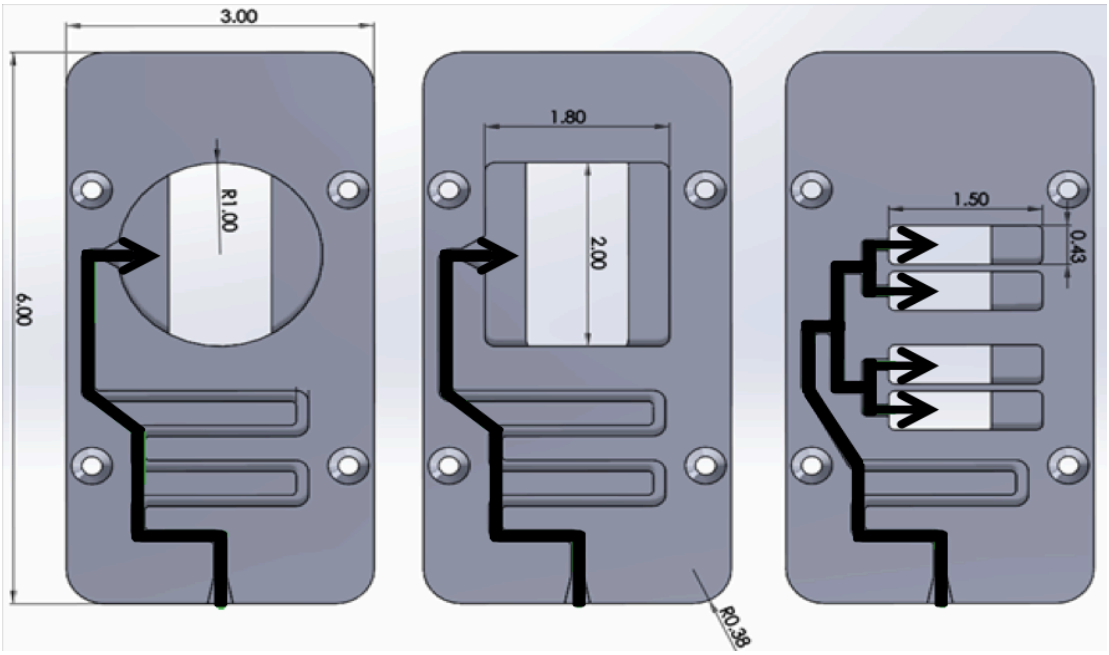

Figure 5-11. Modified runner routes, circular cavity (left), rectangular cavity (middle), and split-cavity (right)

In order to assure that these cuts would work, only the circular cavity insert plate was machined at first. Although these new cuts would shorten the runner, the existing runners needed to be blocked. The square geometry insert plate (Figure 5-11, middle), which the shortcuts had not been machined onto yet, was used to create these blocks.

Polystyrene was used to fill the length of the runner, since polystyrene is a more rigid polymer with a higher melting temperature than polypropylene. As the runners for all three insert plates were essentially the same, multiple polystyrene injection molding runs were done to create the blocks in shape of the runner as shown below in Figure 5-12.

Figure 5-12. Polystyrene runner blocks (untrimmed)

Then, these polystyrene runner blocks were cut and fit into the circular geometry insert plate. After successfully testing of the shortened runner route on the circular geometry insert plate, the other two insert plates were cut and fitted with the polystyrene blocks. (Figure 5-13)

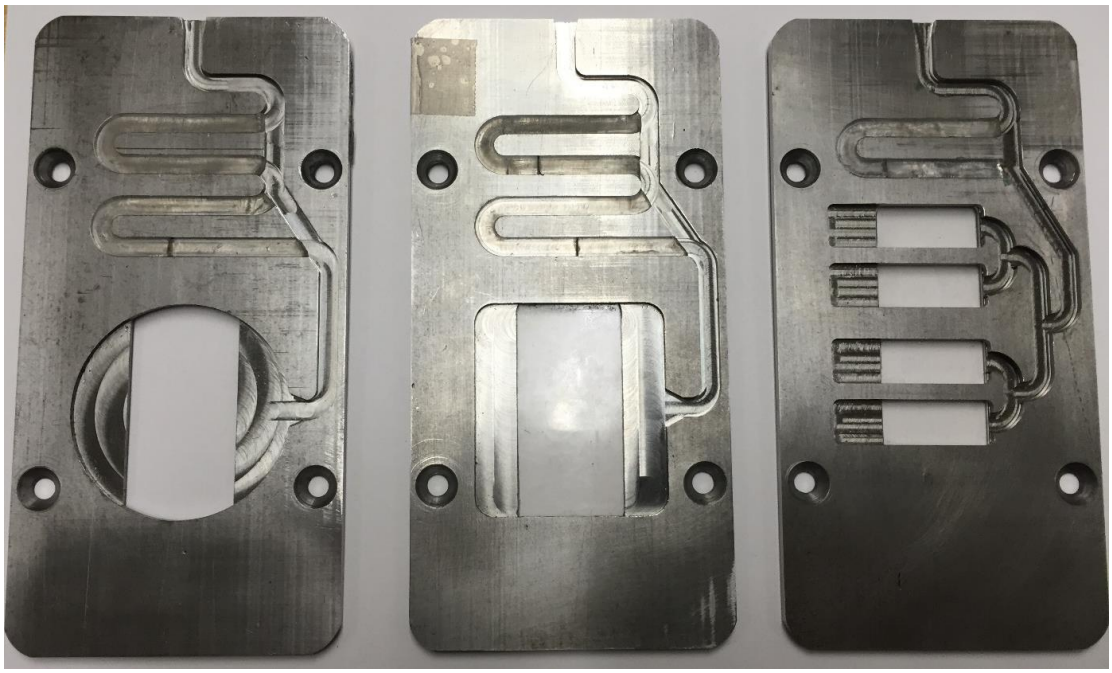

Figure 5-13. Redesigned runner routes, containing polystyrene blocks

5.3.3 Insert Plate Thickness Related Adjustment

5.3.3.1 Further Comparing and Assumptions

In order to further compare and prove the shear results influenced by the cross-section of the runner geometry, additional considerations were made regarding the thickness of the insert plate and the thickness of the runner channel. Simulations of the cavity filling processes were executed which is detailed in Chapter 8. Simulation results of the cavity filling processes on the insert plate showed that the shear rate distribution in the runner varied considerably more between the upper to lower boundary, rather than from side to side. (Figure 5-14)

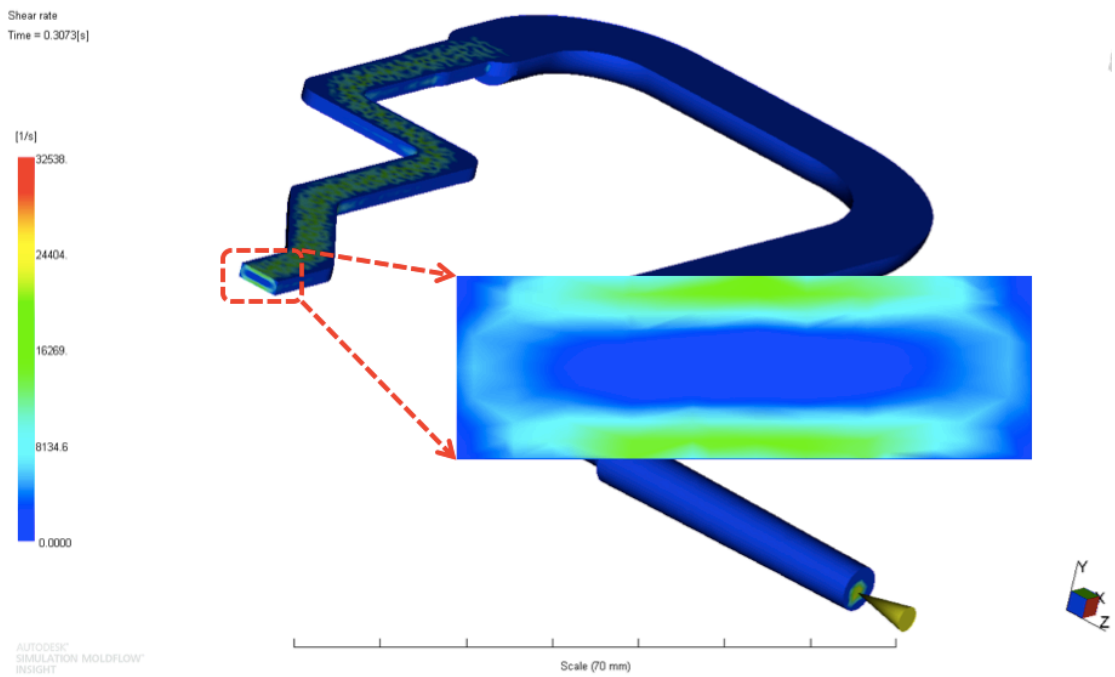

Figure 5-14. Simulated cross-section view of the runner and the shear rate distribution for the melt flow, using the insert plates in Figure 5-13

Due to the runner cross-section geometry, the high shear rate flow was distributed at the top and bottom of the flow tunnel, sandwiching the low shear flow in the middle. As a result, the high and low shear flows are not distinctly separated when the melt material passes the cavity gate or reaches the runner split point. (Figure 5-15)

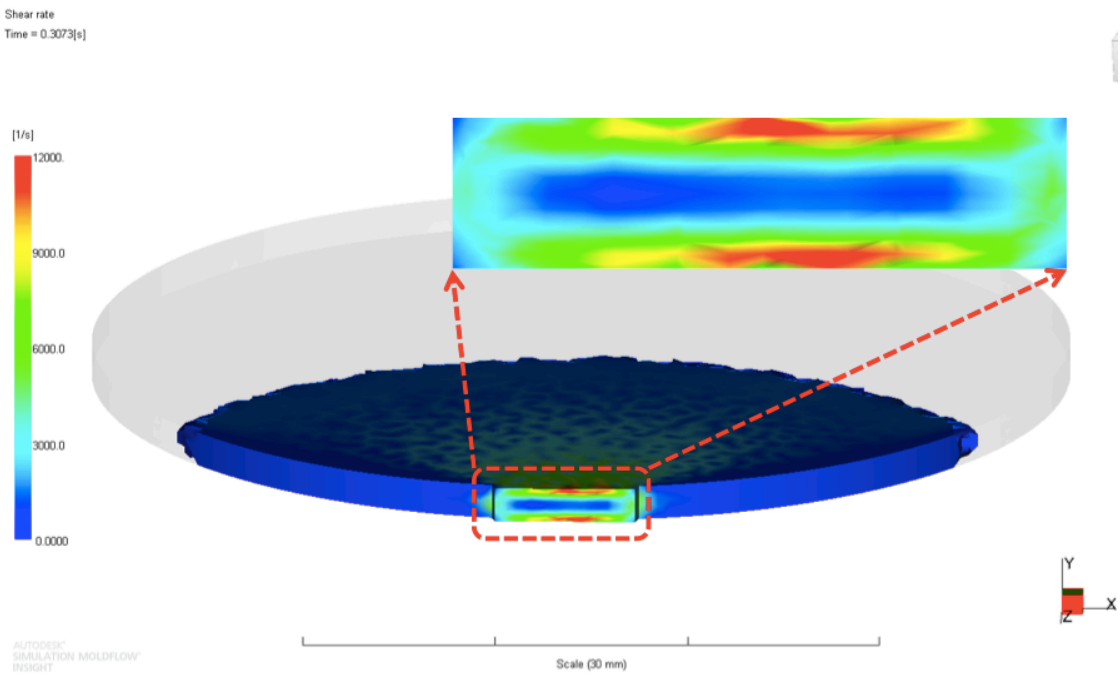

(a)

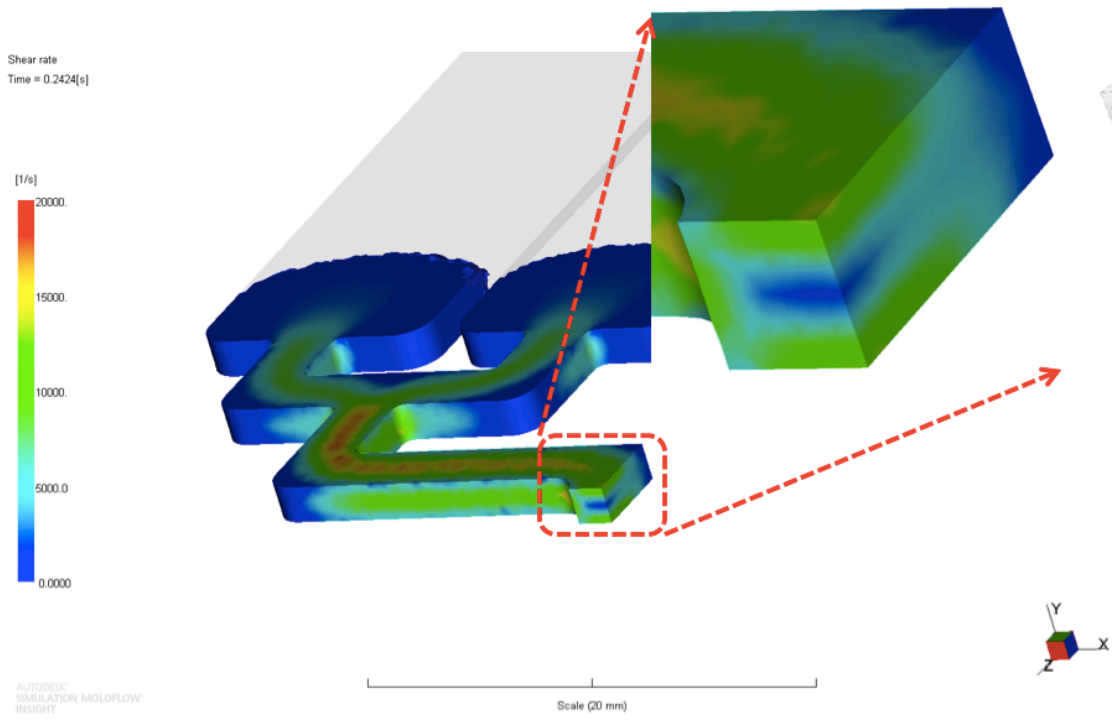

(b)

Figure 5-15. Possible shear rate distribution at cavity gate area for circular and rectangular cavity insert plates (a), and at runner split point for split-cavity insert plate (b)

In order to change the shear rate distribution and compare the molding results, thicker insert plates with modified geometry of the runner cross-section were used. Figure 5-16 shows the modified cross-section and the related shear rate distribution. The modified elements on the insert plates were the width and the depth of the runner. The depth of the cavity was made to be the same with that of the runner depth. The runner path and length, cavity shape, window position, size, and thickness, and other parameters remained the same.

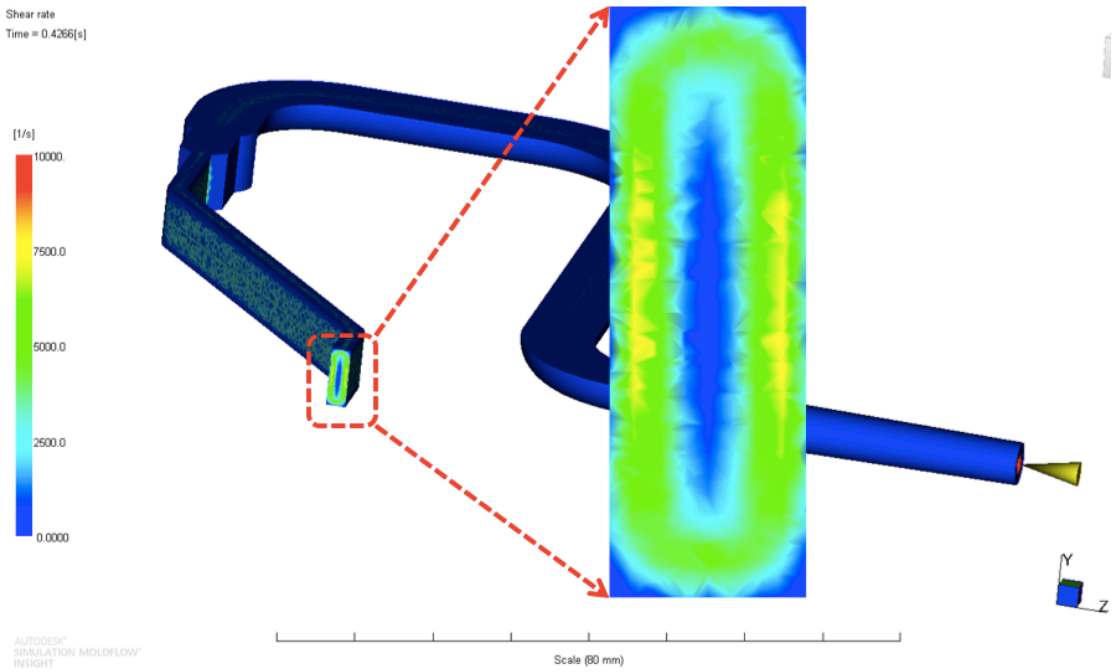

Figure 5-16. Modified results of the runner cross-section and the simulated result of shear rate distributions

In the modified runner system, the high shear flow was found to be more along the two sides of the runner channel, rather than at the upper or lower fields. As a result, distinct flow separation could be generated at cavity gate area or split point along the runner. (Figure 5-17)

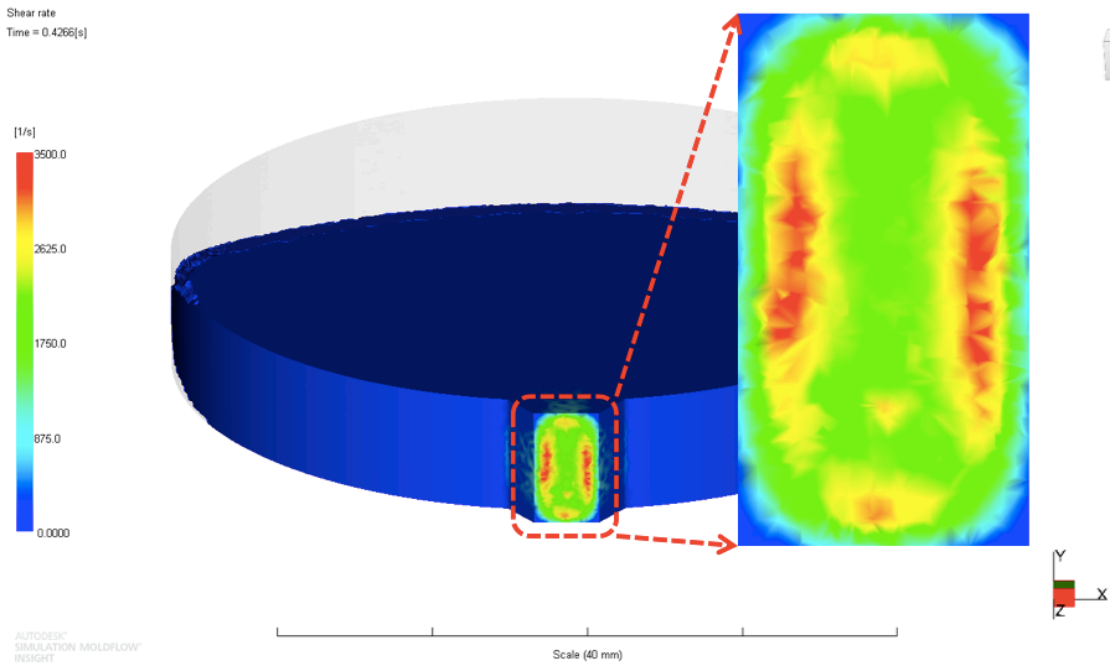

(a)

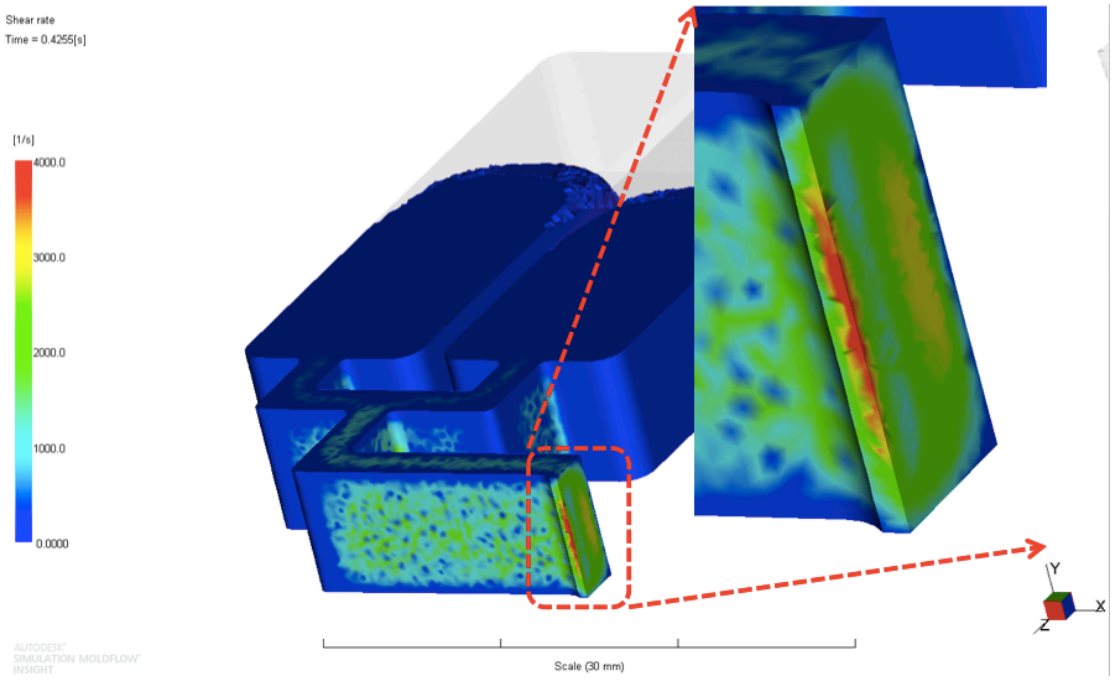

(b)

Figure 5-17. Modified flow separation and related shear rate distribution at cavity gate area for circular and rectangular cavity insert plates (a), and at runner split point for split-cavity insert plate (b)

5.3.3.2 Adjustments for Manufacturing Additional Insert Plates

Figure 5-18 shows the original insert plates in relation to the adjusted version. In order to fit the thicker plates into the mold bases, additional material was milled off from the insert plate bed on the moving mold base, resulting in a deeper insert depression (Figure 5-19). A thinner PC window without a birefringence film on the same side of the mold base was also made, to fit this additional design.

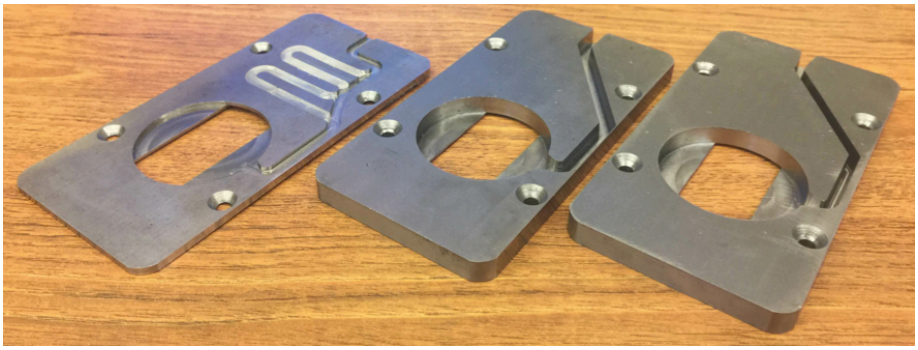

(a)

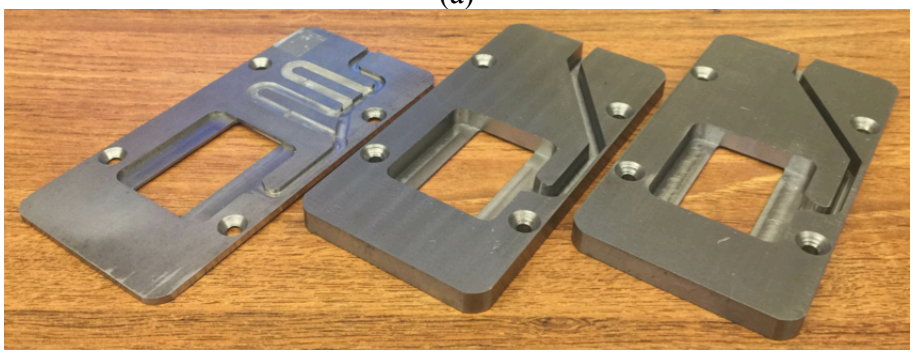

(b)

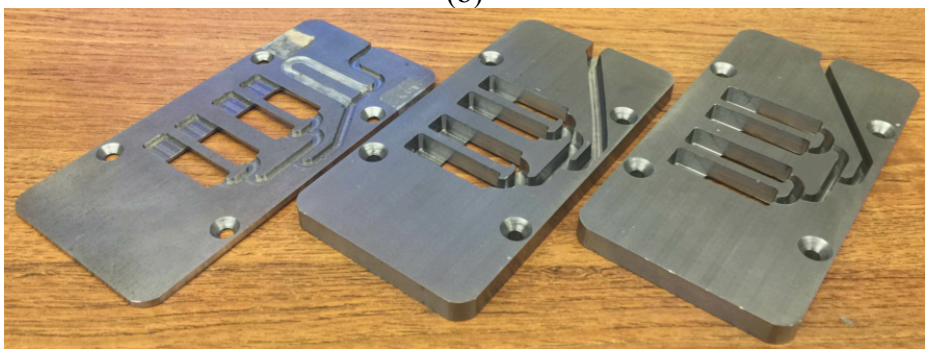

(c)

Figure 5-18. Original thinner insert plates and additional designed thicker insert plates; (a) circular cavity plates, (b) rectangular cavity plates, (c) split-cavity plates

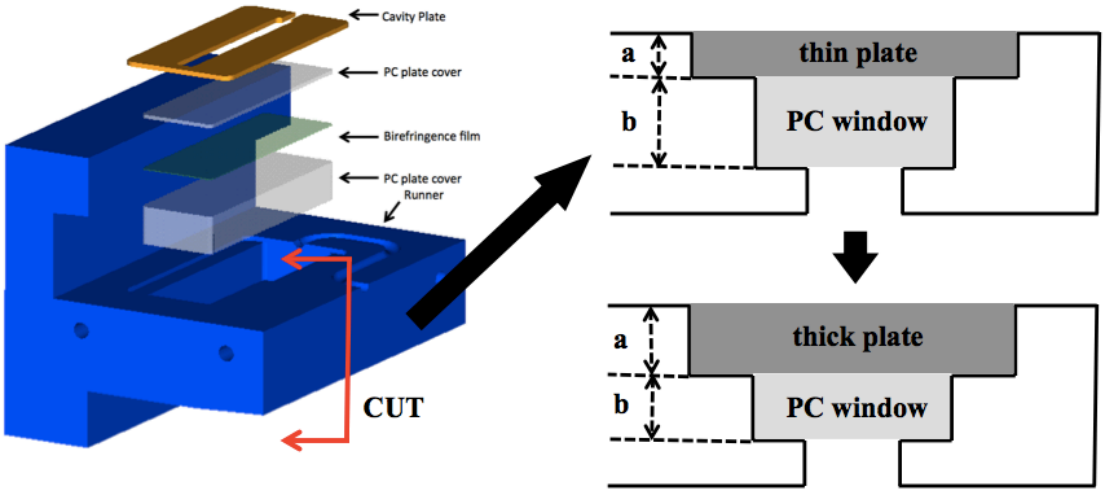

Figure 5-19. Modifications on mold base (moving side)

In reference to the dimensions shown in Figure 5-19, the value of *a* was changed from one eighth of an inch (3.175 mm) to 0.355 inches (9.107 mm), and the value of *b* was changed from 1 inch (25.4 mm) to about 0.788 inches (20.015 mm).

The modifications as noted in this section were executed after the injection molding runs that used the previous thin insert plates.

The additional insert thickness was 0.355 inches (9.017 mm). The depth of the runner and the cavity was 0.3 in (7.62 mm), while the plastic window on the other side of the insert plate remained at 0.055 in (1.40 mm). As shown in Figure 5-18, for the thicker insert plates, two levels of width, 0.1 inches (2.54 mm) and 0.22 inches (5.588 mm), were selected for further comparison of the possible shear differences influenced by runner width. The assumption was that the narrow runner might result in a more significant shear imbalance effect that can be examined.

As the runner was made deeper, the tapered runner had to be made so that the samples could be more easily removed by hand. The taper angle was determined to be 5 degrees after several machining trials by using 1-degree tapered endmill and a 5-degree tapered endmill. The tip diameter of the tool was 3/32 inches (2.381 mm), and the length of cut was 0.5 inches (12.7 mm). As a result, the runner base width remained the same, while at the surface of the insert plate, the width of the runner was slightly larger. This is 0.152 inches (3.861 mm) and 0.27 inches (6.858 mm) for the narrow runner and the wide runner respectively.

5.3.4 Injection Molding and Parameter Determination

The injection molding process was executed using a Nissei PS40E5A 40 ton injection molding machine, with a NC9000G control. Table 5-2 and Table 5-3 lists the parameters that were used. These were kept constant after determining the optimal inputs for all three cavities in the thin insert plates by using iPP.

Table 5-2. Uniform injection molding parameters for using all three thin inserts

Injection Time + Packing Time	10 sec
Cooling Time	15 sec
Packing Pressure	5.5 MPa
Nozzle Temperature	508.15 K (455 °F)
Front Barrel Temperature	494.26 K (430 °F)
Middle Barrel Temperature	488.71 K (420 °F)
Rear Barrel Temperature	488.71 K (420 °F)

Table 5-3. Steady injection molding parameters for each type of thin insert

Insert Plate Cavity Geometry	Injection Pressure	Injection Velocity
Circular	27.5 MPa	31.2 cm^3/s
Rectangular	25.7 MPa	35.5 cm^3/s
Split-Cavity	22 MPa	60.4 cm^3/s

The processing parameters were fixed after a series of initial injection molding trials. It was found that if the injection time was kept within 1 second, the high injection speed and pressure results in significant flash, bending the insert plate and ruining the molded products. Although the injection time in this study was long, in order to keep the mold in good condition and the test repeatable, it was necessary to set the injection time at about 5 seconds with a relatively low injection pressure. It is reasoned that if the shear imbalance phenomenon could still be captured in this circumstance, it is believed that more obvious shear induced imbalances may arise resulted when applying a shorter injection time or a higher injection pressure, as more shear heating effects would be generated.

For molding samples in the additionally designed thick insert plates, the two materials that were molded are iPP and PS. The injection parameters are listed Tables 5-4 to 5-8.

Table 5-4. Uniform parameters for molding iPP samples by using thick insert plates

Injection Time + Packing Time	20 sec
Cooling Time	30 sec
Packing Pressure	0 MPa
Nozzle Temperature	488.71 K (420 °F)
Front Barrel Temperature	483.15 K (410 °F)
Middle Barrel Temperature	483.15 K (410 °F)
Rear Barrel Temperature	483.15 K (410 °F)

Table 5-5. Parameters for iPP injection molding by using thick insert plates with wide runner and narrow runner

Insert Plate Cavity Geometry	Injection Pressure	Injection Velocity	Injection Time
Circular	27.51 MPa	35.5 cm^3/s	0.50 sec
Rectangular	27.51 MPa	35.5 cm^3/s	0.50 sec
Split-Cavity	27.51 MPa	35.5 cm^3/s	0.50 sec

Table 5-6. Uniform parameters for molding PS samples by using thick insert plates

Injection Time + Packing Time	20 sec
Cooling Time	30 sec
Packing Pressure	0 MPa
Nozzle Temperature	510.93 K (460 °F)
Front Barrel Temperature	516.48 K (470 °F)
Middle Barrel Temperature	510.93 K (460 °F)
Rear Barrel Temperature	505.37 K (450 °F)

Table 5-7. Parameters for PS injection molding by using thick insert plates with wide runner

Insert Plate Cavity Geometry	Injection Pressure	Injection Velocity		Injection Time
Circular	91.70 MPa	fast	63.9 cm^3/s	0.34 sec
	36.68 MPa	slow	35.5 cm^3/s	0.7 sec
Rectangular	91.70 MPa	fast	63.9 cm^3/s	0.36 sec
	36.68 MPa	slow	35.5 cm^3/s	0.76 sec
Split-Cavity	91.70 MPa	fast	63.9 cm^3/s	0.17 sec
	36.68 MPa	slow	35.5 cm^3/s	0.34 sec

Table 5-8. Parameters for PS injection molding by using thick insert plates with narrow runner

Insert Plate Cavity Geometry	Injection Pressure	Injection Velocity		Injection Time
Circular	91.70 MPa	fast	63.9 cm^3/s	0.32 sec
	36.68 MPa	slow	35.5 cm^3/s	0.88 sec
Rectangular	91.70 MPa	fast	63.9 cm^3/s	0.35 sec
	36.68 MPa	slow	35.5 cm^3/s	0.96 sec
Split-Cavity	91.70 MPa	fast	63.9 cm^3/s	0.17 sec
	36.68 MPa	slow	35.5 cm^3/s	0.45 sec

The packing pressure was set to 0 for all cases, as the priority in this investigation was to capture live images of the cavity filling processes, especially of the melt flowing past the transparent window. Additionally, in order to investigate the cavity filling differences between the high and low shear flows, short shots were intentionally made. These short shots would solidify and taken out before completely filling the cavity, hence packing pressure is not necessary.

For molding iPP samples, the injection rate was set at 50% of the maximum injection rate (71 cm^3/s). For molding PS samples, a faster injection rate was applied in order to compare the molding results between the fast and the slow molded samples. The injection pressures for fast injection molding were all higher than the pressures applied for the slow injection molding runs, as higher injection pressure would be needed to operate and achieve the increased injection velocity. The fast injection velocity was set at 90% of the maximum injection velocity of the machine, meanwhile the slow injection velocity was kept at 50%. The related injection pressures for fast molding and slow molding experiments were set at 50% and 20% of the maximum injection pressure (183.4 MPa) respectively. As the values of shear rate in the runner

could be influenced by injection velocity, it was hypothesized that by applying higher injection rates during moldings, the shear imbalances would be more obvious for observation. [81]

6 Molded Product Analysis and Equipment

Differential Scanning Calorimetry (DSC) was applied to investigate the crystallinity differences and melting point migration caused by the shear induced imbalances. In addition to this, further aspects of melting behavior were investigated through novel flash DSC testing. Tensile testing was included to explore the differences in yield stress and Young's modulus of the molded samples. Wide Angle X-Ray Scattering was performed to uniquely identify the crystallinity variations.

6.1 Differential Scanning Calorimetry

Traditional DSC testing was used to find the crystallinity levels of samples taken from specific regions of disc-shaped products made from PP ho / iPP, PP co, POM, N66 and N66_50 without application melt rotation during single-cavity injection molding. In addition to single-cavity molded part tests, DSC testing was also carried out to study regional PP co samples and N66_50 samples made with MRT.

Traditional DSC was also applied to explore the crystallinity variations of the iPP, PBT, and N66 samples, which were injection molded into the multi-cavity mold under molding conditions (1), (2) and (3) (as mentioned in Chapter 4), since the samples molded without and with MRT were expected acquire different levels of this parameter.

The additional heat produced by the high shear flow is expected to significantly increase the local melt temperature. As a result, the high shear flow should experience a longer cooling and corresponding crystallization time. [4] [5] An assumption in this

study is that the molded parts would have the enhanced crystallinity for samples taken from Area 1 (or from the cavities which was filled with the high shear flow), while a lower percentage of crystallinity would be acquired in the samples from Area 2 (or from the cavities which was filled with the low shear flow).

The DSC machine used in this study was a TA Q2000. (Figure 6-1) Samples weighing between 5 mg and 10 mg were heated 10 °C/min from room temperature to 190 °C, 200 °C, 300 °C and 290 °C for all polypropylene, polyoxymethylene, polybutylene terephthalate, and all nylon samples respectively. (Table 6-1) The testing samples were taken from both the high and low shear regions, from both the single-cavity and the multi-cavity molded parts.

Table 6-1. Heat up temperatures for DSC test materials

Material	DSC max temperature (°C)
PP ho / iPP	190
PP co	190
POM	200
PBT	300
N66	290
N66_50	290

Figure 6-1. TA Q2000 used for DSC test

Crystallinity was determined through measuring the heat of fusion and use of the heat of fusion of 100% crystallinity samples of the polymer, which are 207 J/g, 326.3 J/g, 142 J/g and 255.8 J/g for all polypropylene samples, polyoxymethylene, polybutylene terephthalate, and all nylon samples, respectively. [82] [83] [84] (Table 6-2)

Table 6-2. Heat of fusion of 100% crystal

Material	DSC max temperature (J/g)
PP ho / iPP	207
PP co	207
POM	326.3
PBT	142
N66	255.8
N66_50	255.8

The heats of melting, ΔH_m, is determined by integrating the areas (J/g) under the DSC peaks. The percent crystallinity was determined using the following Equation 6-1. [82] [85]

$$\% \text{ Crystallinity} = \frac{\Delta H_m}{\Delta H_f^\circ} \times 100\% \qquad \text{[Equation 6-1]}$$

ΔH_f° is the heat of fusion of 100% crystal material.

6.2 Tensile Test

An INSTRON 5667 C 9620_30 kN tensile testing machine (Figure 6-2) was used to study the mechanical properties of dog bone samples molded in the 8 cavity configuration out of both the PP homo-polymer (PP ho / iPP) and the PP copolymer. All of the dog-bone samples produced were manufactured via traditional molding MRT. In all cases, the tensile testing speed was set at 50 mm/min for the ductile polypropylene samples.

The samples molded from the high shear melt flow in Group 1, were expected to acquire a higher levels of tensile stress and Young's modulus.

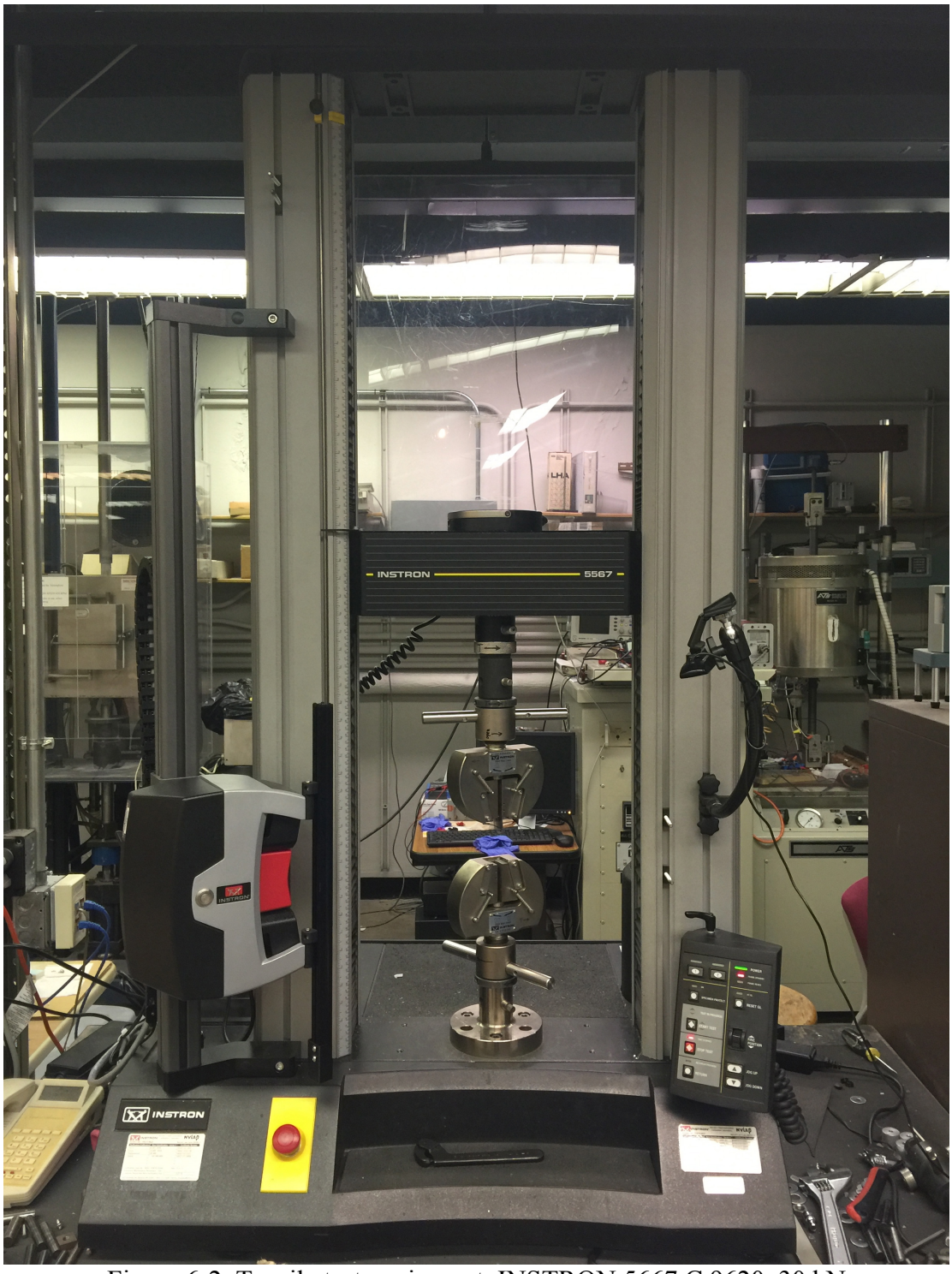

Figure 6-2. Tensile test equipment, INSTRON 5667 C 9620_30 kN

6.3 Flash DSC

Flash DSC is a recently developed DSC testing technology that can apply ultra-high heating rates and ultra-high cooling rates to testing samples. Flash DSC has advantages that the traditional DSC doesn't have. Some of the benefits of using flash DSC are that the influences from cold crystallization or reorganization during normal heating procedures can be minimized or even avoided. During the traditional DSC trial, the cold crystallization could happen during heating process, as the conventional heating rate is usually not sudden enough to withstand the cold crystallization speed. However, the flash DSC is capable of applying a heating or cooling rate up to about 2,000,000 K/min or 200,000 K /min respectively within certain temperature ranges. In addition, materials with defined structural properties such as crystallinity can be readily tested [86] and even a tailored crystallinity level could be realized.

In this study, the Flash DSC 1 machine from Metter Toledo was used. (Figure 6-3) It is able to perform heating and cooling of samples between -95°C to 450°C with the rates of 2,400,000 K/min and 240,000 K/min, respectively. The Flash DSC 1 has a maximum sampling rate of 10 kHz to fit the ultra-high heating and cooling rates.

Figure 6-3. Flash DSC 1, Metter Toledo

In this study the Flash DSC tests were limited to regional polypropylene copolymer samples taken from the disc shaped parts for single-cavity molding. This was done for PP co products that were molded both with and without MRT. The Flash DSC testing temperature ranged from room temperature to 240°C with a heating rate of 6000 K/min. This enabled the relevant PP copolymer melting peaks to be effectively captured.

For multi-cavity molding, Flash DSC was performed only on the iPP samples molded under the three molding conditions (as mentioned in Chapter 4 (4.1.2)). In order to capture the unaffected melting behaviors, especially the melting points, the

samples were all heated from room temperature up to 513 K, at the heating rate of 2000 K/sec.

It was supposed that the samples from the region experienced a higher shear rate would exhibit a higher melting temperature, as more crystals were generated as a result of a longer crystallization duration.

6.4 Wide Angle X-Ray Scattering

Wide Angle X-Ray Scattering (WAXS) was firstly performed on iPP samples molded in split cavities in order to further explore the crystal components.

It is known that iPP crystalline usually includes α and β spherulites. The α crystal has a melting point about 440 K, while the β crystal melts at 421 K. [87] [88] The hexagonal β crystal, first reported by Padden and Keith in 1959, has a higher crystallization rate than the α crystal at temperatures ranging between 373.15 K to 405.15 K. In contrast, the α form crystalizes faster above 413 K, where the β crystal starts to transform into the more stable α crystals. [87] [89] [90] [91]

Since the melt flow during the injection molding process experiences variations of shear induced thermal histories, the crystal composition was expected to vary. WAXS was executed via a Rigaku MiniFlexTM II machine (Table 6-4), in order to study the amount of β crystal formed and affected during the injection molding of iPP.

Figure 6-4. Rigaku MiniFlexTM II

The iPP WAXS pattern usually exhibits five general peaks at 2θ = 14.1°, 16.1°, 16.9°, 18.6°, and 20.3°, corresponding to the x-ray diffraction intensities of related crystal reflections from α (110), β (300), α (040), α (130) and γ (117) planes respectively. [90] [92] [93] The γ crystal content was ignored in this study, since it is the least stable form. It is also the easiest form to that morphs into the α and β form during heating. [87] As a result, there was no obvious peak captured at 2θ = 20.3°. On the other hand, the high shear rate the melt experiences during molding may accelerate the nucleation and the growth of the α crystals. [93] [94]

The scan range was set from 2θ = 15° to 17°, with a scan speed of 0.05° per minute and a sampling width of 0.02°, in order to monitor and compare the β crystal reflection intensities of the samples molded under all three conditions. The assumption was that the sample from the high shear region might contain lower amounts of β crystals relative to samples from the low shear region.

7 Experimental Results and Discussions

7.1 Additional Injection Molding Results

For single-cavity molding, PP co was injection molded with and without MRT. Figures 7-1 to 7-3 provide the geometry comparisons of the results for PP co samples molded without and with MRT. In Figure 7-1, in the sample molded with MRT (Figure 7-1 (b)), it is obvious that the melt front at the center of the cavity leads those flowing at the sides as observed in Figure 7-1 (a). This is as expected, as earlier noted in Figure 2-19 and Figure 4-2.

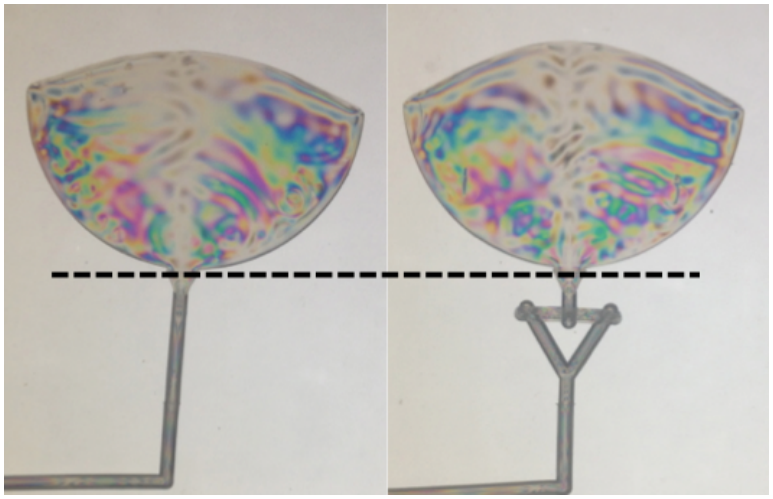

(a) (b)

Figure 7-1. 50% disc-cavity filled results of PP co molded without (a) and with (b) MRT

Figure 7-2 and Figure 7-3 show the consequent molding processes, which were about 85% and 95% disc-cavity filled results of PP co molded with and without MRT. It is noted that similar results were generated. It is obvious that in the 95%-filled samples, there is a significant potential of a gas trap or weld line formation at the top

area of the cavity (Figure 7-3 (a)). However, with MRT (Figure 7-3 (b)), the molding result was ideal.

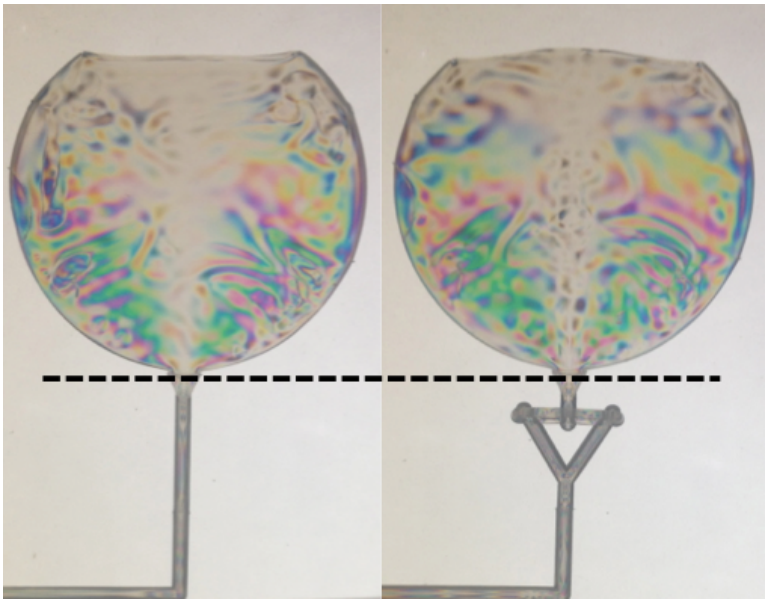

(a) (b)

Figure 7-2. 85% disc-cavity filled results of PP co molded without (a) and with (b) MRT

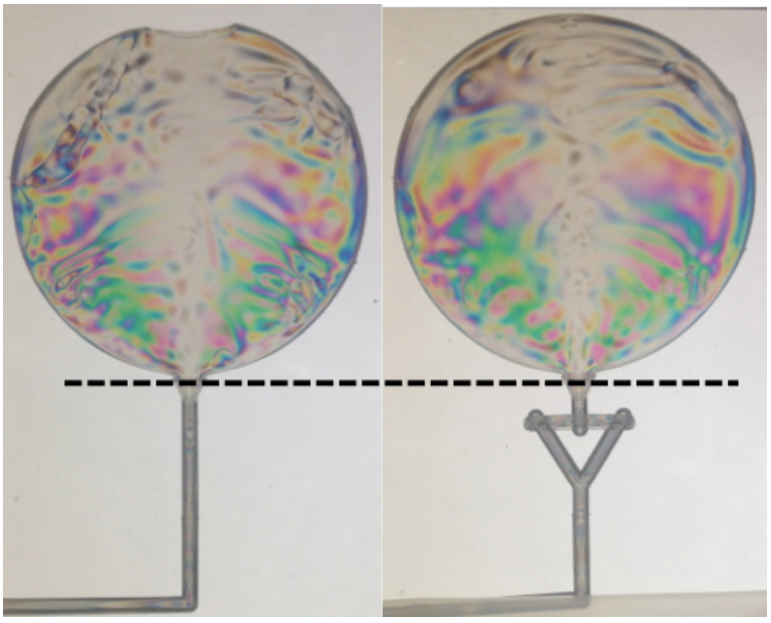

(a) (b)

Figure 7-3. 95% disc-cavity filled results of PP co molded without (a) and with (b) MRT

Furthermore, molding results shown Figure 7-4 and Figure 7-5 reveal that shear rate differences generated during conventional injection molding had a significant effect on the final shape of the short shot iPP samples, especially for the fast molded samples during multi-cavity molding. Once MRT was implemented however, sample shape variations were reduced. (Figure 7-6)

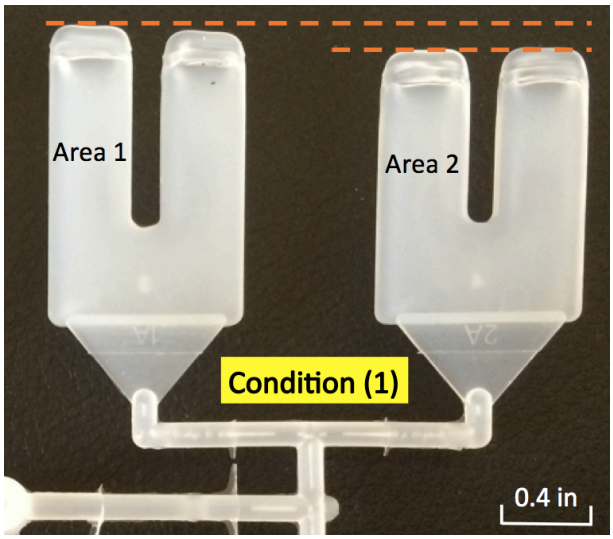

Figure 7-4. Ending tip variations of the samples, fast molded with no MRT (molding condition (1) of multi-cavity molding, iPP)

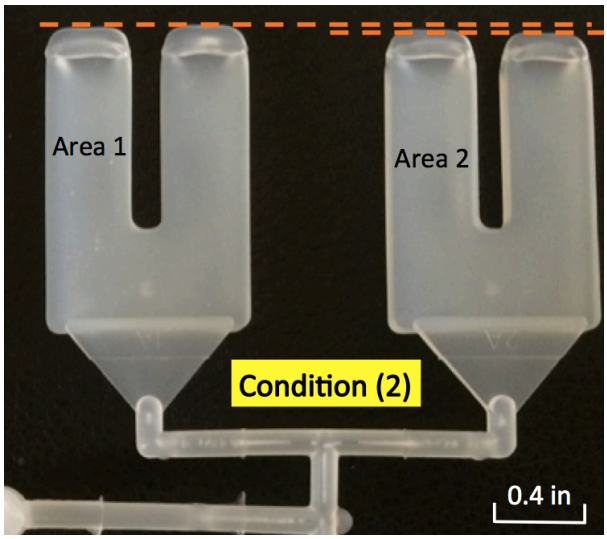

Figure 7-5. Ending tip variations of the samples, slow molded with no MRT (molding condition (2) of multi-cavity molding, iPP)

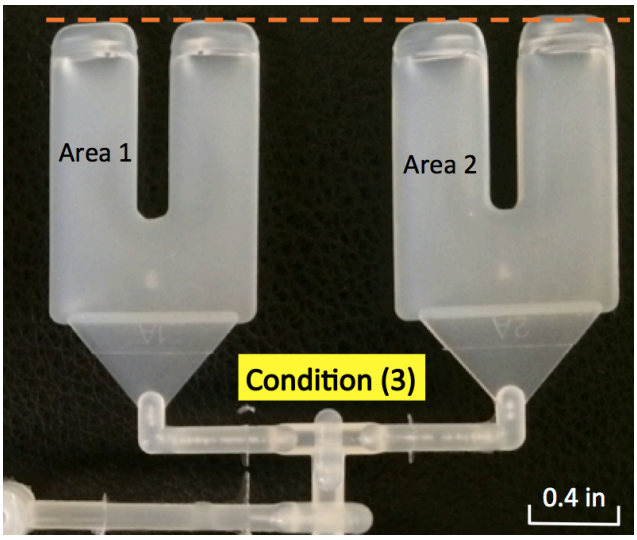

Figure 7-6. More evened ending tips of the samples, fast molded with MRT, showing even melt distribution (molding condition (3) of multi-cavity molding, iPP)

Similar molding results for PBT and N66 are shown in Figures 7-7 to 7-12. These results indicate the obvious dependence of shear imbalanced results on the molding history, and that MRT is able to suppress these effects.

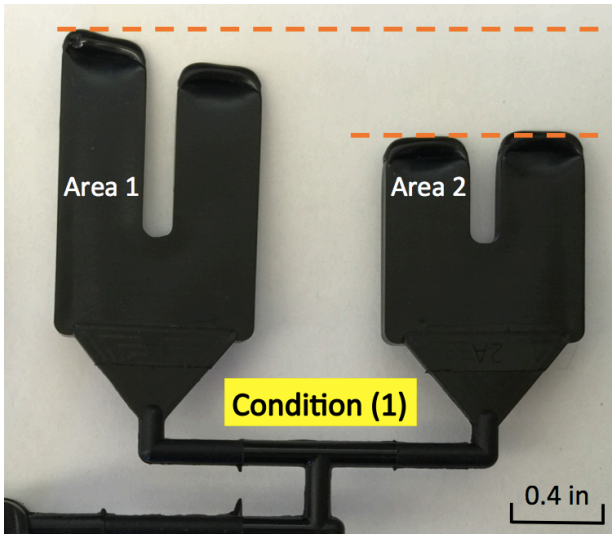

Figure 7-7. Ending tip variations of the samples, fast molded with no MRT (molding condition (1) of multi-cavity molding, PBT)

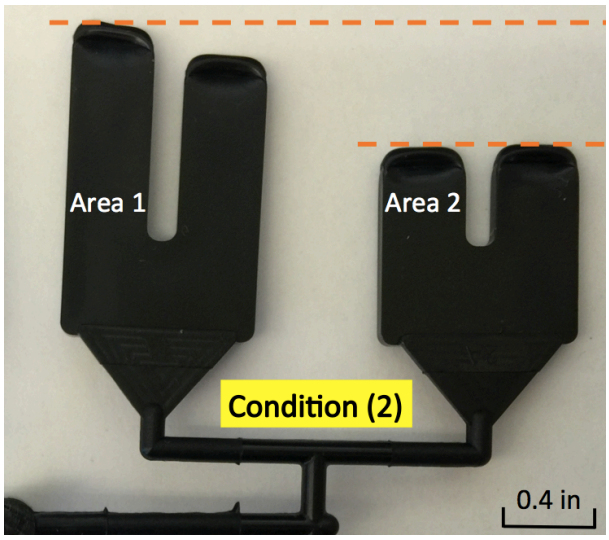

Figure 7-8. Ending tip variations of the samples, fast molded with no MRT (molding condition (2) of multi-cavity molding, PBT)

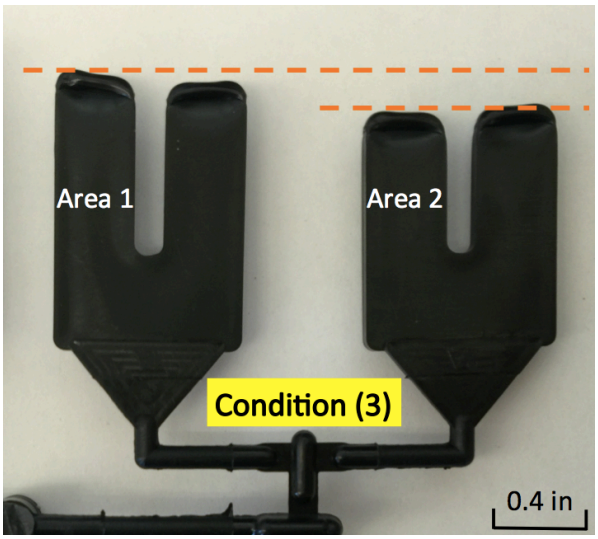

Figure 7-9. More evened ending tips of the samples, fast molded with MRT (molding condition (3) of multi-cavity molding, PBT)

In Figure 7-7 and Figure 7-8, the ending tip variations were all obviously larger than those shown in Figure 7-9. This indicates that the shear imbalance occurs in both fast and slow molded PBT samples. It is interested to note that the results for both fast molding and slow molding were similar. It is possible that for PBT, the imbalanced

cavity filling may not be sensitive to injection rate, or injection speed is not the dominant cause of shear imbalance.

For N66, Figures 7-10, 7-11 and 7-12 provide the large, medium and small ending tip variations for samples molded in condition (1), (2) and (3), respectively. It is believed that the increased injection rate results in a larger shear imbalance. Also, in Figure 7-12, it is obvious that MRT reduced the shear imbalance during injection molding.

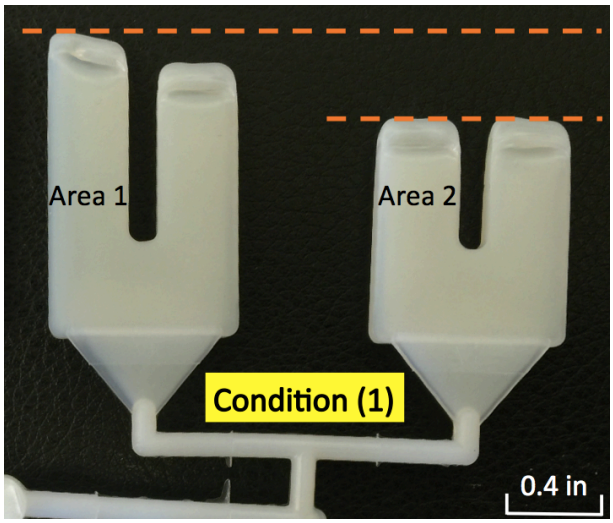

Figure 7-10. Ending tip variations of the samples, fast molded with no MRT (molding condition (1) of multi-cavity molding, N66)

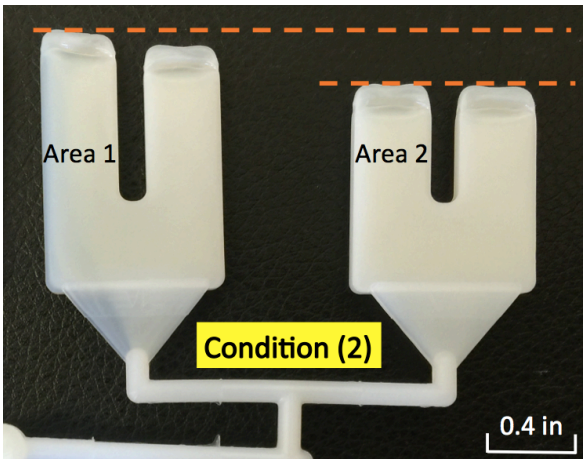

Figure 7-11. Ending tip variations of the samples, fast molded with no MRT
(molding condition (2) of multi-cavity molding, N66)

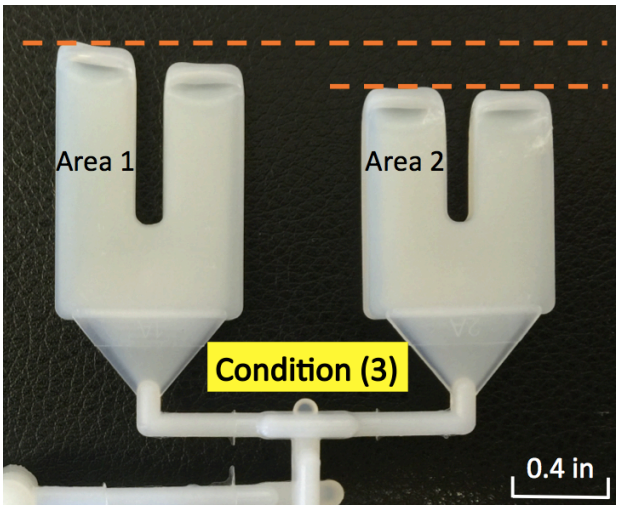

Figure 7-12. More evenly distributed ending tips of the samples, fast molded with MRT
(molding condition (3) of multi-cavity molding, N66)

As previously noted, these results also indicate that shear imbalanced molding depends on the molding history, and MRT is able to reduce this effect.

7.2 Traditional DSC

7.2.1 Experimental Results for Single-Cavity Molded Specimen

As shown in the bar graphs in Figures 7-13 to 7-15, it is clear that the samples exhibit diverse crystallinity from area 1 to area 2 for all of the polymers that were investigated.

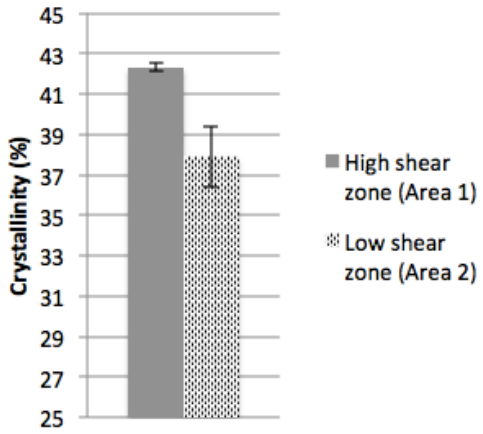

Figure 7-13. The crystallinity of PP ho samples from area 1 and area 2 of the disc molding parts

Figure 7-13 compares the crystallinity difference of the PP ho specimens. It is obvious that the specimens taken from area 1 have a higher crystallinity compared to those from area 2. The specimens taken from the area that experienced relatively higher temperature and shear history exhibited crystallinity of about 42.3%, while the low temperature/low shear specimens exhibited a crystallinity of 37.9%. The observed difference in melting point of the samples from the two regions, however, was insignificant. The test results indicated the averaged melting points were 167.8 °C and 168.7 °C. respectively.

For the PP co and POM samples, melt induced shear imbalances did not have a significant effect on observed regional crystallinity levels. (Figures 7-14 and 7-15)

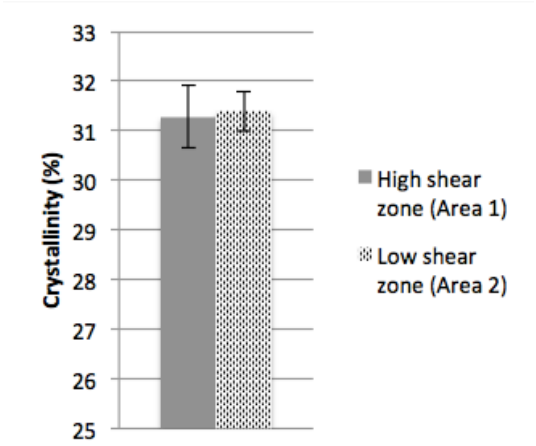

Figure 7-14. The crystallinity of PP co samples from area 1 and area 2 of the disc molding parts

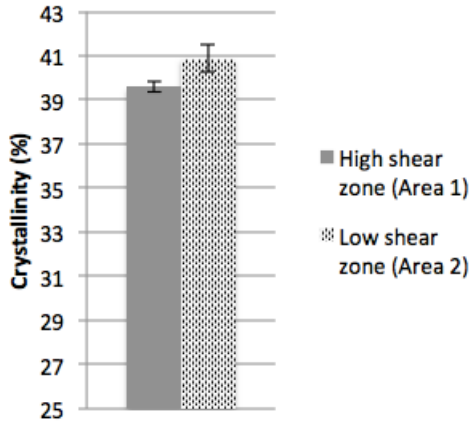

Figure 7-15. The crystallinity of POM samples from area 1 and area 2 of the disc molding parts

For PP co, samples from area 1 had an average crystallinity of 31.3% compared to 31.4% for the samples from region 2. For POM, the average crystallinity of samples taken from areas 1 and 2 were 39.6% and 40.9 % respectively.

The observations may be attributed to the crystallization behaviors of PP co and POM. For PP co, the ethylene comonomer may act as a nucleating agent, making it easy for PP co to crystalize and overcoming the shear influence. [95] As a result, similar levels of crystallinity were generated in the high and low shear regions. For POM, the repeat unit in the backbone is showed in Figure 7-16 (a). Compared to the repeat unit of iPP (Figure 7-16 (b)), the backbone structure of POM is expected to be more regular. According to the crystallization theory mentioned in Chapter 2, it was easier for POM to crystalize. Thus, in this regard, POM samples from different shear regions could exhibit comparable levels of crystallinity.

(a) (b)

Figure 7-16. Repeat unit in the backbone structure of (a) POM and (b) iPP [96] [97]

Another possible explanation could be that it is commonly known that more energy is needed to disrupt the structure of a higher viscosity material. Figure 7-17 provided the viscosity value vs. shear rate for iPP, PP co and POM in molding according to the simulation study, which will be illustrated in Chapter 8. The highest shear rates for iPP, PP co and POM during molding were about 10 000 1/s, 5200 1/s and 5000 1/s respectively. However, the related viscosities for PP co and POM were higher than that of iPP. In this study, because of the relatively high viscosity of PP co and POM materials, it was perhaps less easy to separate the high shear flow and the low shear flow regions for the PP co and POM materials with the runner configuration and processing conditions employed. As a result, the shear flow distribution would be

more even than that of lower viscosity materials. In order to find more obvious results with PP co and POM samples, faster injection rates may be required for the study.

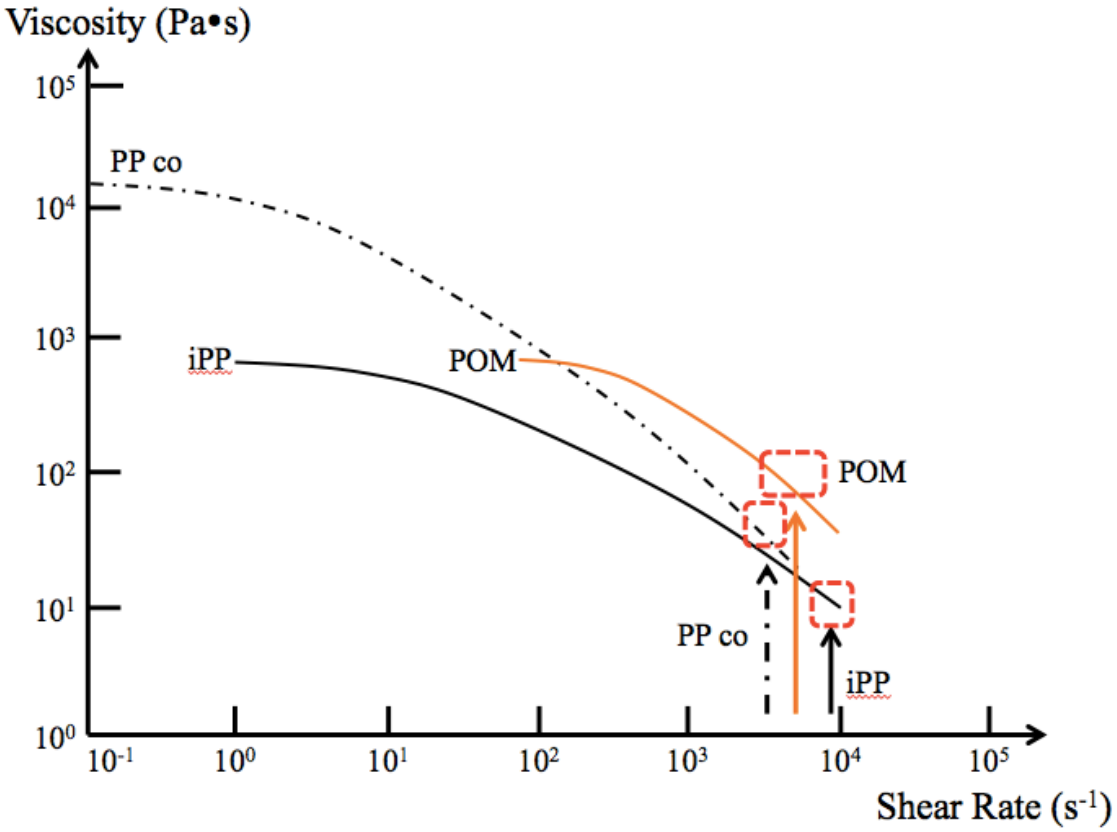

Figure 7-17. Viscosity vs. shear rate for iPP, PP co and POM single-cavity molding

Figure 7-18 shows the crystallinity of the PP co samples molded using MRT. With MRT the crystallinity of the samples from area 1 and area 2 were all approximately 31.0%. The crystallinity difference between samples from these two was less than that observed without MRT.

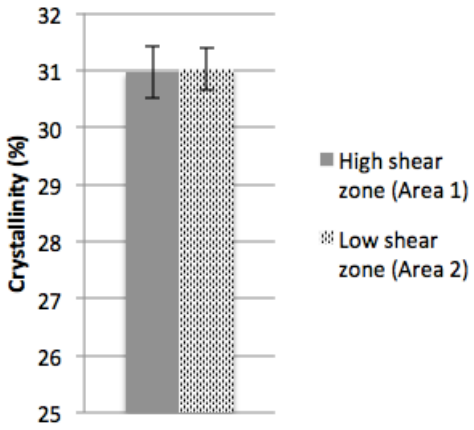

Figure 7-18. The crystallinity of PP co samples from area 1 and area 2 of the disc parts molded using MeltFlipper®

As was observed with the PP ho specimens, the average melting points of the PP co samples and POM samples remained relatively constant at 151.3°C and 173.4°C respectively.

PP co, t contains 20% ethylene copolymer designed for broader transitions and low temperature ductility, but higher viscosity. The ethylene units incorporate into the polypropylene chain, results in a decrease in the melting and glass transition temperatures as well as crystallinity. [98] In this test, it was concluded that MRT as applied did not significantly modify the melting temperatures of the tested materials.

For the nylon specimens molded under different conditions, the test results are provided in Table 7-1.

Table 7-1. Crystallinity comparisons of N66 samples and N66_50 samples resulted from different molding conditions

Material	Molding Condition	Area	Crystallinity (%)	Difference (%)
Neat Nylon 6'6	Fast molded (57.02 cm^3/s)	1 (high shear)	29.25	7.16
		2 (low shear)	27.29	
	Slow molded (9.5 cm^3/s)	1 (high shear)	27.42	1.42
		2 (low shear)	27.03	
50% Glass Filled Nylon 6'6	Without MRT	1 (high shear)	19.30	10.15
		2 (low shear)	17.51	
	With MRT	1 (high shear)	19.31	5.75
		2 (low shear)	18.26	

The neat Nylon 6'6 was molded into the disc-cavity using two different injection speeds. The samples from the high shear area of the fast molded N66 products exhibited an average crystallinty of 29.25%, while the average crystallinty of the low shear samples was 27.29%. The crystallinity difference was 7.16%. However, for the slow molded N66 products, the crystallinity of the high sheared samples and the low sheared samples were 27.42% and 27.03%, respectively, with a smaller difference in crystallinity of about 1.42%, indicating that the shear imbalanced results for this material were strongly dependent on the molding condition history.

For the N66_50 parts molded with and without MRT, the crystallinity, as well as the difference in percentage, of samples taken from high shear regions and low shear regions varied significantly. For samples molded without MRT, the average crystallinity in the high and low shear regions were 19.3% and 17.51%, respectively, with the crystallinity difference of over 10%. However, the MRT results showed that the crystallinity for the high sheared samples and the low sheared samples were 19.31%

and 18.26%, and the crystallinity difference was reduced to a much lower level, at only about 5.75%. The N66_50 test concludes that a more uniform crystallinity distribution is achieved with the help of MRT.

7.2.2 Experimental Results for Multi-Cavity Molded Specimen

The experimental data from the traditional DSC testing, shown in Figure 7-19, 7-20 and 7-21, shows the diversity of the crystallinity for iPP samples produced under different molding conditions.

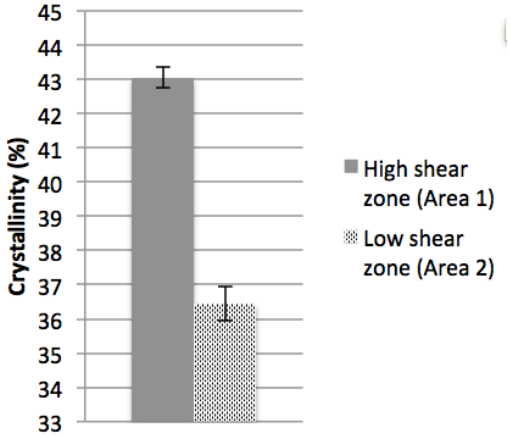

Figure 7-19. The crystallinity of iPP samples from the high shear region (Area 1) and the low shear region (Area 2), molded under condition (1) with no MRT

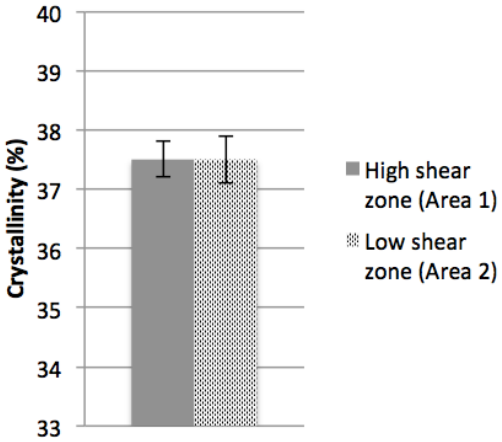

Figure 7-20. The crystallinity of iPP samples from the high shear region (Area 1) and the low shear region (Area 2), molded under condition (2) with no MRT

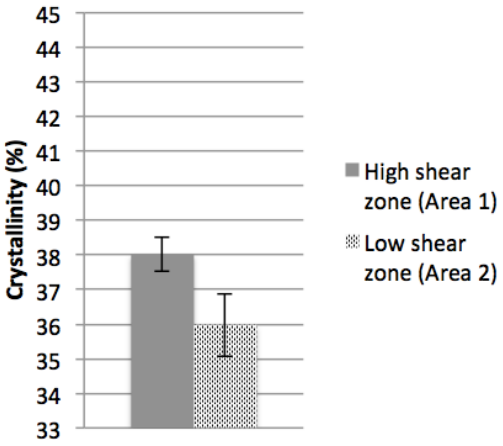

Figure 7-21. The crystallinity of iPP samples from the high shear region (Area 1) and the low shear region (Area 2), molded under condition (3) with MRT

Figure 7-19 gives the crystallinity difference of the iPP samples molded under condition (1). As expected, the high shear experienced samples attains a crystallinity of about 43.05%, while the samples from the low shear region presented a clearly lower crystallinity of 36.45%. Figure 7-20 provides the crystallinity difference of the iPP samples molded under molding condition (2). The crystallinity of the high shear experienced samples and the low shear experienced samples were both about 37.5%. The similar crystallinity levels generated in this case implies that iPP is less sensitive to shear if the injection rate was reduced.

Figure 7-21 compares the crystallinity of the iPP specimens molded with the implementation of MRT. As expected, with MRT, the crystallinity of the samples from both Area 1 and Area 2 didn't show a significant difference, as the samples molded under condition (1) provided. The crystallinity percentages of the specimens from Area 1 and Area 2 were 38.03% and 35.97% respectively, indicating the melt rotation device was able to remix the flows in different shear rate histories, resulting in a more uniform crystallinity in the final product.

PBT testing results didn't show obvious differences referring to initial assumptions. The crystallinity, between the high and low shear regions, did not attain a significant difference for samples molded under condition (1) and condition (2). (Figure 7-22 and Figure 7-23)

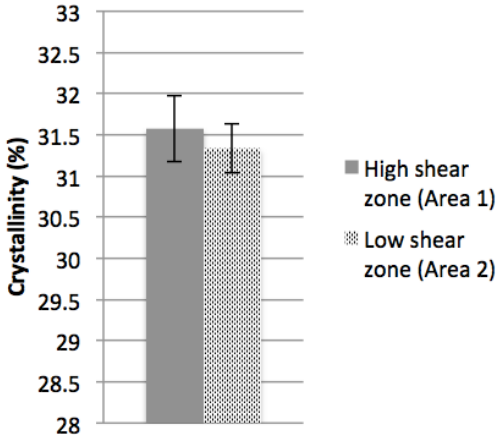

Figure 7-22. The crystallinity of PBT samples from the high shear region (Area 1) and the low shear region (Area 2), molded under condition (1) with no MRT

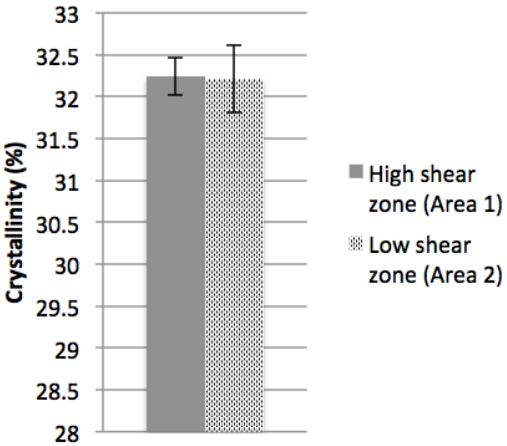

Figure 7-23. The crystallinity of PBT samples from the high shear region (Area 1) and the low shear region (Area 2), molded under condition (2) with no MRT

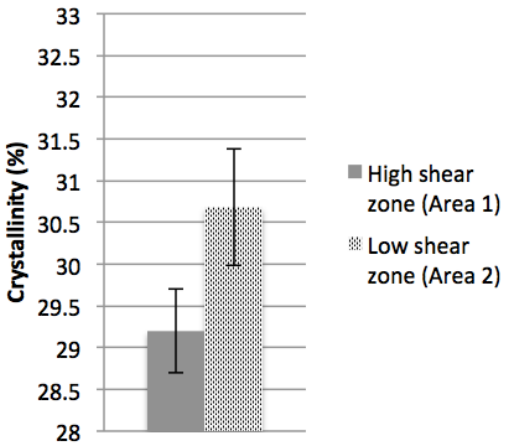

Figure 7-24. The crystallinity of PBT samples from the high shear region (Area 1) and the low shear region (Area 2), molded under condition (3) with MRT

The test results of PBT samples molded in condition (3) were unexpected. (Figure 7-24) The average crystallinity of the samples from high shear regions was even lower than that of the samples from low shear regions.

The possible explanations for the PBT test results could be that the injection speed was not high enough or the injection speed was not the only dominant parameter to generate shear-thinning influences in crystallinity, even though the differences in physical molding shape were obvious, as shown in Figures 7-7, 7-8, and 7-9.

In reference to the crystallinity theory discussed in Chapter 2, in the repeat unit of the PBT backbone structure (Figure 7-25), the ester group and the aromatic ring may have a strong intermolecular force, hence the molecules may stack together easily. As a result, it is easy for PBT to crystalize. This intrinsic characteristic may overcome the shear influence, thereby balancing the crystallization levels.

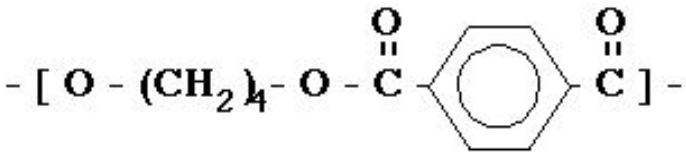

Figure 7-25. Repeat unit in the backbone structure of PBT [99]

For N66 samples, Figures 7-26, 7-27 and 7-28 show relatively better DSC results compared to that of the PBT samples.

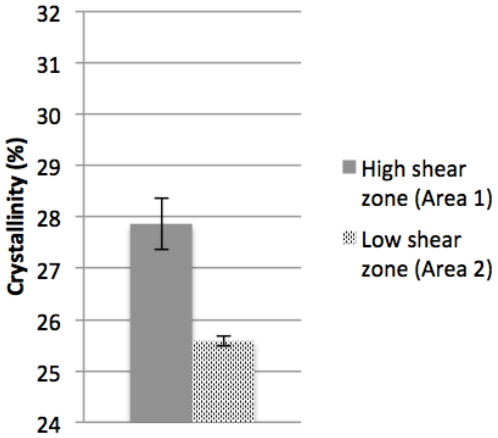

Figure 7-26. The crystallinity of N66 samples from the high shear region (Area 1) and the low shear region (Area 2), molded under condition (1) with no MRT

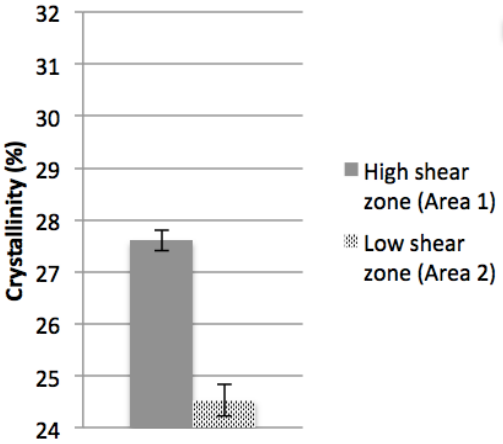

Figure 7-27. The crystallinity of N66 samples from the high shear region (Area 1) and the low shear region (Area 2), molded under condition (2) with no MRT

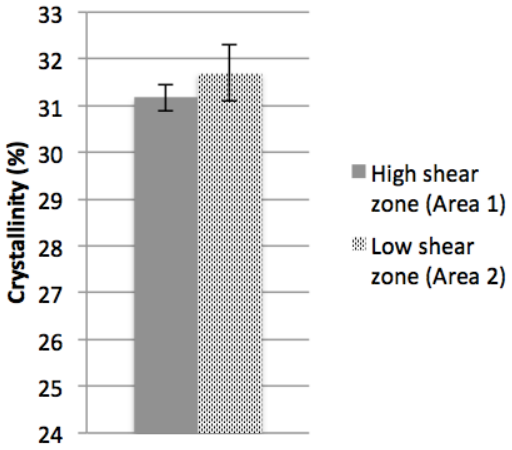

Figure 7-28. The crystallinity of N66 samples from the high shear region (Area 1) and the low shear region (Area 2), molded under condition (3) with MRT

In Figure 7-26 and Figure 7-27, it is obvious that the crystallinity of the high shear samples are higher than those of the low shear samples. The crystallinity of the high shear samples molded under condition (1) was about 27.86% and that of the low shear samples molded under the same condition was 25.58%. The crystallinity of the high shear and low shear samples molded in condition (2) were 27.61% and 24.53%, respectively. These DSC results are as expected, where high shear samples should exhibit higher crystallinity. However, comparison of Figures 7-26 and 7-27 also reveal that lowering the injection rate did not reduce the difference in crystallinity of the fast molded (condition(1)) and the slow molded (condition(2)) N66 samples. It may be that N66 is sensitive to shear history. Hence the low injection rate could still generate obvious shear imbalance induced difference in crystallinity, particularly under the molding conditions set in this investigation.

Figure 7-28 shows that more uniform, but slightly higher crystallinity was generated for both high shear and low shear samples molded using condition (3). MRT

generated a more even shear distribution, similar average crystallinity among separate cavity fillings.

7.3 Tensile Test

It was revealed from the tensile tests that the dog-bone specimens had obvious distinctions in yield stresses and Young's Moduli due to the imbalanced shear flow during molding.

The PP ho dog-bones formed from high shear flow regions exhibited higher yield stress (Figure 7-29) and Young's Moduli levels (Figure 7-30).

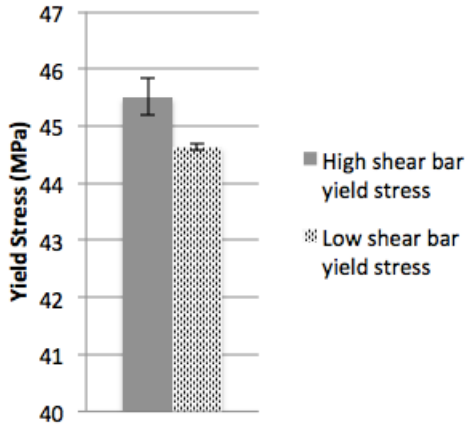

Figure 7-29. Yield stresses of PP ho tensile bars filled with the high shear flow and the low shear flow [53]

The dog-bone filled with the lower shear history material had an average yield stress of 44.6 MPa, while the yield stress of the dog-bone filled with the higher shear material reached over 45.5 MPa. Moreover, the higher shear flow tensile bars had a higher modulus (552.9 MPa) compared to the low shear flow tensile bars (531.0 MPa; Figure 7-30). These mechanical property findings correlate well with the regional crystallinity differences for the iPP as presented in Figure 7-19.

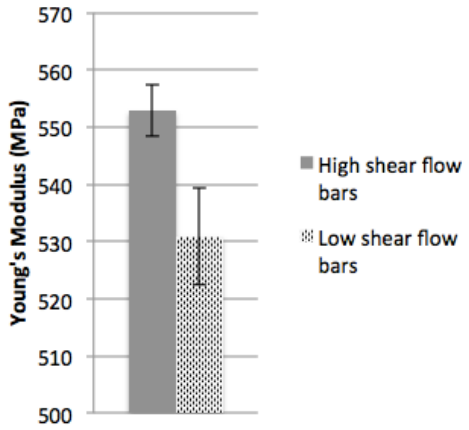

Figure 7-30. Young's Moduli of PP ho tensile bars filled with the high shear flow and the low shear flow [53]

In this study, results indicate that shear rate variation did not have a significant effect on yield stresses of PP co dog-bones. (Figure 7-31)

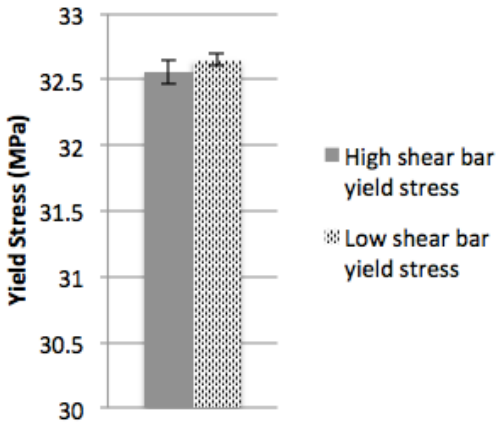

Figure 7-31. Yield stresses of PP co tensile bars filled with the high shear flow and the low shear flow [53]

Figure 7-32 further indicates the trend of Young's Modulus being higher at high shear flow (340.4 MPa) and relatively lower (336.9 MPa) when molded with at a lower shear history region. This difference may be misleading however. It is possible, as previously observed in the single-cavity mold, that the same level of crystallinity in

both the high and low shear flow bars is the major reason of the comparable yield stress and Young's modulus value between these samples.

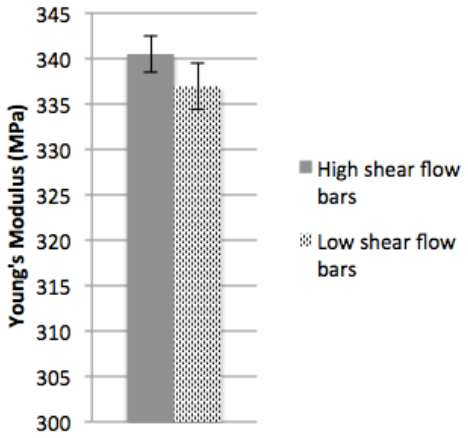

Figure 7-32. Young's Moduli of PP co tensile bars filled with the high shear flow and the low shear flow [53]

7.4 Flash DSC

To perform the ultra high heating rate via flash DSC, the sample weight were kept roughly as small as 100 ng. Unfortunately, a reliable method for recording the exact mass for this testing method is not available. Hence, this method was used to investigate the endothermic peak migration, rather than the degree of crystallinity.

7.4.1 Experimental Results for Single-Cavity Molded Specimen

Three polypropylene copolymer samples from both regions 1 and 2 of single-cavity disc products molded without melt rotation were initially investigated. After ultra-high rate Flash DSC heating, thermogram curves were generated as shown in Figure 7-33.

The plots show that samples from area 1 had a melting point of around 148°C while the corresponding samples taken from area 2 had higher values at approximately

153°C. This shift may be attributed to the shear induced flow imbalances associated with traditional molding.

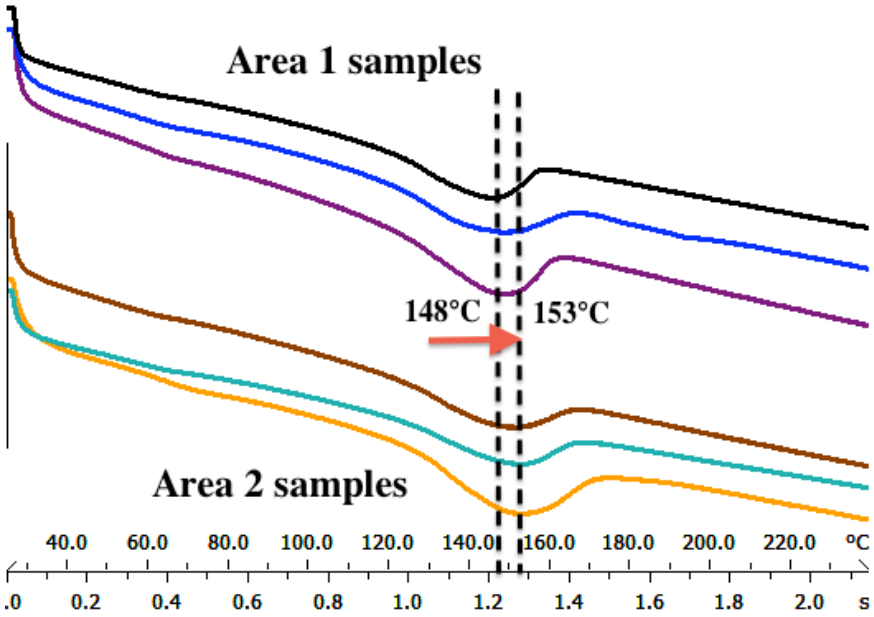

Figure 7-33. Flash DSC 1 heating curves of PP co samples [53]

The crystalline region of polypropylene includes the α and β phase structures. [100] The ethylene copolymerized in the main material could act as a β form nucleating agent. According to previous studies, the α crystalline component has a melting temperature of around 165°C, which is 10°C higher than the melting temperature of the β spherulites. [88] [90] [95] [101] These two types of crystalline structures may form during both cavity filling and subsequent cooling stages of the molding processes. The α spherulites form faster above 140°C or below 100°C, while β spherulites are predominantly formed between these temperatures. [88] The samples from area 1 were expected to contain more higher shear history material, which was hotter and had a slower cooling rate. In this way, a greater amount of crystals should have been generated in region 1 compared to region 2. But β spherulites were easier to

form due to the existence of the ethylene comonomer, acting as nucleating agents. The occurrence of this β form has to be forced by either the addition of specific nucleating agents, or by directional crystallization in a temperature gradient field. [95] [102] [103] This reason may explain the regional melting point difference shown in Figure 7-33.

To explore the effects of MRT, flash DSC testing was also performed on regional samples taken from disc PP copolymer products molded with this method. Typical results that were observed for regions 1 and 2 respectively are presented in Figures 7-34 and Figure 7-35. The thermograms show broadening of the endothermic melting peaks from both the high shear and low shear regions when MRT was applied. In addition to this, the peaks shifted to higher temperatures, perhaps indicating that more α crystals were present in both regions. This supports the concept that MRT, results in a more evenly distributed shear flow throughout the molded specimens. MRT also results in similar melt behavior curves for both outer and inner product regions as shown in Figure 7-36.

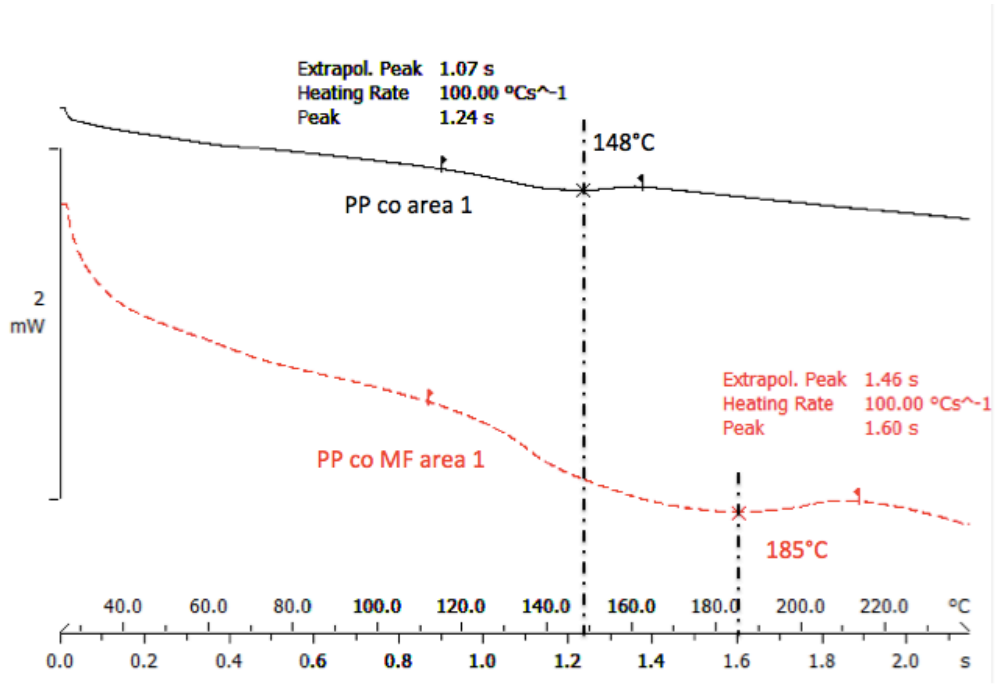

Figure 7-34. Flash DSC 1 heating curves of PP co and PP co MF samples from region 1 (high sheared region) [53]

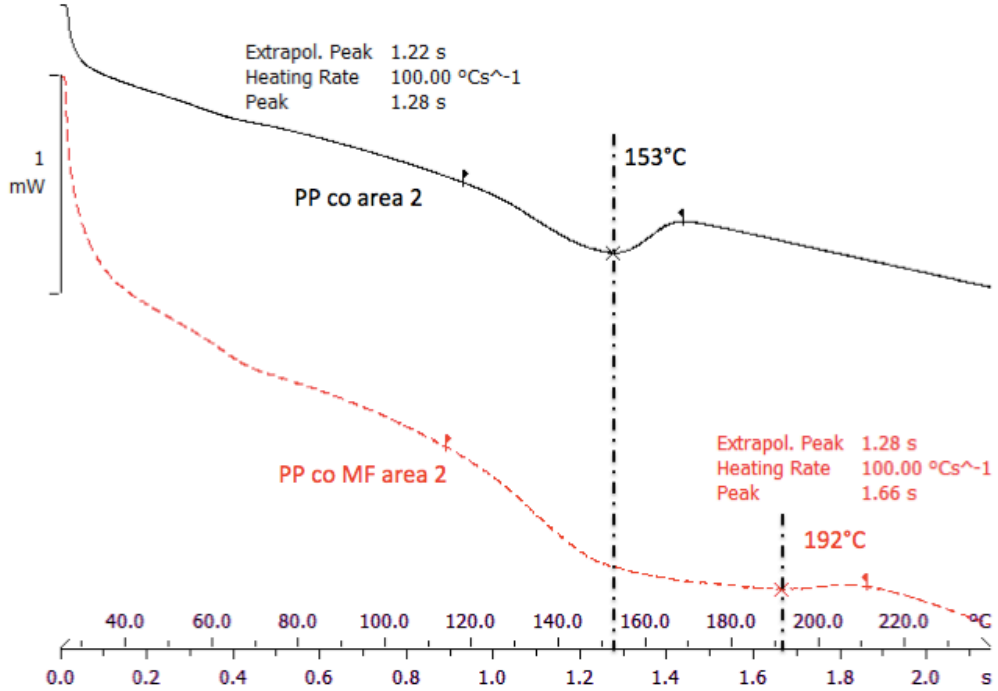

Figure 7-35. Flash DSC 1 heating curves of PP co and PP co MF samples from region 2 (low sheared region) [53]

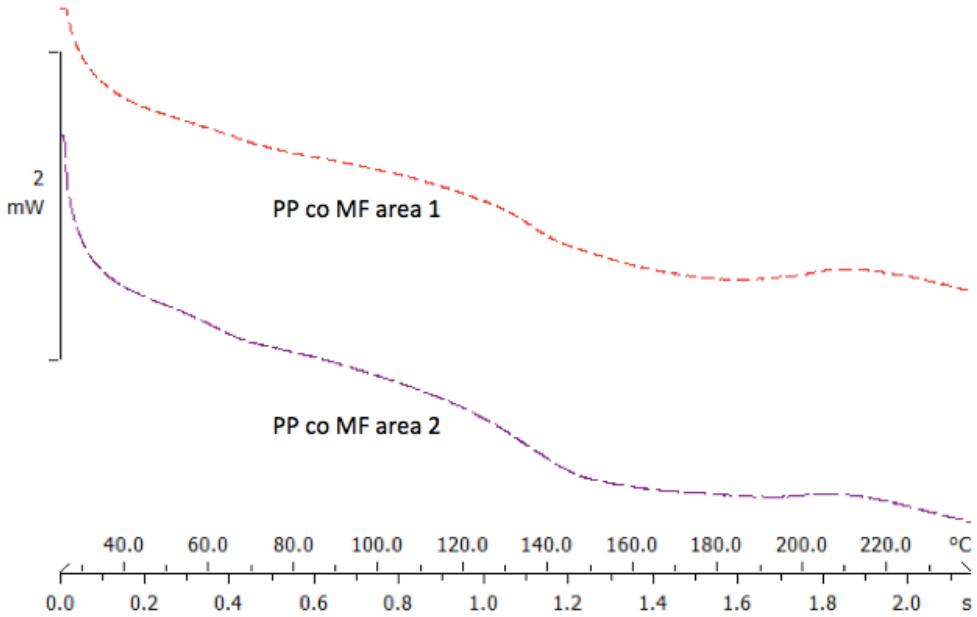

Figure 7-36. Flash DSC 1 heating curves of PP co MF samples from area 1 and area 2 [53]

7.4.2 Experimental Results for Multi-Cavity Molded Specimen

In this section, the melting temperatures obtained from the flash DSC data were higher than those reported in literature values. This may be due to the melting peak temperatures being heating rate dominant. From Figures 7-37 to Figure 7-39, it is clear that the samples exhibited diverse melting peak temperatures from the high shear to the low shear zone for iPP specimens of all molding conditions.

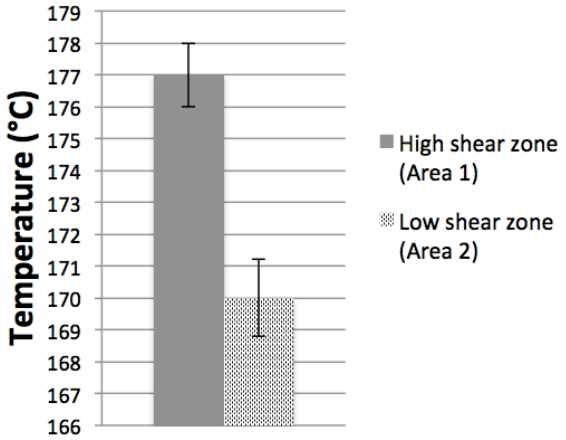

Figure 7-37. The melting temperature of iPP samples from the high shear region (Area 1) and the low shear region (Area 2), molded under condition (1) with no MRT [50]

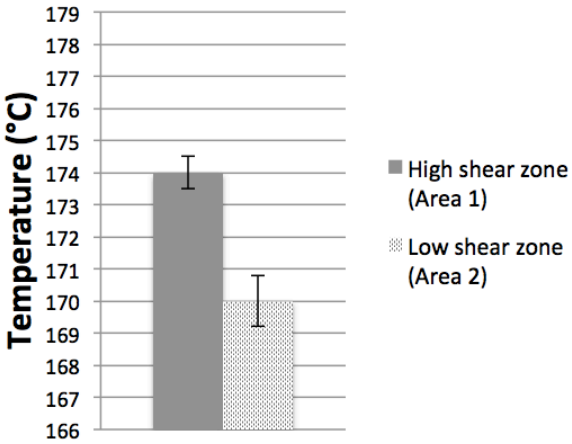

Figure 7-38. The melting temperature of iPP samples from the high shear region (Area 1) and the low shear region (Area 2), molded under condition (2) with no MRT [50]

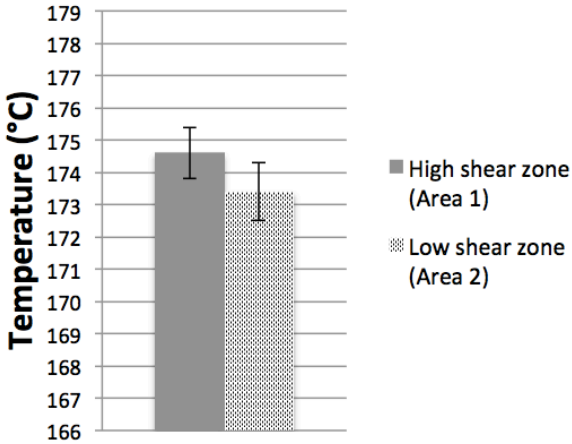

Figure 7-39. The melting temperature of iPP samples from the high shear region (Area 1) and the low shear region (Area 2), molded under condition (3) with MRT [50]

As shown in Figure 7-37, samples which were fast molded without MRT from Area 1 had a melting point of 177 °C (450.15 K). This is about 7 °C higher than the melting point of samples from Area 2. When the injection speed was reduced significantly, the difference of the melting temperature was decreased simultaneously (Figure 7-38). The sample filled with the lower shear history material had a melting peak of 170 °C (443.15 K), while the melting point of the samples filled with the higher shear material reached about 174 °C (447.15 K).

The test results from Figure 7-39 indicates the melting points were about 174.6 °C (447.75 K) and 173.4 °C (446.55 K) for the specimens from Area 1 and Area 2 respectively. With the application of MRT, the difference in melting points between these two regions became less significant. As the high and the low shear flows were rotated, MRT led to a more even distribution of melting temperature in between samples taken from these areas.

7.5 Wide Angle X-Ray Scattering

In this study, the diffraction intensity peak at $2\theta = 16.1°$ roughly indicates the amount of β crystals developed within the three molding conditions. In the curves plotted in Figures 7-40 to 7-45, it is shown that the β crystal peaks at $2\theta = 16.1°$. Although this peak is not very clear, it is still somewhat discernable. For the iPP samples molded in fast and slow injection rate conditions, the patterns of β crystal peaks were found close to one of the α peaks, which is at $2\theta = 16.9°$, as shown in Figures 7-40 to 7-43. But for the iPP samples molded under condition (3), the β crystal

peak was eliminated, especially for samples taken from the low shear regions, as shown in Figures 7-44 and Figure 7-45.

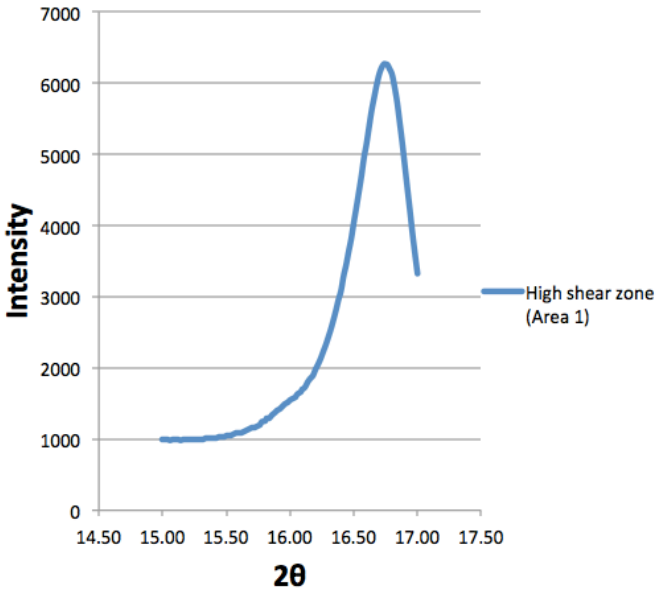

Figure 7-40. WAXS curve for iPP samples from the high shear regions (Area 1), molded under condition (1) with no MRT

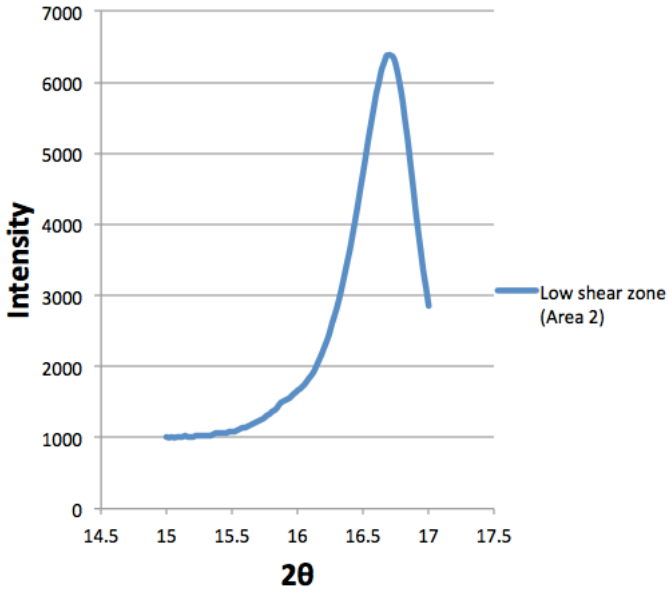

Figure 7-41. WAXS curve for iPP samples from the low shear regions (Area 2), molded under condition (1) with no MRT

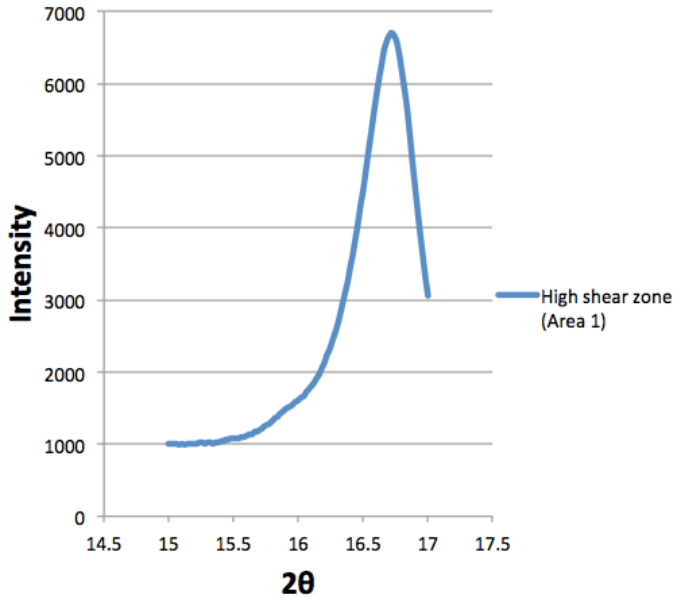

Figure 7-42. WAXS curve for iPP samples from the high shear regions (Area 1), molded under condition (2) with no MRT

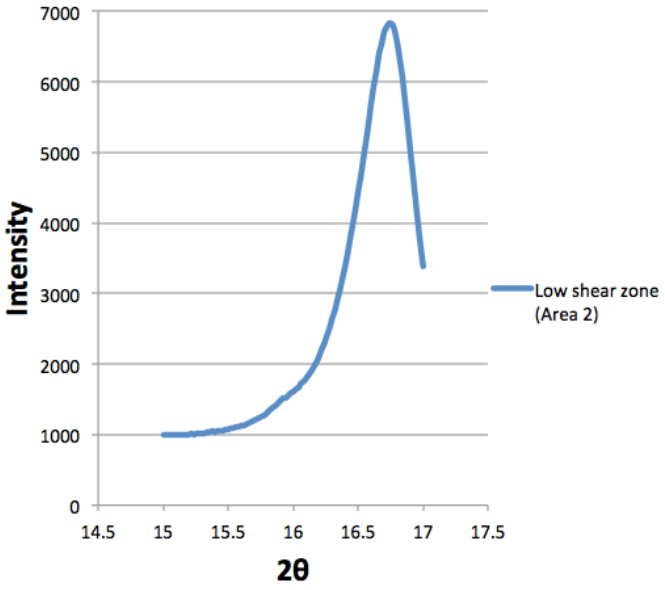

Figure 7-43. WAXS curve for iPP samples from the low shear regions (Area 2), molded under condition (2) with no MRT

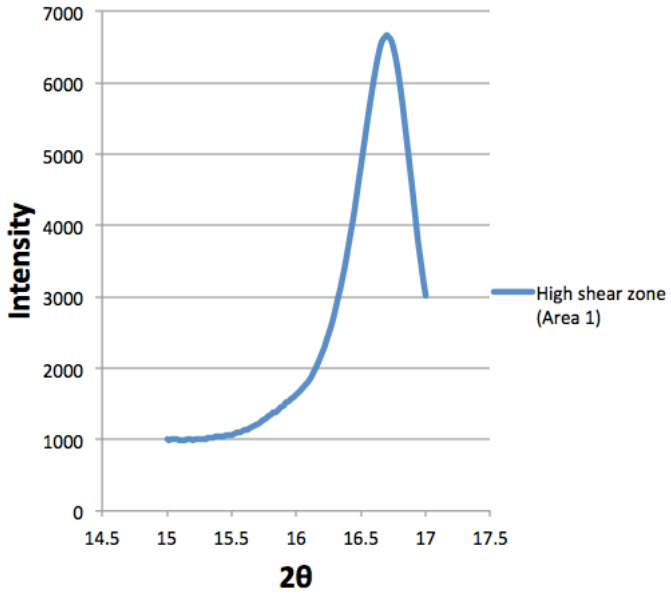

Figure 7-44. WAXS curve for iPP samples from the high shear regions (Area 1), molded under condition (3) with MRT

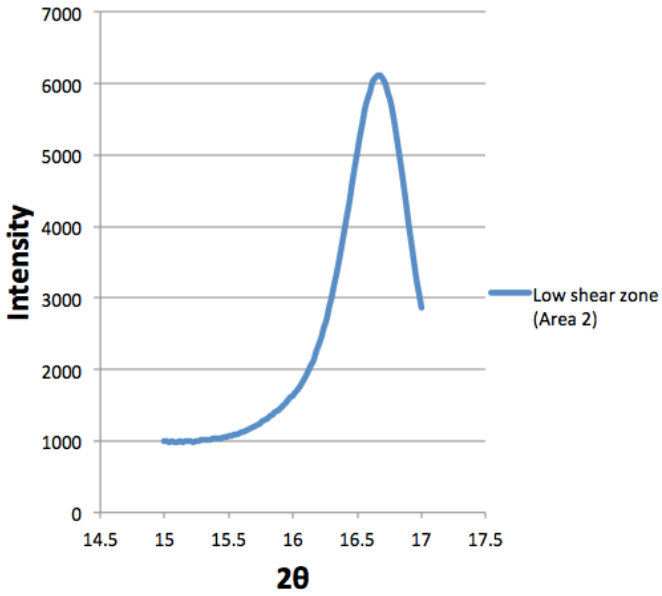

Figure 7-45. WAXS curve for iPP samples from the low shear regions (Area 2), molded under condition (3) with MRT

It was also revealed from the WAXS data that the iPP specimens had distinct differences in intensity at $2\theta = 16.1°$ due to the influence of the imbalanced shear flow.

The normalized values of the intensities for iPP samples, which were taken from the high and the low shear regions, injection molded in all three conditions are provided in Figures 7-46 to 7-48.

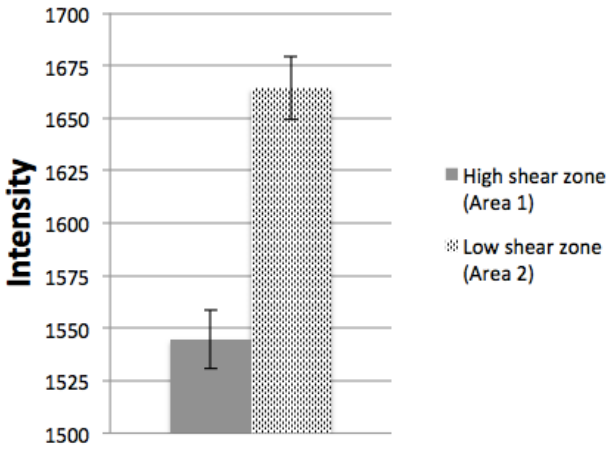

Figure 7-46. The x-ray diffraction intensities of iPP samples from the high shear region (Area 1) and the low shear region (Area 2), molded under condition (1) with no MRT

Figure 7-46 shows that samples which contained melt flow that experienced the higher temperature and shear history has an intensity of 1544.79, while the low temperature and shear samples has an intensity of 1644.37. As previously conjectured, the high shear rate condition may have induced generation of α crystals rather than the β or the γ form. [93] [94] Since the high shear rate prevented the formation of the β crystals more effectively compared to the low shear rate, this may be the reason for the relatively higher intensity of β crystals in Area 2.

For the samples molded under condition (2), the intensity data presented the similar variation of β crystal content from Area 1 to Area 2. (Figure 7-47) Due to the shear rate influence, the samples from the low shear region also exhibited a higher β crystal intensity. However, the intensities revealed from the high shear regions and the

low shear regions were more averaged at 1604.93 and 1618.55, respectively, with a reduced intensity difference. This may have been due to the significantly low injection rate applied, which may have prolonged the crystallization duration, allowing some of the β crystals to transform into the more stable α crystals within that extra time.

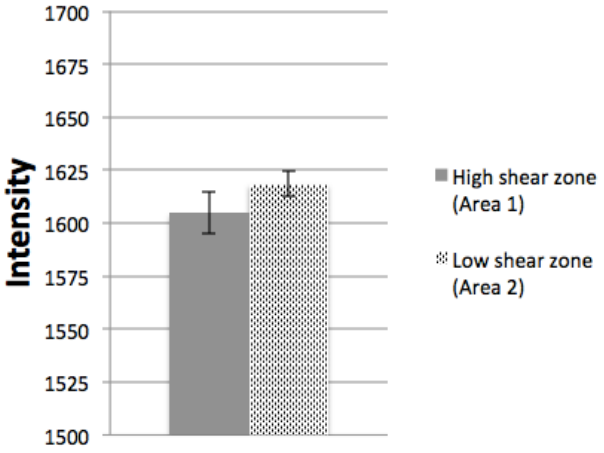

Figure 7-47. The x-ray diffraction intensities of iPP samples from the high shear region (Area 1) and the low shear region (Area 2), molded under condition (2) with no MRT

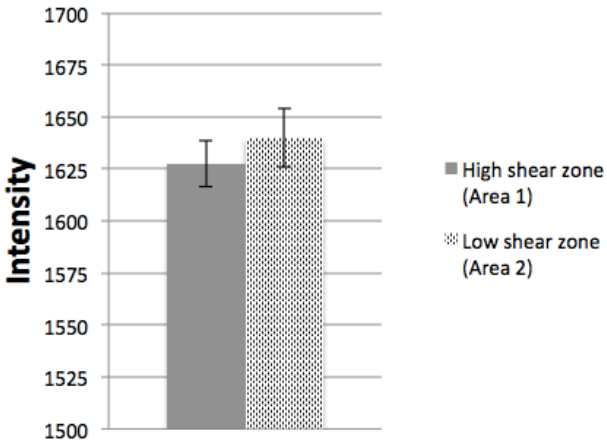

Figure 7-48. The x-ray diffraction intensities of iPP samples from the high shear region (Area 1) and the low shear region (Area 2), molded under condition (3) with MRT

Figure 7-48 indicates that the intensity data still followed the pattern where a lower intensity, 1627.48, is observed for samples associated with the high shear flow, and a higher intensity of 1639.75 from the low shear region. However, with MRT applied, the difference these intensities decreased significantly.

From flash DSC data, it can be concluded that MRT is able to effect the crystallization behavior of iPP, reducing the difference of the β crystal content in the molded product. The content variation of the β crystal may also be a reason for the distinction in melting points between the iPP molding samples (Figures 7-37 to 7-39). The samples taken from the low shear region contained relatively more β crystals. These also exhibited lower melting peaks, which is expected since β crystals melt at lower temperatures relative to α crystals.

7.6 Real-Time Monitoring

By incrementally adjusting the processing parameters as mentioned in Chapter 5, results indicate that the most significant variables in the study are: (i) injection pressure, (ii) shot size (screw displacement), and (iii) injection velocity.

From numerous experimental runs for each insert plate, images and high-speed videos of the cavity-filling stage were successfully recorded. Flow induced shear-thinning and shear heating effects during cavity filling were evident for specific cavity geometries. The melt flow during cavity fillings were observed to be imbalanced, favoring the sides since shear rates were the greatest due to the higher shear regions along runner walls.

7.6.1 iPP Molding Results by Using Thin Insert Plates

The shear effect is obvious from the succession of images, captured from video frame sequences, shown Figure 7-49. The image set for filling the circular and rectangular cavities (Figure 7-49 (a) and (b), respectively) did not exhibit the shear effects from the runner as well as that of the split-cavity geometry (Figure 7-49 (c)).

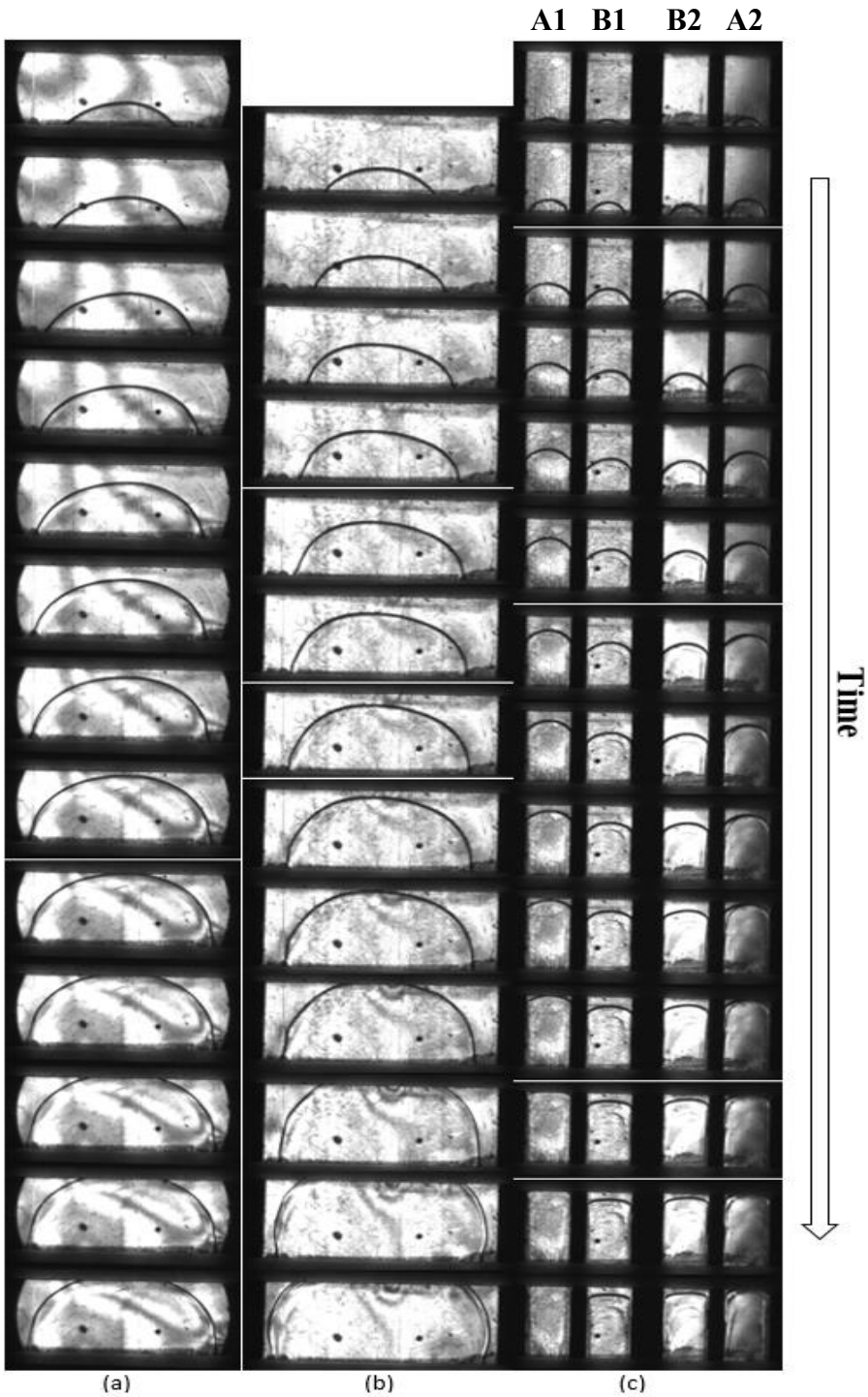

Figure 7-49. Video frame sequences of cavity filling for circular caivty (a), rectangular cavity (b), and split-cavity (c) by using thin insert plates [51]

The split-cavity geometry video sequence showed that the outer two cavities (A1 and A2) were filled ahead time, relative to the inner two cavities (B1 and B2). This observation is as predicted due to shear imbalance in melt flow.

Repeatable results were available for split-cavity molding. Figure 7-50 shows that there is a consistent shear induced filling imbalance occurring in the cavities. Figure 7-51 provides the time variation for the respective high and low shear flow filling the corresponding cavities.

Figure 7-50. Trials of consistent filling imbalances in split-cavity molding by using thin insert plates [51]

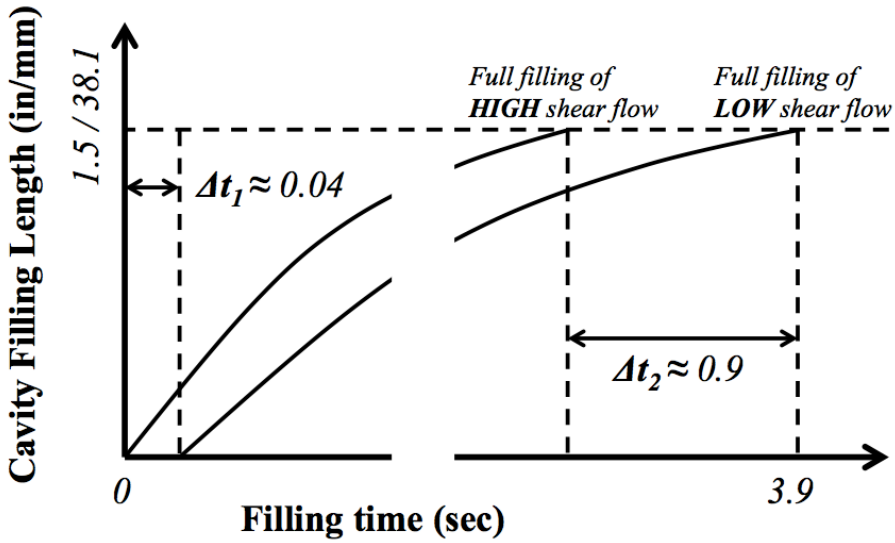

Figure 7-51. Differences of split-cavity filling duration for high shear flow and low shear flow

The times shown in Figure 7-51 above were roughly calculated according to the number of frames that were taken by the high-speed camera. The entire cavity filling time was about 3.9 seconds. The high shear flow entered the outer cavities (A1 and A2) first. After about 0.04 seconds, the low shear flow melt front showed up in the inner cavities (B1 and B2). When the high shear flow finished filling their cavities, A1 and A2, it took approximately about 0.9 seconds more for the low shear melt flow to reach the end of the cavity, B1 and B2.

During the injection runs with the circular cavity insert, there were several results that showed shearing effects. Previously in Figure 5-2 (Chapter 5), it was shown that the melt region with a high shear flow should fill the edge section of the cavity, while the low shear region would fill the center. By measuring the filling distances on the short shot samples, it was clearly observed that the high shear flow, went further upthe cavity edge relative to the low shear region flowing to the cavity

center, with the distances of $1\frac{3}{16}$ inches (30.16 mm) and $1\frac{2}{16}$ inches (28.58 mm) respectively. This difference is approximately 6% in length. (Figure 7-52 and Figure 7-53)

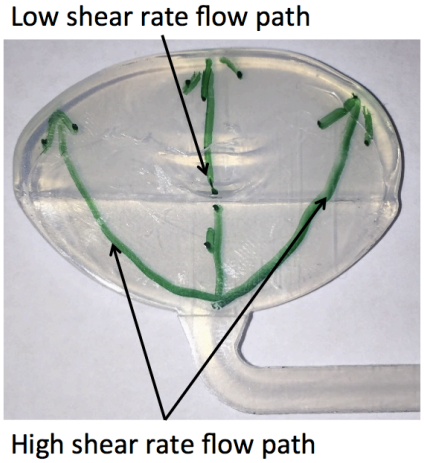

Figure 7-52. The paths of high and low sheared flowing material in single mold cavity (circular) [51]

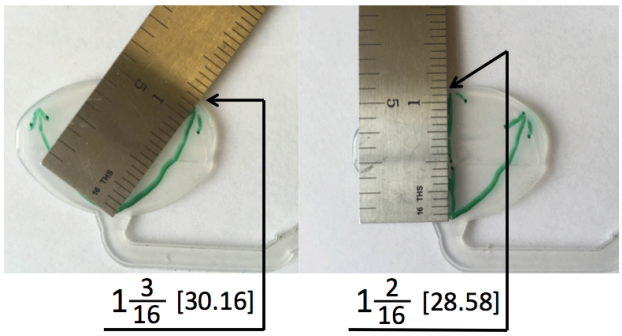

(a) (b)

Figure 7-53. High and low shear flow filling distances (in [mm]) in circular cavity [51]

However, these results were not consistent and were only apparent in a couple of trials. For the single-cavity rectangular geometry trials, there was no clear filling differences observed. In both the circular and rectangular geometry tests, there was a common and frequent issue during the cavity filling process. Unlike the split-cavity

geometry insert, where the end of the runner at the cavity gate met the polycarbonate window as soon as the cavity starts, there was a transition from steel to polycarbonate, at the mid-cavity filling stage, for the circular and rectangular geometry inserts (as circled in Figure 7-54).

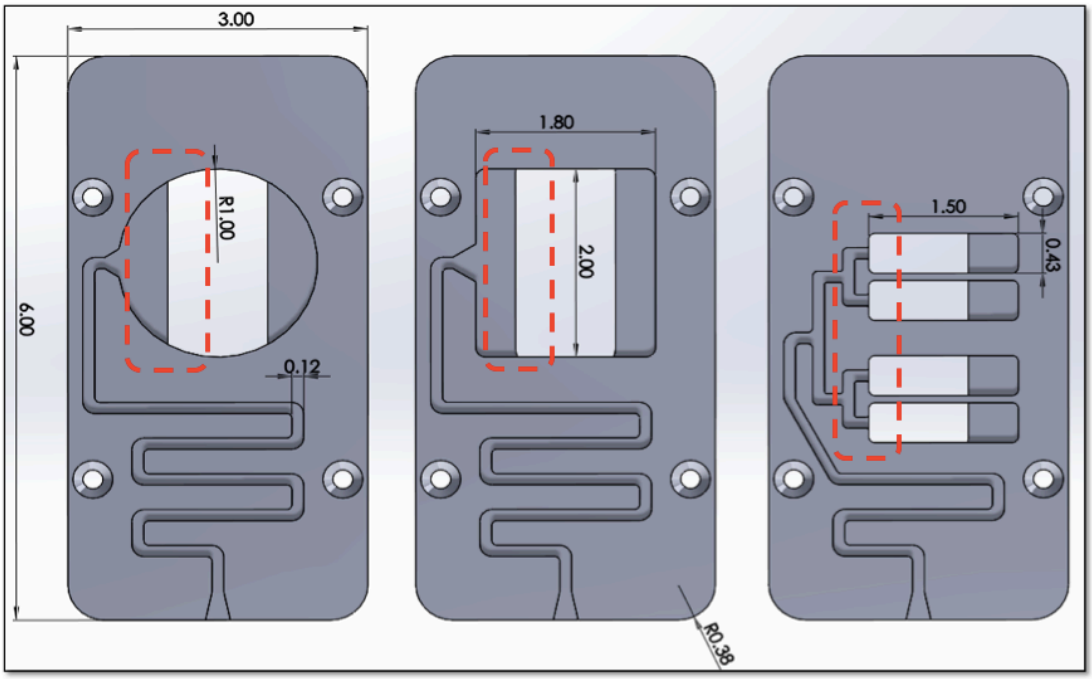

Figure 7-54. Locations of the transition from steel to polycarbonate in cavities on the insert plates [51]

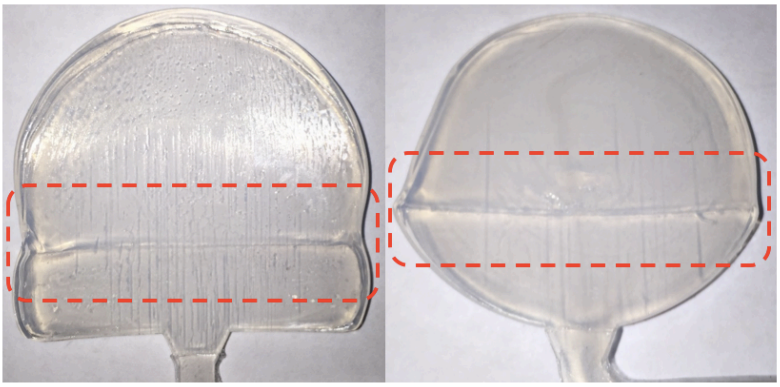

(a) (b)

Figure 7-55. Material transition from steel to polycarbonate window for rectangular cavity (a) and circular cavity (b) [51]

In Figure 7-55, an evident clear weld-like line can be observed. This marks the transition from steel to polycarbonate as mentioned. It is thus evident that this transition affected the cavity filling process. The disruption was apparent in both geometries, but more severely in the rectangular geometry case. The disruption can also be due to a tolerance issue when fitting the polycarbonate window into the mold. Another reason for this fill disruption could be the material property differences between steel and polycarbonate, especially since there could be temperature differences between the two materials.

Another possible reason may due to the geometry of the runner on the thin insert plates. The design may have not ideally facilitate separation of the high and low shear flow rate melt flows. As most of the high shear rate flow could be distributed with the low shear rate flow parallel into the same space in the mold cavity, a "mixed" flow could result in the unexpected uniform cavity fillings as observed. This is especially the case for single-cavity moldings, where it may be even more difficult to split these melt flows completely as the cavity is filled.

7.6.2 Molding Results by Using Thick Insert Plates

In order to confirm that the geometry of the runner cross section would influence the shear condition and its consequences, both iPP and PS were applied for molding by using the thick insert plates.

7.6.2.1 Real-time monitoring by using iPP

Figure 7-56 provides captured images from the video frame sequence of iPP injection molding of the circular cavity, rectangular cavity, and the split-cavity.

(a1) (a2) (b1) (b2) (c1) (c2)

Figure 7-56. Video frame sequences of iPP cavity filling for circular cavity with wide runner (a1) and narrow runner (a2), rectangular cavity with wide runner (b1) and narrow runner (b2), and split-cavity with wide runner (c1) and narrow runner (c2) by using thick insert plates

The molding processes captured by utilizing both the thin and thick circular cavity plates are showed in Figure 7-57. Figure 7-57 (b) and (c) compares the filling stage by using thick insert plates with a wide runner and a narrow runner respectively. By comparing from Figure 7-57 (a), (b), and (c), it is apparent that by using the thick insert plates, the left and the right sides of the melt flow has already touched the cavity edge, when the flow front reached the upper visible limit of the window (Figure 7-57 (b), (c)), while in the thin plate case, there were still extra spaces left at the two sides within the cavity, when the flow front reached the same limit (Figure 7-57 (a)).

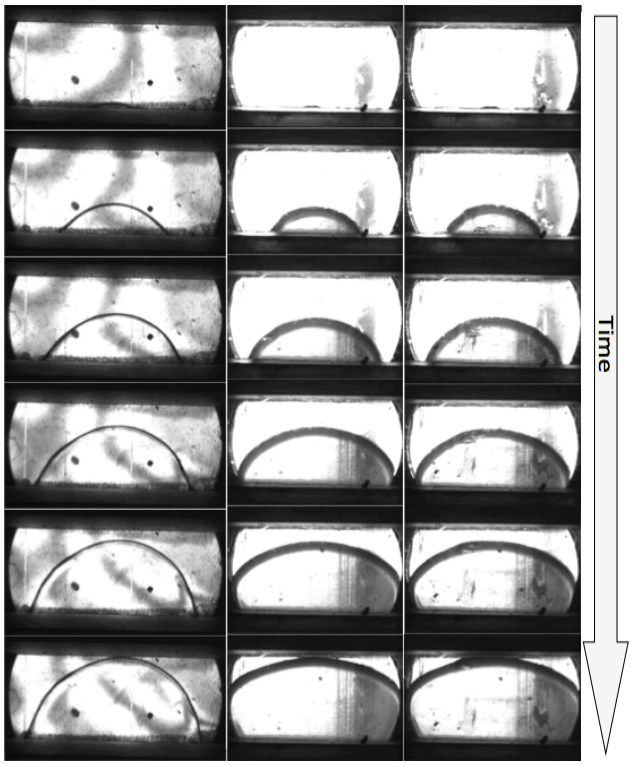

(a) (b) (c)

Figure 7-57. Cavity filling processes for iPP molding by utilizing circular cavity insert plates: (a) thin plate, (b) thick plate with wide runner, (c) thick plate with narrow runner

This difference in melt flow indicates that the modified runner system mentioned in Chapter 5 resulted in a varied shear imbalanced during cavity filling. By using the modified runner system in the thick insert plates, the melt flow located close to the left side and the right side of the runner wall had higher levels of shear rates. (Figure 5-16 and Figure 5-17) As a result, the melt flow in the thick insert plates filled the edge sections of the cavity faster than the melt flow in the thin insert plates. This is in line with the shear-thinning theory of polymer melt flow.

Although the cavity filling differences by using the wide and the narrow runner systems were not obvious in the video sequences, the solidified flow front confirmed

the shear imbalance variations, compared from the short shot samples taken out from the cavities. (Figure 7-58)

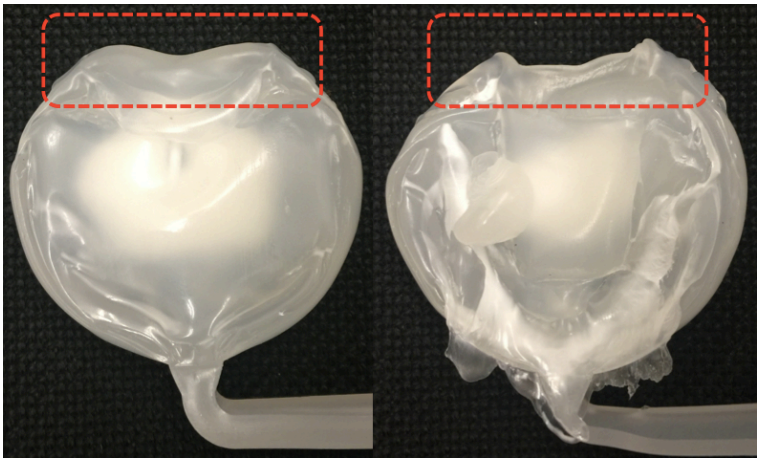

(a) (b)

Figure 7-58. Molded iPP circular samples (short shots) by using thick insert plates with (a) wide runner and (b) narrow runner

In Figure 7-58, for both of the samples, the melt flow front at the sides of the sample was ahead of the flow in the center of the sample. By comparing the solidified flow fronts, as indicated in Figure 7-58, it is apparent that the shear imbalance is more significant for samples molded via a narrow runner system. The narrower runner led to a higher shear imbalanced result, which corroborates the assumption made in Chapter 5.

Similar cavity filling processes and molding results were found by using rectangular cavity insert plates. This is presented in Figure 7-59. By using a modified thicker insert plate, with a deeper runner, a different cavity filling pattern is observed. Comparisons made between the solidified flow fronts n Figure 7-60 again shows that the narrower runner generates a significantly higher shear imbalance.

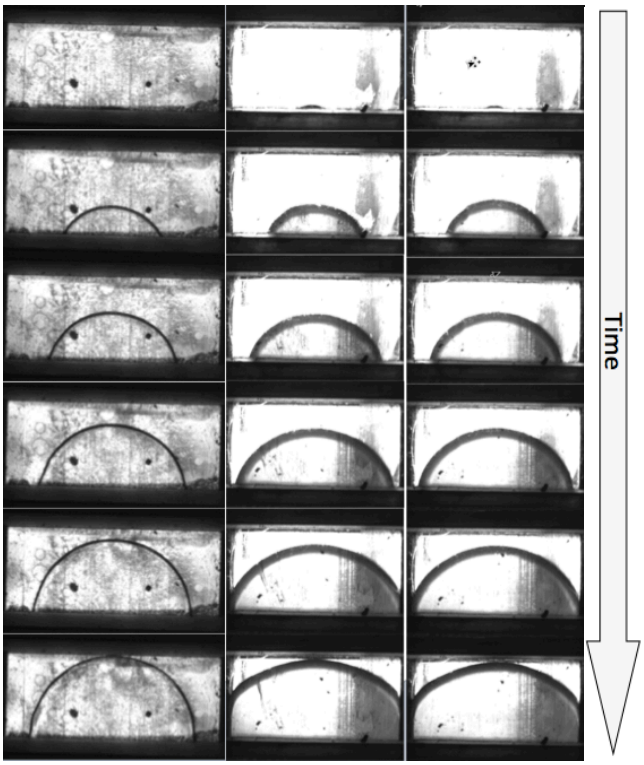

(a) (b) (c)

Figure 7-59. Cavity filling processes for iPP molding by utilizing rectangular cavity insert plates: (a) thin plate, (b) thick plate with wide runner, (c) thick plate with narrow runner

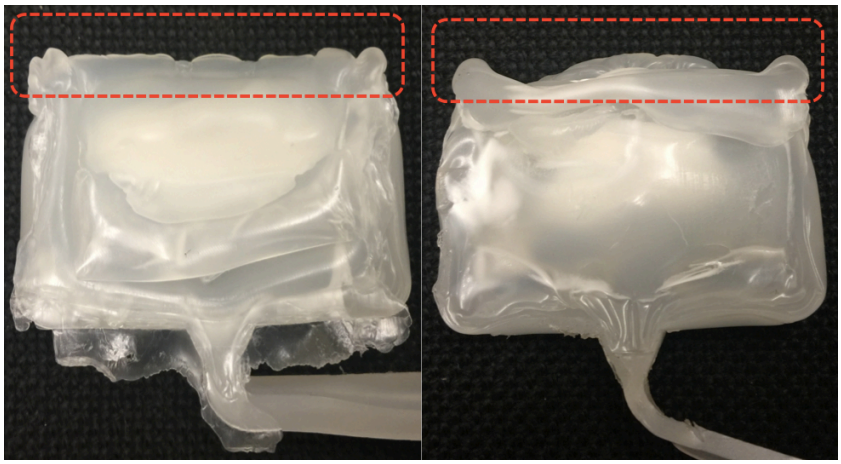

(a) (b)

Figure 7-60. Molded iPP rectangular samples (short shots) by using thick insert plates with (a) wide runner and (b) narrow runner

Figure 7-61 shows captured sequences of molding using the split-cavity insert plates, using the three injection molding conditions. Figure 7-61 (a) shows the molding sequence using the thin insert plate, while Figure 7-61 (b) and (c) shows results using the thick insert plate with the deeper runners. It is obvious that shear imbalances exist in all of the three injection molding processes. The iPP melt flow filled the outer two cavities (A1 and A2), faster than it filled the inner two cavities (B1 and B2).

In the thin plate case, the last image frames in the time line show that when the melt in the outer two cavities reached the upper visible limit of the window, the melt flowing in the inner two cavities had already reached the sketched horizontal line. (Figure 7-62 (a)) However, by using the thick plates with deeper runners, there was still a distance between the horizontal line and the flow front in the inner two cavities. (Figure 7-62 (b) and (c)) This result agrees with those generated in the single-cavity molding case. The thick insert plates with deeper runner system appear to exacerbate the shear imbalances in cavity filling.

(a) (b) (c)

Figure 7-61. Cavity filling processes for iPP molding by utilizing split-cavity insert plates: (a) thin plate, (b) thick plate with wide runner, (c) thick plate with narrow runner

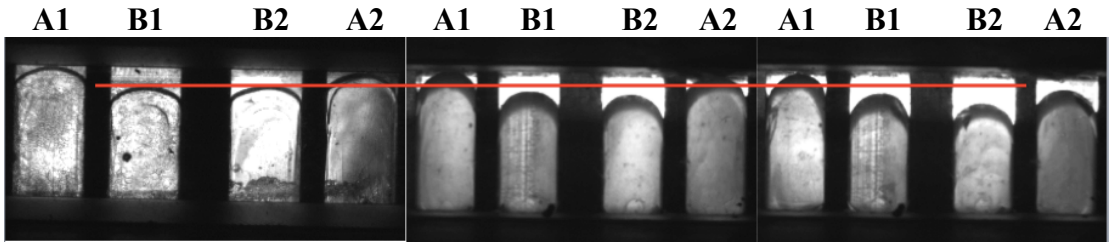

(a) (b) (c)

Figure 7-62. The last frames in the time line of cavity filling processes for iPP molding by utilizing split-cavity insert plates: (a) thin plate, (b) thick plate with wide runner, (c) thick plate with narrow runner

In reference to Figure 7-61, another cavity filling phenomenon is noted: in the second and the third frames of the time line images in both Figure 7-61 (b) and (c), the

melt flowing in the outer two cavities either (i) reached the outer cavity walls before they reached the inner cavity walls of cavity A1 and A2, or (ii) even turned towards the outer cavity walls after entering the cavities. (Figure 7-63)

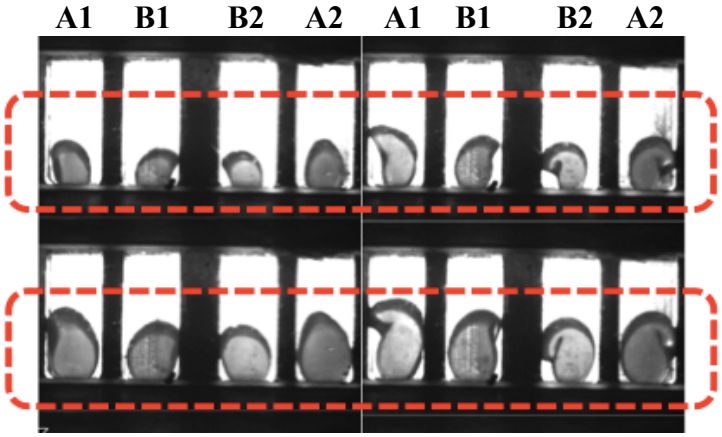

(a) (b)

Figure 7-63. Some frames in the time line pictures of cavity filling processes for iPP molding by utilizing split-cavity insert plates: (a) thick plate with wide runner, (b) thick plate with narrow runner

This observation was repeatable, and is shown in Figures 7-64 and 7-65. As indicated by the dotted areas, it is obvious that the melt flows in the outer two cavities, A1 and A2, and touches the outer cavity walls before reaching the inner cavity walls. Additionally, it is more obvious that the flow fronts in cavity A1 and A2 turned towards the outer cavity walls when the narrow runner system was used. Folding of the flow tips was also more significantly observed (Figure 7-65), which means that as a result of the shear imbalance, the melt flows preferred to flow towards the outer cavity walls after it enters cavity A1 and A2.

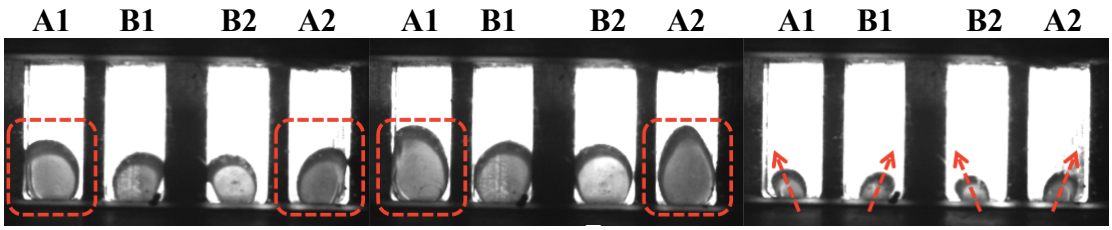

Figure 7-64. Repeatable iPP cavity filling processes by using the thick insert plate with the wide runner

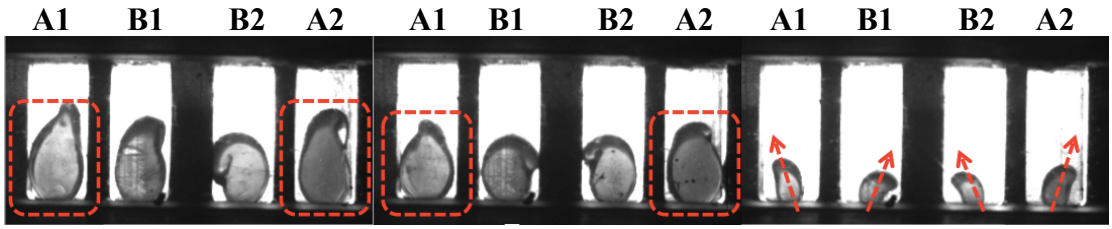

Figure 7-65. Repeatable iPP cavity filling processes by using the thick insert plate with the narrow runner

The characteristic turns and folds of the melt flow front in the inner cavities, B1 and B2, may be due to the consequences of the shear additionally generated in the secondary and tertiary runners when the melt flow split from the primary runner.

Figure 7-66 compares the results of samples molded using the thick insert plates with split-cavities. Variation in the distance achieved by the solidified flow fronts can be observed. It is obvious that by using the narrow runner system, the difference in cavity filling due to shear is accentuated.

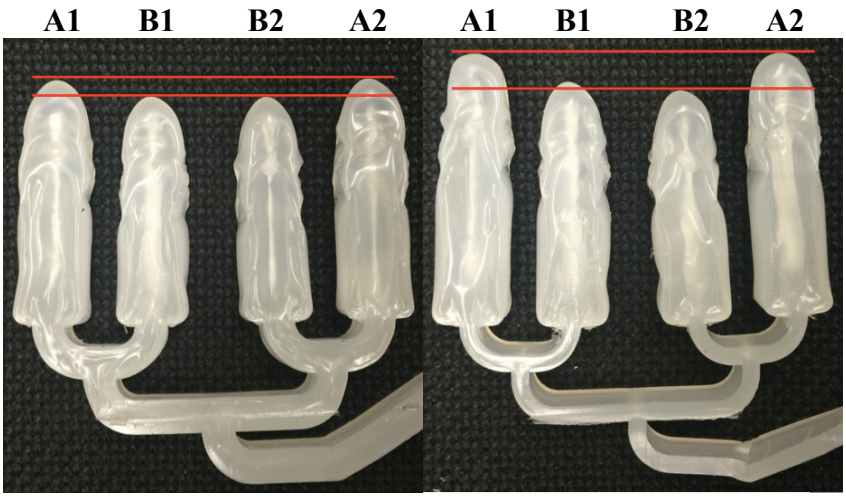

(a) (b)

Figure 7-66. Molded iPP split-cavity samples (short shots) by using thick insert plates with (a) wide runner and (b) narrow runner

The results presented for the iPP molding investigation provided in this sub-section verifies the idea proposed by the shear imbalance theory. The results show that the modified geometry of the runner cross section influenced the shear rate distribution along the runner path, thereby also influencing the melt flow during cavity filling. This also agrees with simulation results, which is presented in detail in Chapter 8.

The shear rate distribution or the relationship between the slope of shear rate with distance may be dependent of the geometry of the runner. If runner cross section is rectangular, the high shear rate values would be found more along and close to the long edges rather than the shorter edges. As exemplified in Figure 7-67, the shear rate is expected to change faster in Y direction, rather than the X direction

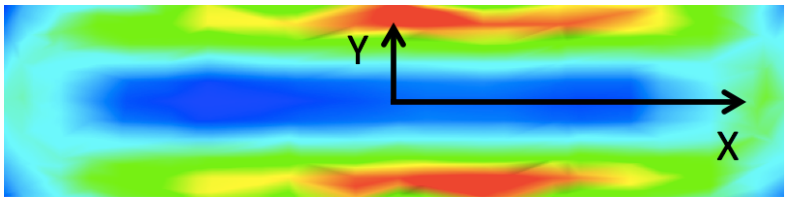

Figure 7-67. Shear rate distribution in the runner with a rectangle cross section

7.6.2.2 Real-time monitoring by using PS

In this part of the investigation, polystyrene was injection molding using the thick insert plates. In addition to the objective of confirming the results observed in the iPP investigation, different injection rates were applied for molding PS samples. The objective was to prove the earlier assumption that higher injection rates increase the shear imbalance effect.

Figure 7-68 provides the captured video frame sequences of PS injection molding in filling a circular cavity under different molding conditions: (i) wide runner with 50% IR (injection rate), (ii) wide runner with 90% IR, (iii) narrow runner with 50% IR, (iv) and narrow runner with 90% IR. The sequence of images does not show an obvious change that can be attributed to the shear imbalance effect. This was true for both cases of using wide and narrow runners, and also that of either applying slow or fast injection rates. However, as shown in Figure 7-69, the molded PS samples did reveal evidences of the shear imbalance effect under different molding conditions.

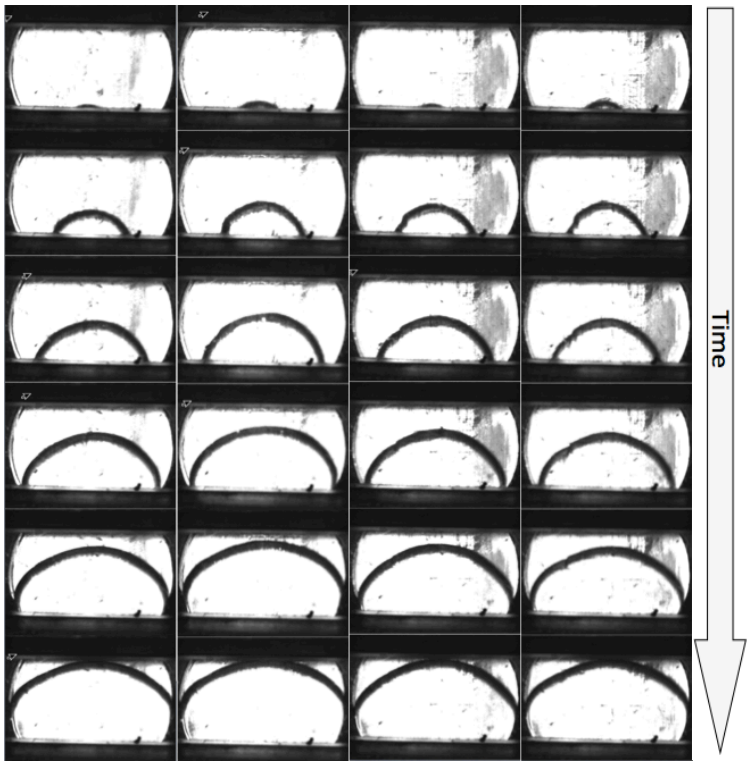

(a) (b) (c) (d)

Figure 7-68. Cavity filling processes for PS molding by utilizing thick insert plates with the circular cavity: (a) wide runner / 50% IR, (b) wide runner / 90% IR, (c) narrow runner / 50% IR, (d) narrow runner / 90% IR

(a) (b) (c) (d)

Figure 7-69. Molded PS circular samples (short shots) by using thick insert plates with (a) wide runner / 50% IR, (b) wide runner / 90% IR, (c) narrow runner / 50% IR, (d) narrow runner / 90% IR

Figure 7-69 shows that for all molding conditions, the solidified flow fronts flowing along the side walls were all ahead of those at the center. With the narrow runner, the shear imbalance effect was more obvious (Figure 7-69 (c) compared to (a);

Figure 7-69 (d) compared to (b)). Application of the higher IR also appears to increase the shear imbalance effect (Figure 7-69 (a) compared to (b); Figure 7-69 (c) and (d)).

For the rectangular cavity molding results, although the video frame sequences did not show evidence of various shear imbalances caused by different molding conditions (Figure 7-70), the final solidified samples in Figure 7-71 revealed this effect which were similar to the results of circular cavity moldings.

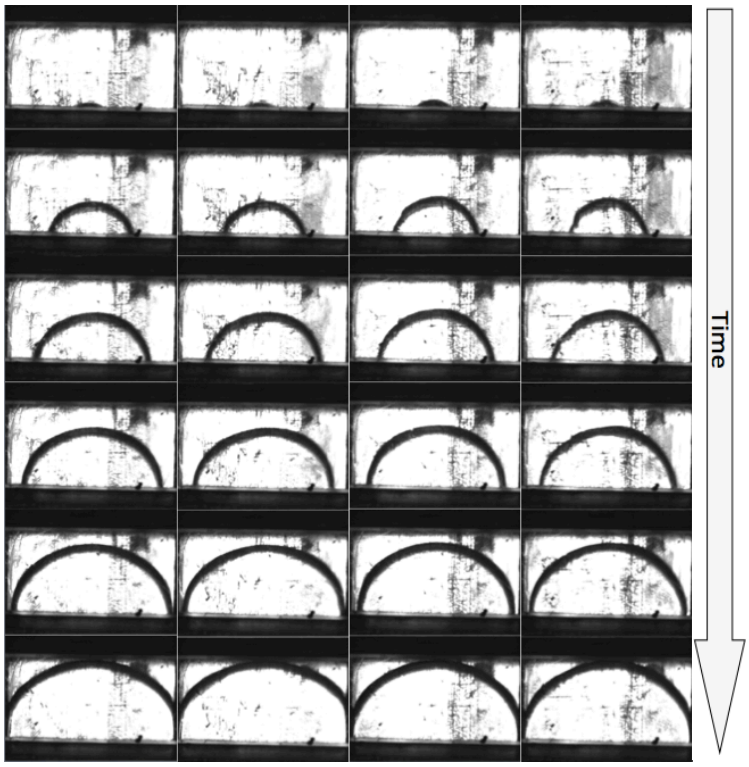

(a) (b) (c) (d)

Figure 7-70. Cavity filling processes for PS molding by utilizing thick insert plates with the rectangular cavity: (a) wide runner / 50% IR, (b) wide runner / 90% IR, (c) narrow runner / 50% IR, (d) narrow runner / 90% IR

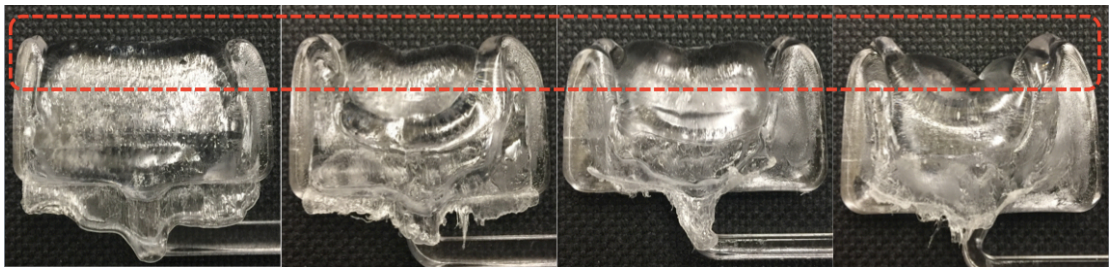

(a) (b) (c) (d)

Figure 7-71. Molded PS rectangular samples (short shots) by using thick insert plates with (a) wide runner / 50% IR, (b) wide runner / 90% IR, (c) narrow runner / 50% IR, (d) narrow runner / 90% IR

By using the narrow runner, the shear imbalance effect became more obvious (Figure 7-71 (c) compared to (a); Figure 7-71 (d) compared to (b)). As in the previous case, application of the higher IR also appears to increase the shear imbalance effect (Figure 7-71 (a) compared to (b); Figure 7-71 (c) and (d)).

The video frame captures for both cavity filling of circular and rectangular cavities did not show results as postulated by the shear imbalance theory. One possible reason could be due to the non-uniform cooling conditions within the cavity. For instance, in the circular cavity (Figure 7-72), when the melt flow passes the window area, the material close to the left and right side of the cavity was surrounded by the steel cavity wall (dashed rectangles), the same flowing material, and the PC window (dashed circles). However, the material at the core was surrounded by the same melt material and the PC window (dashed circles). Since the heat conductivity of steel is higher than polycarbonate, the melt flow close to the left and right side of the cavity, or that touching the cavity boundary, would cool down faster compared to the melt core. The core would thus be less viscous, and is able to be driven further ahead by the injection pressure. Additionally, the different cooling conditions throughout the

cavity may have also caused shrinkage or warpage of the molded products. This may also explain similar cavity filling observations in iPP molding when using the thick insert plates with the wide and the narrow runner systems, shown previously in Figure 7-57 (b) and (c), and Figure 7-59 (b) and (c).

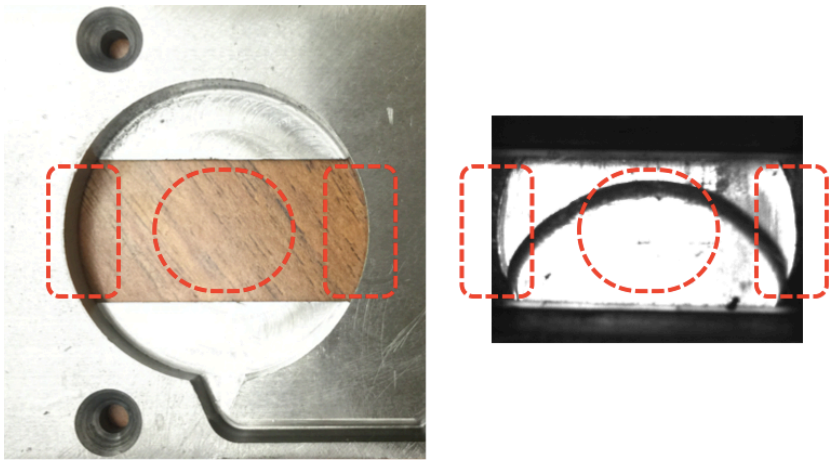

(a) (b)

Figure 7-72. Circular cavity boundary conditions, (a) the real cavity, (b) a video frame of half cavity filling with PS

Figure 7-73 provides the captured video frame sequences for molding of split-cavity insert plates. Figure 7-73 (a) and (b) show the cavity filling sequence when using the wide runner with 50% IR and 90% IR respectively, while Figure 7-73 (c) and (d) is for the case if using the narrow runner with 50% IR and 90% IR respectively.

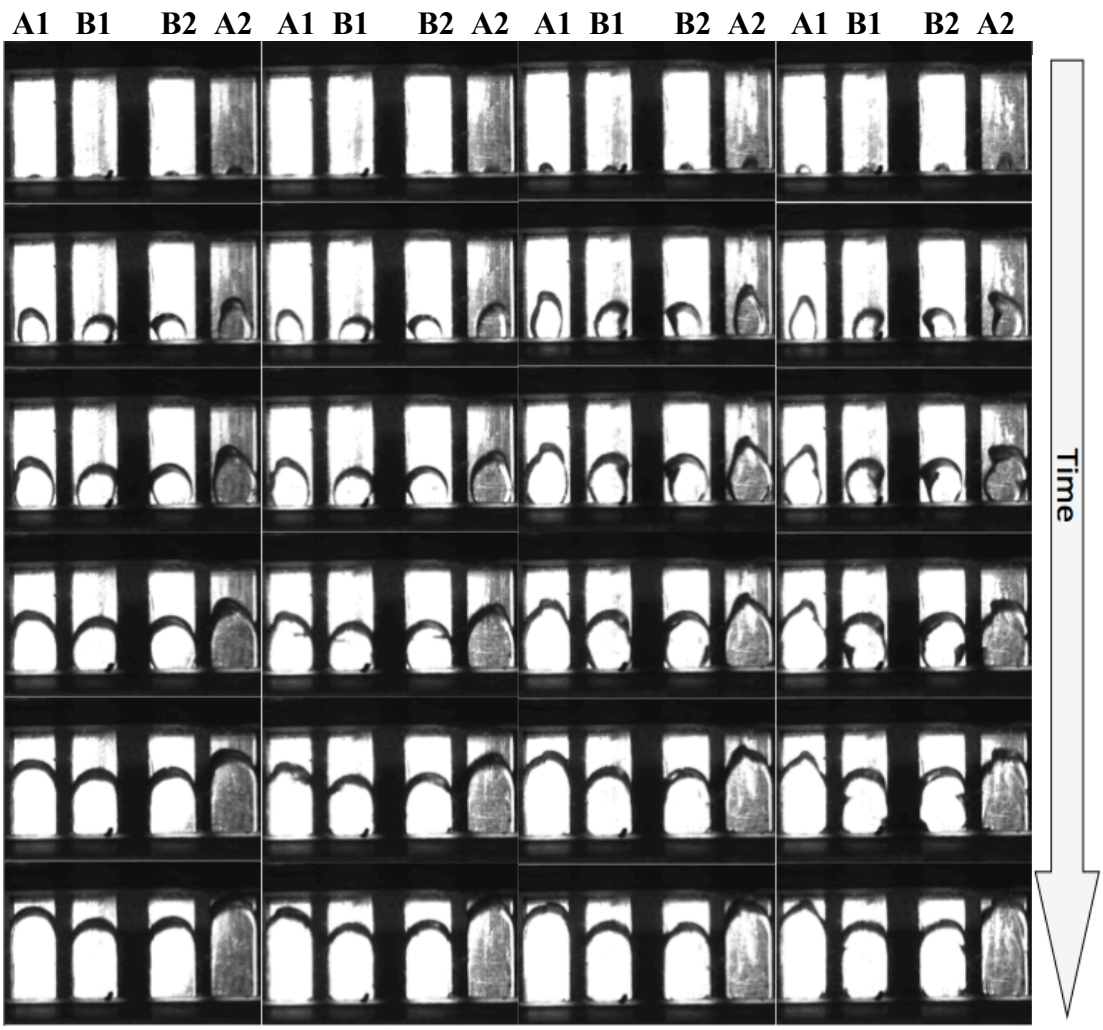

Figure 7-73. Cavity filling processes for PS molding by utilizing thick insert plates with the split-cavity: (a) wide runner / 50% IR, (b) wide runner / 90% IR, (c) narrow runner / 50% IR, (d) narrow runner / 90% IR

The images show that there is an obvious shear imbalance effect for all the applied injection molding cases. The PS melt flow filled the outer two cavities, A1 and A2, faster than it did the inner two cavities, B1 and B2. By comparing the last frames of the videos in the time line, when the melt flows in the outer two cavities reached the upper visible limit of the window, the flows in the inner two cavities had already reached the sketched horizontal line by using the wide runner with 50% IR. (Figure 7-

74 (a)) However, in the other conditions, there was still a distance between the horizontal line and the flow front in the inner two cavities. (Figure 7-74 (b), (c) and (d)) It was clear that using narrower runner system, or applying faster injection rate, causes an increase in shear imbalances during cavity filling.

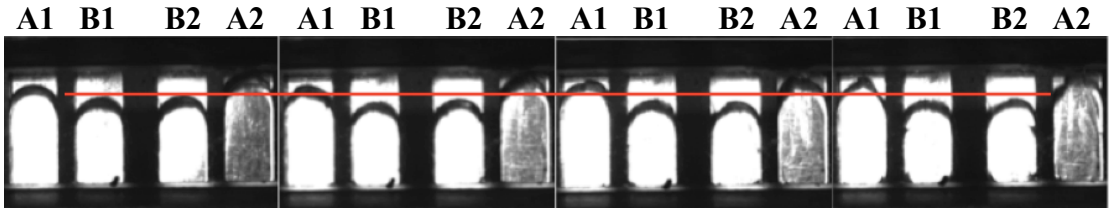

(a) (b) (c) (d)

Figure 7-74. The last frames in the time line of cavity filling processes for PS molding by utilizing thick insert plates with the split-cavity: (a) wide runner / 50% IR, (b) wide runner / 90% IR, (c) narrow runner / 50% IR, (d) narrow runner / 90% IR

For split-cavity filling, the cooling conditions in different cavities were similar, as the melt flow in each cavity was surrounded by the steel cavity wall and the PC window. This was quite different from the cooling conditions in the single-cavities. As a result, the similar cooling condition in the split-cavity design ensured the high shear flow and the low shear flow were investigated in the same environment for both iPP and PS.

Similar to the cavity filling phenomenon observed in the iPP investigations, Figure 7-75 (the dotted circled areas) shows that the melt flows in the outer two cavities, A1 and A2, and reaches the outer cavity walls before the inner cavity walls. This further proves that as a result of the shear imbalance, the melt prefers to flow towards the outer cavity walls after it enters cavity A1 and A2.

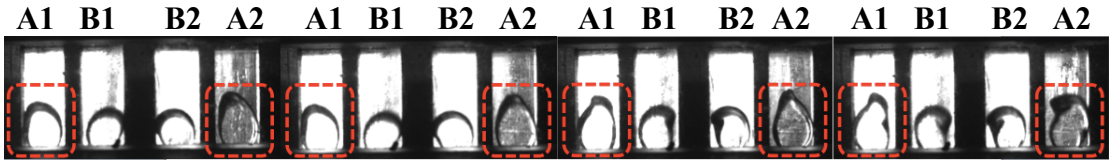

(a) (b) (c) (d)

Figure 7-75. Repeatable PS cavity filling processes by using the thick insert plate in the different molding conditions: (a) wide runner / 50% IR, (b) wide runner / 90% IR, (c) narrow runner / 50% IR, (d) narrow runner / 90% IR

Figure 7-76 compares the results of the samples molded by using the thick insert plates with split-cavities. The variation in distance of the solidified flow fronts was not obvious among the samples molded in different conditions.

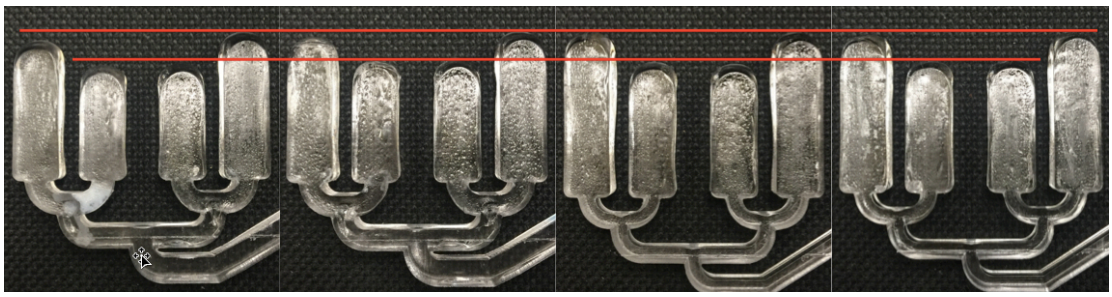

(a) (b) (c) (d)

Figure 7-76. Molded PS split-cavity samples (short shots) by using thick insert plates with (a) wide runner / 50% IR, (b) wide runner / 90% IR, (c) narrow runner / 50% IR, (d) narrow runner / 90% IR

For molding samples using the split-cavities, it was not easy to keep the shot sizes the same in the four molding conditions. As a result, samples in some outer/inner cavities (in Figure 7-76 (c)) is observed to be longer than the samples in other outer/inner cavities (in Figure 7-76 (a) or (b)). Hence the flow front variation was difficult to measure and compare.

The real-time monitoring investigation data presented in this section indicates that in both the iPP and PS study, the injection rate was another key parameter, that

influences shear rate levels, and thus the injection molding results. This is in agreement with the assumptions made in Chapter 5.

8 Theoretical Basis for Investigations

In order to prove the shear imbalance theory, a series of simulations for all the injection molding processes and materials used in this investigation were executed with Autodesk Moldflow 2016®.

8.1 Simulations for Real-Time Monitoring Study

Polypropylene and polystyrene were the major materials used in real-time monitoring study. The injection models of the single-cavity molding (circular cavity and rectangular cavity) and multi-cavity molding were created via SolidWorks®. Figures 8-1, 8-2 and 8-3 show the SolidWorks® models for the simulations of the thin cavity molding. The raw SolidWorks® models were created based on actual geometries of the injection molded samples (as examplified in Figure 8-4). These were then converted to the readable files for Moldflow®.

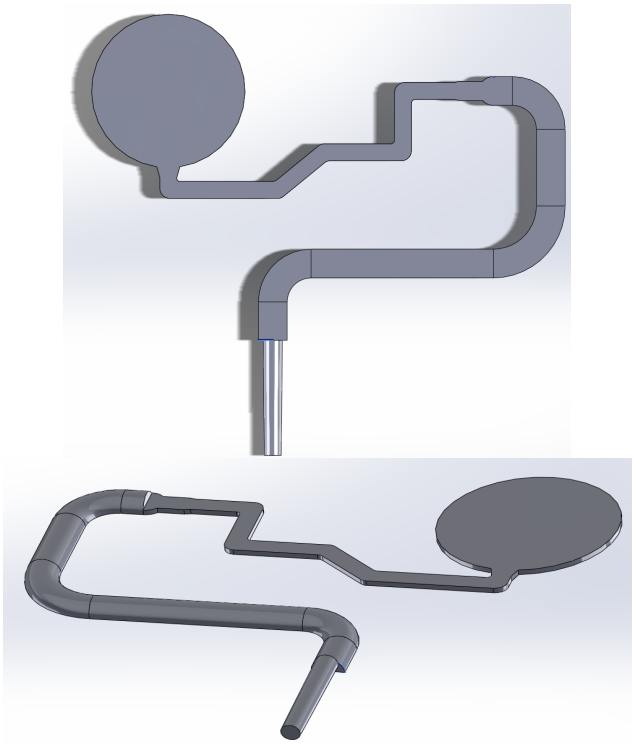

Figure 8-1. The simulation model of single-cavity molding (circular cavity filling)

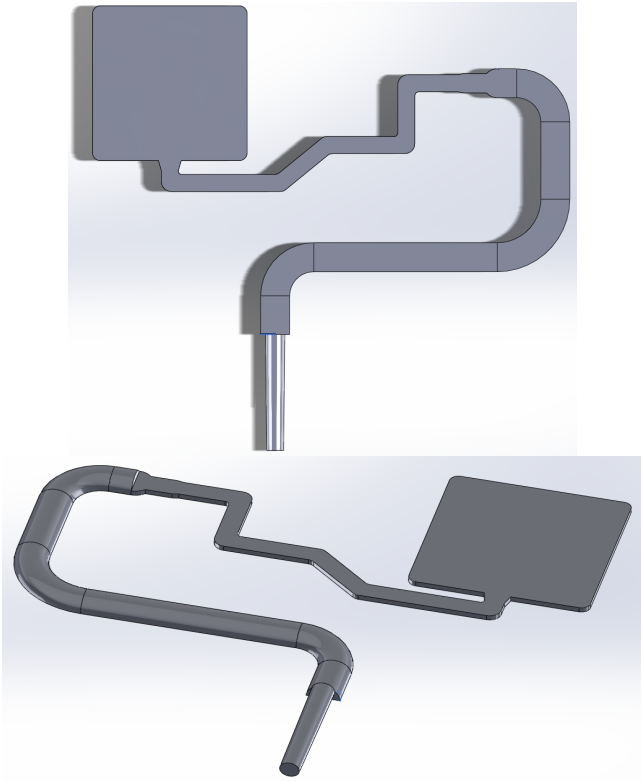

Figure 8-2. The simulation model of single-cavity molding (rectangular cavity filling)

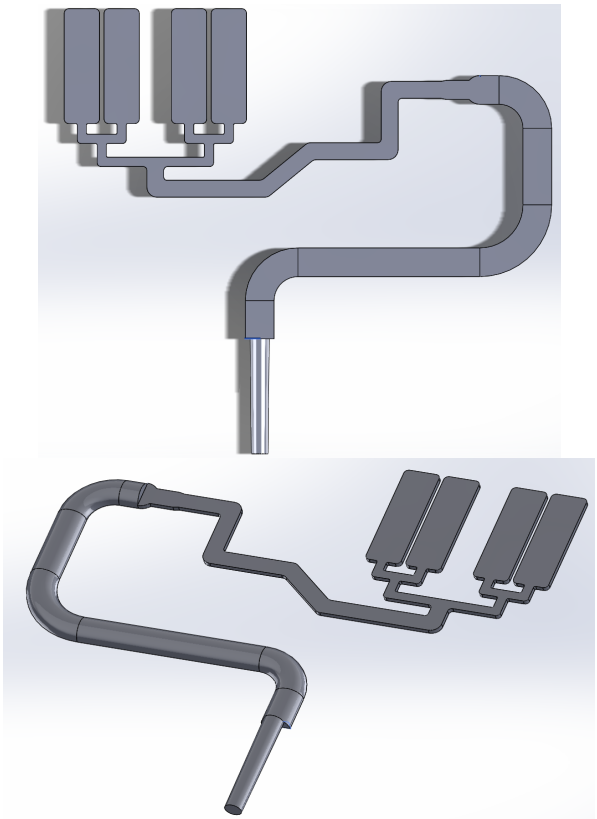

Figure 8-3. The simulation model of multi-cavity molding (split cavity filling)

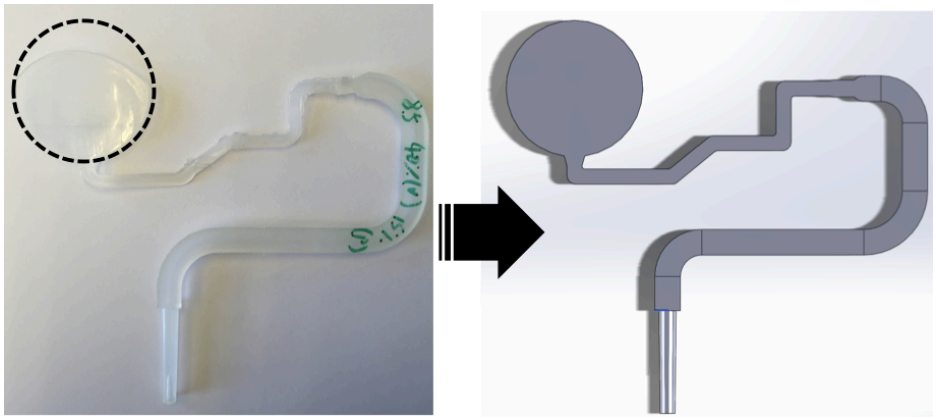

Figure 8-4. Example showing a simulation model created according to the actual molded sample

The processing parameters, which include material information, injection speed, and cooling time, were applied in the simulations according to actual injection molding conditions.

8.1.1 Simulations for iPP Injection Moldings

For the simulations using iPP in the thin insert plates, the mesh sizes were over 1.9 million, 3.2 million and 2.9 million for the circular cavity, rectangular and split-cavity respectively. Figure 8-5 shows the simulated cavity filling results in the three different molding cavities.

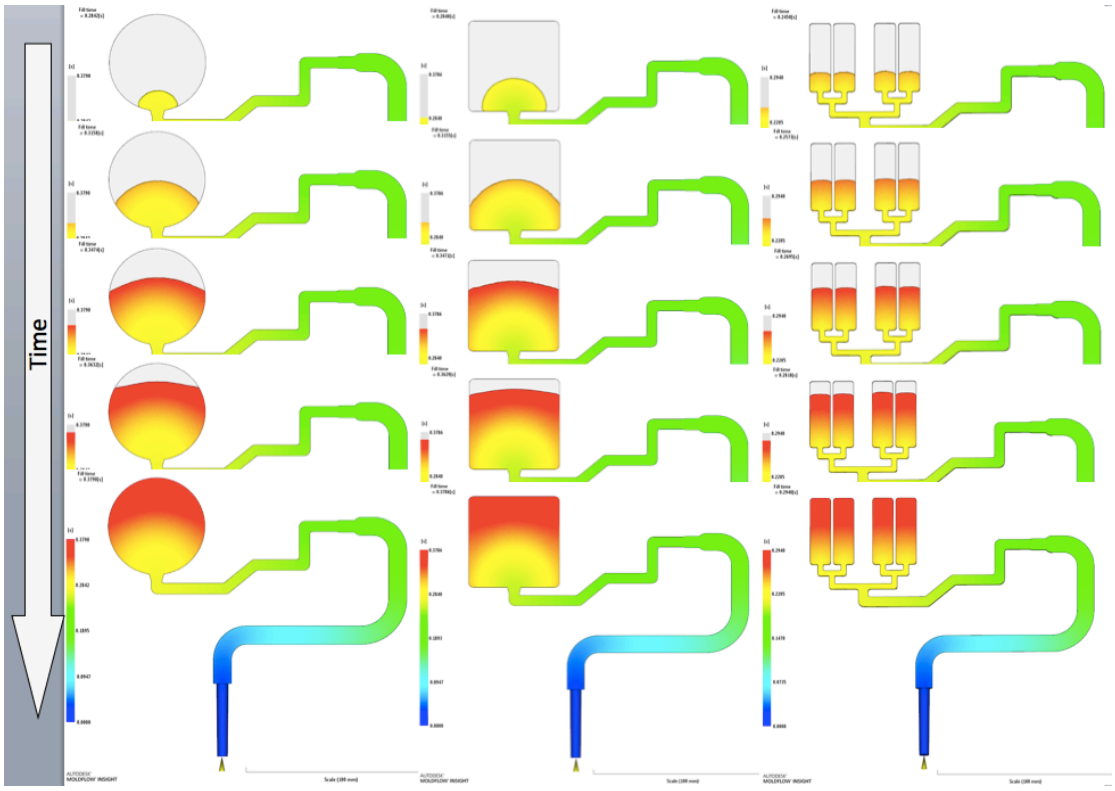

(a) (b) (c)

Figure 8-5. Simulations of iPP cavity filling sequences by using the thin insert plates with three different cavities, (a) circular cavity molding, (b) rectangular cavity molding, and (c) split-cavity molding

Figures 8-6 and 8-7 provide enlarged images of a half-filled cavity in the single cavity filling case. Judging from the flow front, the melt flow at the cavity edge regions appear to travel faster relative to that at the cavity center.

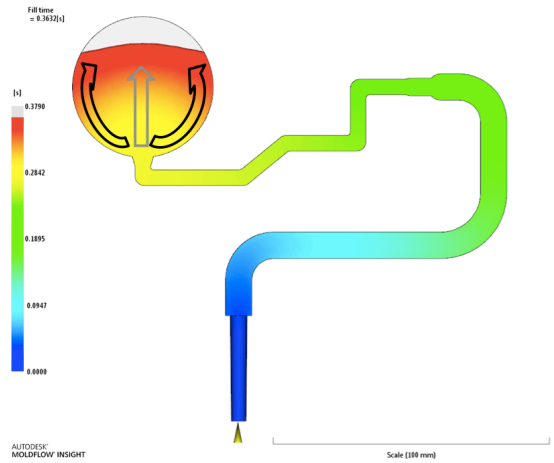

Figure 8-6. Enlarged image showing cavity filling patterns of iPP molding simulation by using the thin insert plate with a circular cavity

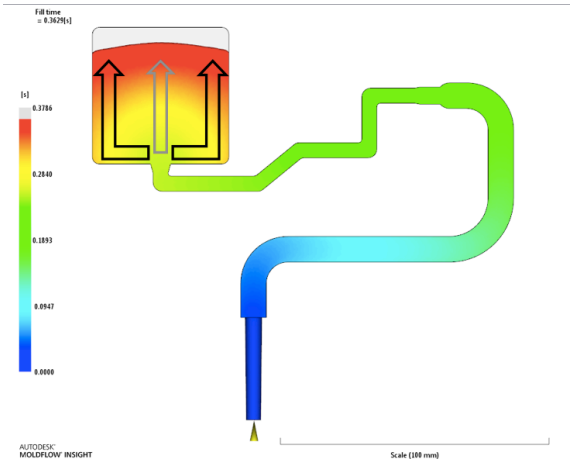

Figure 8-7. Enlarged image showing cavity filling patterns of iPP molding simulation by using the thin insert plate with a rectangular cavity

For the split cavity molding of iPP, the simulation seemed not the same to previous assumptions. In Figure 8-8, it was noted that one of the inner cavities was filled a little faster than the outer cavities in the simulation.

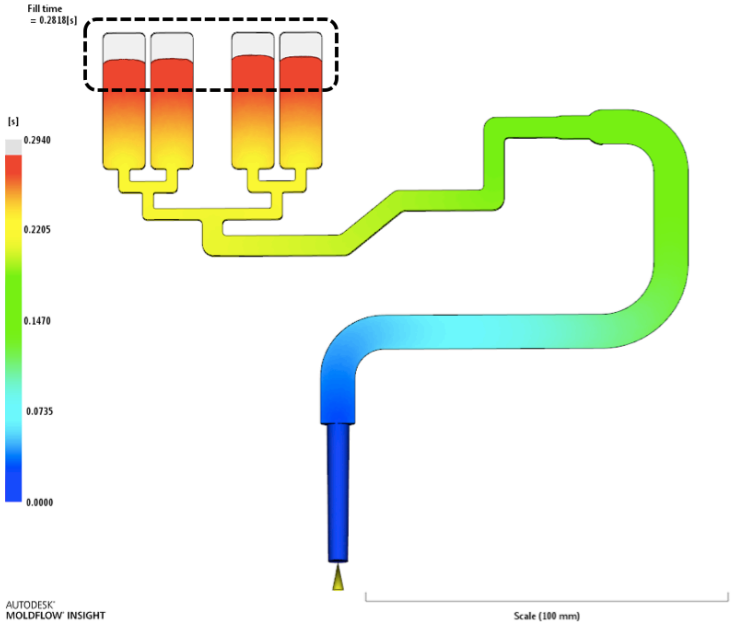

Figure 8-8. Enlarged image showing cavity filling patterns of iPP molding simulation by using the thin insert plate with a split-cavity

As previously noted in Chapter 5, in the thin insert plates, the runner cross section has a flat rectangular (Figure 5-14). The high-sheared is generated close to the upper and bottom boundary. This results in a stacking of the high and low flow rate melt regions, one on top of the other (Figures 5-15 and 8-9) The melt flowing at the central region in the single cavity case, and in the inner two cavities of the split-cavity case may acquire rates of shear rate that are higher than expected. This may explain why cavity filling results using the thin insert plates did not exhibit the expected shear imbalance patterns.

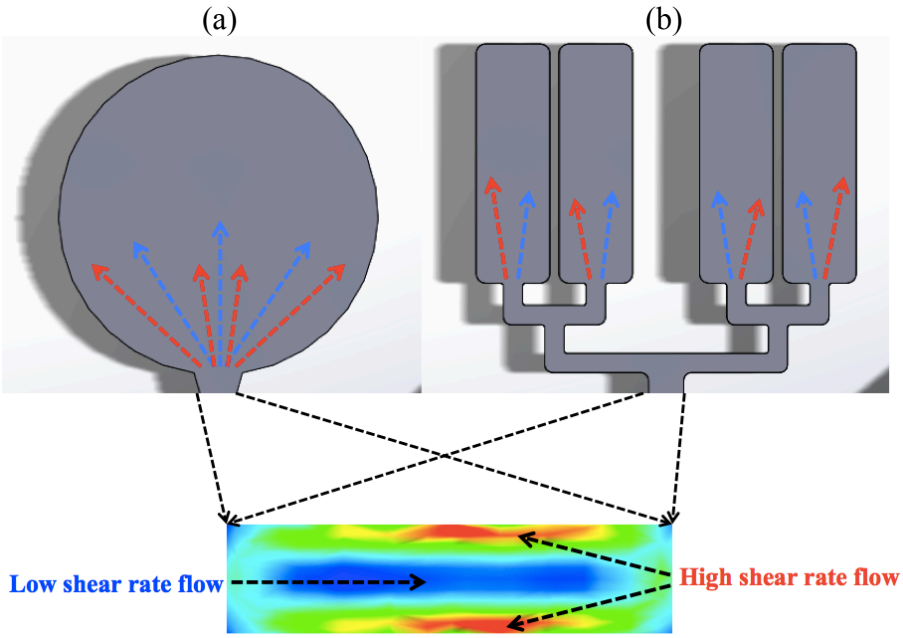

Figure 8-9. The high shear rate low and the low shear rate flow distributions in cavities by using the thin insert plates: (a) single cavity distributions, (b) split-cavity distributions

Figure 8-10 shows areas where the highest shear rate values exist in the runner cross section. The shear rate values were sampled from the cross sections that are close to the cavity gate, and half-way into the runner. The highest values were observed to be at the same level, as the geometry of the runner cross section was the same.

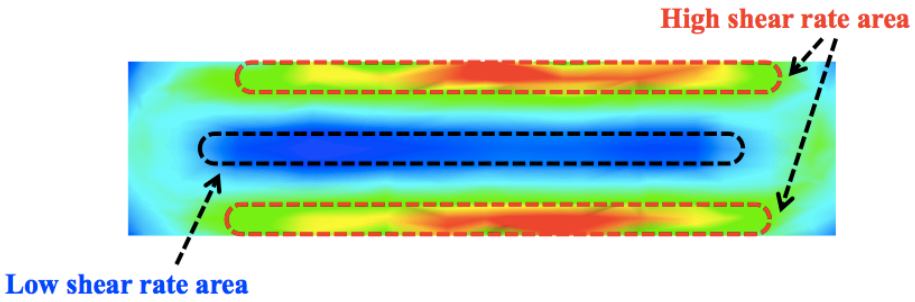

Figure 8-10. Sampling areas in the cross section of the runner in the thin insert plates

According to the shear thinning theory, the lowest viscosities should be at the areas of highest shear rates. From the simulated results, the highest shear rate values ranged from 13657 to 15656 s^{-1} for the three cavity conditions, with respective viscosities ranging between 19.27 to 15.05 Pa•s. These values lay within the theoretical limits plotted in Figure 8-11.

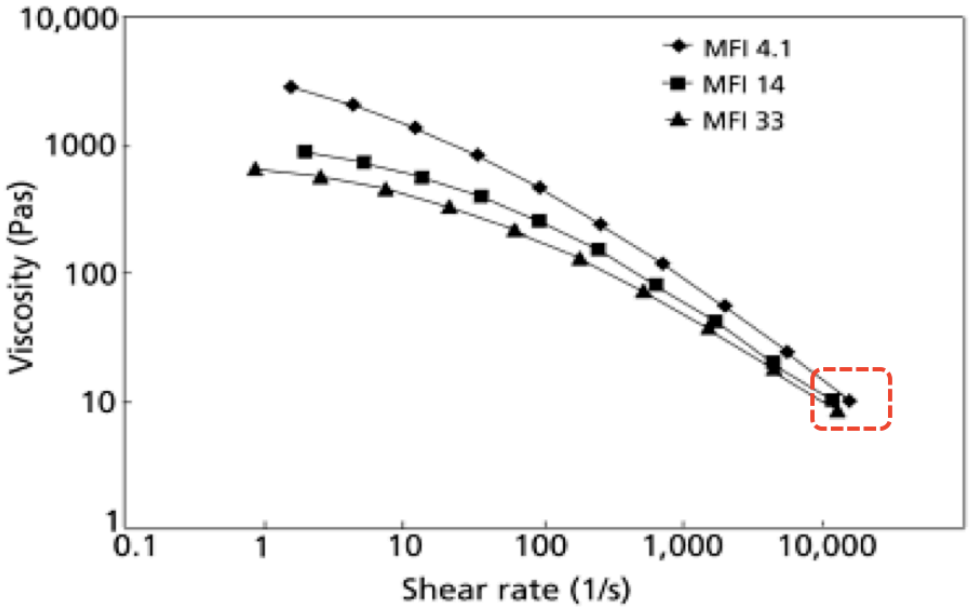

Figure 8-11. Simulated values lay in the range of the theoretical reference, for using the thin insert plates of iPP moldings

For simulations using iPP in the thick insert plates with wide and narrow runners, the mesh sizes are listed in Table 8-1 for the circular, the rectangular, and the split-cavity respectively. The number of elements had a minimum of 2.3 million, with the highest being over 7.8 million.

Table 8-1. Number of elements used in thick insert plates in the iPP molding simulation runs

Insert Plates	Circular Cavity	Rectangular Cavity	Split-Cavity
Wide Runner	2 343 474	7 524 208	7 848 719
Narrow Runner	5 935 717	6 869 000	7 189 905

Figures 8-12 and 8-13 show the simulated iPP cavity filling results in the circular and rectangular cavity. Similar to the experimental real-time monitored results, there was no obvious difference between using the insert plates with the wide and the narrow runner. Even when comparing the results to cavity filling of the thin insert plates, the difference was not apparent. (Figure 8-14)

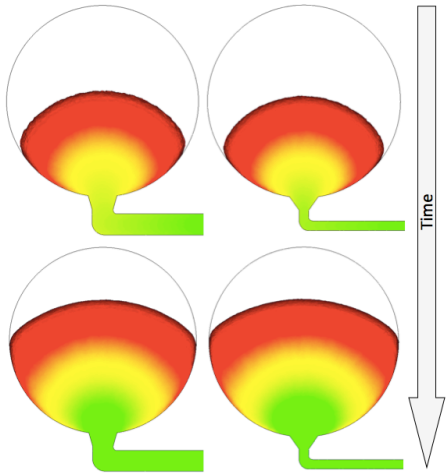

(a) (b)

Figure 8-12. Simulated iPP filling of the circular cavity when using hick insert plates with (a) the wide and (b) the narrow runner

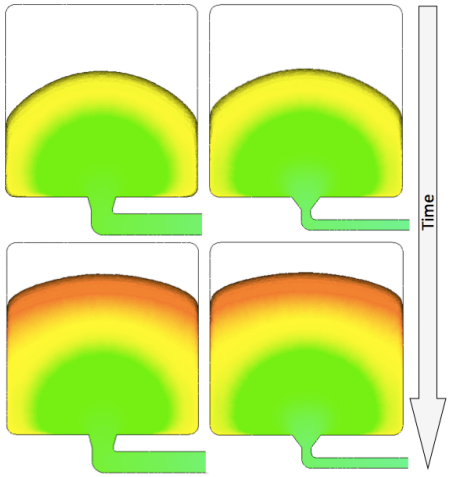

(a) (b)

Figure 8-13. Simulated iPP cavity fillings in the rectangular cavity by using thick insert plates with (a) the wide and (b) the narrow runner

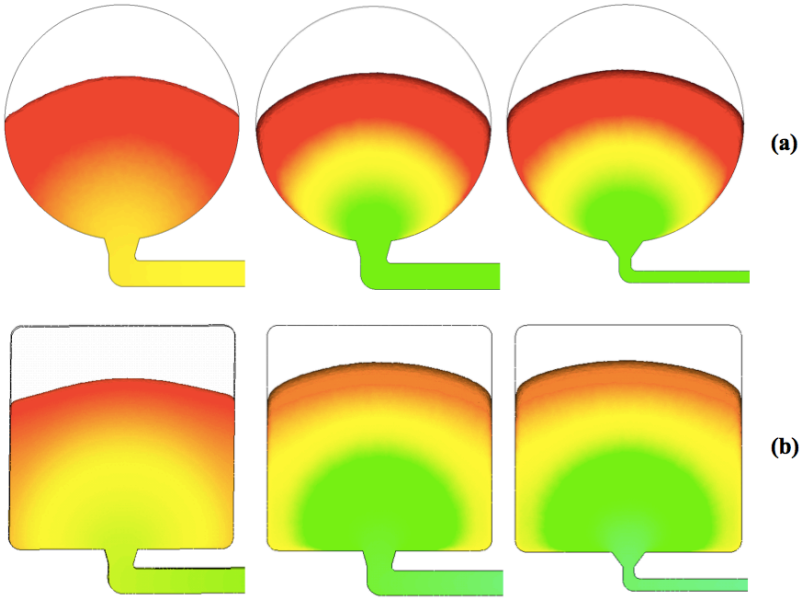

(thin plate) (thick plate/wide runner) (thick plate/narrow runner)

Figure 8-14. Comparison among iPP cavity fillings by using the thin and the thick insert plates: (a) circular cavity fillings and (b) rectangular cavity fillings

There are several possible reasons for the observations gathered from the simulations and the real-time monitored results. It is possible that the mesh size was not large enough, or the boundary conditions for the simulation model might not be

appropriate to properly mimic the cavity filling processes in real-time. As a result, the melt flow during injection molding was not accurately simulated. Another possible reason could be that the injection rates were not high enough to generate any obvious difference in result. To improve the simulation results or the monitored results in real time, higher mesh sizes or faster injection rates may be required.

However, in Figure 8-15, there was a discovery that could provide proof of cavity filling imbalance. The dashed lines indicated the distance between the flow front in the cavity center and the sides. During cavity filling, it is obvious that the distances were all reduced over time. It is possible that the melt flowing at the sides were catching up to the melt flowing at the cavity center. This is similar to the assumption that the melt flow fills the sides of the cavity faster.

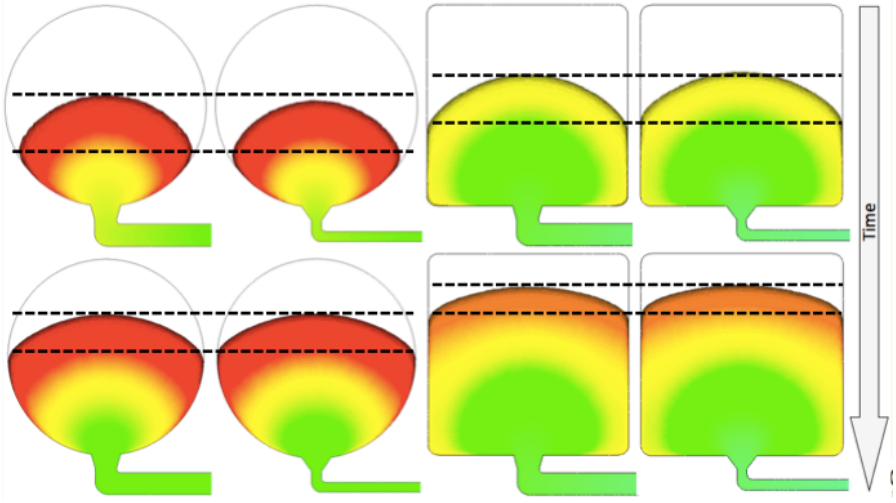

(a) (b) (c) (d)

Figure 8-15. Simulated iPP cavity fillings in the circular and rectangular cavities by using the thick insert plates with the wide runner, (a) and (c), and the narrow runner, (b) and (d)

The cavity filling simulation result when using the split-cavity is provided in Figure 8-16. It is apparent that the shear imbalance in the split-cavity is more serious

when using the thick inert plates. (Figure 8-16 (b) and (c)). The result also shows that that by using the narrow runner system, the shear imbalance in cavity filling becomes more significant (Figure 8-16 (c)). This confirms that the shear imbalance in the cavity filling processes is also depends on the geometry of the runner cross section.

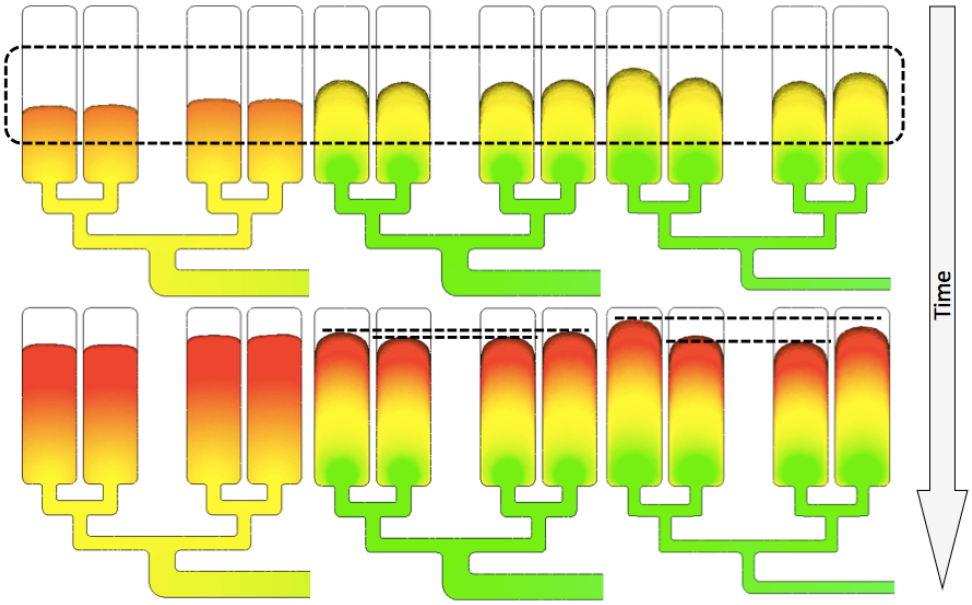

(a) (b) (c)

Figure 8-16. Comparison among iPP cavity fillings by using the thin and the thick insert plates with the split-cavity: (a) thin insert plate, (b) thick insert plate with wide runner, and (c) thick insert plate with the narrow runner

Figure 8-9 shows the shear rate distribution when using the thin insert plates. By using the thick insert plates however, the shear rate distribution in the runner and near the cavity gates is observed to be different. (Figure 8-17)

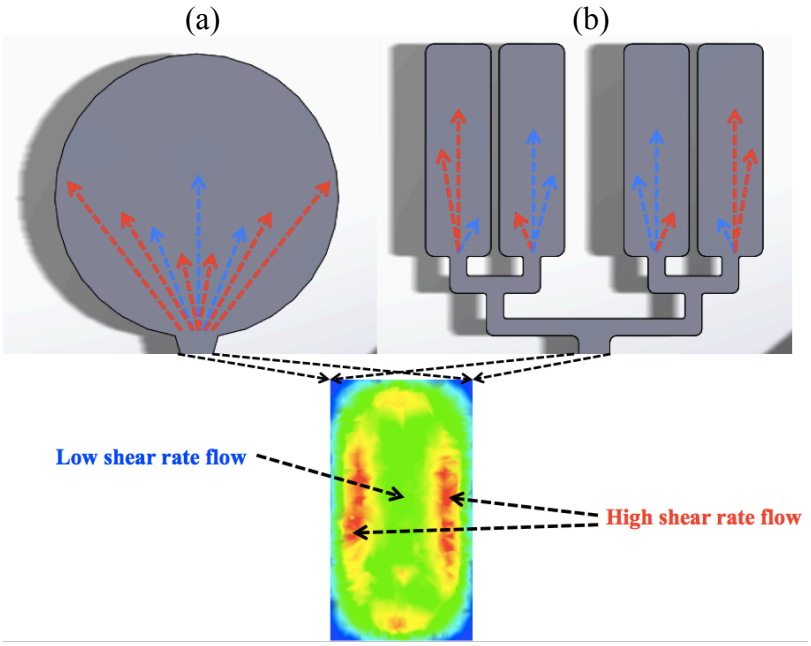

Figure 8-17. The high shear rate and low shear rate flow distributions in cavities by using the thick insert plates: (a) single cavity distributions, (b) split-cavity distributions

In the thick insert plates, the cross section of the runner channel is a tall rectangle. (Figure 5-17). The highly sheared flow was observed to be more close to the left and right boundary. As a result, the high shear rate flow could be separated from the low shear rate flow, and be distributed towards different major directions into the cavity. (Figure 5-17 and Figure 8-17). The melt flow, at the center area in the single cavity or in the inner two cavities of the split-cavities, mainly contained the low shear rate flow. The high shear rate flow is observed to be dominant at the left and right side in the single cavity, or the outer two cavities of the split-cavities.

Figure 8-18 shows the areas where the highest shear rate values exist in the runner cross section when using the thick insert plates. The highest shear rate values range from 2019 to 2588 s^{-1} for the three cavity conditions when using the wide runner.

The related viscosities range from 84.19 to 67.25 Pa•s. The highest shear rate values range from 7510 to 9270 s^{-1} for the three cavity conditions when using the narrow runner. The corresponding viscosities range from 34.62 to 30.49 Pa•s. Compared to the theoretical values plotted in Figure 8-19, these values roughly lay within the expected range.

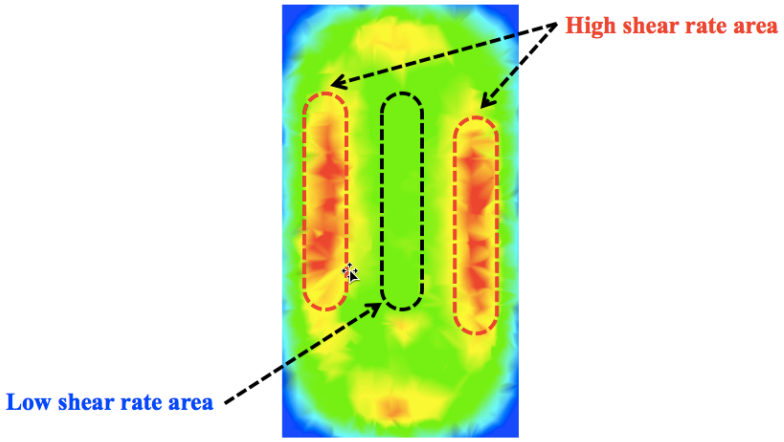

Figure 8-18. Sampling areas in the cross section of the runner in the thick insert plates

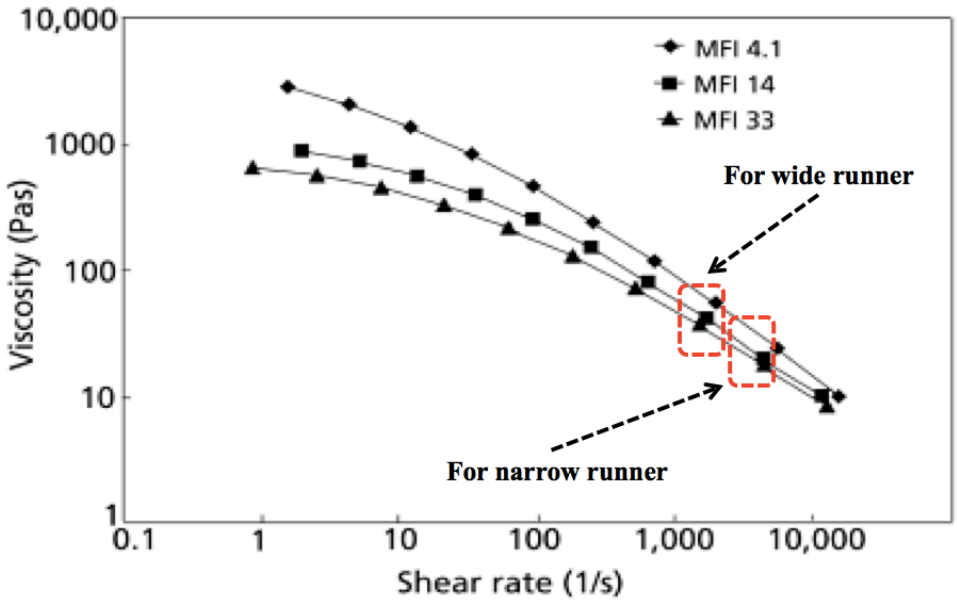

Figure 8-19. Simulated values lay in the ranges of the theoretical reference, for using the thick insert plates of iPP moldings

By comparing Figures 8-11 and 8-19, it is observed that the shear rate values and the related viscosities are sensitive to the geometry of the runner cross section. For these iPP simulations, the highest high shear rate value with the lowest viscosity exist in the thin insert plates, while the lowest shear rate value with the relatively higher viscosity exist in the thick insert plates with the wide runner.

Table 8-2. Comparisons of aspect ratios, highest shear rate values and viscosities among simulated iPP results by using the insert plates with different runner systems

Runners	Depth (in)	Width (in)	Aspect Ratio	High S.R. (1/s)	Viscosity (Pa•s)
In Thin Plates	0.07	0.22	3.143	15656	15.05
In Thick Plates / Wide Runner	0.3	0.22	1.364	2588	67.25
In Thick Plates / Narrow Runner	0.3	0.1	3	9270	30.49

(S.R. means shear rate; 0.22 in = 5.588 mm, 0.07 in = 1.78 mm, 0.3 in = 7.62 mm, 0.1 in = 2.54 mm)

By calculating the aspect ratios of the three runner cross sections (Table 8-2), it was found that for the iPP melt flow, the largest value of the high shear rates with the lowest viscosity exist in the runner, of which the cross section had the largest aspect ratio. By reducing the aspect ratio, the largest value of the high shear rates was reduced and the viscosity was increased. However, it is believed that there could still be some other factors, such as injection rates, which may influence the shear rate values. However, by observing the data trends in Table 8-2, it is apparent that the shear rate values may change depending on the aspect ratio of the runner cross section.

Another important parameter related to shear imbalances was temperature distributions. The simulated temperature distributions in cavities are shown in Figures

8-20 to 8-22. The sampling plane was cut about half-way into the cavity thickness. According to the shear thinning theory, the highest temperatures should exist at the locations where the highest shear rate values are observed.

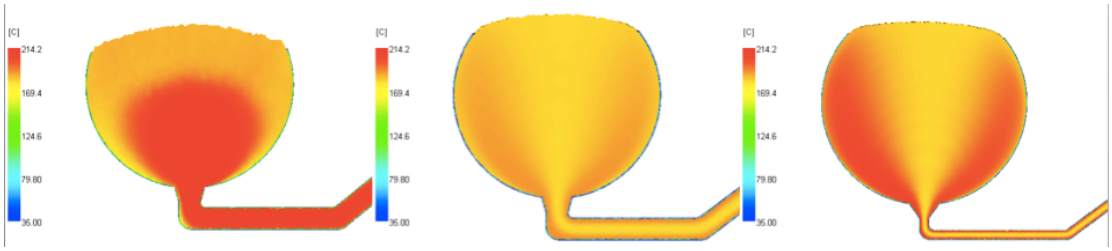

(a) (b) (c)

Figure 8-20. Temperature distributions in circular cavity fillings for iPP molding simulations: (a) in thin insert plate, (b) in thick insert plates with the wide runner, and (c) in thick insert plates with the narrow runner

(a) (b) (c)

Figure 8-21. Temperature distributions in rectangular cavity fillings for iPP molding simulations: (a) in thin insert plate, (b) in thick insert plates with the wide runner, and (c) in thick insert plates with the narrow runner

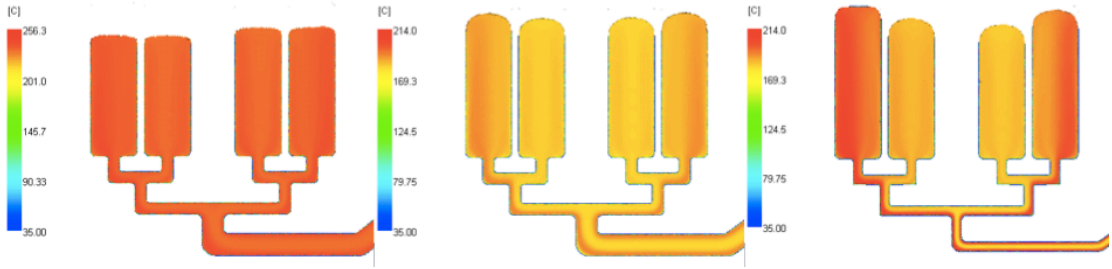

(a) (b) (c)

Figure 8-22. Temperature distributions in split-cavity fillings for iPP molding simulations: (a) in thin insert plate, (b) in thick insert plates with the wide runner, and (c) in thick insert plates with the narrow runner

For the single cavity moldings, the higher temperatures were found at the two sides within the cavities, while for the split-cavity molding, the higher temperatures were found in the outer two cavities. The simulated temperature differences from the high shear region and the low shear region were at least greater than 10°C. By again comparing Figures 8-20 to 8-22, simulations using the narrow runner in the thick insert plates has a high temperature zone that was much more obvious in the high shear flow regions in the runner tunnel and in the cavities - these were the two sides in single cavities or outer two cavities for the split-cavity. This may be the result from the shear rate distributions in the three different runner systems. As mentioned before, by using the narrow runner system in the thick insert plate, the melt flow with the high shear rate and the high temperature could be more separated from the flow with the low shear rate and the low temperature. These results agree well with the assumptions related to the shear imbalance theory.

8.1.2 Simulations for PS Injection Moldings

For the simulations of using PS, the mesh sizes (number of elements) for different molding conditions are listed in Table 8-3. The least is about 2.34 million, while the largest mesh was over 7.8 million.

Table 8-3. Simulation mesh sizes for using different cavities and different injection rates in thick insert plates of PS molding

Insert Plate	Injection Rate	Circular Cavity	Rectangular Cavity	Split-Cavity
Wide Runner	Slow	2 343 474	7 524 208	7 848 719
	Fast	2 343 474	7 524 208	7 848 719
Narrow Runner	Slow	5 935 717	6 869 000	7 189 905
	Fast	5 935 717	6 869 000	7 189 905

According to the shear imbalance theory and simulation results shown in Figure 8-16, the high shear rate melt will fill the side regions in the single cavity faster than the low shear rate melt filling the center region; or the high shear rate melt will fill the outer two cavities in the split-cavity faster than the low shear rate melt filling the inner two cavities.

Figures 8-23 and 8-24 shows the simulated PS cavity filling results in the circular and rectangular cavity by applying different injection rates (IR). The simulated results are similar to the real-time monitored results, in that there was no obvious difference between using the insert plates with the wide runner and the narrow runner, or applying slow or fast IR. Although shear imbalances in cavity fillings is not apparent, by comparing the flow front distances, it is possible that the melt flowing at the sides were catching up to the melt flowing in the cavity center.

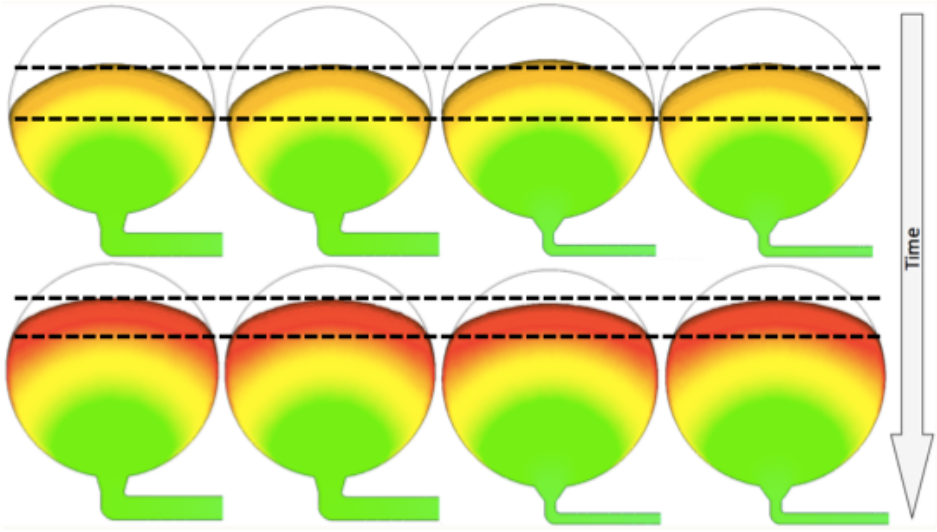

(a) (b) (c) (d)

Figure 8-23. Simulated PS cavity fillings in the circular cavities with (a) wide runner / 50% IR, (b) wide runner / 90% IR, (c) narrow runner / 50% IR, (d) narrow runner / 90% IR

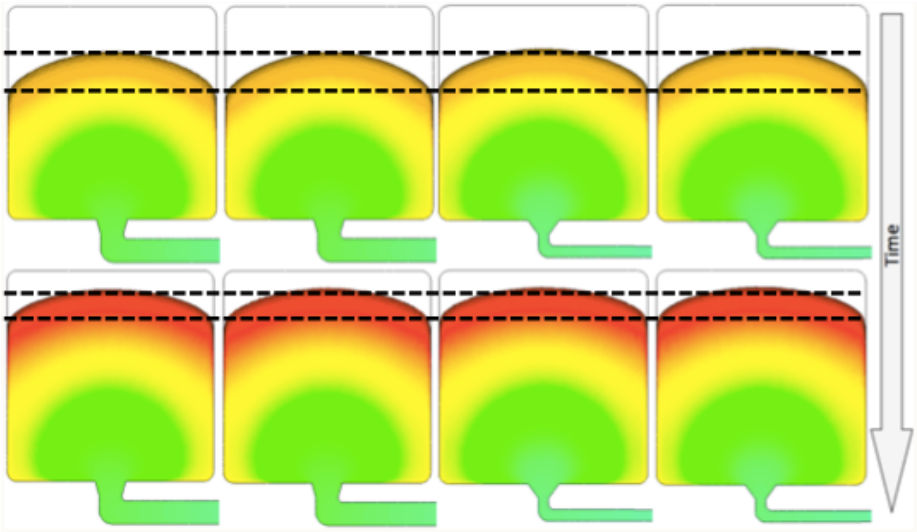

(a) (b) (c) (d)

Figure 8-24. Simulated PS cavity fillings in the rectangular cavities with (a) wide runner / 50% IR, (b) wide runner / 90% IR, (c) narrow runner / 50% IR, (d) narrow runner / 90% IR

However, the simulations for the split-cavity fillings were more convincing. The PS cavity filling simulation result using the split-cavity is provided in Figure 8-25. The shear imbalanced cavity filling existed for all molding conditions. It is apparent that the outer two cavities were filled faster than the inner two cavities.

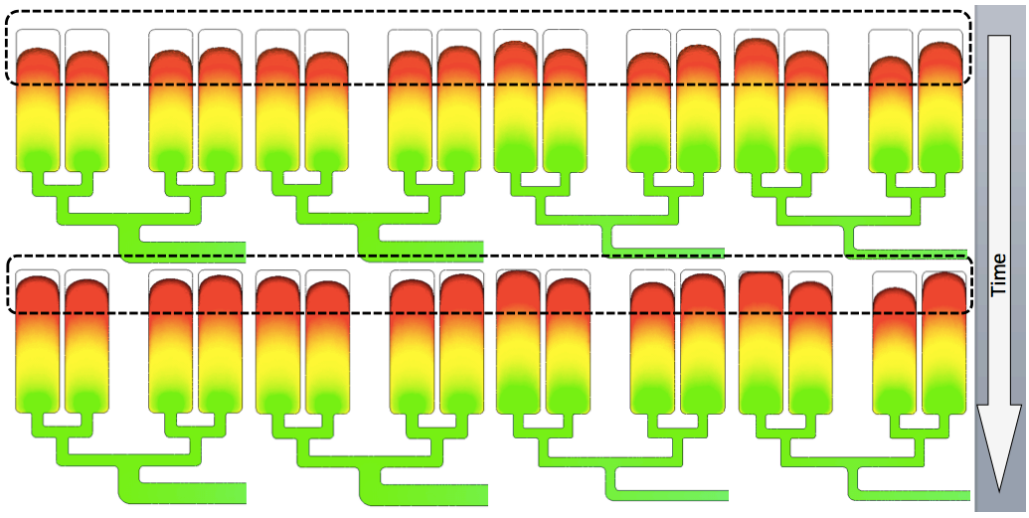

(a) (b) (c) (d)

Figure 8-25. Simulated PS cavity fillings in the split-cavities with (a) wide runner / 50% IR, (b) wide runner / 90% IR, (c) narrow runner / 50% IR, (d) narrow runner / 90% IR

By comparing simulation details shown in the dotted/circled areas, shear imbalances is observed to be more serious when using the inert plates with narrow runners (Figure 8-25 (c) and (d)), relative to the case when wide runners (Figure 8-25 (a) and (b)). It is also noted that by applying 90% IR, the shear imbalances is more significant, (Figure 8-25 (c) and (d)). This further confirms that the shear resulted imbalance in cavity filling is sensitive to the geometry of the runner cross-section and the IR.

According to Figure 8-18 and the simulated results, the highest shear rate values and the related viscosities in the runner system for all the PS molding conditions were provided in Table 8-4. Compared with the theoretical values in Figure 8-26, these values roughly lay in the reasonable ranges in the plot.

Table 8-4. Comparison of the highest shear rates and the related viscosities among different PS molding conditions

Runner	Injection Rate	High S.R. (1/s)	Viscosity (Pa•s)
Wide	50%	1512	61.69
	90%	2925	35.54
Narrow	50%	4225	30.81
	90%	11985	12.29

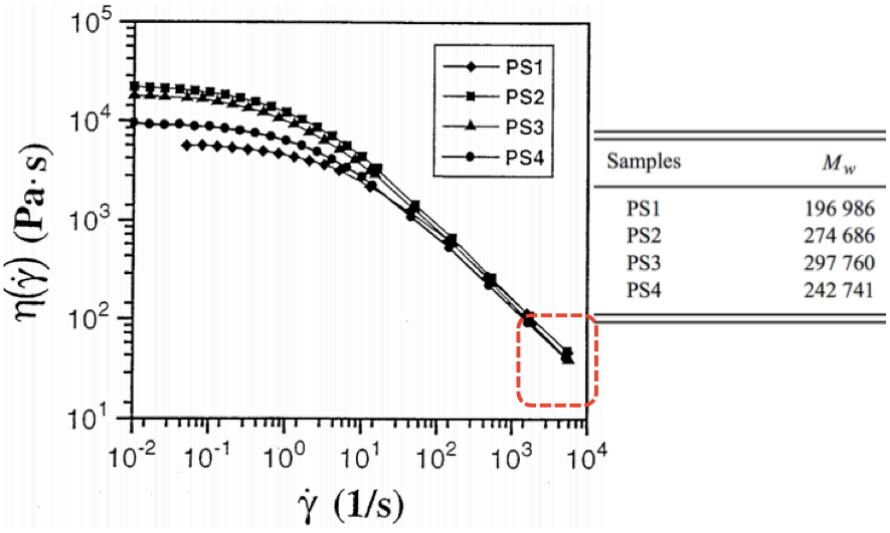

Samples	M_w
PS1	196 986
PS2	274 686
PS3	297 760
PS4	242 741

Figure 8-26. Simulated values lay in the ranges of the theoretical reference for PS moldings

By comparing the values listed in Table 8-4, it can be observed that the shear rate and related viscosities are not only sensitive to the geometry of the runner cross section, but also to the IR. For PS molding simulations, the highest high shear rate with the lowest viscosity were generated by using the narrow runner and by applying the fastest IR, while the lowest high shear rate with the relatively higher viscosity is exhibited when using the wide runner and by applying the lowest IR. Furthermore, by increasing the aspect ratio of the runner cross-section, or by increasing the IR, the maximum high shear rate was increased (resulting in a corresponding reduction in viscosity).

The simulations of the temperature distributions in the cavities were also reasonable. Figures 8-27 to 8-29 show the temperature distributions in the dominant planes. Similar to the iPP results, the higher temperatures were found at the two sides in the cavities for single-cavity moldings, while for the split-cavity molding, the

higher temperatures were found in the outer two cavities. The simulated temperature differences from the high shear region and the low shear region range between 4°C to 20°C. The largest temperature differences exist in the simulations using the narrow runner, and applying 90% IR. (Figure 8-27 (d), Figure 8-28 (d) and Figure 8-29 (d))

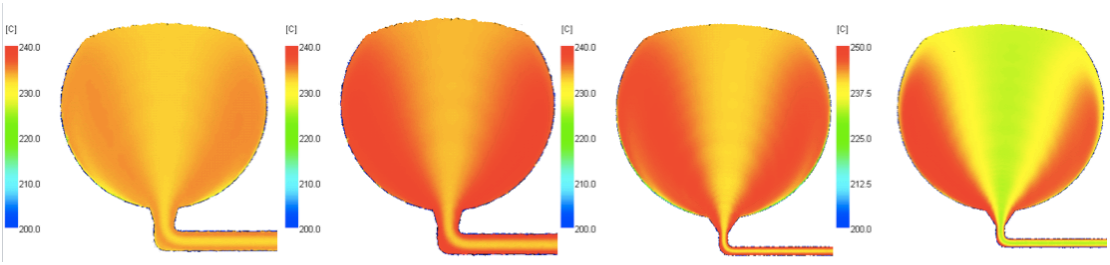

(a) (b) (c) (d)

Figure 8-27. Temperature distributions in circular cavity fillings for PS molding simulations: (a) wide runner / 50% IR, (b) wide runner / 90% IR, (c) narrow runner / 50% IR, (d) narrow runner / 90% IR

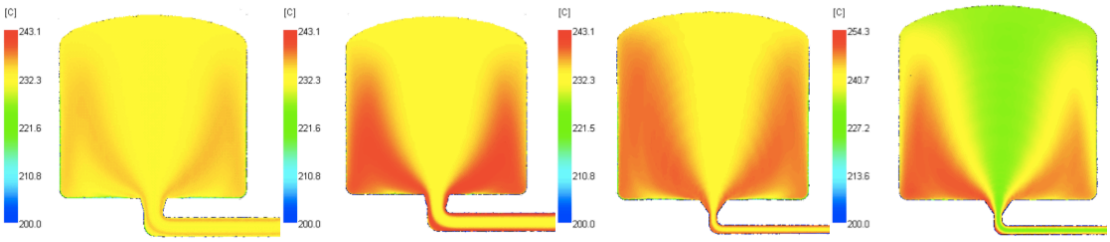

(a) (b) (c) (d)

Figure 8-28. Temperature distributions in rectangular cavity fillings for PS molding simulations: (a) wide runner / 50% IR, (b) wide runner / 90% IR, (c) narrow runner / 50% IR, (d) narrow runner / 90% IR

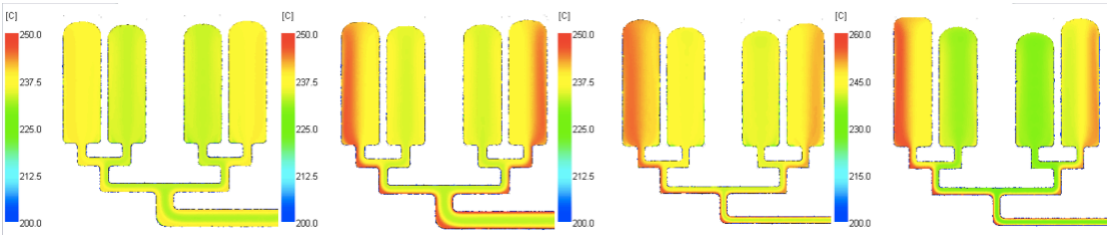

(a) (b) (c) (d)

Figure 8-29. Temperature distributions in split-cavity fillings for PS molding simulations: (a) wide runner / 50% IR, (b) wide runner / 90% IR, (c) narrow runner / 50% IR, (d) narrow runner / 90% IR

By comparing Figures 8-27 and 8-29 again, using simulations with the narrow runner and applying the fast IR, the high temperature zone was much more obvious in the high shear flow regions in the runner tunnel and in the cavities, which were the two sides in single cavities or outer two cavities for the split-cavity. As mentioned before, by using the narrow runner system and applying a faster IR, the melt with high shear rate and high temperature can be better separated from that with the low shear rate flow and low temperature. These results also agree well with the shear imbalance theory.

8.2 Simulations for Traditional Injection Moldings

8.2.1 Single-Cavity Molding Simulations

According to the previous investigations, iPP, PP co, POM, N66 and N66_50 were the materials used in the single-cavity injection molding experiments. The mesh sizes (number of elements) for different materials are listed in Table 8-5 and they are all above 5.4 million.

Table 8-5. Simulation mesh sizes for using different materials and different injection rates in disc single-cavity moldings

Material	Injection Rate (cm3/sec)	MRT Usage	Mesh Size
PP ho	32.31	No	5 408 207
PP co	32.31	No	5 408 207
PP co	32.31	Yes	5 596 699
POM	32.31	No	5 408 207
N66	57.02 (fast)	No	5 408 207
N66	9.5 (slow)	No	5 408 207
N66_50	57.02	No	5 408 207
N66_50	57.02	Yes	5 596 699

Figure 8-30 shows the simulated iPP cavity filling results in the disc cavity. Compared with the assumptions in Figure 2-17 and Figure 4-1, it is obvious that the melt flow at the cavity edge regions appear to traveling faster than the melt flow at the cavity center.

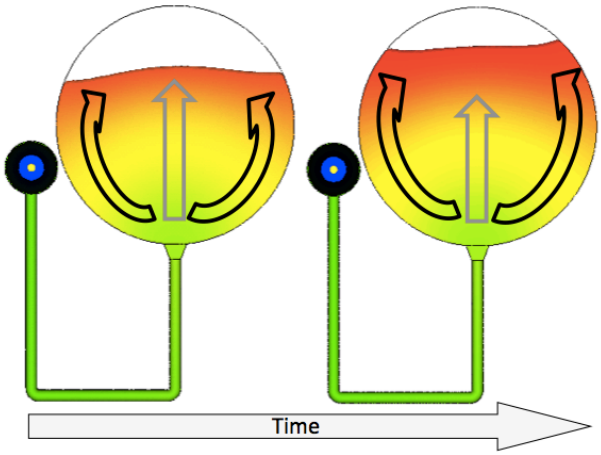

Figure 8-30. Cavity filling patterns of iPP molding simulation by using the disc single-cavity

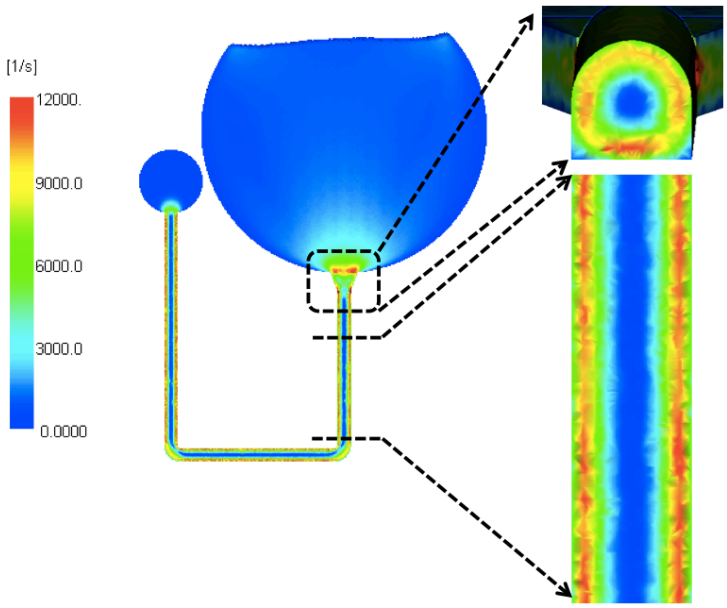

Figure 8-31. Shear rate distributions in the runner tunnel by using the insert plate with the disc cavity

Figure 8-31 shows the shear rate distribution in the runner system. For iPP, the highest shear rate value was about 11387 s^{-1} with the corresponding viscosity of about 14.18 Pa•s. Compared with the theoretical values shown, Figure 8-32, these values are within the reasonable range in the plot.

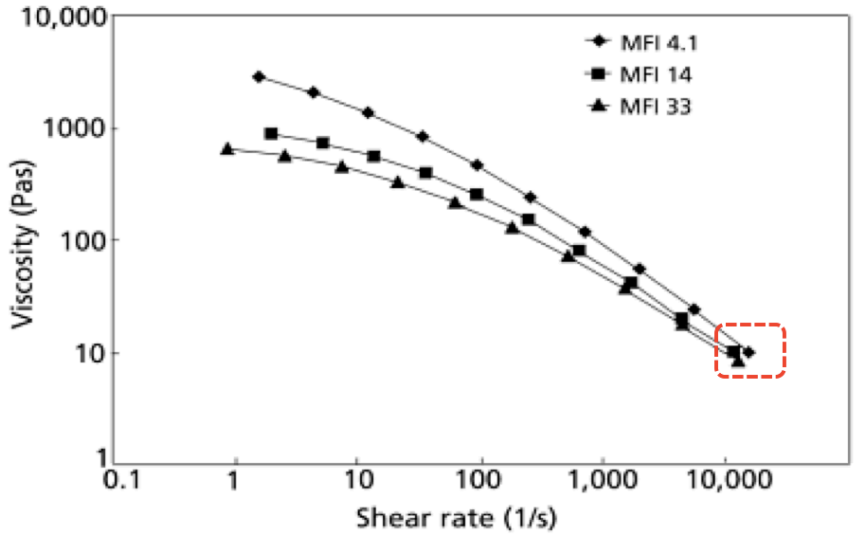

Figure 8-32. Simulated values lay in the ranges of the theoretical reference for iPP moldings in the disc-cavity

Figure 8-33 shows the temperature distribution on the dominant planes. It was found that the higher temperatures were at the two sides in the disc cavity, and the temperature difference from the high shear region to that of the low shear region is about 20°C.

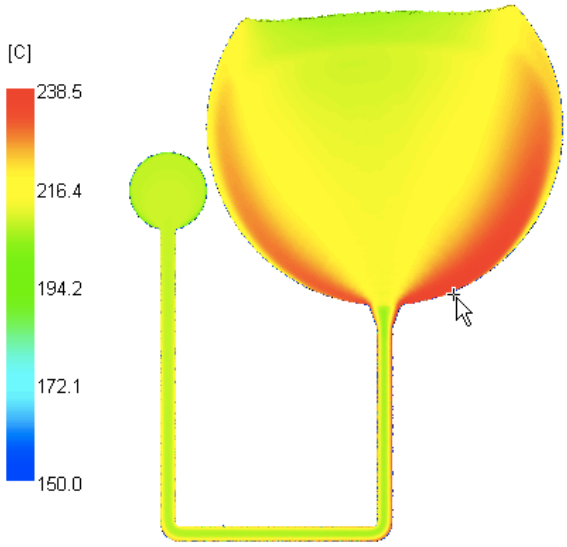

Figure 8-33. Temperature distributions in disc cavity fillings for iPP molding simulations

For simulation study for POM in the disc-cavity fillings, similar cavity filling results were generated. (Figure 8-34)

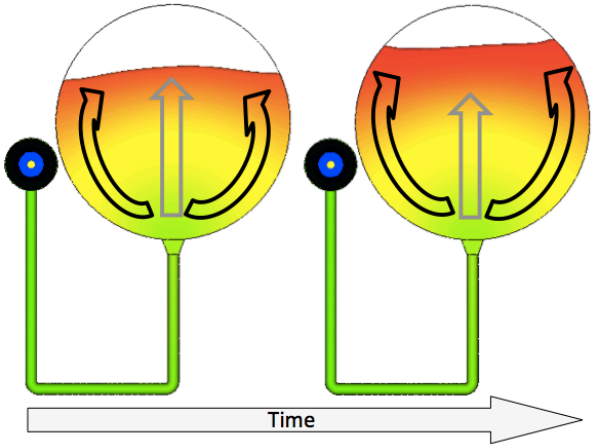

Figure 8-34. Cavity filling patterns of POM molding simulation by using the disc single-cavity

The highest shear rate value in the runner was about 5323 s^{-1} with a corresponding viscosity of about 85.84 Pa•s. Compared with the theoretical values shown in Figure 8-35, these values lay within the reasonable range.

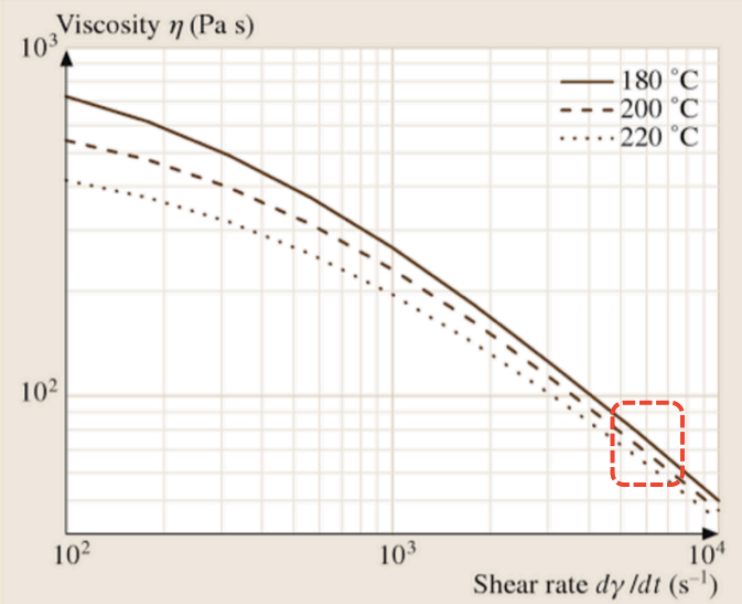

Figure 8-35. Simulated values lay in the ranges of the theoretical reference for POM moldings

Figure 8-36 shows the temperature distributions on the dominant planes for POM. It was found that the higher temperatures were at the two sides in the disc cavity again, and the temperature difference between the high shear region to that of the low shear region is about 30°C.

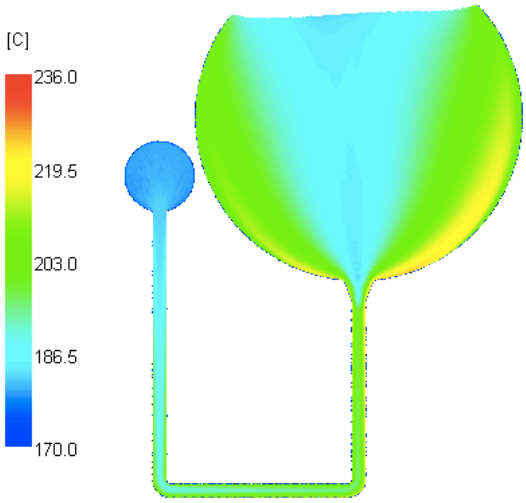

Figure 8-36. Temperature distributions in disc cavity fillings for POM molding simulations

N66 was molded into the disc-cavity by applying two injection rates (Table 8-5). Figure 8-37 shows the simulated N66 cavity filling results in the disc-cavity by applying different IR.

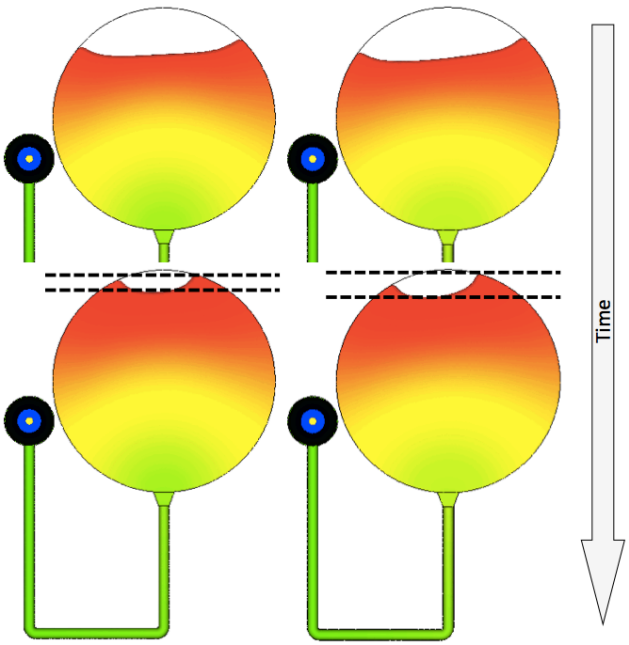

(a) (b)

Figure 8-37. Simulated N66 cavity fillings in the disc-cavity by applying (a) slow IR and (b) fast IR

The simulated results confirm the assumptions shown previously in Figures 2-17 and 4-1. Shear imbalance is obvious in all the molding conditions. The high shear rate melt fills the edge section of the disc cavity faster than the low shear rate melt fills the center region, and formation of a gas trap or a weld line became possible in the final product. (Figure 8-38)

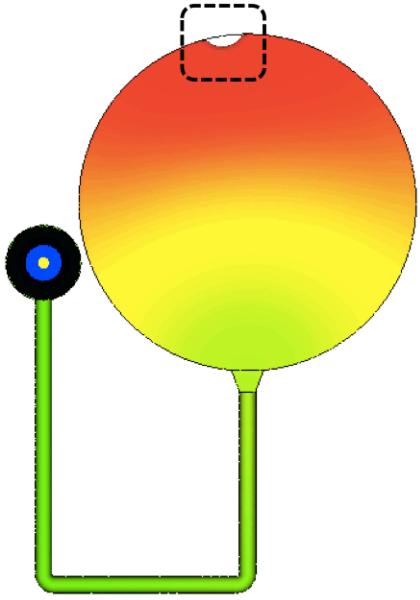

Figure 8-38. Final point during the disc-cavity filling of N66 moldings

It can also be observed that by applying the fast IR, the shear imbalances are more prominent. This agrees well with some of the previous assumptions.

The highest shear rate values and the related viscosities in the runner for N66 molding at different IR are provided in Table 8-6. Compared with the theoretical values in Figure 8-39, these values roughly lay in the reasonable ranges of the plot.

Table 8-6. Comparison of the highest shear rates and the related viscosities by applying different IR for N66 moldings in the disc-cavity

Injection Rate	High S.R. (1/s)	Viscosity (Pa•s)
slow	2731	80.68
fast	13750	21.44

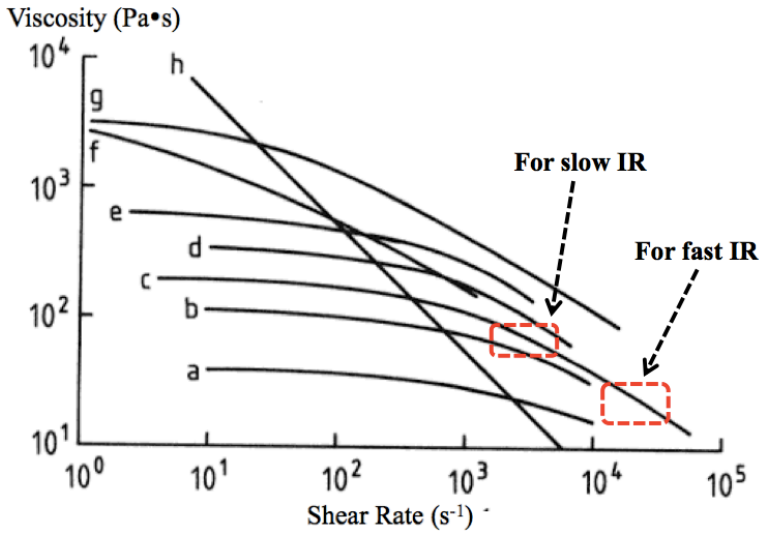

Figure 8-39. Simulated values lay in the ranges of the theoretical reference for N66 moldings in the disc-cavity, N66 (c)

The simulation result showing the temperature distribution in cavities is shown in Figure 8-40. Higher temperatures are observed at the two sides in the cavities. The simulated temperature differences from the high shear region and the low shear region are about 16°C and 56°C for using the slow and fast IR respectively.

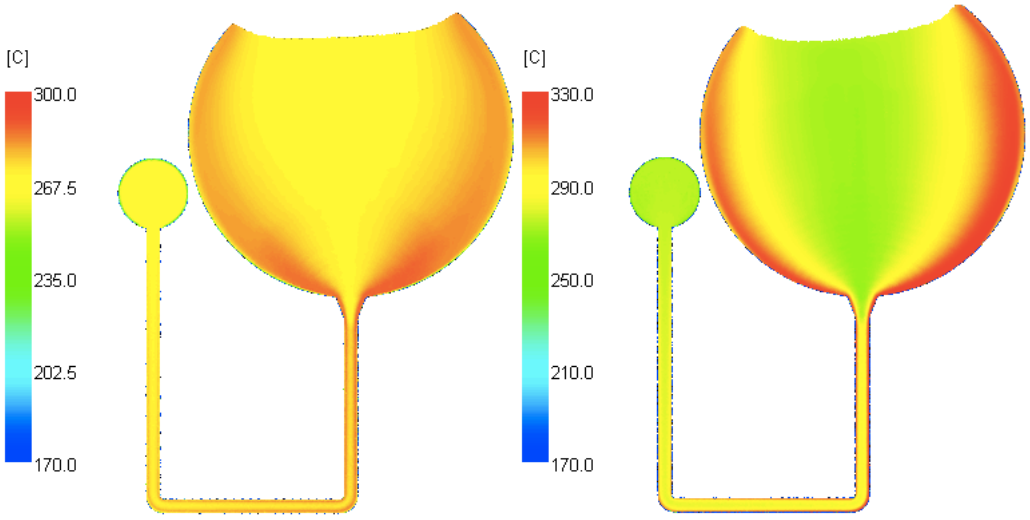

(a) (b)

Figure 8-40. Temperature distributions in disc cavity fillings for N66 molding simulations: (a) slow IR and (b) fast IR

For the simulations in applying the fast IR, the high temperature zone was more obvious in the high shear flow regions at the two sides in the disc-cavity.

PP co and N66_50 were injection molded by using MRT. The simulations between the molding results of using and not using MTR were investigated. Figure 8-41 shows the simulated PP co cavity filling results in the disc cavity. Compared to the previous assumptions and the sample in Figure 2-19, it is obvious that the melt flow at the cavity center is ahead of the melt flow at the cavity edge regions as a result of applying MRT.

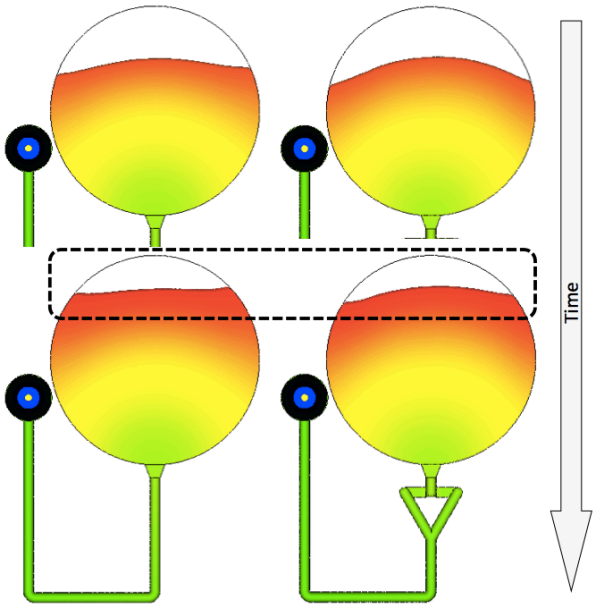

Figure 8-41. Cavity filling patterns of PP co molding simulation by using the disc single-cavity: (a) molding with no MRT, (b) molding with MRT

The shear rate distributions in the flow before and after the melt rotation device should be the same, however the viscosity and the temperature distributions may be influenced by applying MRT. Figure 8-42 and Figure 8-43 provide the viscosity

distribution and the temperature distribution in the runner system before and after the melt rotation device.

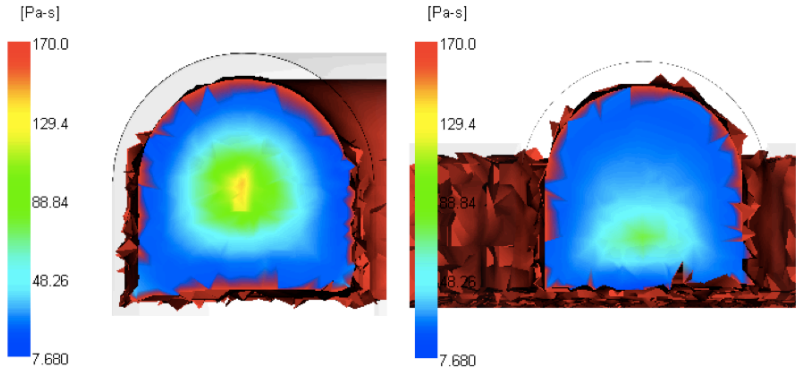

(a) (b)

Figure 8-42. Simulated viscosity distribution (a) before and (b) after the melt rotation device for PP co moldings in the disc-cavity

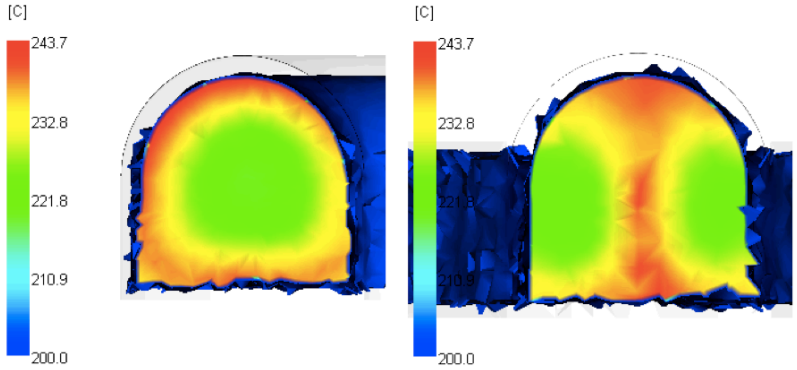

(a) (b)

Figure 8-43. Simulated temperature distribution (a) before and (b) after the melt rotation device for PP co moldings in the disc-cavity

By observing Figures 8-42 and 8-43, it is clear that the viscosity is evenly distributed after using the melt rotation device. The high temperature zone was "rotated" in the center of the runner tunnel from the edge areas by MRT. As a result, the melt flow with the higher temperature flows to the sides of the disc-cavity and the

melt flow with lower temperature flows into the center area, thus changing of the temperature distribution in the disc-cavity. (Figure 8-44)

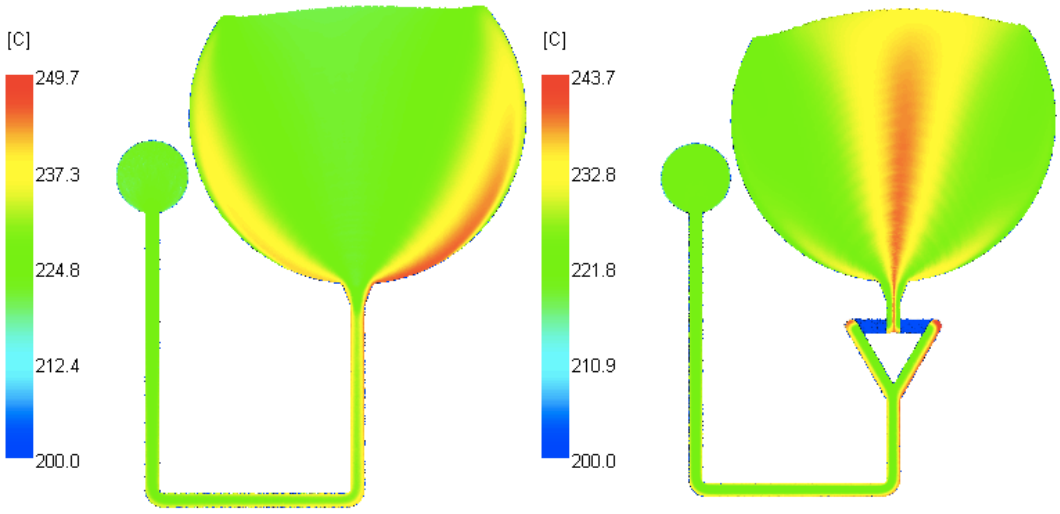

(a) (b)

Figure 8-44. Temperature distributions in disc cavity fillings for PP co molding simulations: (a) not applying MRT, (b) applying MRT

It is apparent that the higher temperatures are found at the two sides in the disc-cavity, but by applying MRT, the higher temperatures are observed at the center area of the cavity.

The investigation for N66_50 shows similar results to PP co simulations. By applying MRT, the flow front pattern in the disc-cavity changed again (Figure 8-45), meanwhile the viscosity and the temperature distributions were also modified (Figure 8-46 and Figure 8-47) after applying the melt rotation device, resulting in a changed temperature distribution. (Figure 8-48)

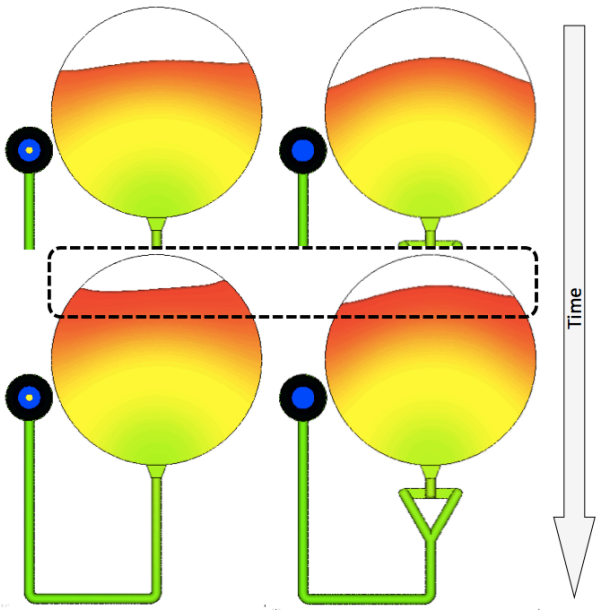

(a) (b)

Figure 8-45. Cavity filling patterns of N66_50 molding simulation by using the disc single-cavity: (a) molding with no MRT, (b) molding with MRT

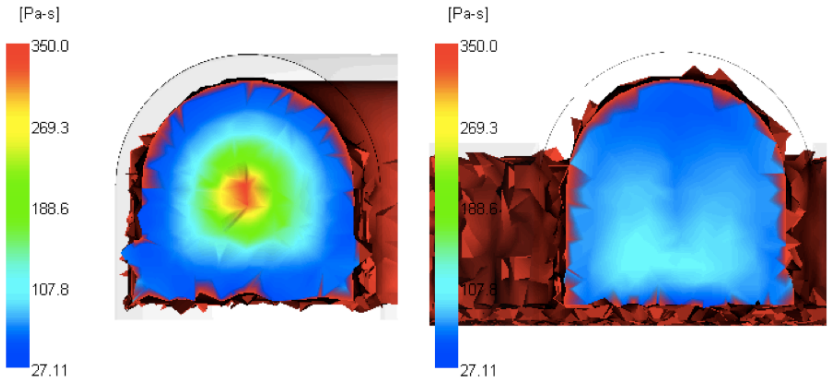

(a) (b)

Figure 8-46. Simulated viscosity distribution (a) before and (b) after the melt rotation device for N66_50 moldings in the disc-cavity

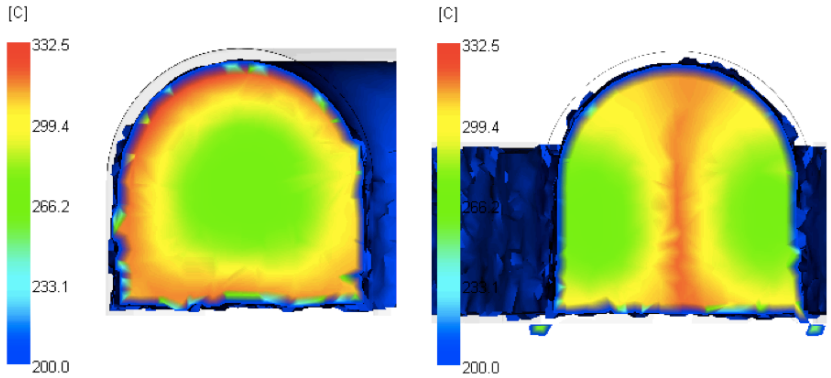

(a) (b)

Figure 8-47. Simulated temperature distribution (a) before and (b) after the melt rotation device for N66_50 moldings in the disc-cavity

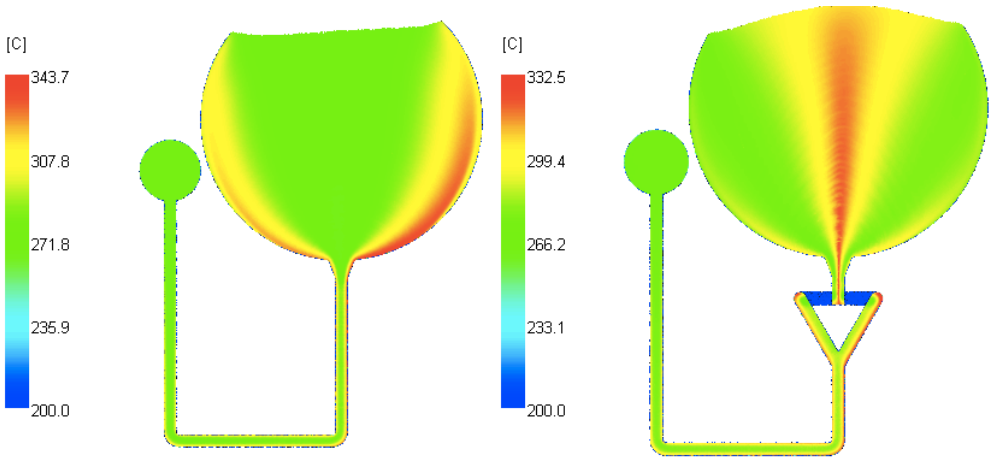

(a) (b)

Figure 8-48. Temperature distributions in disc cavity fillings for N66_50 molding simulations: (a) not applying MRT, (b) applying MRT

These simulation results confirm the shear imbalance theory, and proved that the melt rotation device has the ability to modify the viscosity and temperature distribution during injection molding.

8.2.2 Multi-Cavity Molding Simulations

8.2.2.1 Tensile Bar Simulations

iPP and PP co were the materials used for molding the tensile test samples. The mesh sizes (number of elements) for simulating these molding processes are listed in Table 8-7.

Table 8-7. Simulation mesh sizes for using different materials in multi-cavity moldings for producing tensile bars

Material	Mesh Size
PP ho / iPP	1 283 396
PP co	1 283 396

The simulation results in molding iPP and PP co samples are provided in Figure 8-49. It is apparent that the shear resulted imbalance in cavity fillings occurs in both the iPP and PP co simulations. The outer cavities, (A1) (A2) (A3) (A4), filled faster than the inner cavities, (B1) (B2) (B3) (B4).

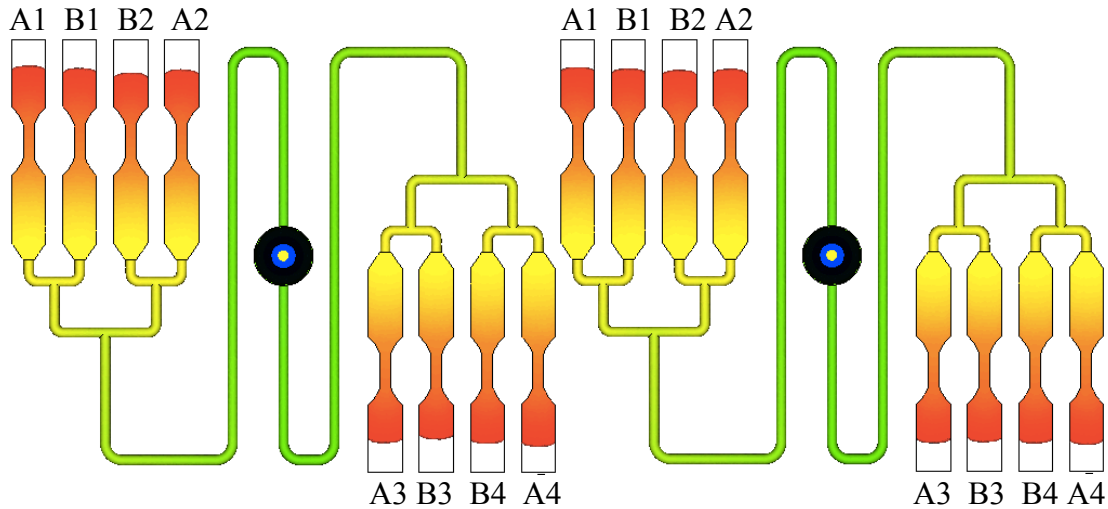

(a) (b)

Figure 8-49. Simulated cavity filling patterns of molding (a) iPP tensile bars and (b) PP co tensile bars

For the tensile bar molding and the U-shape molding, the shear rate distribution in the runner was similar to that for the disc-cavity molding, as the shapes of the runner cross sections were similar. The highest shear rate values are provided in Table 8-8. Compared to the theoretical values plotted in Figure 8-50 and 8-51, these values lay in the reasonable ranges in the plots.

Table 8-8. Highest shear rates and the related viscosities for iPP and PP co tensile bar moldings

Material	High S.R. (1/s)	Viscosity (Pa•s)
iPP	4762	34.13
PP co	4932	29.72

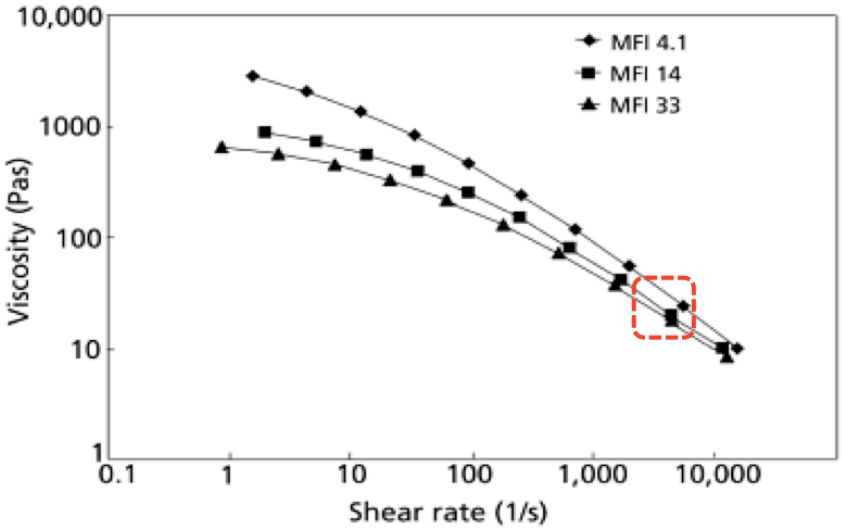

Figure 8-50. Simulated values lay in the range of the theoretical reference for iPP tensile bar moldings

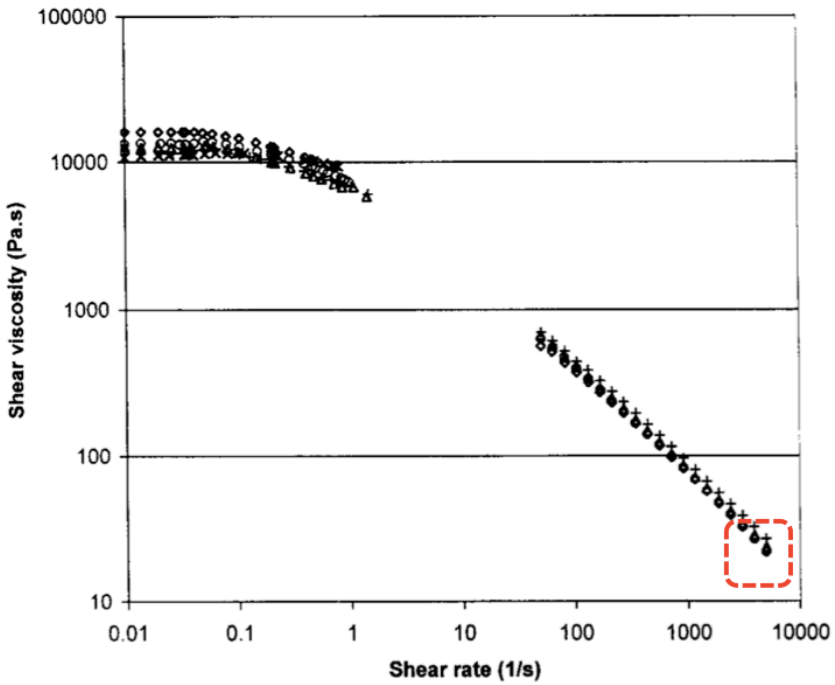

Figure 8-51. Simulated values lay in the range of the theoretical reference for PP co tensile bar moldings

Figure 8-52 shows the temperature distributions in the tensile bar cavities. For both these materials, the higher temperatures were found in the outer cavities.

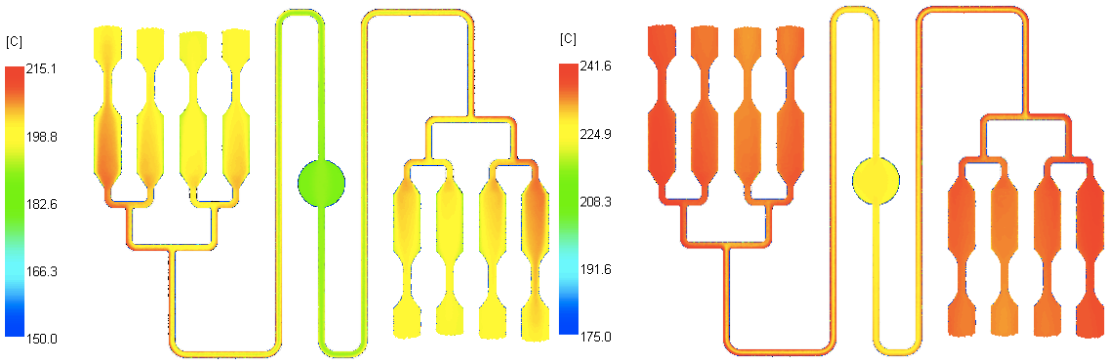

(a) (b)

Figure 8-52. Temperature distributions in tensile bar cavity fillings for (a) iPP and (b) PP co molding simulations

PP co showed less serious shear imbalance in cavity filling. This is indicated in Figure 8-49. This is also less difference in temperature simulations, compared to the

temperature difference for iPP simulation, as the temperature scales were set to the similar range of about 65°C. It is possible that PP co was less sensitive to the shear rate variation. This may explain why, the yield stress of PP co tensile bars, filled with the high shear flow, didn't show a significant difference to the yield stress of PP co tensile bars filled with the low shear flow. (Figure 7-28)

8.2.2.2 U-Shape Sample Simulations

The materials used for producing the U-shape samples were iPP, PBT and N66. These were injection molded using three processing conditions. In the simulations, the mesh sizes for different molding conditions are provided in Table 8-9. The mesh sizes (number of elements) were all over 5.1 million.

Table 8-9. Simulation mesh sizes for using different materials in the U-shape multi-cavity moldings with different molding conditions

Molding Condition	Material & Mesh Size		
	iPP	PBT	N66
1) Fast no MRT	5 150 909	5 150 909	5 150 909
2) Slow no MRT	5 150 909	5 150 909	5 150 909
3) Fast MRT	5 365 183	5 365 183	5 365 183

The simulated cavity filling processes by using iPP in different molding conditions are provided in Figure 8-53. For molding condition (1), the cavity filling imbalance is apparent. Similar to the assumptions and patterns mentioned in Figures 2-14 to 2-16, and Figure 7-4, the high shear rate flow filled the related cavities, (A1) (B1) (C1) (D1), faster than it did the other cavities. However, by reducing the IR in molding condition (2) or by applying MRT in molding condition (3), the cavity filling imbalance problem is solved. Evenly distributed cavity filling results were generated.

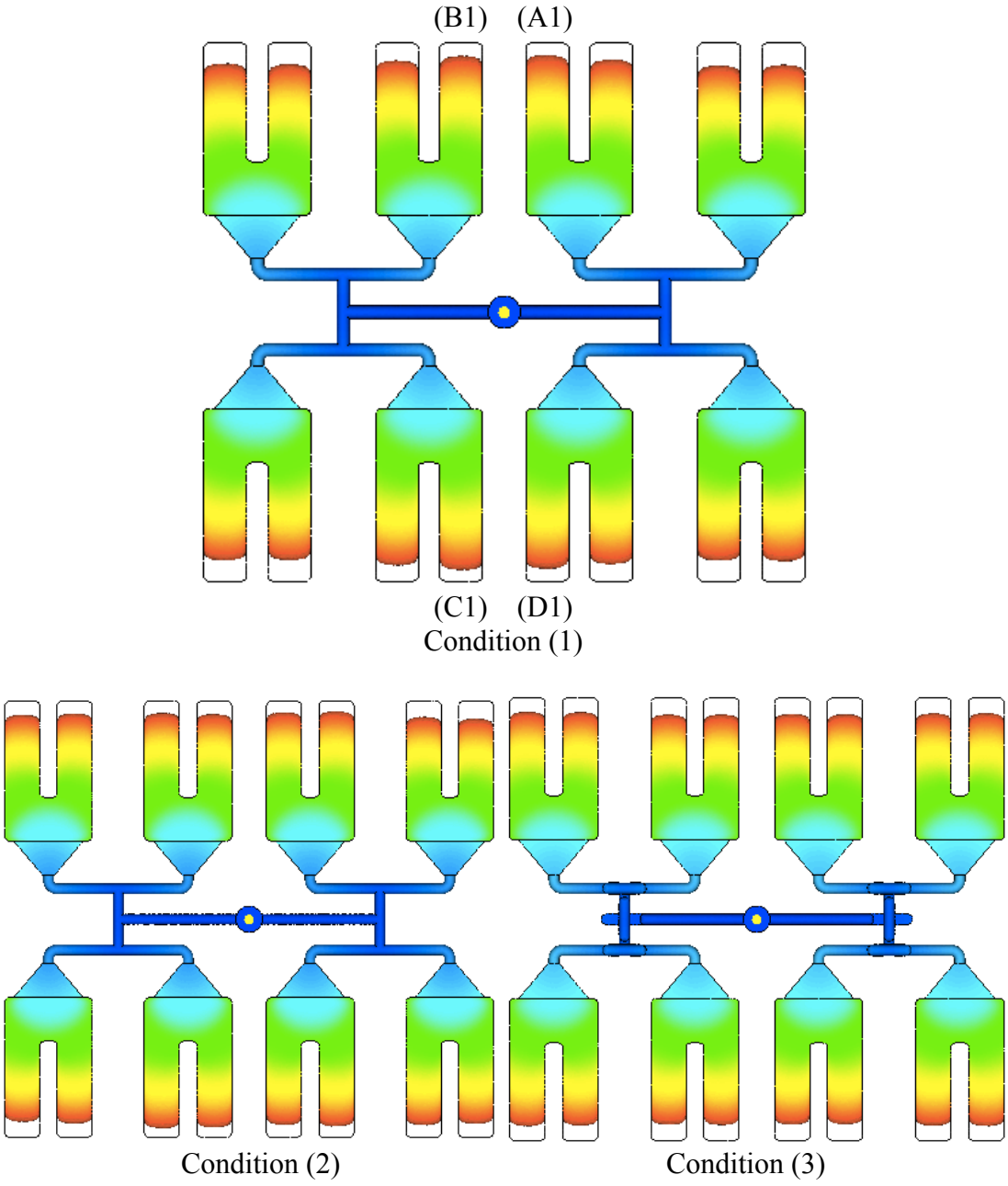

Figure 8-53. Simulations of the U-shape cavity filling patterns by using iPP in the three molding conditions

Table 8-10. Comparison of the highest shear rates and the related viscosities during iPP U-shape cavity moldings

Molding Condition	High S.R. (1/s)	Viscosity (Pa•s)
1) Fast no MRT	14751	19.57
2) Slow no MRT	2014	94.25

From Table 8-10, it is clear that the highest shear rate value in the runner tunnel is reduced by applying a slow IR. All the simulated values lay in the reasonable ranges in the plot (Figure 8-54). For molding condition (2), as the IR was reduced, the high shear rate value or the shear rate difference in the runner was reduced simultaneously, resulting in improved viscosity distributions in the runner, and a more even temperature distributions in the cavities. (Figure 8-58)

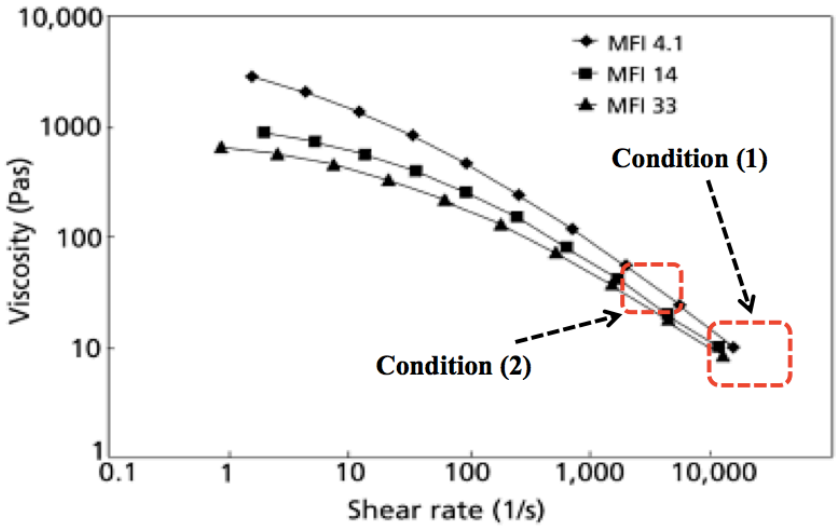

Figure 8-54. Simulated values lay in the ranges of the theoretical reference for iPP U-shape cavity moldings

The viscosity and temperature distribution in the runner before and after applying the melt rotation device are shown in Figures 8-55 and 8-57. Although, the viscosity distributions didn't show obvious variations in color by applying MRT, in Figure 8-55, the sampled values of viscosity show variations in Figure 8-56.

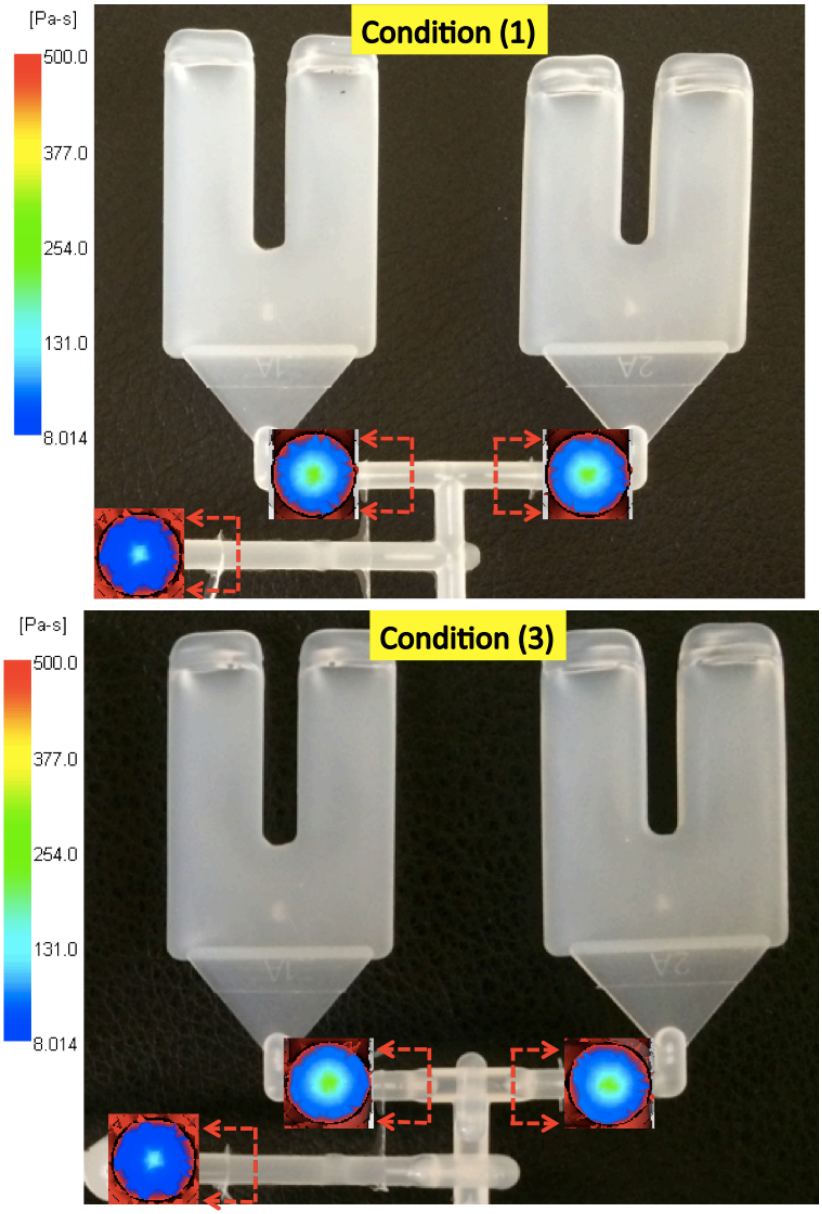

Figure 8-55. Simulated viscosity distributions for the iPP U-shape cavity molding in different conditions

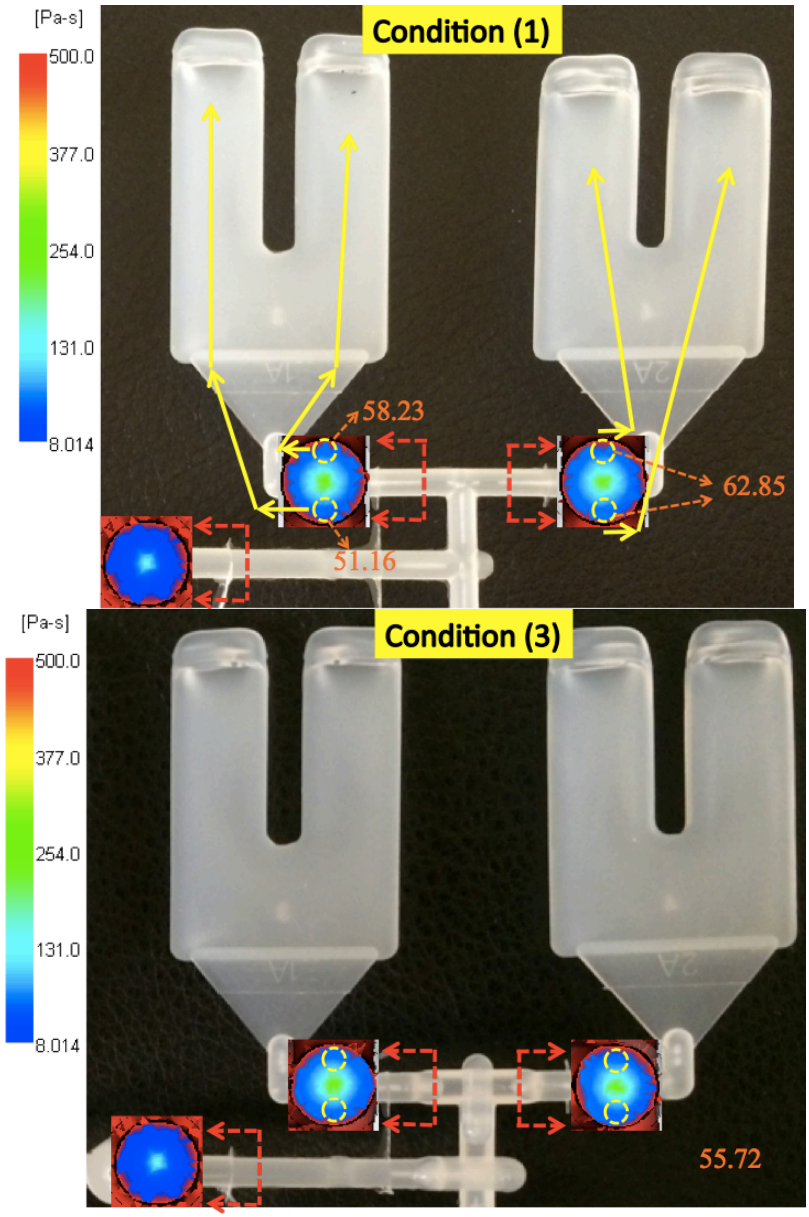

Figure 8-56. Simulated viscosity distributions for the iPP U-shape cavity molding in different conditions, with sampled values

The viscosity values were sampled in the yellow circled areas in Figure 8-56. For the molding condition (1), the viscosity was about 51.16 Pa•s in the left lower circle, and the value was about 58.23 Pa•s in the left upper circle. The melt flow with the low viscosity followed the yellow path and filled the related side in cavity, while the flow with the viscosity of 58.23 Pa•s filled the other side of the cavity, leading to

the imbalanced filling result. In the other tertiary runner branch, the viscosity in the two circled areas were all about 62.85 Pa•s. As a result, the related cavity was less filled. For Condition (3), the values sampled from the same areas were all about 55.72 Pa•s after applying MRT, resulting in more balanced cavity fillings.

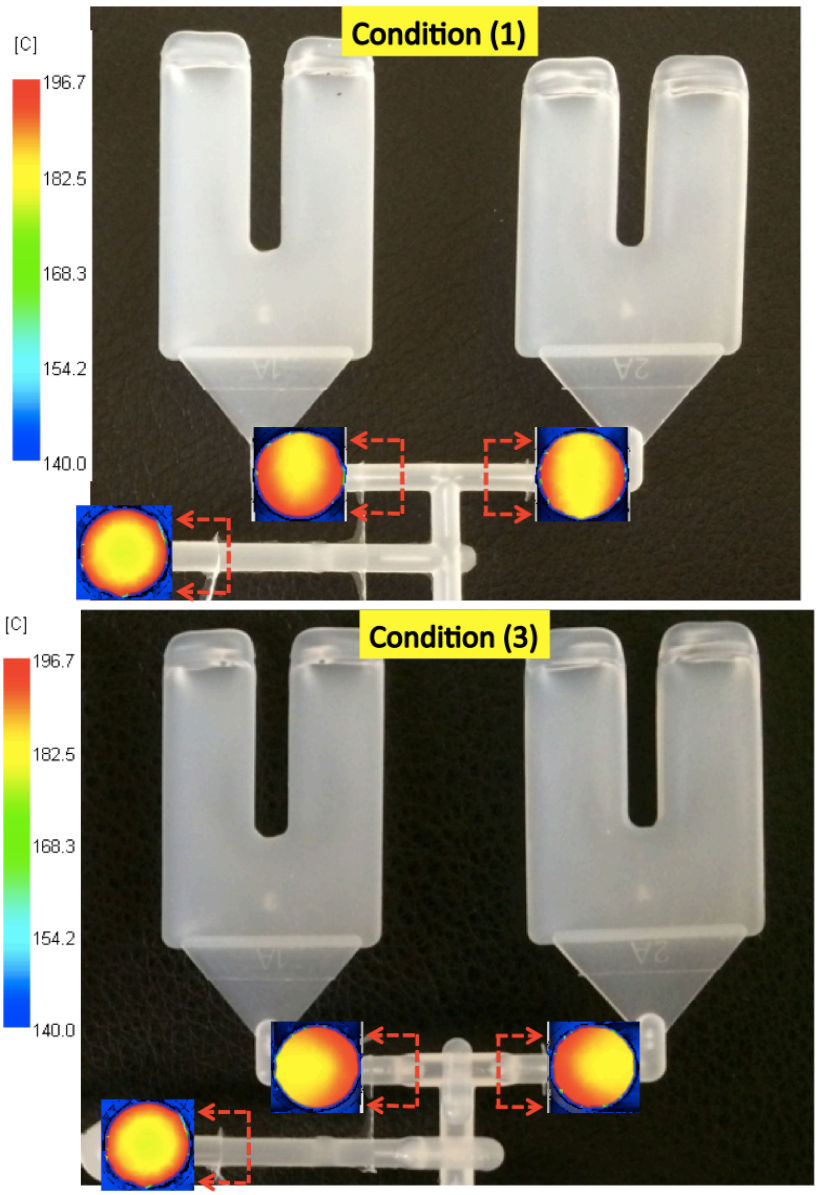

Figure 8-57. Simulated temperature distributions for the U-shape cavity molding in different conditions

The temperature distribution was "rotated" by 90° after applying MRT, compared with the temperature distributions in the runner without MRT. As a result, the temperature distributions in cavities were different for different molding conditions. (Figure 8-58)

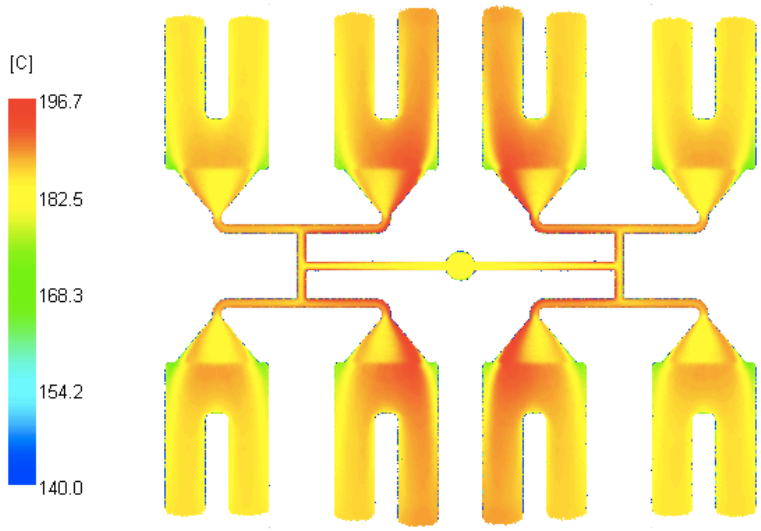

Condition (1)

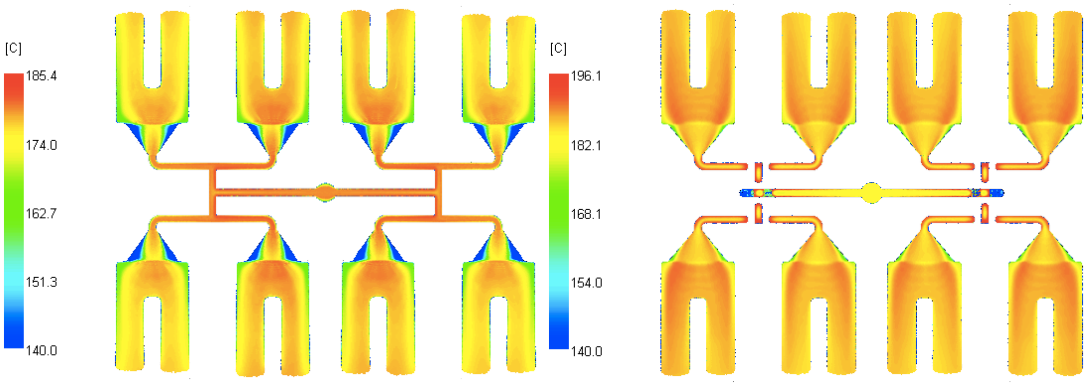

Condition (2) Condition (3)

Figure 8-58. Temperature distributions in iPP U-shape cavity fillings in different molding conditions

From Figure 8-58, an improved temperature distribution was generated either by applying the lower IR, or by using MRT. Similar simulation results were generated in molding PBT and N66. (Figure 8-59 and Figure 8-60)

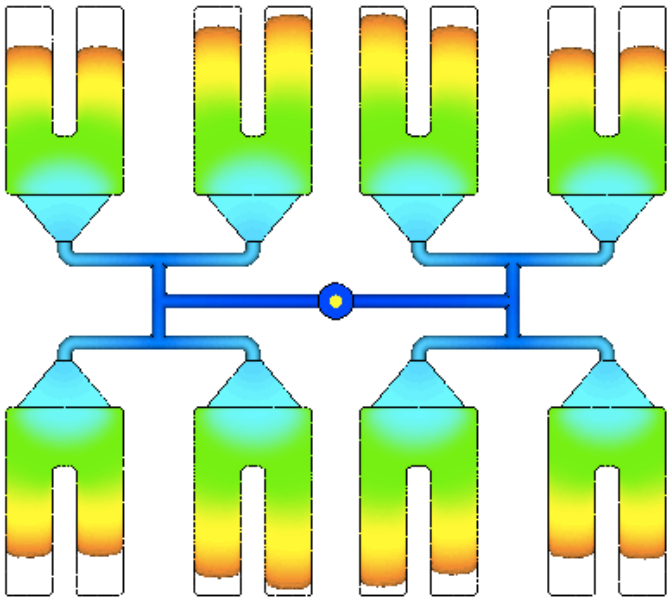

Condition (1)

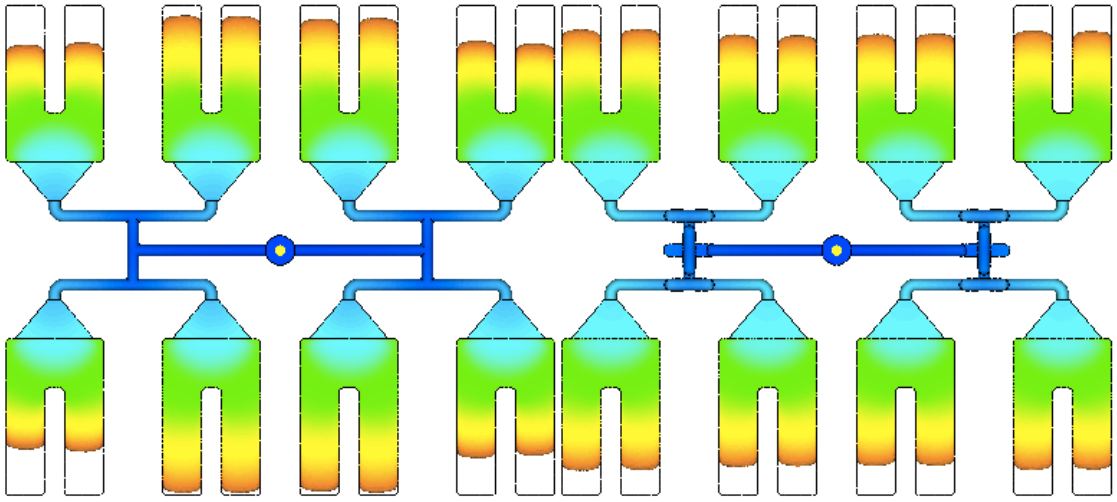

Condition (2) Condition (3)

Figure 8-59. Simulations of the U-shape cavity filling patterns by using PBT in the three molding conditions

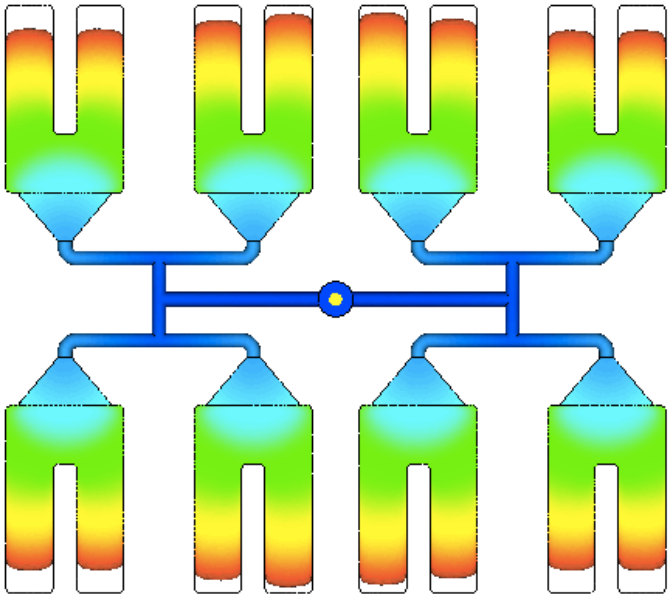

Condition (1)

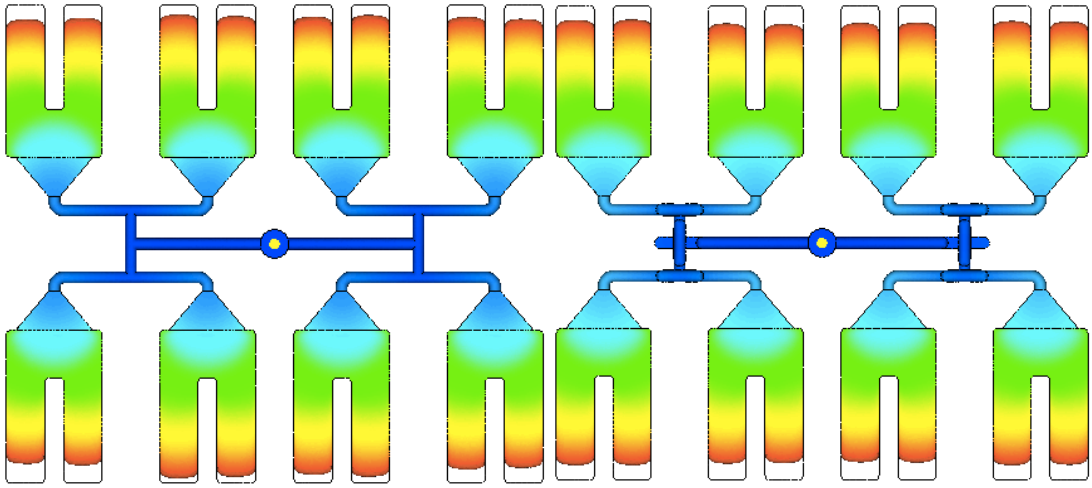

Condition (2) Condition (3)

Figure 8-60. Simulations of the U-shape cavity filling patterns by using N66 in the three molding conditions

In Figures 8-61 and 8-62, variations of the viscosity distribution in the runner before and after the melt rotation device were observed. Following the rotation illustrated in Figure 8-57, the viscosity distribution appears to be "rotated" by 90° after applying MRT, especially in molding PBT. PBT and N66 may have viscosity distributions that are much more sensitive to the temperature distributions in the

runner. The sampled values from similar areas are provided in Figures 8-63 and 8-64 for PBT and N66 respectively. It is obvious that for both PBT and N66, the viscosity is more evenly distributed in the tertiary runners by applying MRT.

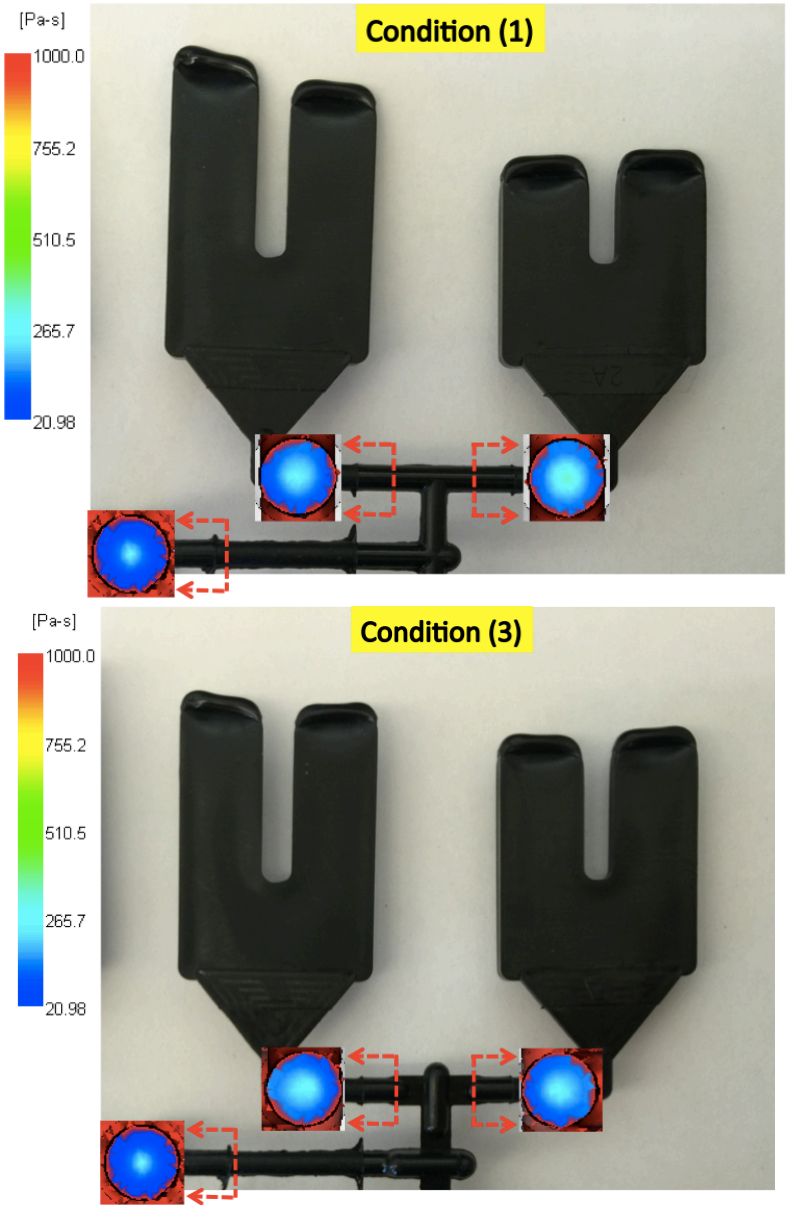

Figure 8-61. Simulated viscosity distributions for the PBT U-shape cavity molding in different conditions

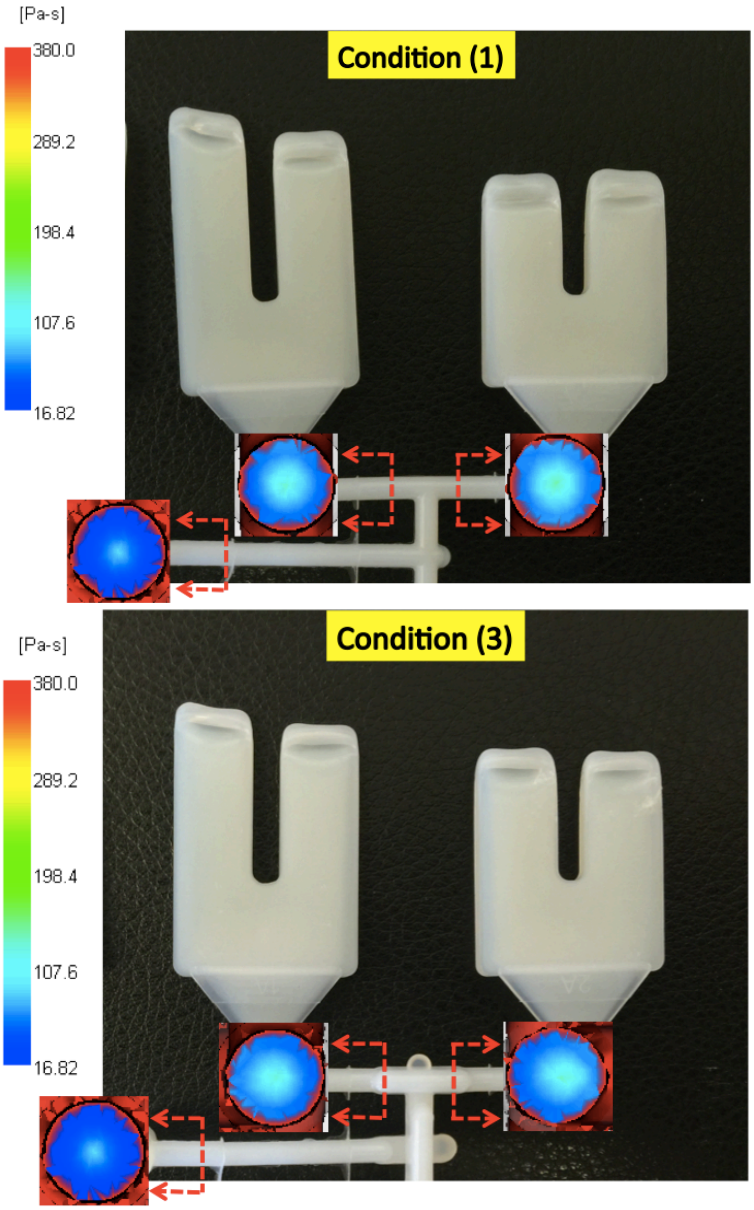

Figure 8-62. Simulated viscosity distributions for the N66 U-shape cavity molding in different conditions

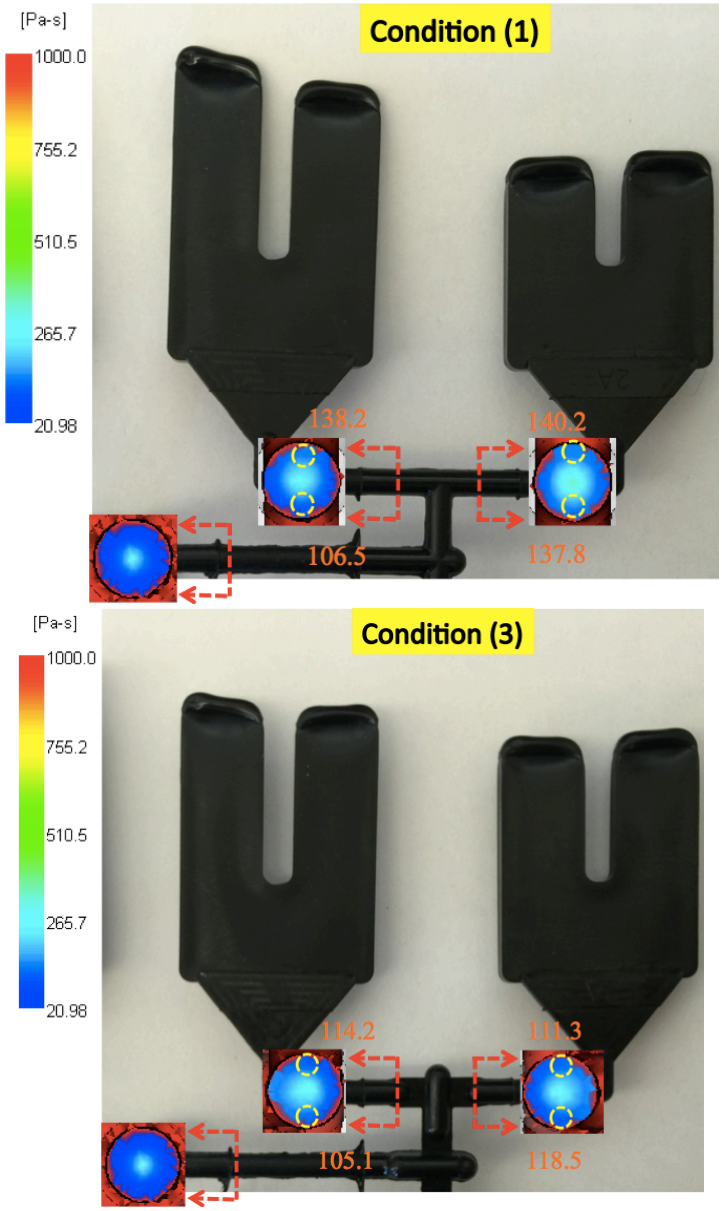

Figure 8-63. Simulated viscosity distributions for the PBT U-shape cavity molding in different conditions, with sampled values

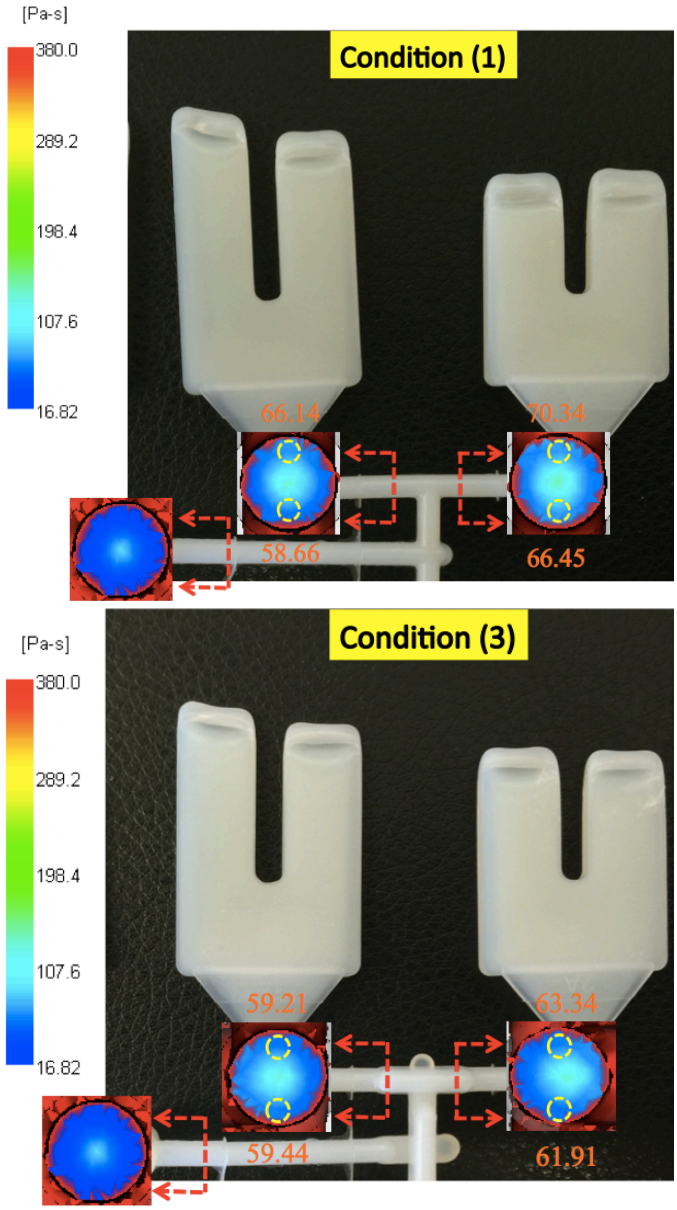

Figure 8-64. Simulated viscosity distributions for the N66 U-shape cavity molding in different conditions, with sampled values

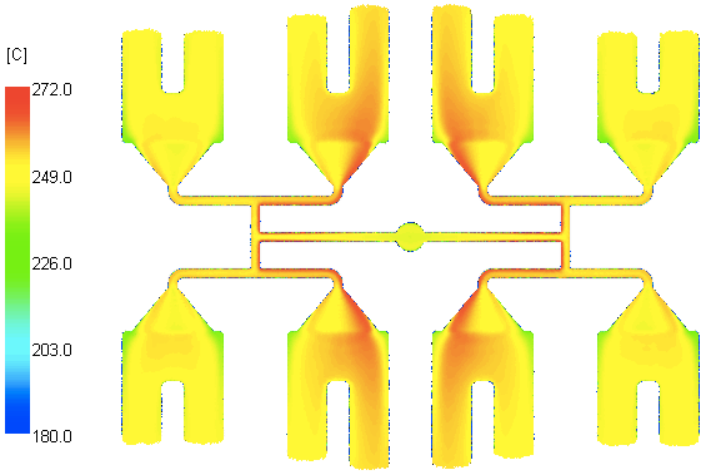

Condition (1)

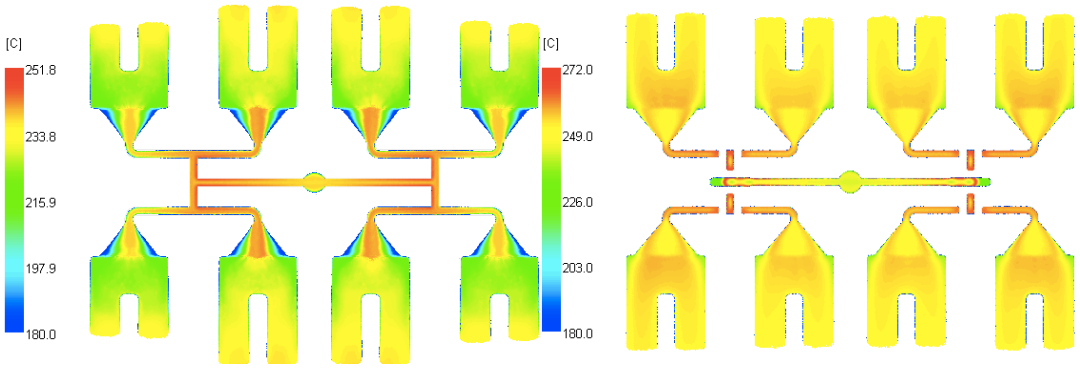

Condition (2) Condition (3)

Figure 8-65. Temperature distributions in PBT U-shape cavity fillings in different molding conditions

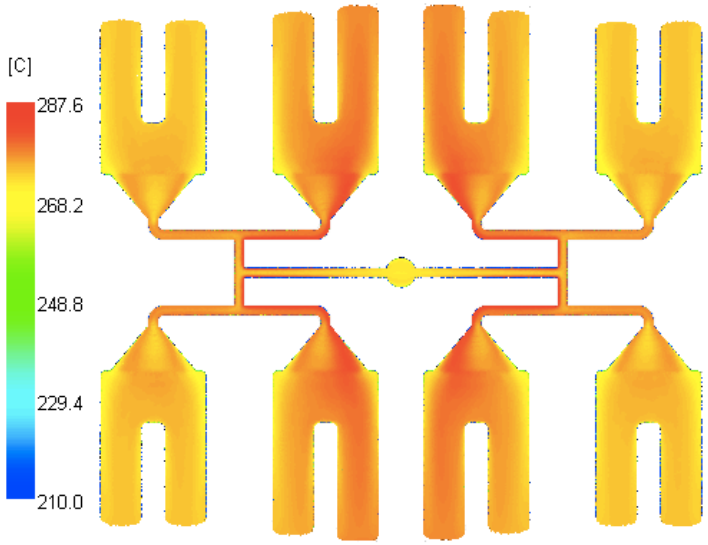

Condition (1)

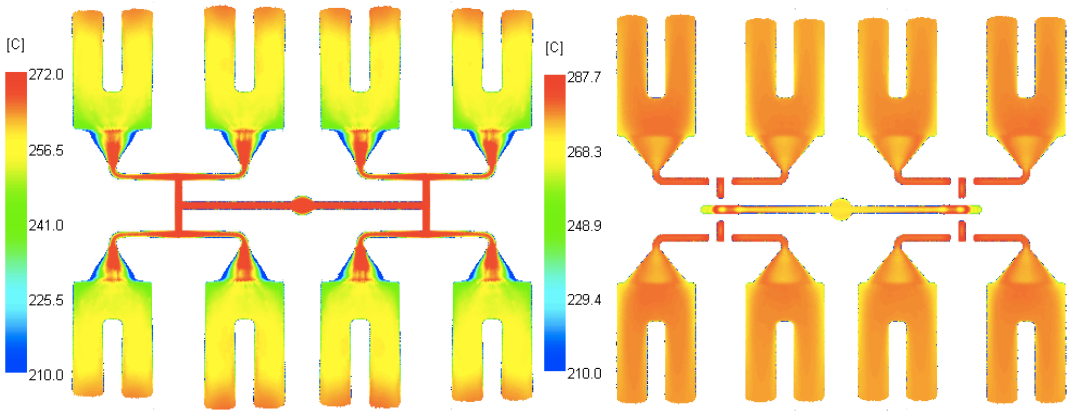

Condition (2) Condition (3)

Figure 8-66. Temperature distributions in N66 U-shape cavity fillings in different molding conditions

The resultant temperature distributions in cavities are shown in Figures 8-65 and 8-66. From the simulated results, it is apparent that PBT and N66 are more sensitive to shear variations. This is in line with assumptions made in Chapter 3.

The highest shear rate values and corresponding viscosities in the runner under different molding conditions are provided in Table 8-11. Compared with the theoretical values plotted in Figure 8-67, these values lay in the reasonable range.

Table 8-11. Comparison of the highest shear rates and the related viscosities during PBT and N66 U-shape cavity moldings

Molding Condition	PBT		N66	
	High S.R. (1/s)	Viscosity (Pa•s)	High S.R. (1/s)	Viscosity (Pa•s)
1) Fast no MRT	13084	48.29	13374	22.33
2) Slow no MRT	2294	163.9	2281	76.75

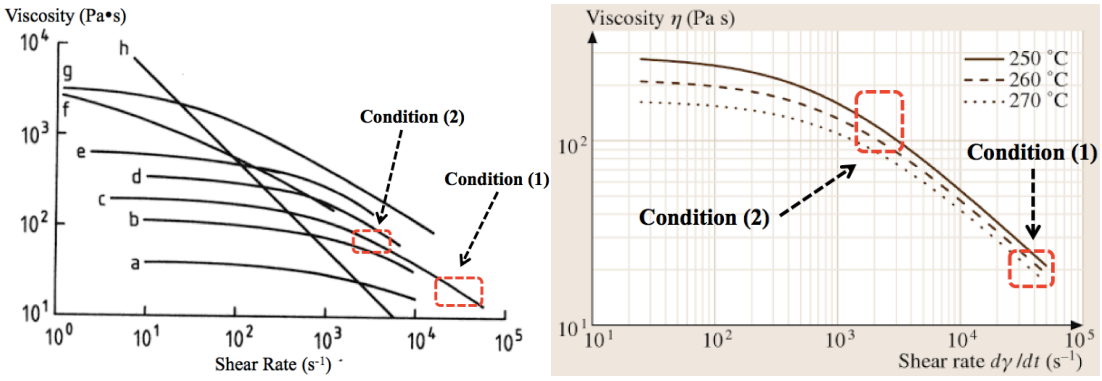

(a) (b)

Figure 8-67. Simulated values lay in the ranges of the theoretical reference for U-shape cavity moldings by using (a) PBT and (b) N66

8.3 Shear Duration Influence on Temperature Distribution

The temperature distribution was also explored in the simulation study, and is presented in this section. Since the shear rate distribution in the runner and in the cavity was only determined by injection rate, runner cross-section geometry, and the intrinsic property of the material, this parameter does not change along the runner with time. This is proved in the simulation. Results show that the shear rate value in the same area of the runner cross section (at the beginning, middle, and near the cavity gate) remained at the same level, even after MRT application. Figure 8-68 shows the high shear rate values sampled and averaged under different molding conditions. The shear rate values did not undergo an obvious change along the melt flow direction

within the runner. In N66 molding, the shear rate stayed at about 11800 s^{-1}. For PP co MRT molding, the shear rate values were kept at about 7400 s^{-1}. However, as can be observed in the temperature distribution figures, shear variation-induced heating can change or accumulate in the melt flowing along the runner.

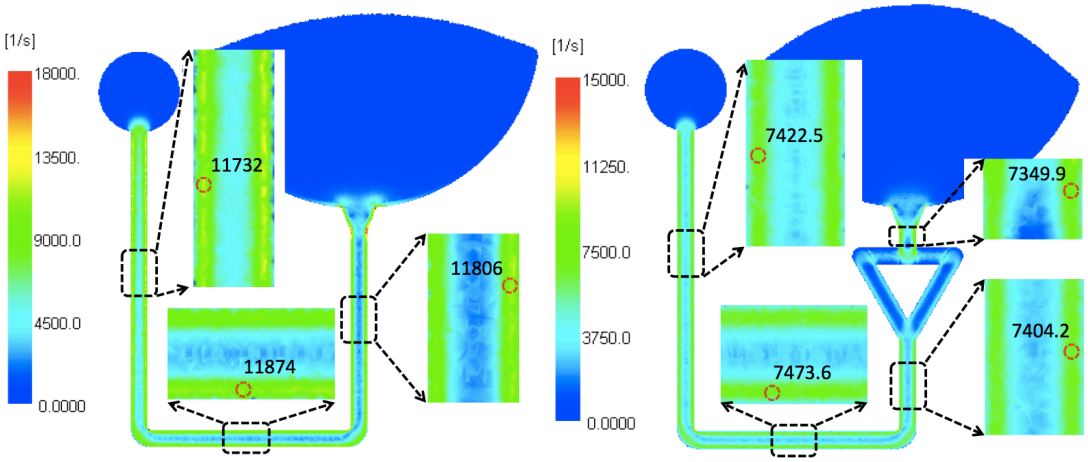

(a) (b)

Figure 8-68. Shear rate values (1/s) sampled along the flow direction in the runner: (a) N66 disc-cavity molding with no MRT, (b) PP co disc-cavity molding with MRT

In this part of the study, the temperature values were sampled in the high shear low shear rate region separately along the melt flow direction, in both the runner and the cavity. The simulating target was N66 disc-cavity molding since simulation results showed that N66 disc-cavity molding does not present an obvious shear imbalanced effect. (Figure 8-69)

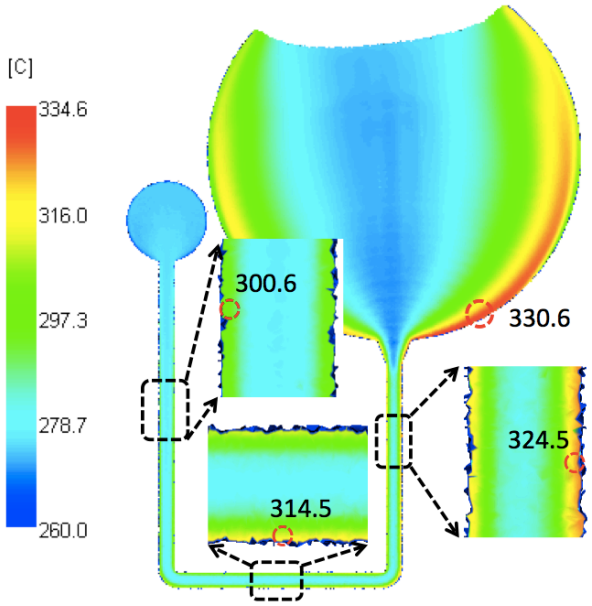

Figure 8-69. Temperature values (°C) sampled along the flow direction in the runner of N66 disc-cavity molding

In the results shown in Figure 8-69, the temperatures are 300.6°C, 314.5°C, 324.5°C, and 330.6°C at the sampling points in the high shear region. It is obvious that the temperature increases along the melt flow direction, indicating that the shear history could accumulate in the runner and influence the temperature level. Table 8-12 and Figure 8-71 presents the values of temperature vs. time in the high and low shear region during injection molding. (Figure 8-70 gives the sampling points according to time.)

Table 8-12. Sampled temperature values over time during N66 disc-cavity molding

Sampling Point	Injection Time (sec)	Temperature (°C)	
		High Shear Region	Low Shear Region
1	0.176	287.4	276.2
2	0.180	295.8	277.9
3	0.185	304.8	279.3
4	0.193	310.5	281.5
5	0.199	319.8	283.3
6	0.207	320.7	286.1
7	0.212	324.5	287.1
8	0.222	329.8	275.4
9	0.245	328.8	272.6
10	0.285	326.1	272.8
11	0.315	318.7	273.0
12	0.335	311.5	273.9

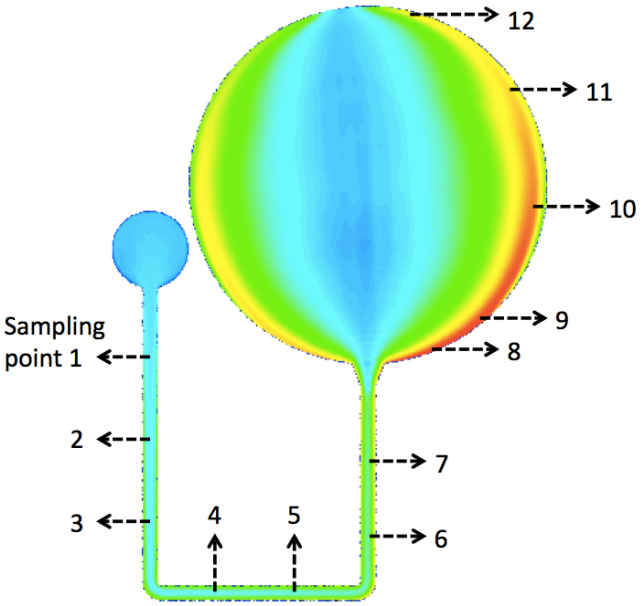

Figure 8-70. Sampling points in runner and cavity over time during N66 disc-cavity molding

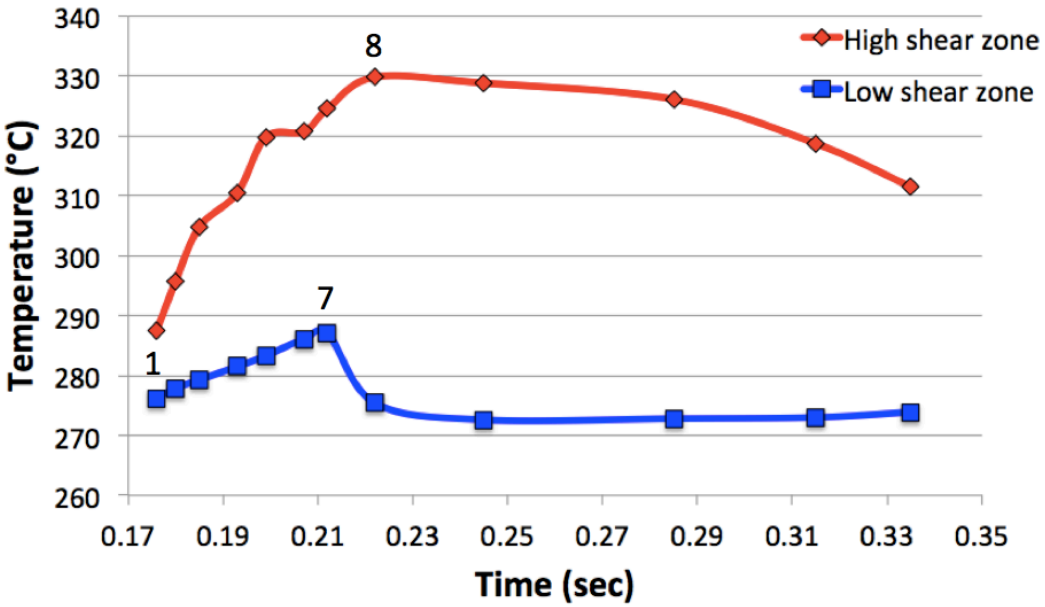

Figure 8-71. Temperature values sampled in the high shear region and the low shear region along the flow direction in the runner of N66 disc-cavity molding

When the melt flows in the runner and into the cavity, the temperature increases increased from 287.4°C (at point 1) to 329.8°C (at point 8) in the high shear region, while the temperature only increases from 276.2°C (at point 1) to 287.1°C (at point 7) in the low shear region. In the high shear region, the temperature variation is about 42.4°C, which is larger than the temperature variation (10.9°C) in the low shear region.

For the high shear rate flow in the cavity, it may have higher temperatures and slower cooling procedures, leading to a longer cooling and crystallization time. This also influences other related properties of the molded products. It could also be conclude that the shear heating was more effective in the high shear region and the heating result could be accumulated in the runner along the melt flow direction. The temperatures started to decrease when the melt flow filled about 1/3 of the cavity and upon further cooling.

In this section of the research, it has been shown that the simulations agree well with the actual injection molding results. The simulations duplicated results of the actual cavity filling processes in terms shear rate, viscosities, and temperature distributions. The results, from a theoretical aspect, support the shear imbalance theory.

9 Conclusions and Future Recommendations

9.1 Melt Rotation Studies

In this component of the research, it was shown that polymer products manufactured through injection molding with traditional runner systems can exhibit a spatial range of properties due to shear induced imbalanced melt flow generated within the runner system. The study showed that the degree of spatial property deviation can be significant, and depends on the material, process, and cavity/product geometry.

The investigation demonstrated that Melt Rotation Technology was capable of rearranging the product level effects of shear induced melt flow imbalances in runner systems. If applied appropriately, this can be used to redistribute (or reduce, if desired) the regional intra-product or inter-product disparity of important thermal and mechanical properties throughout molded products. Further experimentation should be planned that will more deeply explore this new potential of melt rotation technology to optimize the outcome of injection molding processes.

The results of both single-cavity molding and multi-cavity molding were greatly influenced by the shear history of the melt flow and the injection molding speed. Clearly, for some of the investigated materials, a faster injection molding speed, with no MRT involved, leads to the apparent shape distinctions of the molding products, and the melting temperature variations.

In this study, it was demonstrated that the shear induced imbalance effect, significantly influenced the characteristics of the final products via traditional injection molding. The high crystallinity, the high melting temperature and the low content of the β crystals were present in the high shear regions, especially in the iPP sample.

The preliminary testing data has also shown that, with the application of MRT, the shape distinction was evened at the sample ending tips. Additionally, the technology could be used to yield a more uniform distribution of crystallinity, leading to the related results of more identical melting temperatures and crystal components for the most of the materials in the current study.

There are still a lot of aspects in the work to further explore. The next phase of the work will be concentrated on exploring more MRT potential of modifying the results of injection molding using more materials, especially which are highly sensitive to shear heating and shear rate variations. As an example, PS has not been tested in the melt rotation study yet. It would be worth trying to compare the shear imbalanced results of PS to the results of the other materials, as PS is expected to exhibit a more serious response to shear variations. More molding parameters, which should not be limited to just injection rates, runner geometries or cavity conditions, should be utilized appropriately in future works.

9.2 Real-Time Monitoring Studies

The real-time monitoring of the cavity filling processes was successfully achieved by using a custom designed mold system. The insert and runner

modifications to an existing transparent mold were successfully developed to allow for the real-time observations and video recording of shear induced polymer fill imbalances during the injection molding process. Although some of the circular and rectangular geometry insert plate results were not as conclusive as those of the split-cavity geometry insert plate case, there were still consistent evidence of shear induced fill imbalances for all the injection molding cycles. It was also determined that the injection pressure, shot size, runner geometry, and injection velocity had the greatest effects on the injection molding process.

This newly developed real time monitoring system of molding process, allow researchers for the first time, to investigate injection molding from an internal cavity point of view.

This study recognizes that polypropylene has a relatively low sensitivity to shear induced filling effects. However its ease of processing provided good feedback regarding the potential for its use in the custom built mold with transparent windows. Together with the study using polystyrene, this proof of concept device provides the foundation for further work that would include improvements to the mold and cavity, more strategic design of the flow paths, use of other runner geometries, use of different molding parameters, and use of materials such as PBT, nylon or other shear sensitive materials. These improvements would allow future work to better represent the significant shear induced problems regularly seen in industry.

As the melt flow path in the cavity, especially in the single-cavities, was not very clear for direct observation, fluorescent or colored ingredients may be added

along the runner or in the mold cavity. This will allow for facilitate observation of the melt flow path during the cavity filling process.

References

[1] A. B. Strong, Plastics: Materials and Processing (3rd Edition), 2006.

[2] "Transparency Market Research," [Online]. Available: http://www.transparencymarketresearch.com.

[3] J. P. Beaumont, Runner and Gating Design Handbook, vol. 99, 2004.

[4] J. P. Beaumont, C. Stewart and M. Ezzo, "Controlling Intra-Cavity Melt Flow and Weld Strength through New Runner Design Technology," 2005.

[5] K. Takarada, J. P. Coulter, J. P. Beaumont and M. Myers, "The Effect of Primary Runner Length on Fill-Imbalance in a Geomatrically Balanced Eight Cavity Polymer Injecion Mold," in *ANTEC*, Sharlotte NC, 2006.

[6] J. Beaumont, "Molding High-Precision Parts in High-Cavitation Molds," MoldMaking Technology, 2001.

[7] J. Beaumont, "New Runner-Design Concept Boosts Quality & Productivity," *Plastics Technology,* April 2001.

[8] D. C. Angstadt, C. H. Gasparian, J. P. Coulter and R. A. Pearson, "In-Situ Observation of Birefringence during Vibration-Assisted Injection Molding," *ANTEC Conference Proceedings,* vol. 1, pp. 783-787, 2004.

[9] D. C. Angstadt and J. P. Coulter, "In-Situ Observation of Orientation during Injection Molding with A Delayed packing Stage," in *ANTEC*, Boston, 2005.

[10] "Wikipedia," [Online]. Available: http://en.wikipedia.org/wiki/Injection_molding.

[11] Q. Li, "Biodegradation Study of Polymeric Material with Various Levels of Molecular Orientation Induced via Vibration-Assisted Injection Molding," *Master Thesis,* 2011.

[12] D. V. Rosato, D. V. Rosato and M. G. Rosato, Injection Molding Handbook, 3rd ed., Kluwer, 2000.

[13] P. A. L. R. J. Young, "Introduction to Polymers," p. 10, 1991.

[14] "How Plastics Are Make," 25 May 2000. [Online]. Available: http://www.plasticsresource.com/plastics_101/manufacture/how_plastics_are_made.html.

[15] G. W. Ehrenstein and R. P. Theriault, Polymeric Materials: Structure - Properties - Applications, Hanser Verlag, 2001, pp. 67-78.

[16] George, "Spherulite figure after Odian," in *Principles of Plymeriazation*, New York, John Wiley & Sons, 1991, p. 27.

[17] A. Keller, M. Warner and A. H. Windle, Self-order and Formin PolymericMaterials, London: Chapman& Hall, 1995.

[18] J. E. Mark, Polymer Data Handbook, London: Oxford Univ. Press, 1999.

[19] "pp molecule tacticity," [Online]. Available: http://steinwall.com/pages/Polypropylene.

[20] J. A. Brydson, Plastics Materials, 7th ed., BH, 1999.

[21] "nylon 66 chain," [Online]. Available: http://www.chinafilament.com/html/2014/daminews_1224/88.html.

[22] "ester group in pet," [Online]. Available: https://commons.wikimedia.org/wiki/File:Polyethylene_terephthalate.svg.

[23] E. Piorkowska and G. C. Rutledge, Handbook of Polymer Crystallization, John Wiley & Sons, 2013.

[24] K. J. A. Storcks, *Chem. Soc.,* vol. 60, no. 1753, 1938.

[25] W. Schlesinger and H. J. Leeper, *Polym. Sci.,* vol. 11, no. 203, 1953.

[26] R. Jaccodine, *Nature,* vol. 176, no. 305, 1955.

[27] P. J. Till, *Polym. Sci.,* vol. 24, no. 301, 1957.

[28] A. Keller, *Phil. Mag.,* vol. 2, no. 1171, 1957.

[29] E. Z. Fischer, *Naturforsch.,* vol. 12a, no. 753, 1957.

[30] J. W. Gibbs, The scientific works of J. Willard Gibbs, vol. I, New York:

Longmans Green, 1906, p. 219.

[31] B. Wunderlich, "Crystal Nucleation, Growth Annealing," *Macromolecular Physics,* vol. 2, 1976.

[32] G. Cao, "Nanostructures & Nanomaterials: Synthesis, Properties & Applications".

[33] H. Keith and F. J. Padden, *J. Appl. Phys.,* vol. 35, no. 1270, 1964.

[34] J. Marentette and G. Brown, *J. Chem. Edu.,* vol. 70, no. 435, 1993.

[35] F. Price, *J. Polym. Sci.,* vol. 37, no. 71, 1959.

[36] H. Keith, F. J. Padden and R. Vadimisky, *J. Polym. Sci. Part A-2,* vol. 4, no. 267, 1966.

[37] C. E. Carraher, Seymour/Carraher's polymer chemistry, CRC Press, 2003, p. 43–45.

[38] G. Menges, E. Haberstroh and . W. Michaeli, Ernst Schmachtenberg: Plastics Materials Science, Hanser Verlag, 2002.

[39] T. Kobayashi and L. Broutman, *Polym. Eng. Sci.,* vol. 14, no. 260, 1974.

[40] "BASF AG," [Online]. Available: www.basf.com.

[41] W. Woebcken and K. Stöckhert, HBP Gupta: Plastics Encyclopedia, Hanser Verlag, 1998.

[42] E. A. Campo, The Complete Part Design Handbook, Hanser, 2006.

[43] C. Paolucci, "Simple Models that Predict Shear-Thinning Behavior in Dilute Polymer Fluids".

[44] "Viscosity of Newtonian and non-Newtonian Fluids," RheoSense, [Online]. Available: http://www.rheosense.com/applications/viscosity/newtonian-non-newtonian.

[45] J. Vlachopoulos and D. Strutt, "The Role of Rheology in Polymer Extrusion," Hamilton, Ontario, Canada.

[46] SABIC, "HIGH & LOW SHEAR RATE RHEOLOGY," *INNOVATIVE PLASTICS.*

[47] C. Mnekbi, M. Vincent and J.-F. Agassant, "Polymer rheology at high shear rate for microinjection moulding," in *ESAFORM Conference on Material Forming*, Brescia, Italy, 2010.

[48] R. Shankar Subramanian, "Non-Newtonian Flows".

[49] K. R. Slye, J. P. Coulter, B. Bekisli and T. J. Skiba, "The Effect of Melt Rotation Technology on Particle Distribution during Injection Molding," in *ANTEC*, Boston MA, 2011.

[50] Q. Li, J. P. Coulter, J. P. Beaumont and R. M. Alicyn, "Influences of Melt Rotation Technology on Polymeric Material Injection Molding Process and Final

Product Properties," *ANTEC,* 2015.

[51] Q. Li, S. R. Choo, J. P. Coulter, J. P. Beaumont and A. M. Rhoades, "An Investigation of Real-Time Monitoring of Shear Induced Cavity Filling Imbalances during Polymer Injection Molding," in *ANTEC*, Indianapolis, 2016.

[52] Beaumont Technologies, Inc., "BTI and Moldex3D Provide The Most Advanced Solutions For Runner Design," vol. No. 14, March 2006.

[53] Q. Li, J. P. Coulter, J. P. Beaumont and A. M. Rhoads, "Effects of Melt Rotation on Resulting Localized Material Properties throughout Injection Molded Polymeric Products," in *ANTEC*, Las Vegas, 2014.

[54] J. P. Beaumont, J. H. Young and M. Jaworski, *Journal of Injection Molding Technology,* vol. 18, p. 572, 1999.

[55] D. T. Leighton and A. Acrivos, *Fluid Mechanics,* vol. 177, p. 109, 1987.

[56] D. T. Leighton and A. Acrivos, *Fluid Mechanics,* vol. 181, p. 415, 1987.

[57] R. J. Phillips, R. C. Armstrong, R. A. Brown, A. L. Graham and J. R. Abbott, *Phys. Fluids,* vol. 4, p. 30, 1992.

[58] Y. C. Lam, X. Chen, K. W. Tan, M. Jan, K. C. Tam and S. C. Yu, *Journal of Injection Molding Technology,* vol. 6, p. 45, 2002.

[59] I. M. Krieger, *Adv. Colloid Interface Sci.,* vol. 3, p. 111, 1972.

[60] M. Allende and D. M. Kalyon, *Journal of Rheology,* vol. 40, p. 79, 2000.

[61] M. Allende and D. M. Kalyon, *SPE ANTEC,* vol. 45, p. 1130, 1999.

[62] S. Haber and H. Brenner, *International Journal of Multiphase Flow,* vol. 28, p. 1687, 2002.

[63] D. C. Angstadt and J. P. Coulter, "Investigation of Melt Manipulation Phenomena During Injection Molding via in Situ Birefringence Observation," *Polymer Engineering & Science,* vol. 46, no. 12, pp. 1691-1697, December 2006.

[64] "Global PP market to reach 62.4 million metric ton," 9 September 2013. [Online]. Available: http://www.plasticsnews.com/article/20130909/NEWS/130909948/global-pp-market-to-reach-62-4-million-metric-tons.

[65] Chemical Market Associates, Inc., "Polypropylene Market Report & Survey Results," Manufacturers Association for Plastics Processors, 2011.

[66] "Polyethylene Terephthalate (PET)," *Kunststoffe International,* pp. 106-110, 10 2013.

[67] "Polyethylene Terephthalate - PET Resin & Polybutylene Terephthalate - PBT Resin Market by PET Application, by PBT Application – Global Trends & Forecast to 2019," MarketsandMarkets, 2014.

[68] "Melt Flow Rate (MFR) of Plastics, MISUMI Technical Tutorial," MISUMI Corporation, 13 Jan 2012. [Online]. Available: http://www.misumi-techcentral.com/tt/en/mold/2012/01/107.html.

[69] D. Tripathi, "Rheology," *Practical Guide to Polypropylene,* pp. 76-80, 2002.

[70] S. Paul and D. D. Kale, "Rheological Study of Polypropylene Copolymer/Polyolefinic Elastomer Blends," *Journal of Applied Polymer Science,* vol. 84, pp. 665-671, 7 July 2011.

[71] W. Martienssen and H. Warlimont, Handbook of Condensed Matter AndMaterials Data, Frankfrut: Springer, 2005.

[72] Wiley-VCH, Ullmann's Polymers and Plastics: Products and Processes, John Wiley & Sons, 2016.

[73] "NYPLA Industrial Co., Ltd," [Online]. Available: http://www.nypla.com/en/ub.phtml.

[74] D. Nichetti and I. Manas-Zloczower, "Viscosity model for polydisperse polymer melts," *J. Rheol.,* vol. 42, no. 4, pp. 951-968, 1998.

[75] L. J. Fetters, D. J. Lohse, D. Richter, T. A. Witten and A. Zirkel, "Connection between Polymer Molecular Weight, Density, Chain Dimensions, and Melt Viscoelastic Properties," *Macromolecules,* vol. 27, no. 17, p. 4639–4647, 1994.

[76] M. Sepe, "Density & Molecular Weight in Polyethylene," *Plastics Technology ,*

June 2012.

[77] "Molecular Weights," [Online]. Available: http://pslc.ws/macrog/weight.htm.

[78] "Intrinsic viscosity of a polymer and its density," Physics Forums, [Online]. Available: https://www.physicsforums.com/threads/intrinsic-viscosity-of-a-polymer-and-its-density.762933/.

[79] R. Zheng, R. I. Tanner and X. Fan, Injection Molding: Integration of Theory and Modeling Methods, Springer, 2011.

[80] J. Bicerano, Prediction of Polymer Properties, New York: Marcel Dekker, Inc., 2002.

[81] J. Beaumont and D. A. Hoffman, "A New Look at Evaluating Fill Times For Injection Molding," *Plastics Technology,* 2013.

[82] W. J. Sichina, "DSC as Problem Solving Tool: Measurement of Percent Crystallinity of Thermoplastics," PerkinElmer Instruments.

[83] R. L. Blaine, "THERMAL APPLICATIONS NOTE, Polymer Heats of Fusion".

[84] B. Rawlings, "Crystallinity in Polymers," 2009.

[85] J. A. Currie, E. M. Petruska and R. W. Tung, Heat of Fusion of Crystalline Polypropylene by Volume Dilatometry and Differential Scanning Calorimetry.

[86] "Flash Differencial Scanning Calorimetry for Research and Development,"

Mettler-Toledo International Inc..

[87] T. Sterzynski, P. Calo, M. Lambla and M. Thomas, "Trans- and Dimethyl Quinacridone Nucleation of Isotactic Polypropylene," *Polymer Engineering and Science,* vol. 37, no. 12, pp. 1917-1927, December 1997.

[88] P. Tordjeman, C. Robert, G. Martin and P. Gerard, "The Effect of α, β Crystalline Structure on The Mechanical Properties of Polypropylene," *The European Physical Journal E,* vol. 4, no. 4, pp. 459-465, April 2001.

[89] F. J. Padden and H. D. Keith, *Applied Physics,* vol. 30, p. 1485, 1959.

[90] A. Romankiewicz, T. Sterzynski and W. Brostow, "Structural Characterization of α- and β-Nucleated Isotactic Polypropylene," *Polymer International,* vol. 53, pp. 2086-2091, 2004.

[91] J. Broda, "WAXS investigations of Mass-coloured Polypropylene Fibers," *Fibers & Textiles in Eastern Europe,* vol. 11, no. 5, pp. 115-119, January/December 2003.

[92] G. Subramanian and R. Ozisik, "Simultaneous Estimation of the Phase Content and Lamellar Thickness in Isotactic Polypropylene by the Simulated Annealing of Wide-Angle X-Ray Scattering Data," *Journal of Applied Polymer Science,* vol. 117, pp. 2386-2394, 2010.

[93] J. Bao, T. Liu, L. Zhao and G. Hu, "Carbon Dioxide Induced Crystallization for Toughening Polypropylene," *Industrial & Engineering Chemistry Research,* vol.

50, pp. 9632-9641, 2011.

[94] Y. H. Chen, G. J. Zhong, Y. Wang, Z. M. Li and L. Li, "Unusual Tuning of Mechanical Properties of Isotactic Polypropylene Using Counteraction of Shear Flow and β-Nucleating Agent on β-Form Nucleation," *Macromolecules,* vol. 42(12), pp. 4343-4348, 2009.

[95] D. G. Papageorgiou, D. N. Bikiaris and K. Chrissafis, "Effect of crystalline structure of polypropylene random copolymers on mechanical properties and thermal degradation kinetics," *Thermochimica Acta,* vol. 453, p. 288–294, 2012.

[96] "poly(oxymethylene)," PolymerProcessing.com, [Online]. Available: http://www.polymerprocessing.com/polymers/POM.html.

[97] "polypropylene," PolymerProcessing.com, [Online]. Available: http://www.polymerprocessing.com/polymers/PP.html.

[98] J. T. Uan-Zo-li, "Morphology, Crystallization and Melting Behavior of Propylene-Ethylene Statistical Copolymers," Blacksburg, Virginia, 2005.

[99] "poly(butylene terephthalate)," PolymerProcessing.com, [Online]. Available: http://www.polymerprocessing.com/polymers/PBT.html.

[100] J. Karger-Kocsis, Polypropylene Structure, blends and composites, vol. 1, Chapman & Hall, 1995.

[101] M. Amon, "β Nucleating Agents for Polypropylene," 30 January 2015.

]

[102] J. Varga, I. Mudra and G. Ehrenstein, "Highly active thermally stable β nucleating agents for isotactic polypropylene," *J. Appl. Polym. Sci.,* vol. 74, p. 2357–2368, 1999.

[103] E. Devaux and B. Chabert, "Nature and origin of the trancrystalline interphase of polypropylene glass–fiber composites after a shear–stress," *Polym. Commun.,* vol. 31, p. 464–468, 1991.

Vita

Qi Li was born on May 4th in Taiyuan, Shanxi, China to Jiangang Li and Sufang Wen. He received a B.S. in Mechanical Engineering and Automation in May of 2009 from Beihang University, and an M.S. in Mechanical Engineering and Mechanics in January of 2012 from Lehigh University. He then continued to pursue his doctorate degree at the same Institution.

Qi has written numerous conference and journal papers. Some of his prominent publications are in the Plastics Engineering Magazine. Qi received a Graduate Student Merit Award for his academic excellence, and exemplary character and leadership in 2014. He has also been obtained multiple awards from The Society of Plastics Engineers, Lehigh Valley Chapter. He has presented his research at both professional conferences and in university lectures. During his graduate study at Lehigh, Qi also served as a teaching assistant at the Department of Mechanical Engineering and Mechanics.

Qi Li was the president of Lehigh University's Chinese Students and Scholars Association from 2012 to 2013, the captain of Lehigh University Chinese Basketball Team and a member of The Lehigh University Choral Union. Qi is very appreciative of his time at Lehigh, and grateful for the knowledge he has gained at the University.